3-6-2009

Wind Tunnel Analysis and Flight Test of a Wing Fence on a T-38

Michael D. Williams

WIND TUNNEL ANALYSIS AND FLIGHT TEST OF A WING FENCE ON A T-38

THESIS

Michael D. Williams, Major, USAF

AFIT/GAE/ENY/09-M20

DEPARTMENT OF THE AIR FORCE
AIR UNIVERSITY

AIR FORCE INSTITUTE OF TECHNOLOGY

Wright-Patterson Air Force Base, Ohio

AFIT/GAE/ENY/09-M20

WIND TUNNEL ANALYSIS AND FLIGHT TEST OF A WING FENCE ON A T-38

THESIS

Presented to the Faculty

Department of Aeronautical and Astronautical Engineering

Graduate School of Engineering and Management

Air Force Institute of Technology

Air University

Air Education and Training Command

In Partial Fulfillment of the Requirements for the

Degree of Master of Science in Aeronautical Engineering

Michael D. Williams, BS

Major, USAF

March 2009

AFIT/GAE/ENY/09-M20

WIND TUNNEL ANALYSIS AND FLIGHT TEST OF A WING FENCE ON A T-38

Michael D. Williams, BS
Major, USAF

Approved:

//signed//	6 Mar 09
Dr. Mark F. Reeder, PhD (Chairman)	Date
//signed//	6 Mar 09
LtCol Christopher M. Shearer, PhD (Member)	Date
//signed//	6 Mar 09
LtCol Richard D. Branam, PhD (Member)	Date

Abstract

A low-speed wind tunnel study and flight tests were performed to examine the effects of a wing fence on the T-38A. Wind tunnel results were based upon force and moment data collected with a six-component balance and flow visualization at Reynolds numbers up to 0.3×10^6, based on mean aerodynamic chord. The model did not include the last 7.79 feet of the aircraft, and the engine and exhaust were modeled as through-holes. Five fence geometries, placed at wing station 125 (±0.825 semispan), were compared. The best performer of these designs, based on drag polar, was the fence that wrapped the leading edge and extended 84.6 percent of the local chord length along the wing's upper surface. Wind tunnel data showed that this fence increased the lift coefficient by up to 6.3 ± 0.6 percent and reduced spanwise and separated flow outboard the fence. The flight-tested fence was based on the best performing fence design from the wind tunnel study. The results were based on aircraft instrumentation and flow visualization at Reynolds numbers up to 9.98×10^6. It was inconclusive whether the fence caused an increase in lift coefficient. The fence reduced the roll-off tendency and wing rock during approaches to stall. Tuft visualization on the aircraft wing suggested that the fence reduced spanwise and separated flow outboard the fence, which agreed with the wind tunnel results.

Acknowledgments

I owe a great deal of gratitude to all those who supported me through this process. I would like to express my sincere appreciation to my faculty advisor, Dr. Mark Reeder, for his direction, help, and support throughout the course of this thesis effort. Additionally, I am extremely appreciative of Dr. Hugh Thornburg for helping me keep this project on time. His efforts were essential in completing the computer drawing work required to get the model printed and into the tunnel. Special thanks go to Rudy Johnson of AFRL/RBAI who supplied the original T-38 drawing data. Thanks to Jay Anderson, Chris Zickefoose, John Hixenbaugh, and LtCol Raymond Maple for their help along the way. Thanks to Roger Tanner with whom the idea originated. Thanks to team Ocho Lift from TPS class 08A for their efforts. Finally, a special thanks to my wife and family for their support and prayers throughout this process.

Michael D. Williams

Table of Contents

List of Figures

Page

Page

Page

Page

Page

Page

Page

Page

List of Tables

List of Symbols

A	Axial load force	lbs
AFB	Air Force Base	---
AFIT	Air Force Institute of Technology	---
AFFTC	Air Force Flight Test Center	---
ANOVA	Analysis of Variance	---
AOA	Angle of attack	deg
AR	Aspect ratio	---
a_x	Body longitudinal acceleration	ft/sec^2
a_y	Body lateral acceleration	ft/sec^2
a_z	Body normal acceleration	ft/sec^2
b	Wing span	in
CFD	Computational Fluid Dynamics	---
CG	Center of gravity	in
C_D	Drag coefficient	---
C_{Do}	Minimum drag coefficient	---
C_L	Lift coefficient	---
C_{Lmax}	maximum lift coefficient	---
C_m	Pitching moment coefficient	---
C_{mcg}	C_m relative to reference CG	---
D	Drag	lbs
DAS	Data Acquisition System	---
FLTS	Flight Test Squadron	---
F_e	Propulsive drag	lbs

F_g	Gross thrust	lbs
F_N	Net thrust	lbs
G	Gravity	ft/sec^2
gal	Gallon	---
GPM	Gallons Per Minute	gal/min
IAW	In Accordance With	---
IRIG	Inter-Range Instrumentation Group	---
i_t	Thrust incidence angle	deg
KCAS	Knots Calibrated Airspeed	kts
L	Lift	lbs
L/D	Lift-to-drag ratio	---
$(L/D)_{max}$	Maximum lift-to-drag ratio	---
$L_{x\alpha}$	Distance from center of gravity to AOA vane	feet
l_{xx}	X-distance from cg to x-accelerometer	in
l_{xz}	X-distance from cg to z-accelerometer	in
l_{zx}	Z-distance from cg to x-accelerometer	in
l_{xz}	Z-distance from cg to z-accelerometer	in
MIL	Military power	---
N	normal load force	lbs
N_{xaccel}	Longitudinal load factor at x-accelerometer	---
N_{zaccel}	Normal load factor at x-accelerometer	---
N_{xcg}	Longitudinal load factors corrected for cg	---
N_{zcg}	Normal load factors corrected for cg	---
PA	Pressure Altitude	feet

PMP	Propulsion Modernization Program	---
PSIA	pounds square inch, absolute	lbs/in^2
p_{xx}	X axis distance to x-accelerometer	in
p_{xz}	X axis distance to z-accelerometer	in
p_{zx}	Z axis distance to x-accelerometer	in
p_{zz}	Z axis distance to z-accelerometer	in
q	Pitch rate	deg/sec
q	Dynamic pressure	lbs/ft^2
r	Yaw Rate	deg/sec
R	Turn radius	feet
Re	Reynolds number	---
RPM	Revolutions Per Minute	---
S	Aerodynamic reference area	ft^2
SETOS	Single Engine Takeoff Speed	kts
TIM	Technical Information Memorandum	---
TMP	Test Management Project	--
TPS	Test Pilot School	--
USAF	United States Air Force	---
V	Airspeed	ft/sec
W	Weight	lbs
WPAFB	Wright-Patterson Air Force Base	---
α	Angle of attack	deg
α_t	True angle of attack	deg
α_u	Upwash angle of attack	deg

α_v	Vane angle of attack	deg
δ	blockage correction factor	---
λ	wind tunnel aspect ratio	---
θ	Pitch attitude	deg
ρ	Ambient air density	slugs/ft^3
γ	Flight path angle	deg

WIND TUNNEL ANALYSIS AND FLIGHT TEST OF A WING FENCE ON A T-38

I. Introduction

1.1 Background

Northrop Grumman built the T-38 Talon and delivered more than 1,100 aircraft. It first flew in March 1959 and was fielded in 1961. As of January 2006, approximately 509 aircraft remained in service (31). The aircraft is undergoing several programs designed to increase its structural service life to 2020, improve training, increase thrust, and improve engine reliability and maintainability. These programs included Pacer Classic, Wing Life Improvement Program, Avionics Upgrade Program, and Propulsion Modernization Program (PMP) (31). Because the aircraft was expected to have an extended service life, it made sense to research a modification to the T-38 that might reduce approach and touchdown speeds (reduced vehicle wear) and improve approach-to-stall characteristics.

The T-38 was 46 feet and 4 inches long with a wing span of 25 feet and 3 inches. The T-38A had a takeoff gross weight of approximately 12,500 pounds. It was powered by two J85-GE-5 turbojet engines with afterburners capable of producing 2,900 pounds of thrust each (3,300 pounds with the PMP modification). These engines pushed the aircraft to a maximum level-flight speed of approximately 1.26 Mach. Maximum permissible symmetric load factors were -3.0 to 7.33 g's (30).

The T-38 Talon has fulfilled many roles because of its "design, economy of operations, ease of maintenance, high performance, and exceptional safety record" (31).

As a trainer, it has provided more than 60,000 pilots with their wings and is used for the Introduction to Fighter Fundamentals (IFF) course to prepare pilots for the Replacement Training Unit (RTU) (14). It is used to train test pilots and flight test engineers at the United States Air Force (USAF) Test Pilot School (TPS) and as an astronaut trainer by the National Aeronautics and Space Administration (NASA). It was even used as the aircraft of choice by the USAF Thunderbirds from 1974 to 1983 (14).

1.1.1 T-38 High Angle of Attack and Wing Characteristics.

As with many aircraft, the Talon has room for improved high angle of attack (AOA) performance and handling qualities. Ultimately, such improvements can improve training, safety, and life-cycle cost. The primary focus here is on lift coefficient (C_L) and approach-to-stall characteristics. The T-38 rigid wing-and-body model lift curve is shown in Figure 1. The maximum lift coefficient (C_{Lmax}) is undefined in this figure with the flaps up. However, with the flaps full down (45 degrees), C_{Lmax} is approximately 1.01, and with the flaps 45 percent down (20 degrees), C_{Lmax} is approximately 0.88.

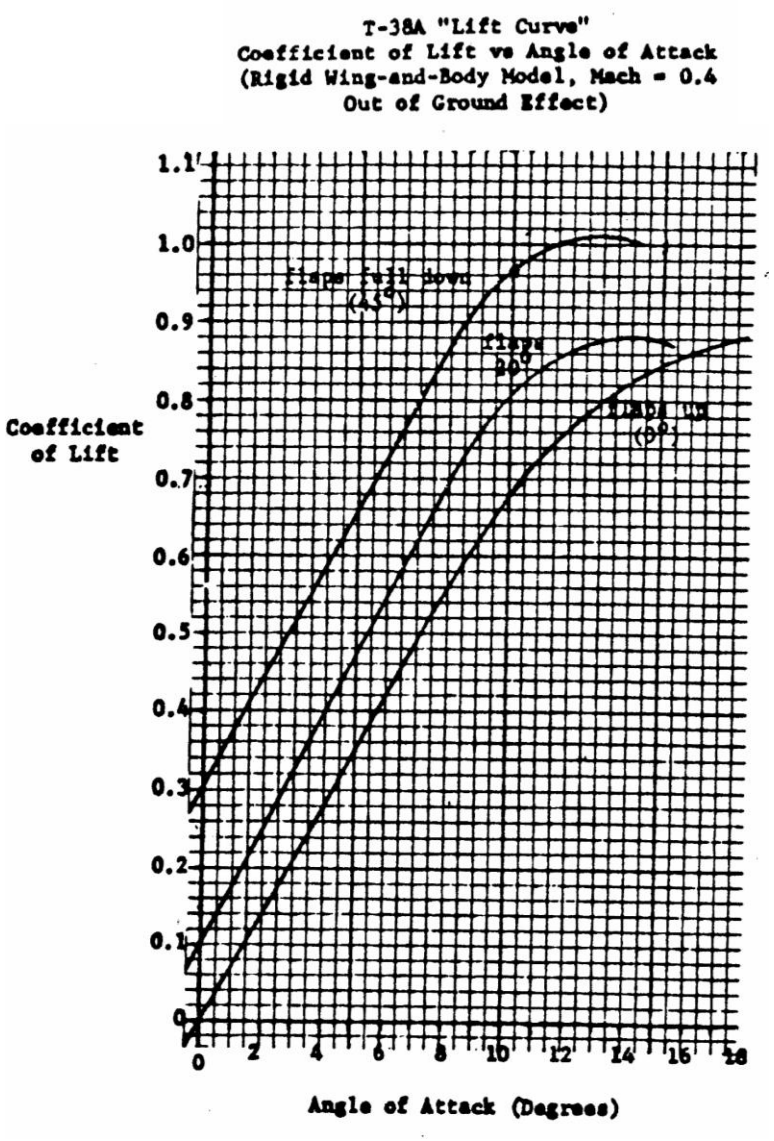

Figure 1. T-38A Lift Curve (20)

In regards to T-38 stall characteristics, the *T-38 Flight Manual* (30) describes stall as follows:

> The stall is characterized by airframe buffet and a high sink rate rather than by a clean nose-down pitch motion. As AOA is increased, there is a corresponding increase in buffet intensity. The buffet is most severe with flaps fully extended. The stall condition is immediately preceded by heavy low-speed buffet and moderate wing rock. The wing rock can be controlled with rudder. The actual stall is normally not accompanied by any abrupt aircraft motion, but is indicated only by the very high sink rate.

USAF TPS provided Figure 2, which allowed for some insight post C_{Lmax}. Note that PA means powered approach (gear and flaps 100 percent down) and CR means cruise (gear and flaps up). In Figure 2, C_m is the pitching moment and cg is center of gravity. Unlike the CR configuration, the PA configuration has a small AOA range with a negative slope. However, the lift coefficient picks back up again and continues to rise. Ultimately, there is not a significant change in lift or pitching moment as AOA is increased, especially compared to an airfoil section like the NACA 23012.

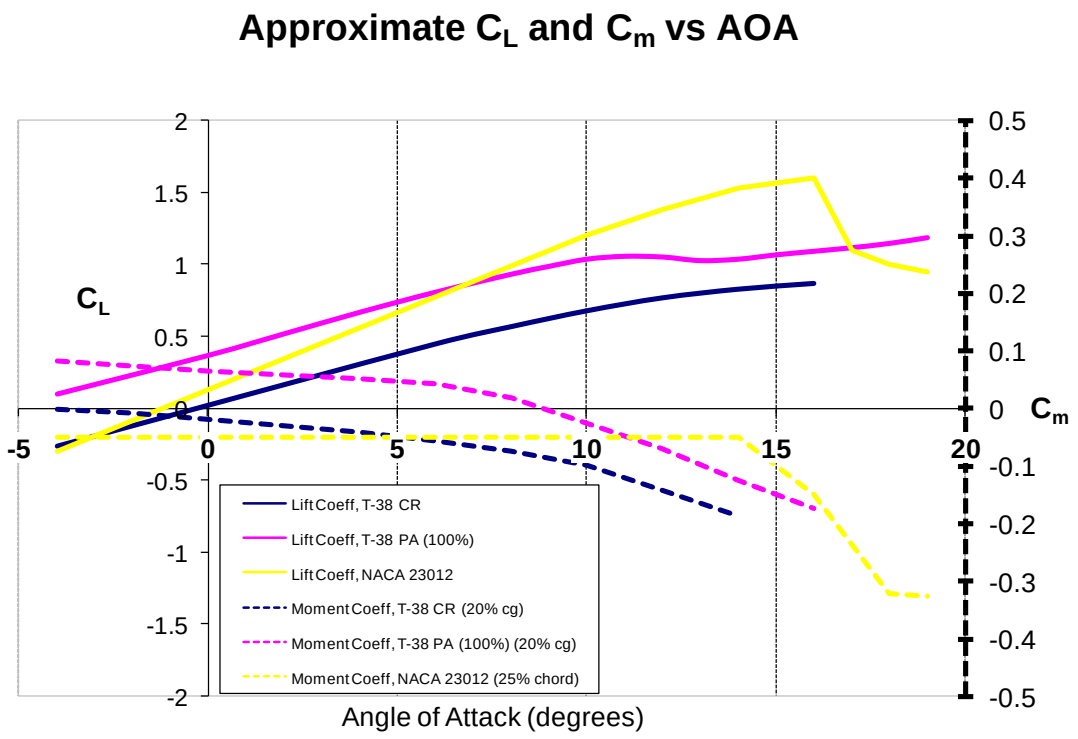

Figure 2. Approximate T-38 Lift and Moment Coefficients (Courtesy of USAF TPS)

This behavior sets the T-38 wing apart from wings composed of more common airfoil sections. The T-38 airfoil was a NACA 65A004.8 with 1 percent chord contrast leading edge droop modified with .65 (50) camber from 0-40 percent chord. A very thin wing, it had an overall thickness ratio of just 4.8 percent and a span-to-thickness ratio of 51.1. The wing span was just 25.25 feet in contrast to the aircraft length of 46.37 feet.

The wing had a mean aerodynamic chord (MAC) of 7.73 feet and an aspect ratio (AR) of just 3.75. It was trapezoidal in shape with a planform area of 170 square feet. The leading edge wing sweep was 32 degrees, and the quarter-chord wing sweep was 24 degrees. Dihedral and incidence angles were both 0 degrees. These characteristics significantly contributed the aircraft's high AOA behavior (20).

1.1.2 Flow Control.

The question became how to improve the high AOA performance and handling qualities without a major redesign. A possible solution was flow control. Flow control devices like wing fences, vortex generators, and winglets are used on numerous aircraft and are often added after the final phase of design. Aircraft have been employing devices such as vortex generators since the 1930's (4). They can be seen today on aircraft such as the C-17 Globemaster III, AV-8B Harrier, and Gulfstream V (6). Wing fences have been used on a myriad of aircraft. One example is the XF-92, which used a combination of fences to stabilize an undesirable pitch-up (8). Another example is the combat capable F-5F as seen in Figure 3. Here, Northrop Grumman concluded that wing fences were worthwhile. This was of great interest since the F-5 and T-38 are very much the same aircraft. Simply put, the F-5 was a beefed up T-38 with bigger engines, capability for stores loading, and a gun. It even used the same wing planform and airfoil except for the addition a wing root leading-edge extension and full-span leading-edge flaps (25). The fences were located at wing station 80.70 and extend along the wing's upper surface from the leading edge to the start of the trailing-edge flap (11). Therefore, the fence length was approximately 80 percent of the local chord length. As estimated from photos in Reference 11, the fence height was approximately two to three inches.

Figure 3. Navy F-5F with Wing Fences (Courtesy of Mr. Dennis Peters)

Lastly, winglets have been used since the 1970s. They are used primarily to take advantage of the resulting increased fuel-efficiency. Lear jets were the first commercial aircraft to use them and many airliners utilize the technology today (16).

The idea to investigate the advantages of adding a wing fence to the T-38 at wing station (WS) 125 was proposed by Roger Tanner, a test pilot in the 416th Flight Test Squadron at Edwards Air Force Base (AFB). The driving force for choosing a wing fence over vortex generators or winglets was the seam located 26.5 inches inboard of the wingtip. This seam spanned the full chord and had a row of fasteners on both sides. These rows of fasteners provided a relatively easy location to attach a fence without making significant aircraft modifications. The seam is depicted in Figure 4.

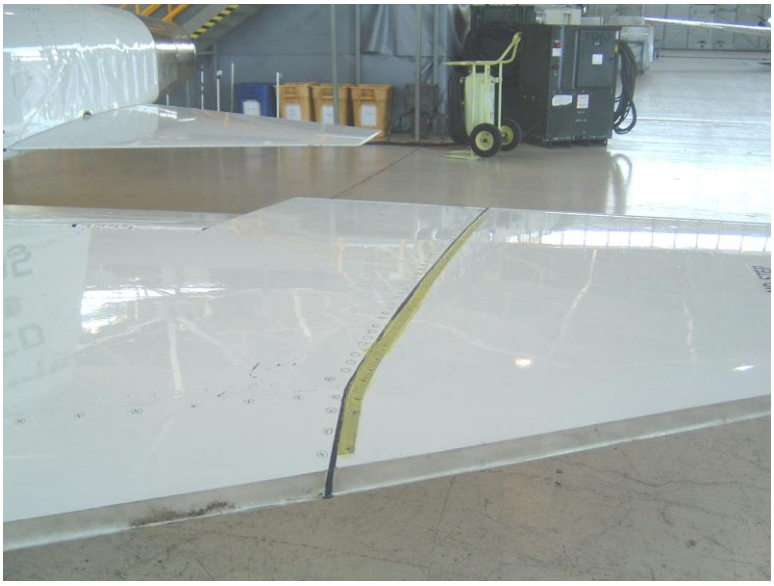

Figure 4. T-38 Wing Seam Located 26.5 Inches from Wingtip

The first step in this investigation was a computational fluid dynamics (CFD) study performed by Solfelt (23). He found that C_L was increased by 4.9 percent at 15 degrees AOA with the flaps fully extended to 45 degrees. He also provided data supporting previous research found in References 18 and 21 that a fence wrapping the leading edge is more effective than one that does not. Lastly, he found that the performance increase was due to increased lift outboard of the fence, primarily caused by two separate vortices.

1.1.3 Fence Success Stories.

The individual credited with the invention of the wing fence is Wolfgang Liebe (18). He received a German patent in 1938 for his work on the Messerschmitt Bf 109B. The stall characteristics of the Bf 109B were peculiar. The stall initiated at the wing root. Due to cross span flow near the leading edge, which traveled outward toward the wing tip at high speed, the entire wing stalled at essentially the same time. This dangerous trait was countered by the installation of a fence that prevented the cross span flow.

Other examples of fence use include the MiG-15, F-86, Fiat G 91 and the BAE Hawk and Harrier. For the SB 13 and Vision 87, undesirable stall, spin, and controllability problems plagued the aircraft. The SB 13's problem, a strong wing over roll moment that led to a spin at increased AOA, specifically arose when its static margin was less than 10 percent. Wing tufts were used to investigate the flow, and the culprit was significant cross flow preceding wing stall. Two wing fences were tested, and the more successful of the two wrapped the leading edge. The cross flow was successfully countered by the use of wing fences (18). Likewise, the Vision 87 had such poor stall characteristics that pilots did not like to fly it at high AOA. Because of the SB 13's success, mid-span fences were tested. The results were excellent, and for all practical purposes, the dangerous stall behavior was eliminated (18). The wing fence has been a widely used device, especially for swept-wing aircraft and was good candidate here.

1.2 Problem Statement

The root question that is to be answered at the conclusion of this report is whether or not wing fences placed at the 82.5 percent spanwise location on each wing improve high AOA performance and approach-to-stall characteristics. Based upon NACA's *Report 1203* (21), performance was not expected to change significantly for fences greater in length than approximately one-third of the local chord. However, because the T-38's stall begins at the tip and works in toward the root, it was unclear whether this was true for the T-38. Wind tunnel runs and flight tests were needed to validate CFD results from Solfelt. The goal of this work, including wind tunnel tests and flight tests, was to clarify these issues.

1.3 Research Focus

Research on the wing fence for the T-38 was structured as a three-tiered approach. Ensign Dan Solfelt accomplished the preliminary CFD modeling, and this research encompassed more advanced modeling, wind tunnel experimentation, and flight testing. Flight testing was completed by a five member team from USAF TPS Class 08A (36).

Metrics for success included the following:

- Increased C_L at given AOA
- Low price in C_D for increased C_L
- Decreased approach and stall speeds
- Reduced wing rock and buffet during the approach to stall

These improvements would enhance safety, training, and life-cycle cost. Lastly, contributing to the understanding of the physics behind wing fences would be beneficial to future aircraft designs.

The wind tunnel model, modified from geometry courtesy of AFRL/RBAI and produced on AFIT's Objet Eden™ 500V rapid prototype machine, was 22.05 inches long, had a wing span of 14.43 inches, and weighed 3.3 pounds. It was a 1:21 scale model that did not include the tail. The omitted length was the last 4.45 inches of the model, which was equivalent to the last 7.79 feet of the aircraft. The tail was left off of the model because the provided geometry did not include this portion of the aircraft and the information needed to complete it was not available. With the help of Dr. Hugh Thornburg of AFRL/RCM, the provided drawings were modified to create a usable model. A photograph of the model is shown in Figure 5 and a 3-D graphical representation from Magics, rapid prototyping software, is shown in Figure 6.

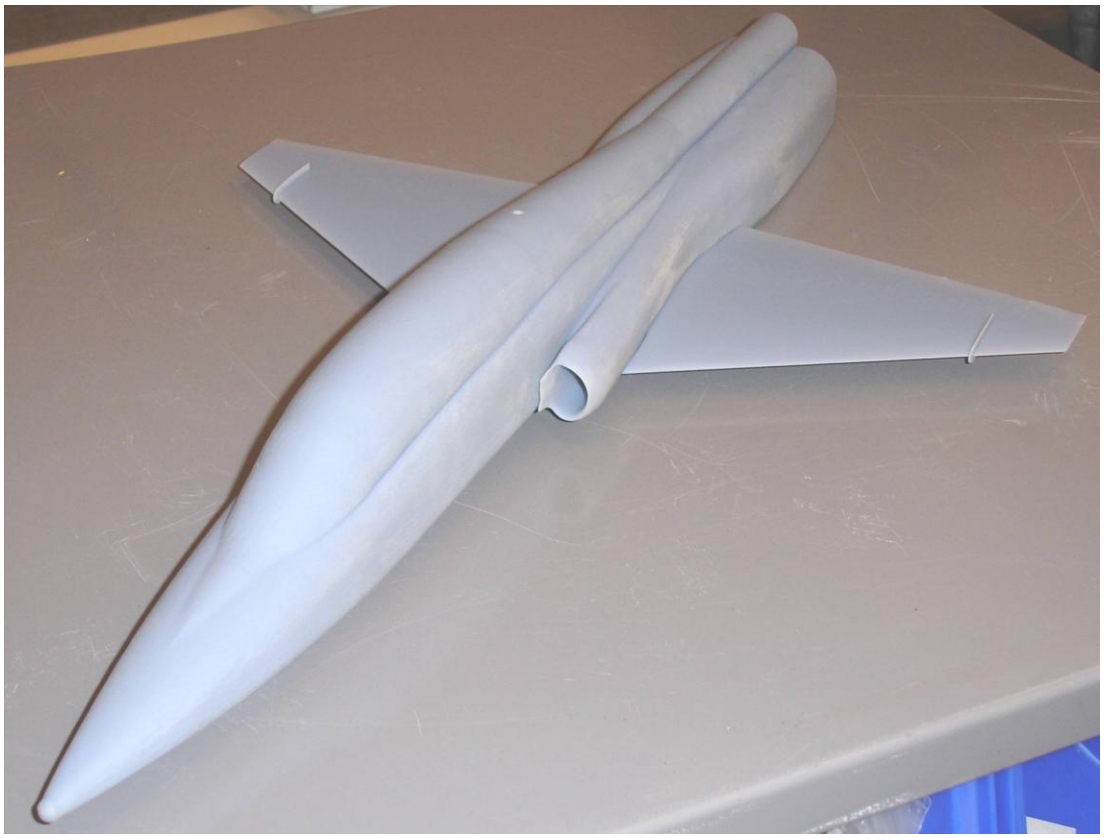

Figure 5. Photograph of T-38 Wind Tunnel Model with a Test Fence Installed

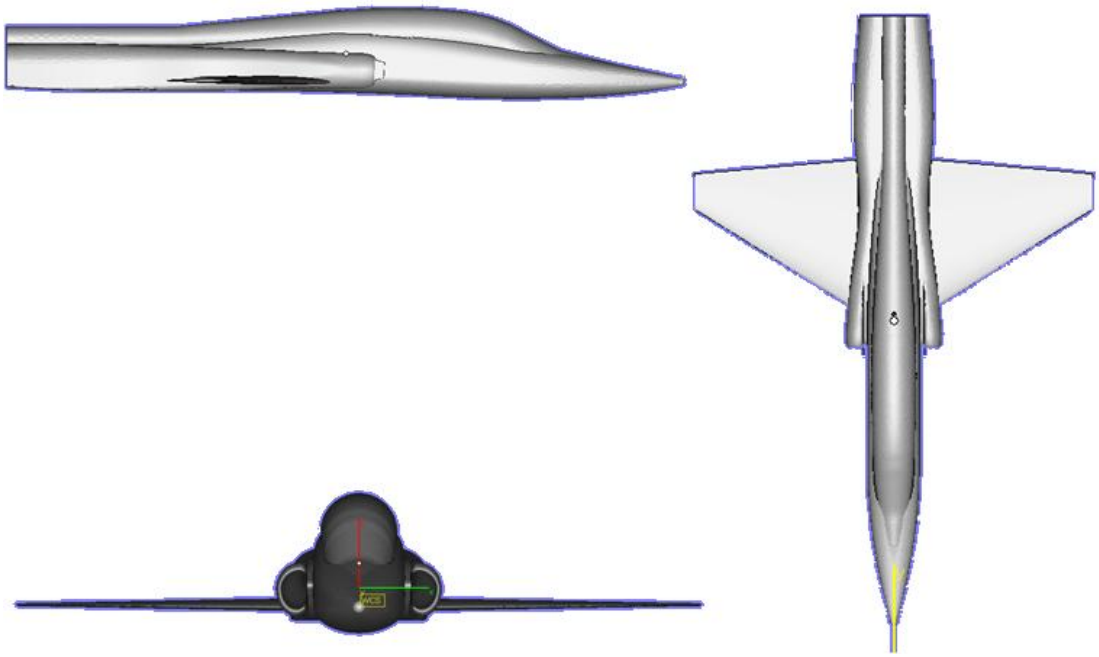

Figure 6. Three-View Representation of T-38 Baseline Model

The wind tunnel analysis compared five fence designs (see Chapter III) with the clean wing. The fence design that was the best performer from the wind tunnel study was used for flight test. The wing fence was attached to the T-38 at wing station 125 or 26.5 inches inboard from the wing tip on both wings. The pre-existing attachment line at this wing station was used to attach the fence to the top and bottom surfaces of the wing. The aircraft's wing span was not increased by the addition of the fences. The wing fence extended from the leading edge to 84.6 percent of the local chord length on the upper surface of the wing. The wing fence wrapped the leading edge and extended from the leading edge to 24.2 percent of the local chord length on the lower surface of the wing. It had a constant height of 2.5 inches above the wing's surface. Each wing fence was made from two pieces of 6061-T6 aluminum. Both pieces were 0.25 inches thick and were welded together. The wing fence was attached to the wing using 18 of the existing wing tip fastener locations. More details may be found in the AFFTC modification package, *T-38 Wing Fence*, M08A205A (1). Figures 7 and 8 depict the flight tested wing fence as a drawing and as installed on the aircraft.

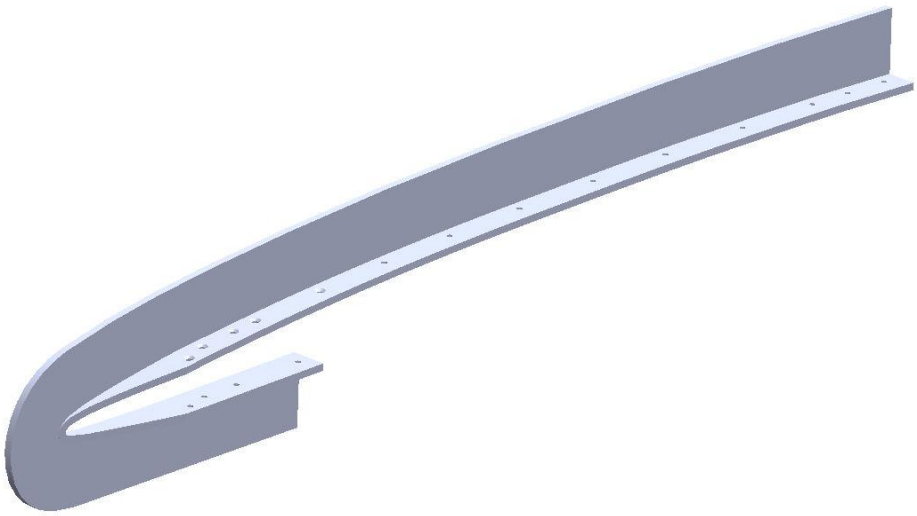

Figure 7. Drawing of Flight Test Left Wing Fence (1)

(a)

(b)

Figure 8. Photographs of the Installed Flight Test Wing Fence (36)
(a) Upper Surface View (b) Lower Surface View

II. Literature Review

2.1 Chapter Overview

There is a constant effort to improve and refine aircraft aerodynamics. Here, an enhancement in high AOA performance and handling qualities is considered. However, before improvements can be made, the fundamentals of flight in this regime must first be understood. Flow under these conditions is turbulent, unsteady, separating, and even reversed. Therefore, the beginning of this chapter begins with a few of the fundamentals of flight that will be the basis of discussion throughout the paper. Next, this chapter will look at flow control theory, specifically in regards to wing fences. Lastly, previous research on wing fences pertinent to this study will be discussed.

2.2 Boundary Layer Theory

A viscous boundary layer is the layer of fluid next to a body where the fluid shears against the surface due to the no-slip condition. The no-slip condition states that the fluid will assume the velocity of the wall at the surface. This causes a frictional drag force due to viscosity and a velocity distribution at any downstream position. The thickness of the shear or boundary layer is defined by distance from the surface to where the velocity is 99 percent of the free stream. This is designated as $\delta_{99\%}$ (33).

Boundary layers can be laminar, transitioning to turbulent, and fully turbulent. A laminar boundary layer's streamlines maintain order as long as viscosity has a damping effect (17). Once the momentum of the flow begins to overcome the viscosity, causing small random disturbances, the flow is said to be transitioning. As these disturbances become amplified and the flow goes through a complicated sequence of spatial changes,

the flow is deemed fully turbulent. Figure 9 depicts this process in an idealized sketch of flat plate flow and these different regions.

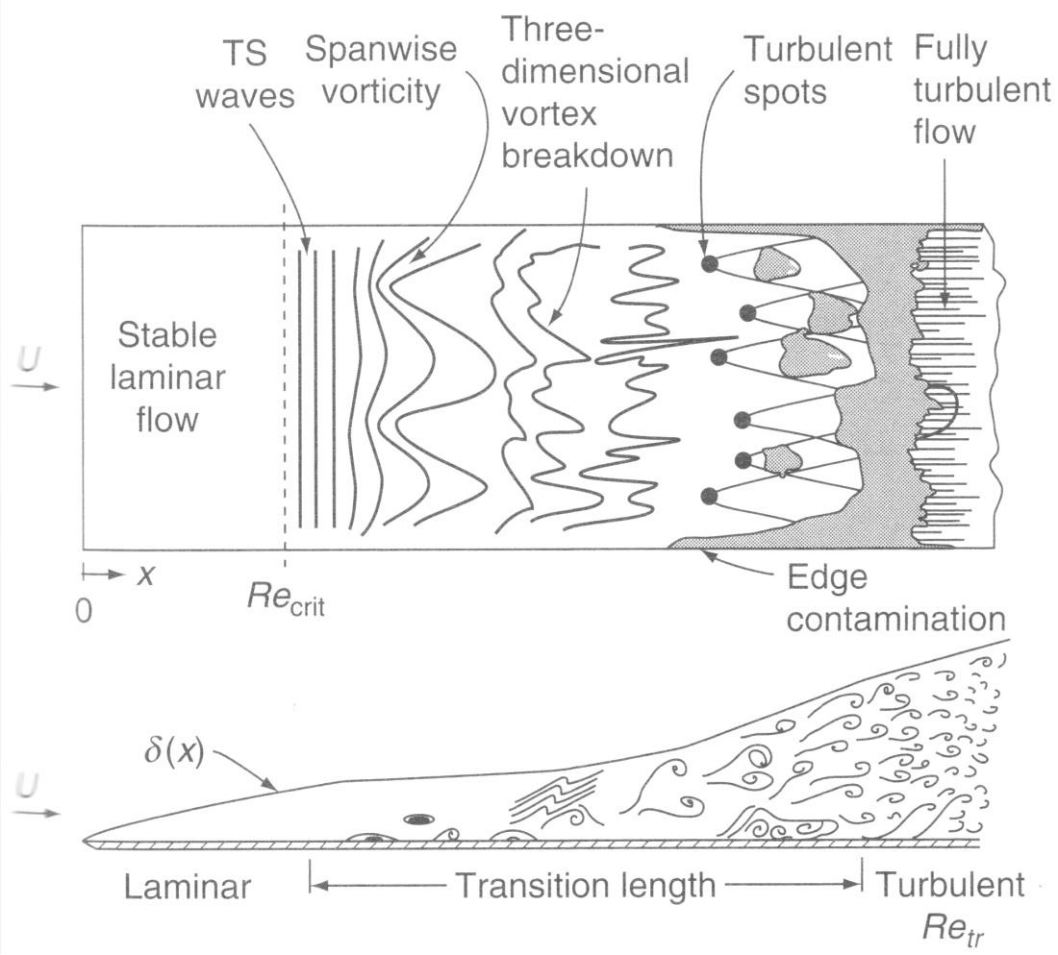

Figure 9. Boundary Layer Transition Process (33)

Each type of boundary layer has its pros and cons. One that is of interest here is that a turbulent boundary layer has more exchange of kinetic energy with the free stream than a laminar boundary layer does. This does, however, come at the price of increased skin friction drag. This exchange of energy leads to the turbulent boundary layer having a higher velocity gradient than the laminar boundary layer near the surface. This is shown in Figure 10.

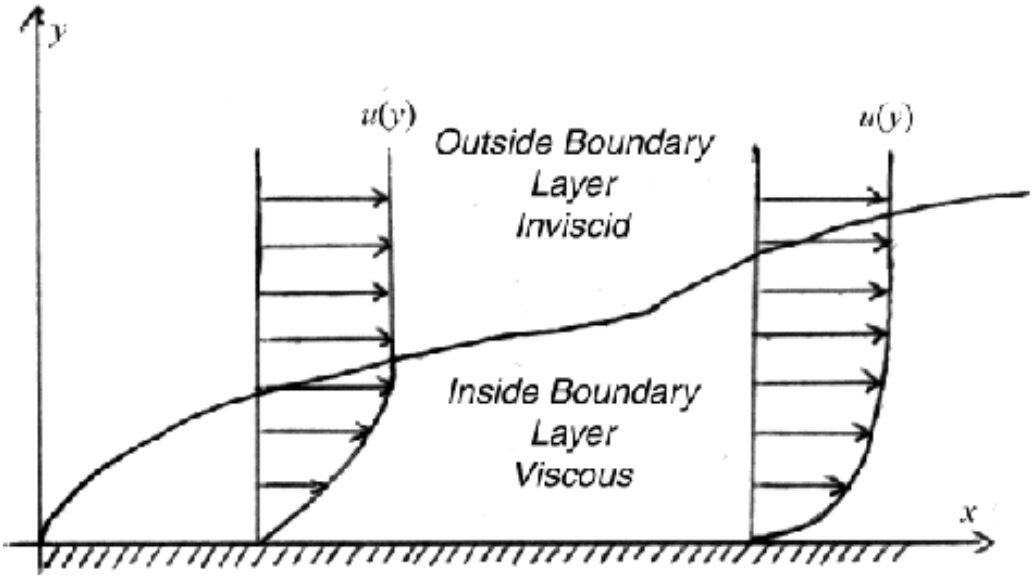

Figure 10. Laminar (left) and Turbulent (right) Boundary Layers (1)

Pressure gradients are extremely important to a boundary layer discussion as well. Adverse pressure (p) gradients are defined as $\frac{\partial p}{\partial x} > 0$ where x increases in the downstream direction. This is most critical inside the boundary layer because it further decelerates the flow. This results in a loss of momentum and continues to the separation point. The separation point is the point where the wall shear goes to zero. After the separation point, the flow near the surface reverses direction. Pressure gradients and associated velocity profiles are shown in Figure 11. An important point here is that laminar flows have poor resistance to adverse gradients and separate easily whereas turbulent boundary layers resist separation longer due to their increased exchange of energy with the free stream (33).

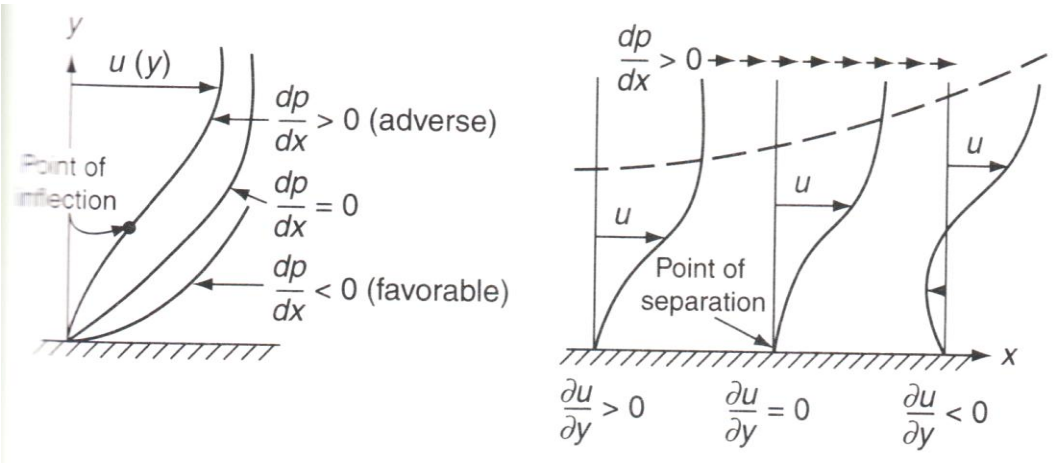

Figure 11. Effects Due to Pressure Gradient (33)

2.3 Stall

The conventional stall is generally defined as a sudden loss in lift at an AOA just above that of maximum lift coefficient. However, for aircraft without a true maximum lift coefficient, it is better to consider the following definition of stall speed. Stall speed is the minimum steady speed attainable or usable in flight. However, it has become increasingly common to define this based on other characteristics such as a high sink rate, an undesirable attitude, loss of control about any axis, or deterioration in handling qualities (27). Stall is normally associated with flow separation that has occurred over large portions of a lifting surface. The results of stall are a decrease in lift, increase in pressure drag, and a change in pitching moment (2).

The type of boundary layer has a significant impact on stall. Because flow separation begins at the boundary layer, higher velocity gradients associated with turbulent boundary layers better resist separation. This ultimately allows the flow to remain attached to the surface longer, thus delaying stall.

2.4 Flow Control

Energizing the boundary layer is the principle that many flow control devices use for the reasons previously mentioned. Flow control devices can be active or passive. For example, active techniques include boundary layer injection or suction, and passive techniques include vortex generators, winglets, and fences. Both are effective, but active is too complex and costly to consider for the T-38. Therefore, only passive devises were considered here.

The wing fence, placed at the 82.5 percent spanwise location, was chosen for a more detailed study for two reasons. First, fences have been and still are successfully used extensively on aircraft. Second, the seam and row of fasteners located there offered a reasonably simple location for attaching a fence to the wing without significant modification to the aircraft.

2.5 Wing Fences

Fences have been used for more than 70 years. The MiG-15, as seen in Figure 12, was one of the earliest examples of their use. It had two fences on each wing.

Figure 12. MiG-15UTI (12)

NACA performed a great deal of research in the 1950's on wing fences. Though only five reports are documented in the bibliography, more than twenty reports of various wing fence tests during that time were found. The most common application was to improve longitudinal stability for swept wing aircraft of the time. However, increases in lift at high angles of attack were also researched as were drag implications.

Wing fences work in a very complex way, and their impact on the flow field is still not completely understood. Liebe believed that stopping the cross flow in the boundary layer was the key to its success on the Bf 109. However, it has been determined that this is only one of the several mechanisms through which they work. Potential flow and altered lift distribution was one early theory. Other early theories recognized that some of the benefit came from the initiation of a sideslip and the resulting vortex generation by the fence (18). Still others, like Zhidkosti, documented the existence of two distinct vortices caused by fences that wrap the leading edge, but he failed to report the cause of the second vortex (39). Solfelt observed two vortices in his study and reported a possible cause of the second vortex. He also observed an increased lift distribution outboard of the fence rather than inboard as the potential flow theory suggested (23). Now, a more detailed look at some of these theories is discussed.

One way fences work is to affect potential flow, or flow with zero vorticity. Installing a wing fence changes the lift distribution on a swept back wing as depicted in Figure 13. On the inside of the fence, the local lift per unit span is higher. On the outside of the fence, lift per unit span is lower. This shift in load is usually beneficial to stall behavior. Generally, the load is reduced on the wing tip and the boundary layer is maintained in such a way that separation is inhibited (18).

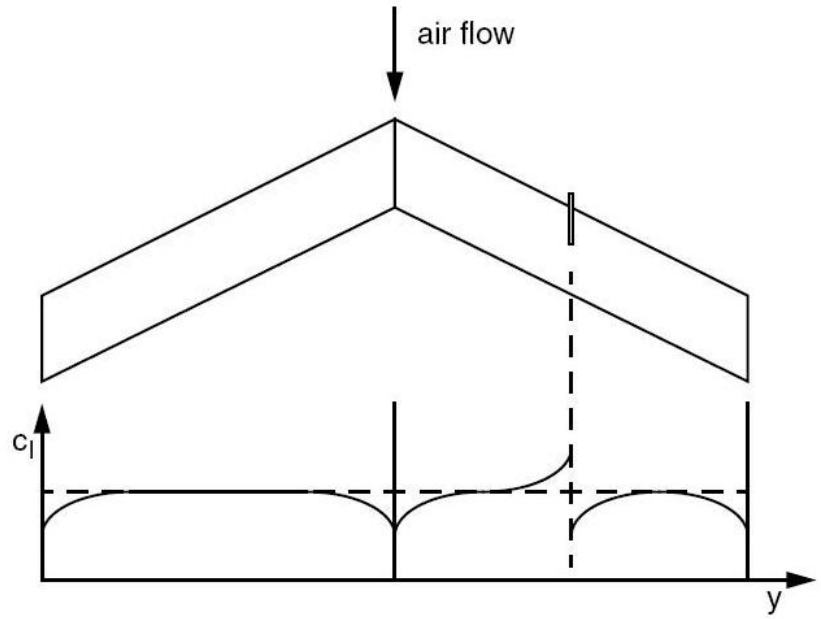

Figure 13. Swept Wing with Fence - Lift Distribution (18)

Fences also work as a vortex generator. In principle, vortex generators are used to delay separation. They are normally small and shaped like an airfoil or thin plane which protrudes from the surface. They are positioned at an angle to provide vortex generation. The key is that the vortex captures energy from the free stream and transfers it to the boundary layer, and this helps to delay separation.

The location, length, height, and shape of the fence are significant variables that must be adjusted dependent upon specific aircraft attributes. Some sources suggested blanket guidelines. Among the design guidelines were suggestions that extending the fence beyond one-third of the local chord does not significantly increase its effectiveness (21). Another was that they are more effective when they wrap around the leading edge (18; 23). The most common spanwise location for wing fences is between 40 percent and 60 percent of the wing span (18). The most outboard spanwise location of a fence found through research was 76 percent semispan (21). Additionally, fences need to be much

taller than the boundary layer to be effective (21). All of these attributes must be optimized for individual aircraft, as will be evident in the following section.

2.6 Results and Conclusions of Fence Tests from Research Documents

Zhidkosti reported in *Flow On A Swept Wing in the Region of a Fence* that a wing fence on a 55 degrees swept wing produced two vortices (39). The first was on the upper part of the fence on the inboard side. This was caused by a pressure differential across the fence. The strength was directly related to AOA and yaw angle and was largest when the angles were the biggest. He found that this caused a pressure minimum inboard of the fence. Although he did not comment in this article on the location or source of the other vortex, he noted that it altered the flow pattern near the wing and caused restructuring of the velocity field that may affect the performance of the horizontal tail. Ultimately, he concluded that the fence caused flow to remain attached outboard of the fence even after separation occurred inboard of it.

NACA report *RM L8I08* utilized a NACA 64_1-112 airfoil with a wing sweep of 52 degrees, an aspect ratio (AR) of 2.88, and a taper ratio of 0.625 (7). One applicable conclusion was that fences located at 0.45 semispan delayed tip stall and caused the pitching moment curve of the wing with 0.575 semispan leading-edge flaps and split flaps to break in a stable direction at the maximum lift coefficient.

NACA's *Report 1203* used a NACA 63-010 airfoil with a wing sweep of 35 degrees, an AR of 3.57, and a taper ratio of 0.565 (21). First a study on the effect of a fence that did not wrap the leading-edge at 0.36 semispan was conducted. The impact was negligible, and it was concluded that the fence should be extended around the leading edge. Using this fence, it was found that, with the slats extended, longitudinal

stability characteristics were improved. Again using this fence, the effects were next investigated at varying spanwise locations from 0.65 to 0.76 semispan in the clean configuration. At 0.65 semispan, the stability was greatest, but at 0.76 semispan, the lift break and unstable break in the pitching moment curve were delayed to higher AOAs. The conclusion was that 0.73 semispan gave the best compromise for pitching moment and lift characteristics. Therefore, it was determined that the longitudinal stability characteristics of the model could be improved for all configurations at moderate angles of attack by placing chordwise wing fences at both spanwise stations of approximately 0.36 and 0.73. This was provided that the nose of the fence extended slightly beyond or around the wing leading edge. Also of note, the authors concluded that in a practical application, it was desirable to use the smallest size fence that provided acceptable aerodynamic characteristics and that varied fence height caused little change in effectiveness except for very short fences. Lastly, removal of as much as the rear two-thirds of fences caused little reduction in fence effectiveness.

NACA report *RM A52K20* utilized a semispan model of a cambered and twisted wing. It had a wing sweep of 40 degrees, an AR of 10, and a taper ratio of 0.4 (5). Thickness, camber, and other airfoil characteristics can be found in the report. The fence configurations included a three and four fence model. Small fences and extended fences were used. Small fences started at 42 percent chord and ended at 100 percent chord. Extended fences started at 8 percent chord and ended at 100 percent chord. It was determined that flow separation originated at the trailing edge near the mid-span of the wing. The separation then spread toward the root and tip with an increase in AOA. It was found that upper surface fences reduced the trailing edge flow separation outboard of the fences. The fences had little effect until trailing edge flow separation started. The

general effect of the fences was to reduce the amount of flow separation immediately outboard of each fence. A region of low pressure developed just outboard of the forward part of the small fences. It was reasoned that the low pressure areas developed when the turbulent separation on the inboard side of the fence extended far enough forward to allow spanwise flow of air over the forward part of the fence. Under these conditions, the small fences acted much the same way as vortex generators. At the higher Mach numbers, the extended fences were somewhat more effective than the small fences in reducing the amount of separation. With four fences, the net result of these changes was an increase of about 16 percent in the maximum lift coefficient of the wing, a delay in the abrupt increase in drag to approximately the maximum lift coefficient, and an elimination of practically all of the longitudinal instability of the wing at the higher lift coefficients. The major differences between the beneficial effects of the two fence configurations occurred over the outer half of the wing. These differences near the tip appeared as increases in section lift and provided an explanation of the large improvement in the longitudinal stability characteristics with the use of four fences. The use of upper-surface fences was found to be effective in producing significant increases in lift over the outer portions of the wing by reducing the amount of separation outboard of each of the fences and thereby causing substantial improvements in the lift, drag, and pitching moment characteristics.

NACA report *RM L52C25* used a NACA 63-010 airfoil with a 35 degrees swept wing, an AR of 3.57, and a taper ratio of 0.565 (10). The use of a fence caused a slight improvement in the static longitudinal stability of the basic wing alone at moderate angles of attack which resulted from an improvement in the flow over the tip of the wing and higher tip loadings for a given AOA. The fence was located at 68 percent semispan.

The fence acted as a physical barrier to the leading-edge separation vortex thereby improving the flow over the wing outboard of the fence. The main effect of the fence was to provide a more favorable variation of downwash angle with AOA at the horizontal tail. The effects of the fence on longitudinal stability varied considerably with the spanwise position of the fence. Apparently, in order to be highly effective for a large AOA range, the fence should be located very close to the point where the separation vortex begins to sweep backward from the wing leading edge which usually occurs at some moderate AOA. In addition, the fence should extend to, or around, the wing leading edge. Addition of slots or flaps to the wing, or a change in AR would alter the vortex behavior and would, therefore, influence the optimum location of the fence as, perhaps, would Reynolds number.

2.7 T-38 and Strakes

Previous research was accomplished in an effort to reduce the T-38 landing speed. In 1990, patent 5249762 was filed for "Strakes for Landing Speed Reduction" by Eidetics International, Incorporated (22). This was specific to the T-38. Strakes were placed on the engine inlet nacelles just forward of the wing leading edge and well above the wing plane, as shown in Figure 14 and labeled 28. The assertions of those applying for the patent are discussed first, and an independent study of these strakes is discussed last.

The following information regarding the strakes and their performance are the assertions of those applying for the patent. The strakes forestalled wing buffet, yet exhibited well behaved longitudinal stability at high angles of attack. This allowed operation at higher coefficients of lift and a reduction in landing speed. It was asserted that the invention substantially delayed the onset of turbulence over the top of the wings,

thereby reducing buffet and allowing operations at higher angles of attack. It also essentially extended the pitching moment curve, resulting in better longitudinal stability. The strakes were claimed to allow the operation of the aircraft with flaps down in the landing configuration at 2 to 3 degrees AOA higher than normal. This resulted in approximately 22 percent increase in lift coefficient and an associated reduction of landing speed by 10 percent (22).

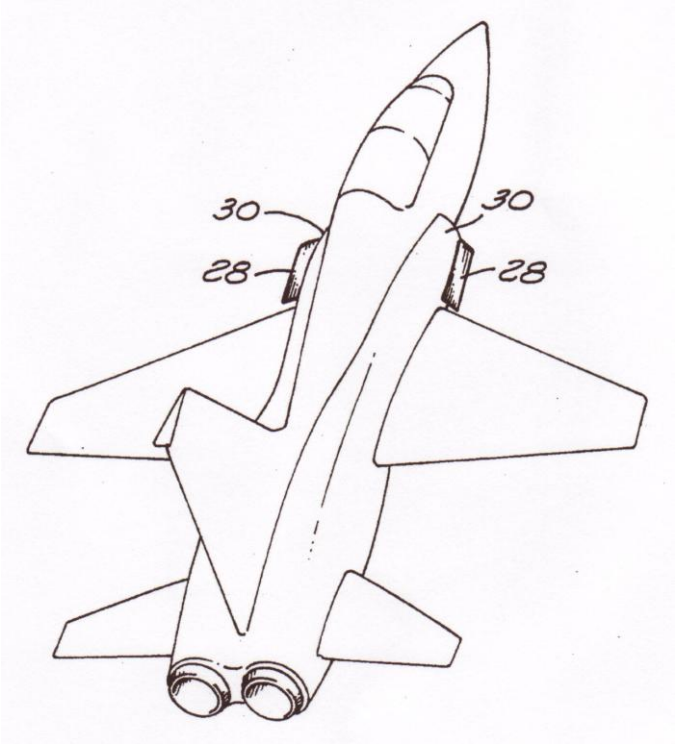

Figure 14. T-38 Drawing with Strakes (22)

An independent study was accomplished by USAF TPS between November 1990 and June 1991 (26). There were 11 flight test sorties accomplished to determine if the landing speed could be reduced. The maximum lift coefficient was increased by over 30 percent in the powered approach (gear and full flaps) configuration. The up-and-away maneuver performance was increased. Buffet intensities were reduced above 12 degrees AOA. However, the buffet onset speeds and characteristics were not significantly

affected. Also, the wing rock and roll-off tendencies were unchanged. Ultimately, the positive impacts of the strakes started nearly 6 degrees above approach AOA, and therefore, it was concluded that they could not effectively reduce the approach speed for landing.

2.8 Solfelt T-38 Wing Fence CFD Conclusions

Solfelt's CFD work contributed to the understanding of the two vortices caused by a wing fence as discussed in section 2.5 (23). The first vortex, as proposed by Zhidkosti's study, was observed along the upper portion of the fence. However, it developed outboard of the fence instead of inboard and was caused by a pressure differential across the fence. Solfelt observed both vortices and concluded that the second vortex, or tip vortex, was formed by the flow outboard of the fence rushing to fill the low pressure region on the wing tip. Solfelt also concluded that these vortices caused the lift to be increased outboard of the fence. This lift distribution was in direct agreement with Boltz, Shibata, and Jaquet in References 5 and 10 but in disagreement with some of the potential flow theory and Zhidkosti. The fence and tip vortices discussed are depicted in Figure 15a, which depicts a T-38 wing with the flaps fully extended and a 2.5 inch tall fence at 0.825 semispan. The Reynolds number is 10×10^6, based on root chord, and AOA is 15 degrees. Figure 15b shows the upper surface flow at the same conditions as Figure 15a with the streamlines depicted.

Additionally, Solfelt examined a fence that wrapped the leading edge and one that did not. He concluded that it was important for the fence to wrap around the leading edge to increase the strength of the vortex. With the fence that wrapped the leading edge, he observed a 4.9 percent increase in lift coefficient at 15 degrees AOA over the clean wing.

Lastly, he found fence height to be important. This was so the cross flow was not too strong and could be captured by the fence vortex.

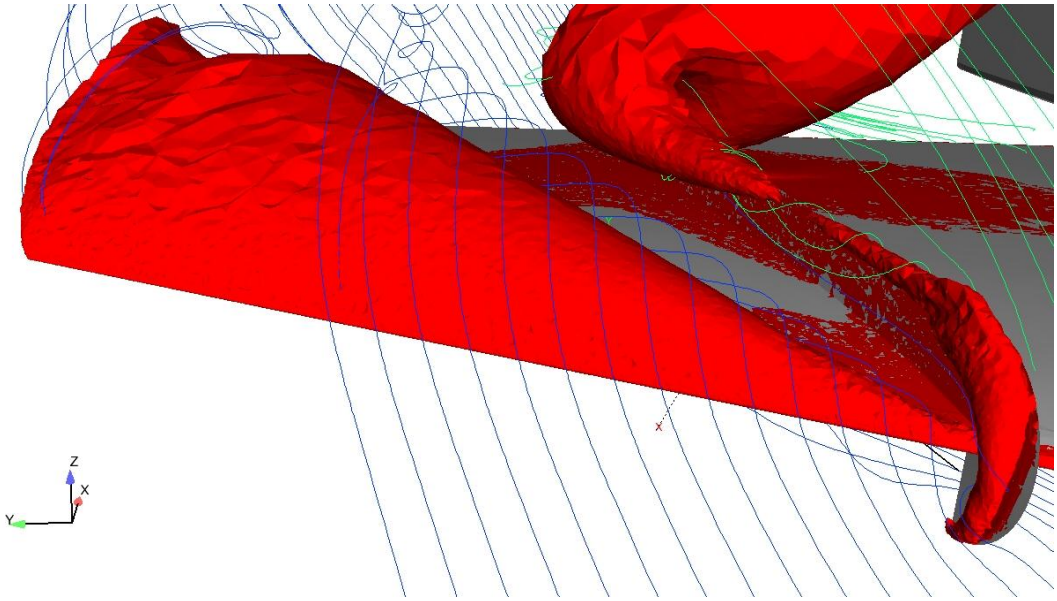

(a)

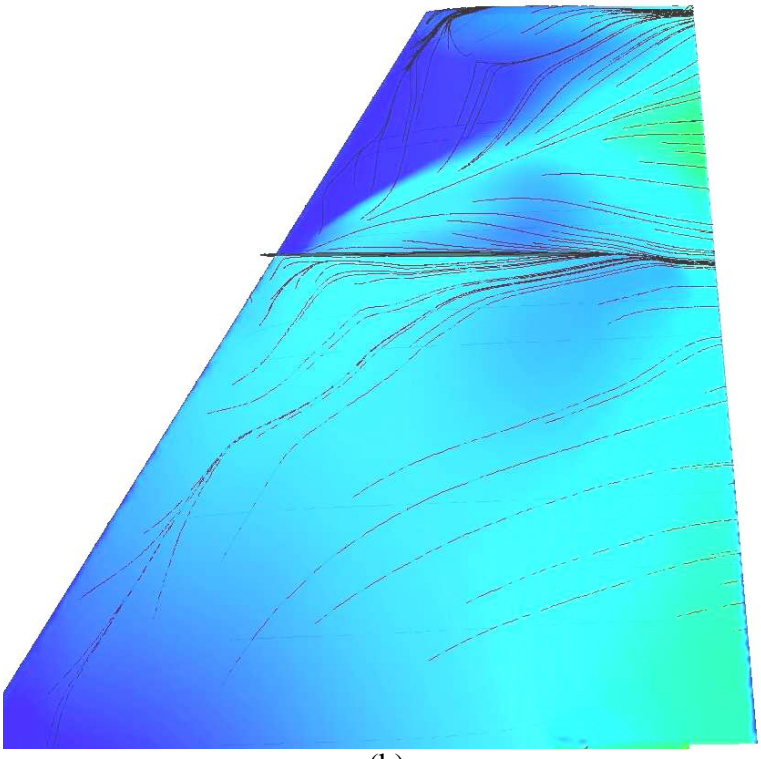

(b)

Figure 15. Flow Visualizations from CFD with Wing Fence (23)
(a) Tip and Fence Vortices with Streamlines (b) Upper Surface Flow

2.9 Solfelt and Maple T-38 Wing Fence CFD Conclusions

Solfelt and Maple further pursued CFD-based results and documented those in Reference 24. The methodology was primarily the same as in Solfelt's previous work except that a finer resolution in AOA (1 degree increments from 5 to 15 degrees) was examined and CFD iterations were allowed to continue until the z-component of the integrated normal force varied by less than 1 percent over the final 400 iterations.

The results were that the maximum increase in lift coefficient occurred with the fence installed at 13 degrees AOA and was 7 percent greater than with no fence installed. However, ±1 degree AOA either way showed almost no difference between the two configurations. At 13 degrees AOA, it was found that the fence affected the flow field inboard of the fence, all the way to the wing root. However, by 14 degrees AOA, the impact inboard of the fence was gone. Figure 16 shows the surface flow on the wing's upper surface at 5, 10, 13, and 14 degrees AOA with flow direction indicated by a blue to red gradient. Based on these figures, Solfelt and Maple drew the following conclusions:

> At 5° AoA, the clean-wing solution shows clear signs of a leading edge vortex extending from the root and extending nearly to the wing tip. The addition of the fence clearly interrupts this vortex, but it appears to reform on the outboard leading edge. Surface flow over the majority of the wing remains unchanged.
>
> At 10° AoA, the leading edge vortex has been swept back to the trailing edge at approximately mid semi-span, and the trailing edge of the outer half of the wing is fully separated. Addition of the fence results in only small changes to flow on the inboard side. Flow outboard of the fence is significantly changed, with clear indications of the formation of both the fence and strengthened leading-edge vortices. Most significantly, flow along the outer trailing edge remains attached.
>
> At 13° AoA, significant differences in surface flow can be observed both inboard and outboard of the fence. On the clean wing, the trailing edge is completely separated, with all of the surface flow moving toward the leading edge. With the addition of the fence, the trailing edge remains attached. Inboard of the fence, flow along the leading edge is

predominantly spanwise, with a weak separation line parallel to the leading edge terminating at the fence. Based on these computed results, it appears that the T-38 wing stall initially develops as a leading edge separation vortex which develops at relatively low AoA. As angle of attack increases, this vortex is swept aft, leading to separation at the tip trailing edge. As angle of attack is further increased, the trailing edge separation moves inboard until the entire wing is stalled. The primary mechanism leading to improved lift with a fence above 8° AoA is the formation of the fence vortex and strengthening of the outboard leading edge vortex, which together prevent the outboard trailing edge from separating. This leads to a delayed stall inboard of the fence. It does not appear that impeding growth of the initial leading edge vortex plays a significant role in this case.

The changes in the surface flow field that accompany the loss of effectiveness of the wing fence at 14° AoA can be seen in Figure 16g. At this angle of attack the wing inboard of the fence has stalled and closely resembles the clean wing solution. (24)

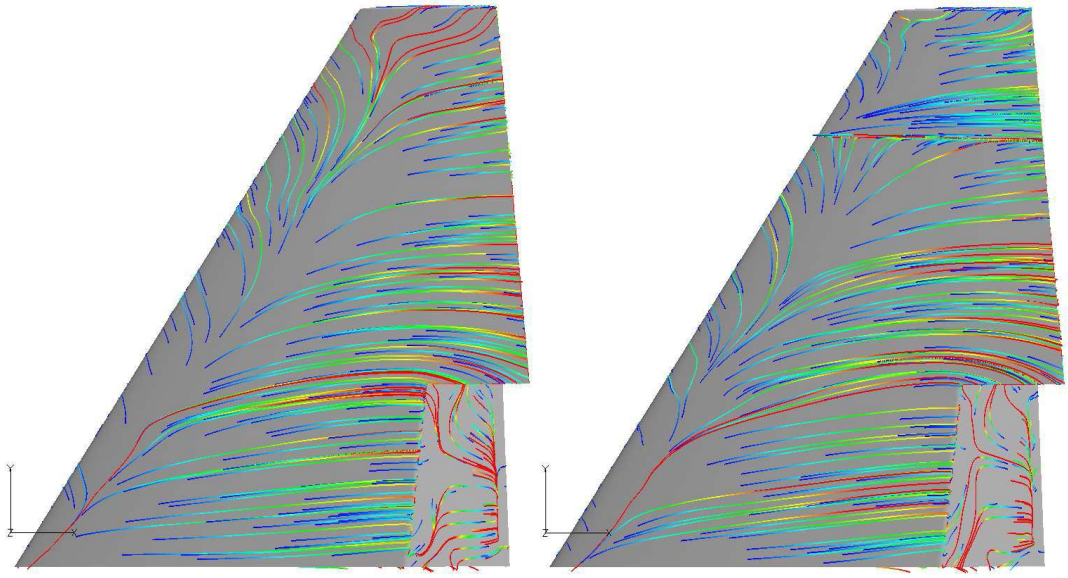

(a) 5 degrees AOA, no fence (b) 5 degrees AOA, fence

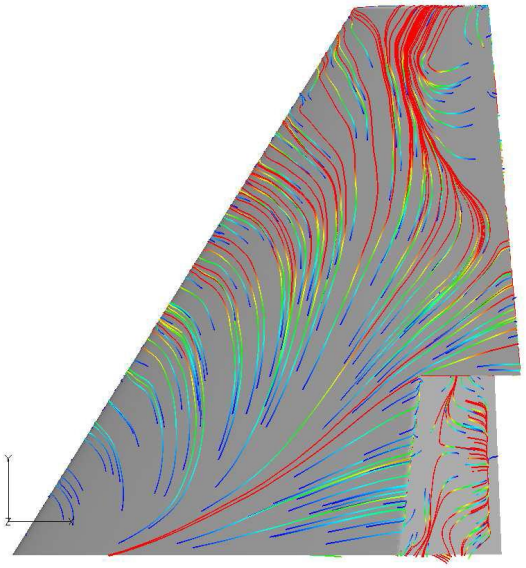

(c) 10 degrees AOA, no fence

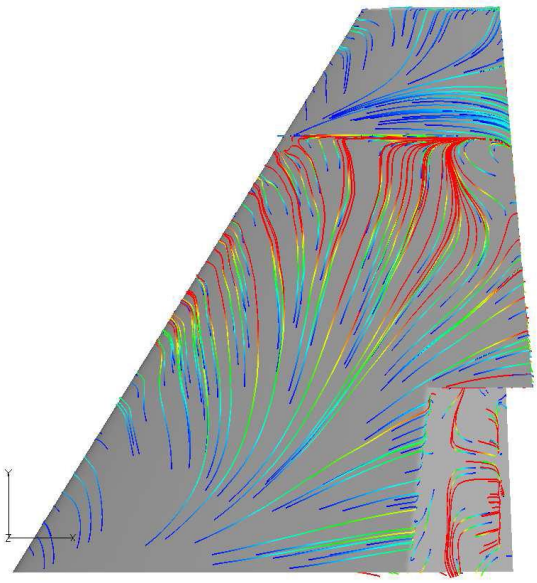

(d) 10 degrees AOA, fence

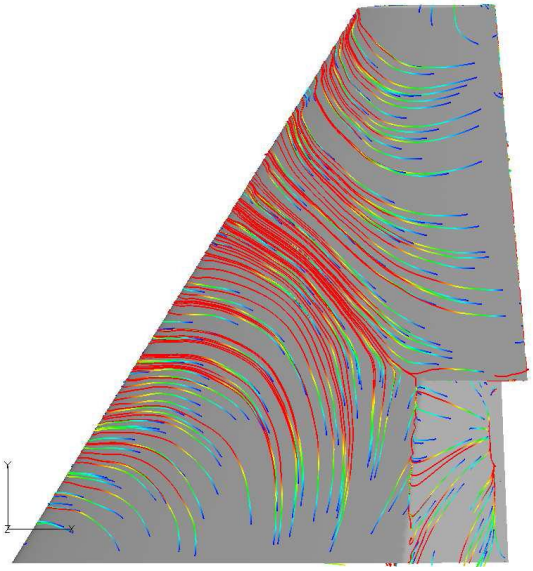

(e) 13 degrees AOA, no fence

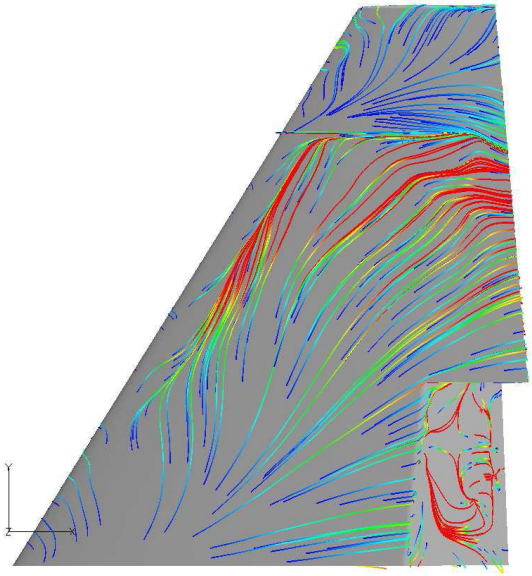

(f) 13 degrees AOA, fence

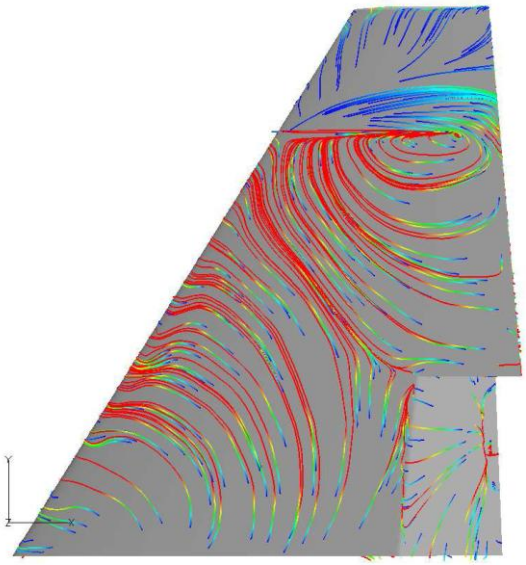

(g) 14 degrees AOA, fence

Figure 16. Upper Surface Flow from CFD with and without Wing Fence (24)

III. Methodology

3.1 Chapter Overview

Model construction in Gridgen, model printing, and each of the analyzed model configurations are presented in detail. The models were mounted in the AFIT low-speed wind tunnel and data were retrieved from the tunnel angle of attack (AOA) sweeps. The test plan that was used to collect these data is outlined. Finally, the flight tested aircraft modification and flight test plan are discussed.

3.2 Model Construction and Printing

3.2.1 Overview.

This study used the same computer-aided-design (CAD) model as Solfelt and Maple. It was modified, as discussed later, using Gridgen (CFD meshing software) with the help of Dr. Hugh Thornburg of AFRL/RCM. The requirement for successful model printing was a water-tight drawing. The resulting file was exported from Gridgen and finalized within Magics, a software package designed to fix small flaws prior to the model being printed. Following this process, the model was sent to the Objet Eden™ 500V printer for a relatively quick design-to-build process from VeroBlue material. Screen shots from both Magics and Gridgen are seen in Figure 17.

The drawing was verified by comparing the real aircraft's dimensions with the full-scale CAD. Areas looked at included wing span, chord length at various spanwise locations, and wing thickness at the root and tip. All dimensions were found to be correct. Additionally, the reference coordinate system exactly matched that of the aircraft maintenance technical orders, further validating the model.

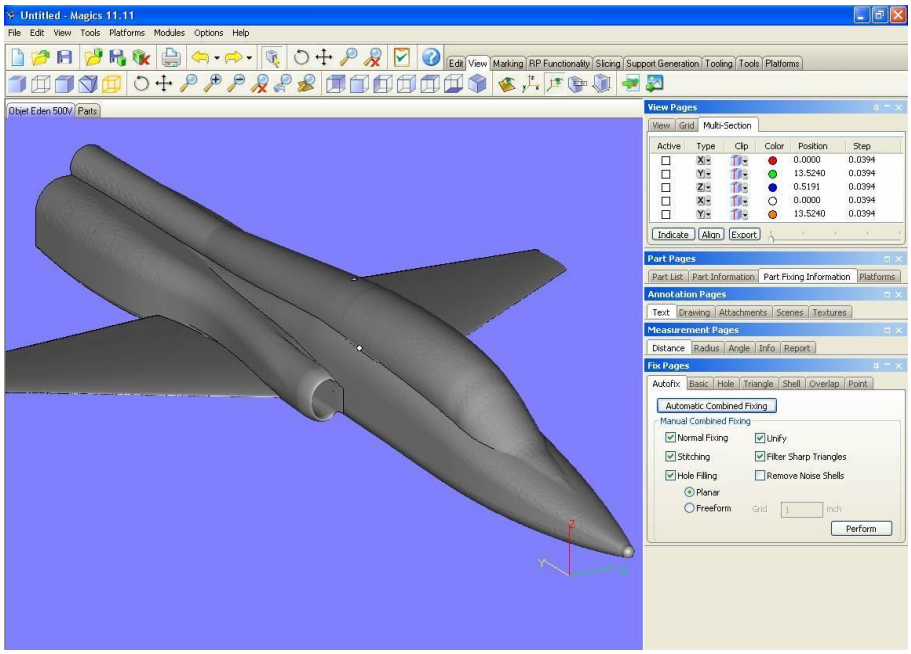

(a)

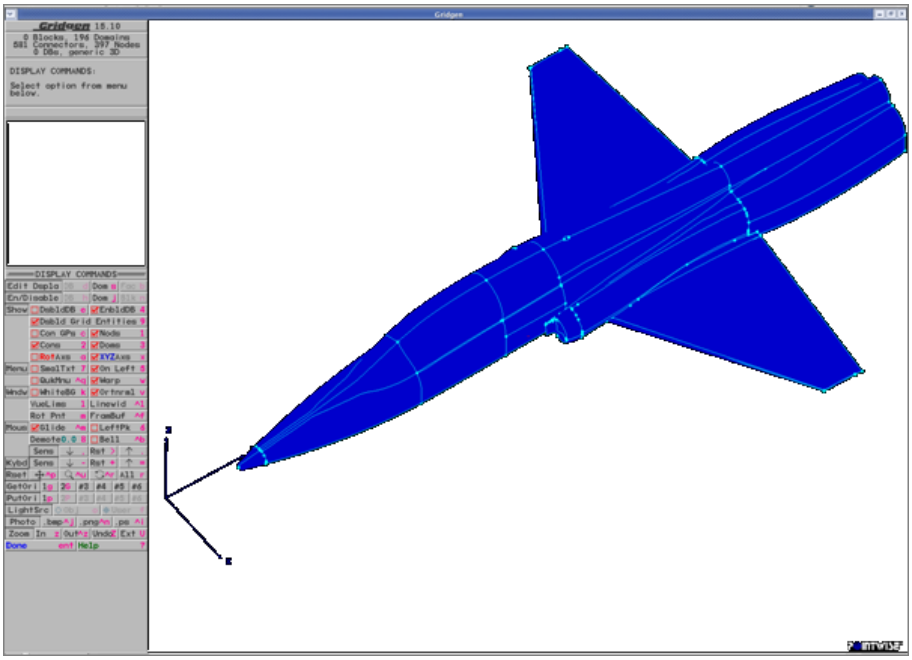

(b)

Figure 17. Modeling Software Screen Shots
(a) Magics (b) Gridgen

The next step was to take the provided geometry and mirror it about the centerline for a symmetric model. After that, the drawing had to be scaled and modified so it could be mounted on the balance in the wind tunnel. The method for changing between wing

fence designs throughout the test also had to be incorporated. Next, different fence designs had to be drawn as part of the wing. Lastly, the model had to be printed on the rapid prototype machine.

3.2.2 Model Mirror.

First, for all full-scale drawing discussions, the reference origin (0,0,0) was located 52.5 inches in front of the aircraft nose and 6 inches above the rear cockpit floor. The x-axis was positive out the left wing, the y-axis was positive out the tail, and the z-axis was positive out the top of the aircraft. The provided geometry was half of an aircraft cut down the centerline. By selecting all of the domains and connectors, Gridgen allowed a single simple step of mirroring the aircraft about the y-axis. Figure 18 shows the half and mirrored aircraft as displayed in Gridgen.

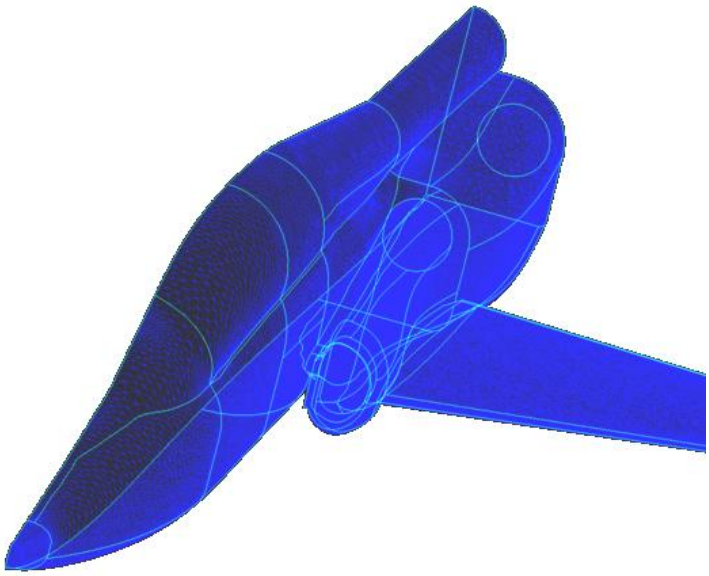

(a)

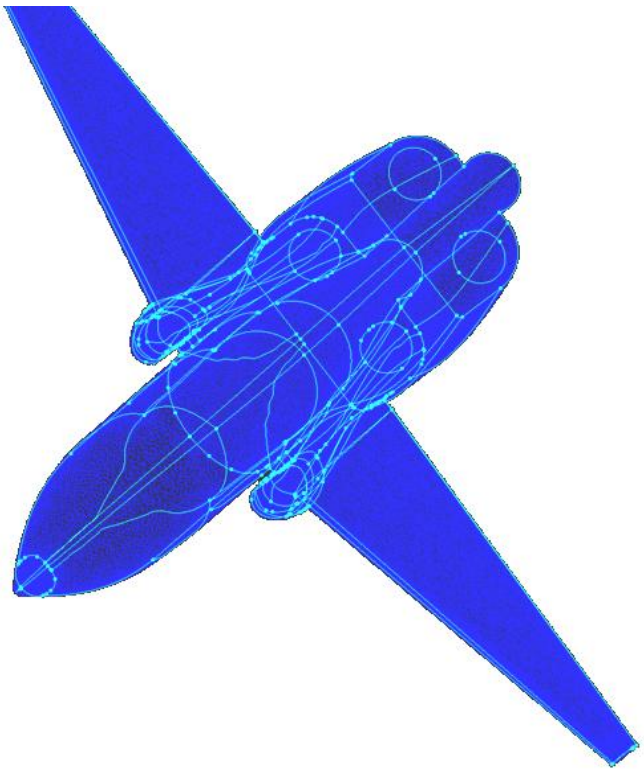

(b)

Figure 18. Model in Gridgen
(a) Half T-38 (b) Mirrored T-38

3.2.3 Model Scaling.

A scale factor of 1:21 was chosen, which resulted in a model that was 22.05 inches long with a wing span of 14.43 inches. The complete scaled dimensions for the aircraft can be found in Appendix E. The size was chosen based upon rapid prototyping equipment, structural and aeroelastic, and wind-tunnel balance constraints. Again, the tail was not included.

The size of the tray in the Objet printer was 19.685 inches x 15.748 inches. This resulted in a maximum theoretical diagonal length of 25.2 inches available. Use of the tray all the way up to the edges was not possible due in part to the way support material was dispensed, and exact corner to corner distances could not be used due to the width of the model.

Another consideration was the thickness of the wing. Because the T-38 wing was quite thin (4.8 percent thickness ratio), scaling caused structural problems for the model for multiple reasons. After printing was complete, the clean-up process included the use of a high pressure water jet. Thin plastic was easily damaged, rendering the model useless. Thin plastic also precluded the use of higher speeds in the wind tunnel due to the increased aerodynamic loads. Breaking part of the wing off in the wind tunnel would cause a number of problems such as tunnel and balance damage. Too much aeroelastic effect and deflection was also not desired. Once the scaling factor was chosen, a single, scaled wing was printed to verify its usability. In regards to the dimensions, an example is the model's maximum thickness at the wing tip was just .062 inches.

Lastly, the limitations of the balance used for force and moment measurements, discussed in detail later in this chapter, were also a constraint for the scaling decision. The balance's normal force limit was 10 pounds, and if that limit was exceeded, the balance would be damaged. The scaled-wing surface area directly impacted the lift forces generated by the model and had to be considered with the speeds and angles of attack of interest.

3.2.4 Wind Tunnel Balance Mounting.

Balance dimensions and limits as well as the model's center of gravity were the driving factors in this process. As seen in Figure 19, the balance diameter was 0.5000 inches, and the length of the balance in contact with the model was 0.725 inches (see red container). Note that the flow direction would be left to right in this figure. The full balance schematic can be found in Appendix A. There were only two 2-56 screws that secured the balance to the model. In this case, one was at the top, and one was at the bottom.

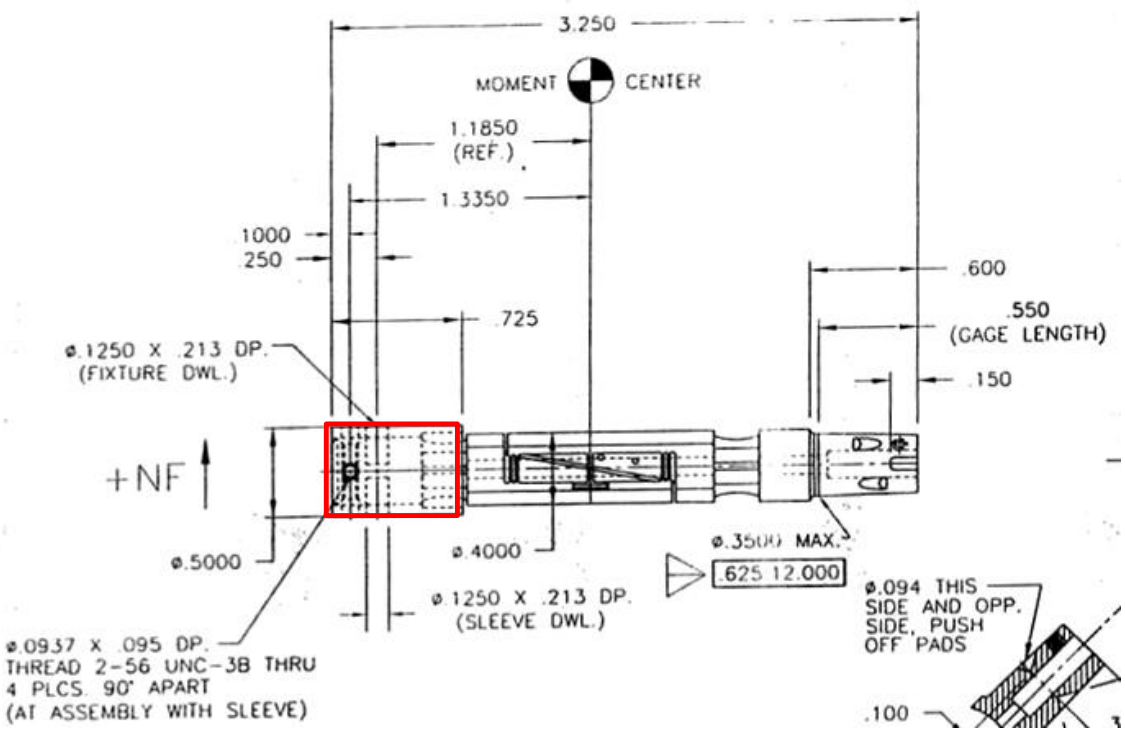

Figure 19. Wind Tunnel Balance Schematic (15)

Because the typical model weight was 3.3 pounds and the balance was limited to 10 inch-pounds for pitching moment, the moment center of the balance needed to be within one inch of the model's center of gravity. This prevented the pitching moment from being the limiting factor on conditions that could be tested.

Initially, there was not a simple way to determine the model's exact center of gravity. Therefore, it was estimated by balancing an initial test model on a point and was found to be 9.5 inches forward of the aft end. Because the balance moment center was 1.4335 inches aft of the balance tip, 1.4 inches was added to 9.5 inches. This meant that the hole would need to be 10.9 inches deep from the aft end of the model. Fortunately, the balance was mounted to a sting that allowed this. The diameter of the hole was set at 0.509 inches to ensure the balance would have a snug fit but could be inserted without exceeding the force limitations (just 5 pounds axially). This diameter extended for the

inner most 2 inches of the hole. The outer 8.9 inches was set to 0.7 inches in diameter. The reason for this was to allow for balance deflection under load without allowing the sting to come in contact with the model and thereby corrupting the data. This diameter of 0.7 inches was limited due to the proximity of the engine holes. Figure 20 depicts the aft end of the model. Figure 20a utilized software called PolyWorks®. This software was only used in this study to produce images like these and to compute the model's centroid.

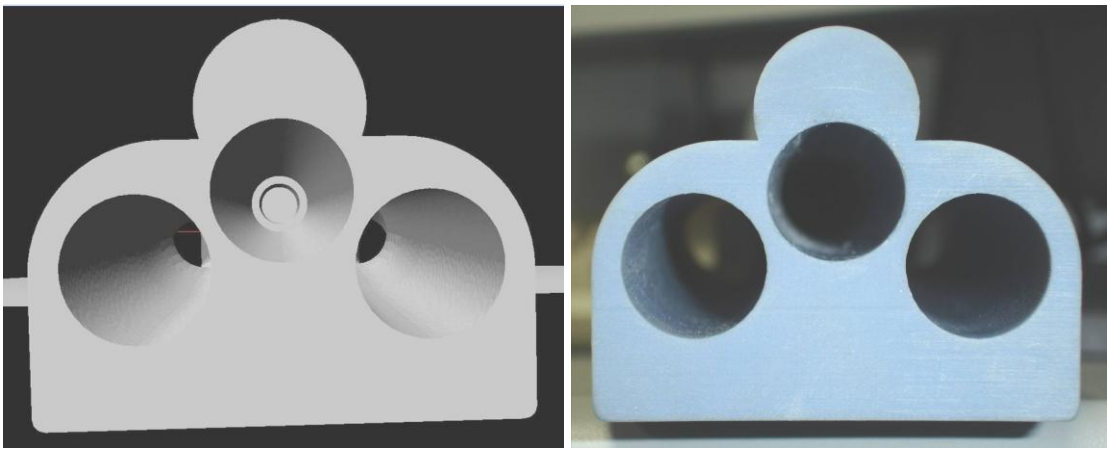

(a) (b)

Figure 20. Aft End of Model with Balance Hole (center)
(a) PolyWorks® (b) Model Photograph

Next, the through holes and counter bore holes for the two 2-56 screws were drawn into the model. These screws attached the model to the balance. The location for these holes was 0.1 inches aft of the balance tip as seen in Figure 19. The hole's center on the model was placed 0.11 inches aft of the balance tip location to prevent problems with holes lining up. Both holes were aligned vertically with the z-axis of the model, with one out of the top and one out of the bottom of the model. The through hole's diameter was 0.085 inches and the counter bore's diameter was 0.15 inches. The through hole's length was set to 0.34 inches. Figures 21 and 22 show the holes discussed here.

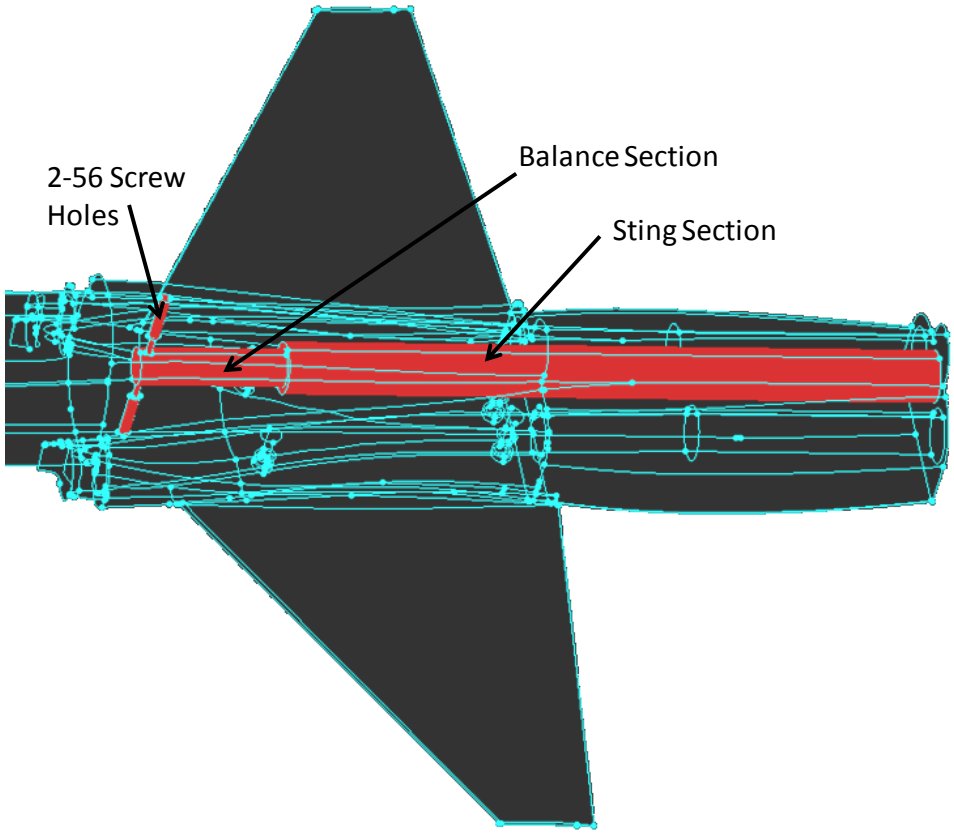

(a)

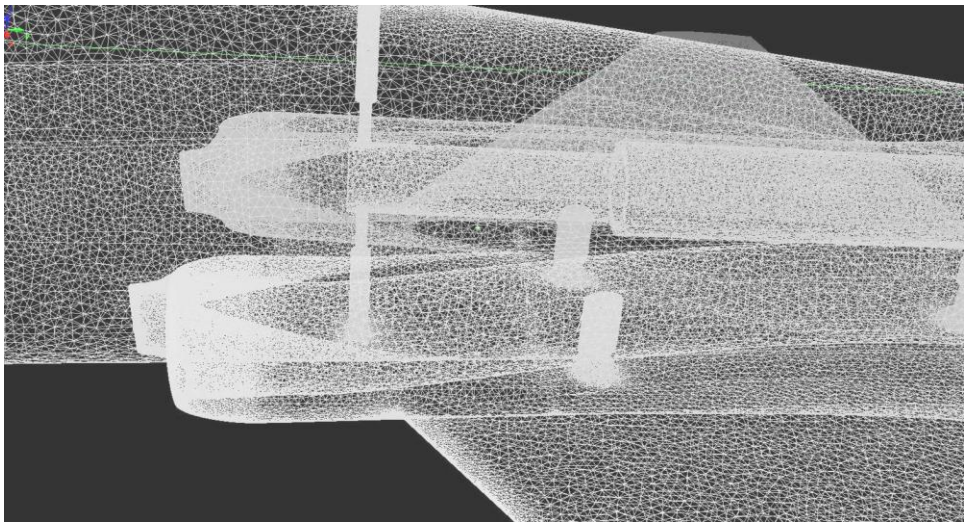

(b)

Figure 21. Side View of Model-to-Balance Screw Holes
(a) Gridgen (b) PolyWorks®

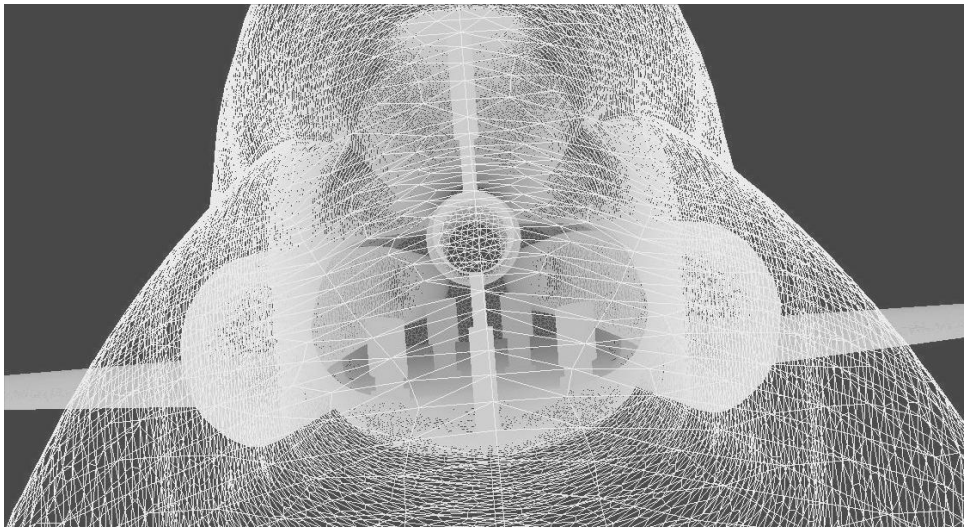

Figure 22. PolyWorks® Front View of Model-to-Balance Screw Holes

3.2.5 Incorporating the Ability to Change Model Configurations.

Due to the small size of the scaled fences, it was challenging to find a way to alter the test configuration with good repeatability. Putting slots in the wing and using metal or plastic fences as well as other options was considered. However, it seemed unlikely that they would be secure in such a thin wing or that they could be removed and replaced with the necessary precision. Ultimately, it was determined that the best way forward was for the fence to be drawn as part of the wing and built by the 3-D printer. Considering printing time, material expense, and the model clean-up process, the best way forward was to have one fuselage with interchangeable wings.

The wings were one solid piece tip to tip. This was accomplished by slicing a rectangular piece out of the bottom side of the fuselage, corresponding to the leading and trailing edges of the wing. The separate pieces, fuselage and wings, can be seen in Figures 23-26. To aid in consistent alignment, a block was extruded from the fuselage and included as a part of the wing. The holes in the bottom of the fuselage were 0.237 inches in diameter and 0.4 inches deep to allow for a brass threaded insert. The insert

was threaded for an 8-32 screw. The position of these holes was dictated by the engine ducts due to the depth required for the insert. On the wing, through holes were made for the screws at a diameter of 0.17 inches with a counter bore diameter of 0.28 inches. The counter bore's depth was 0.09 inches. This allowed the 8-32 screws that held the wing to the fuselage to be essentially flush with the underbody. Gridgen was used for the above model modifications.

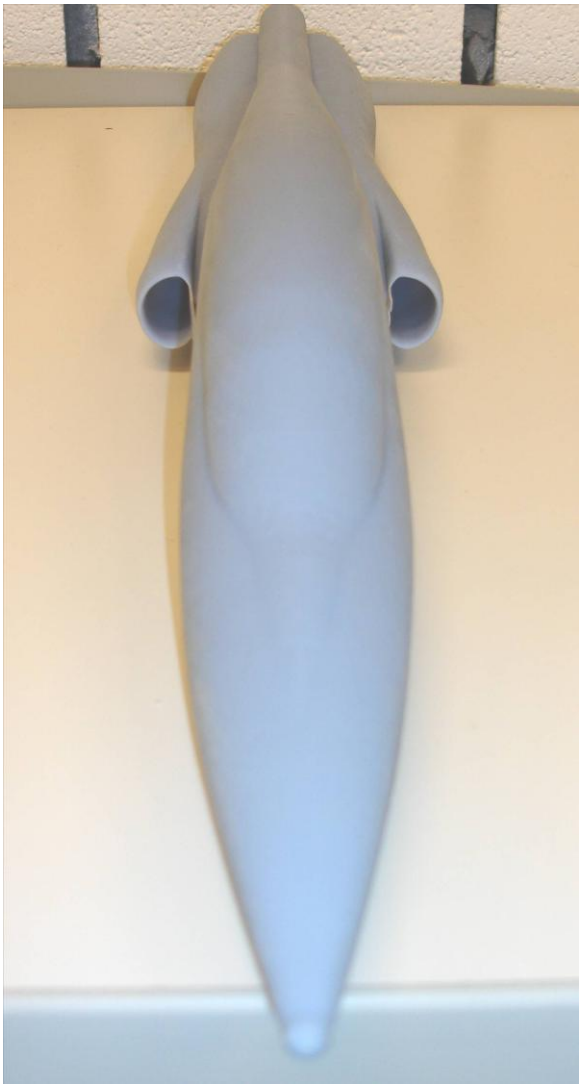

Figure 23. Top View Model Fuselage Photograph

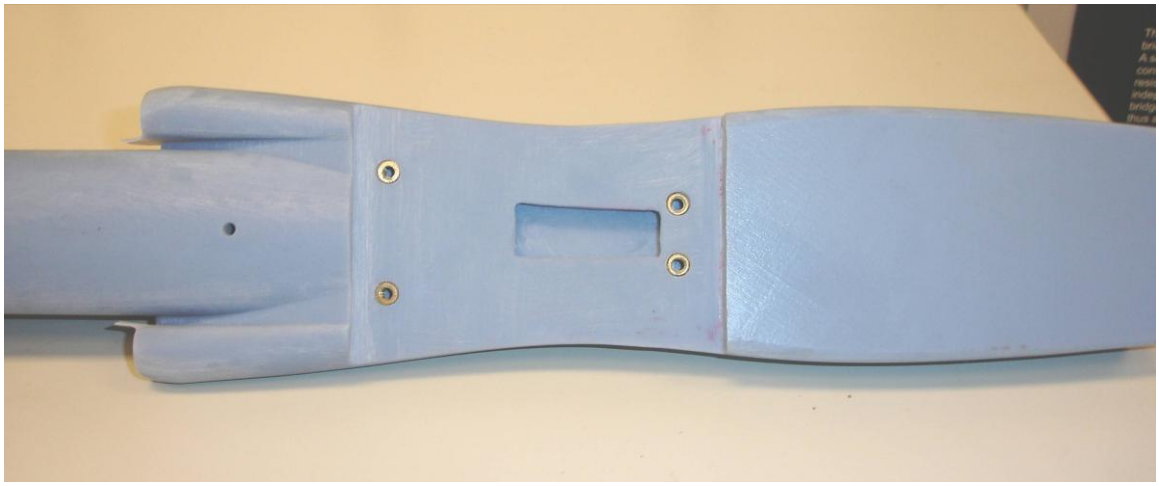

Figure 24. Model Fuselage Bottom

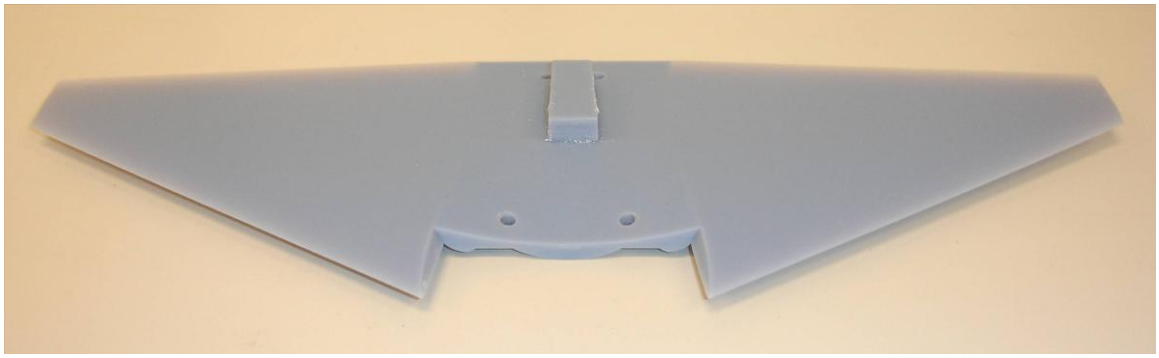

Figure 25. Top View Model Clean Wing

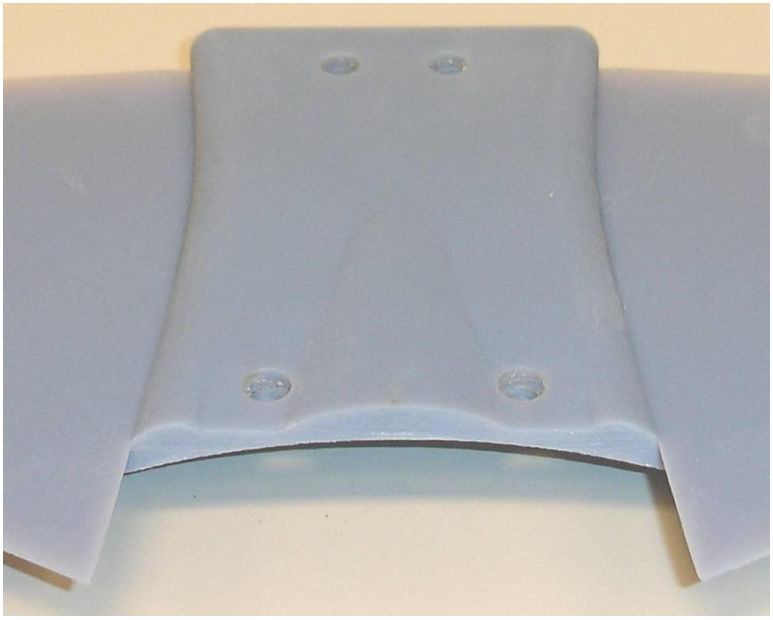

Figure 26. Bottom View Model Wing

3.2.6 Model Fence Building.

Once the wing was separated from the fuselage, the fence designs were incorporated with the wing and printed as one solid piece. The important research considerations were spanwise location, height, thickness, and wrapping the leading edge.

The spanwise location was set due to the wings' seam as previously discussed (Figure 27). This was at wing station (WS) 125. WS 0 was the aircraft centerline. However, WS 125.5 was chosen as the spanwise fence location for the wind tunnel model because of the change in direction of this seam at the leading edge of the wing, depicted in Figure 27. This is referred to as the "jink" in further discussions. The fence location of one-half inch outboard of WS 125 was intended to make it easier to use existing fasteners when installing a fence on the flight-test aircraft. Additionally, this location corresponded to 26 inches in from the wing tip, which matched the fence location studied by Solfelt (23).

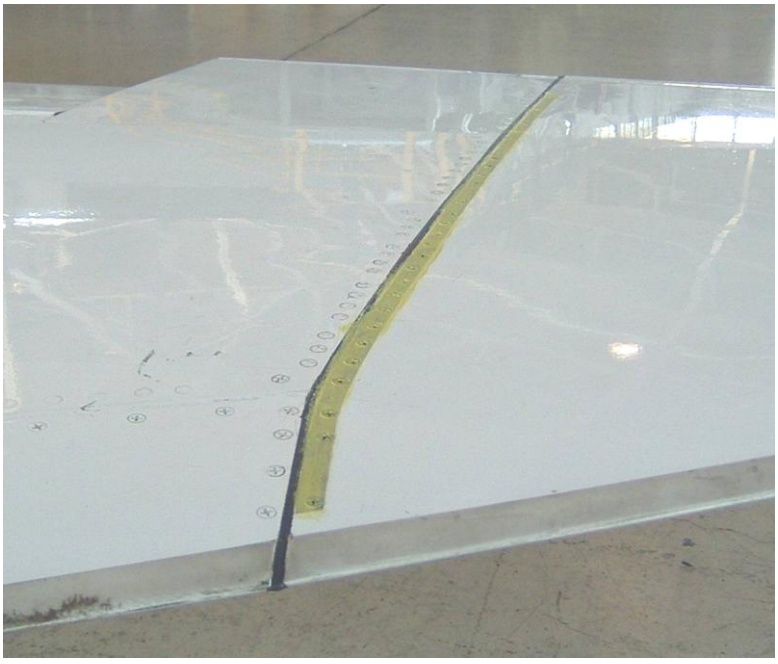

Figure 27. Jink in Wing Tip Seam

The fence height was chosen to be a constant height above the surface of 2.5 inches or 0.119 inches scaled, which was also consistent with the CFD study. Additionally, the full-scale maximum wing thickness at this spanwise location was approximately 2.18 inches. Research indicated that a good starting point for fence height was approximately the maximum thickness of the wing at the spanwise location for the fence (21). Otherwise, specific guidance from previous studies for fence height, beyond the need to be several times taller than the boundary layer thickness, was sparse.

The scaled-down fence thickness was artificially chosen as a uniform 0.03 inches, which was approximately half of the maximum thickness at the wing tip. This resulted in a scaled-up fence thickness of 0.63 inches. This was much thicker than the flight tested fence, which was 0.25 inches. However, the artificially thick fence was required for material strength considerations. This was one difference between Solfelt's fence, which was infinitely thin, and the fences used in this study (23).

Wrapping the leading edge was the next step. The fence's leading edge used in this study was built in the following manner. From an anchor point that allowed fence continuity from the top to the bottom of the wing, a circle with a radius of 2.5 inches was drawn. Because the fence height at the leading edge was not quite 2.5 inches, the circle was scaled in the streamwise-direction by a factor of 1.2. This caused the nose of the fence to have a slightly elliptical shape, similar to the leading edge. The fence extended 6.93 inches on the bottom of the wing, approximately 15 percent of the local chord length. This length nearly corresponded to the length of the jink in the streamwise-direction. Figures 28-30 show a wing fence drawing and two printed model wings with fences.

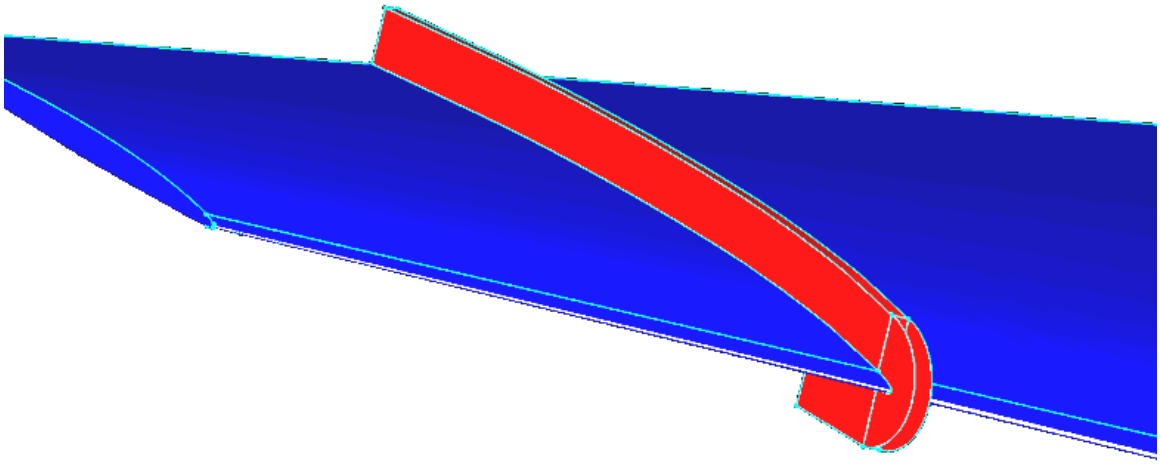

Figure 28. Gridgen Wing Fence Graphic

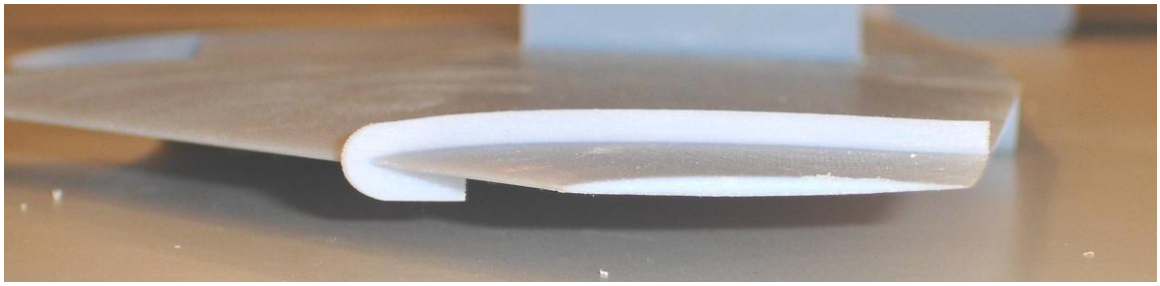

Figure 29. Side View Model Wing Fence

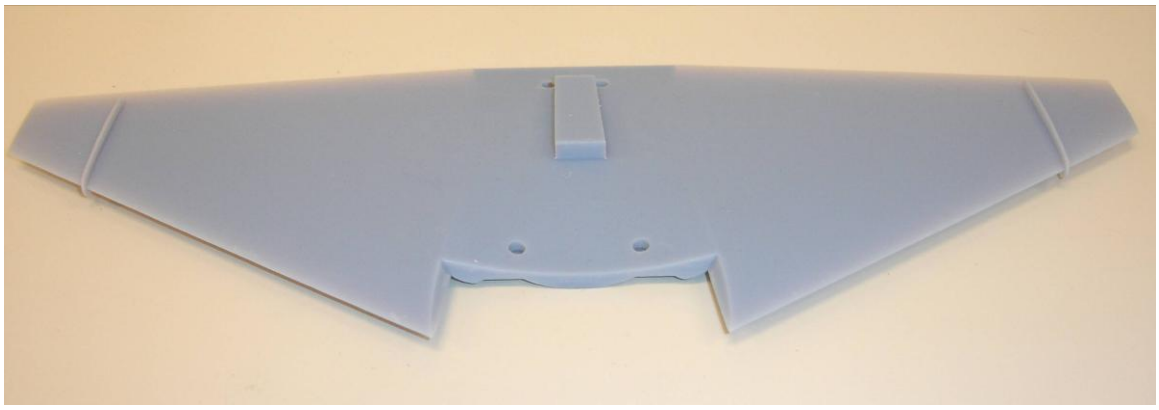

Figure 30. Top View Model Wing Fence

3.2.7 3-D Printing.

The printer was the Objet Eden™ 500V. The printer built the model by layering acrylic in approximately 16 micron horizontal layers with a print-head on a tray that

dropped along the vertical axis. The acrylic was cured by the ultraviolet lamps that were built into the printer head (Figure 31).

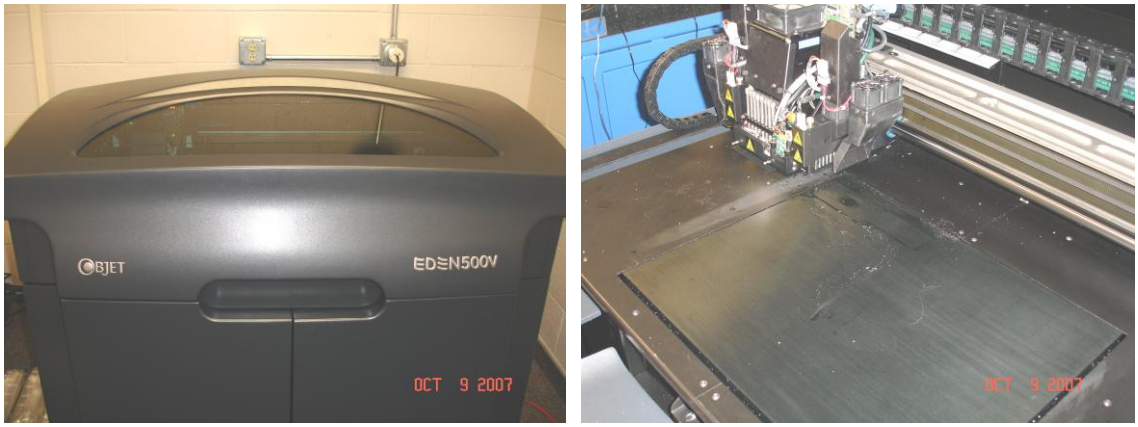

Figure 31. The Objet Eden™ 500V Printer, Printer Head, and Tray

The printing process for the fuselage was approximately 38 hours, and each wing required about 5 hours. Each model required support material and build material. Once the model was built, the support material was pressure washed away and the model was complete (Figure 32).

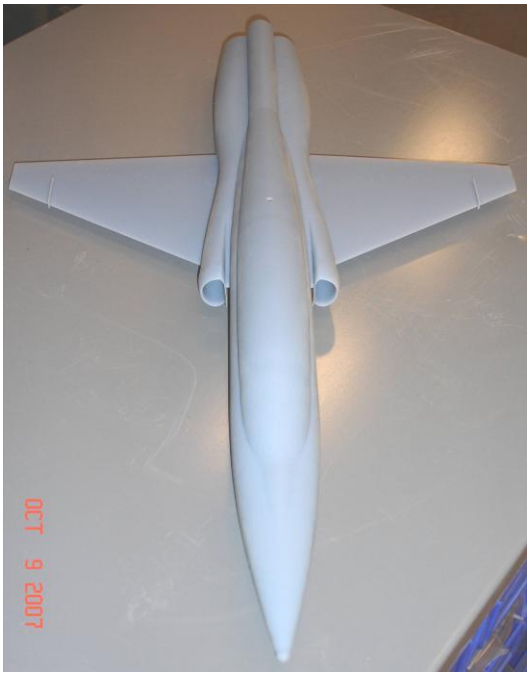

Figure 32. Completed Model with Wing Fences

3.3 Wind Tunnel Models

3.3.1 Overview.

There were eleven different configurations used in this investigation. This included the baseline or clean configuration, five different fences, two with trip tape, two with tufts, and one fuselage only.

3.3.2 Baseline and Fence Configurations.

The baseline or clean configuration was the fuselage plus the wing with no fence. This was used to determine the relative effects of the fences. The five fence configurations were located at the same spanwise position. The fence heights and thicknesses were all the same. The differences are summarized in Table 1. Also, see Figures 33-37 for photographs of the various fence designs. For the clean wing, refer back to Figure 25b.

Knowing the full-scale chord length was necessary in determining the length of the fences relative to chord length. That was determined by the use an equation from a proprietary, Northrop Grumman document (19). At WS 125.5, the chord length was 45.42 inches.

Table 1. Fence Design Descriptions

Configuration	Fence Length	Comments
Fence 1	100 percent chord	Wrapped leading edge
Fence 2	84.6 percent chord	Wrapped leading edge and was closest to Solfelt's model
Fence 3	50 percent chord	Wrapped leading edge
Fence 4	50 percent chord and linearly tapered to 100 percent chord	Wrapped leading edge
Fence 5	84.7 percent chord	Did not wrap leading edge but started at 15 percent chord and extended to 100 percent chord

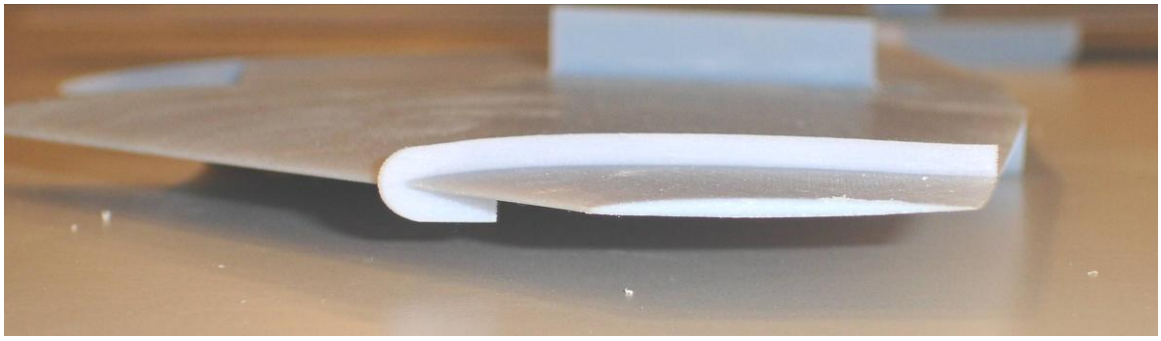

Figure 33. Model Fence 1

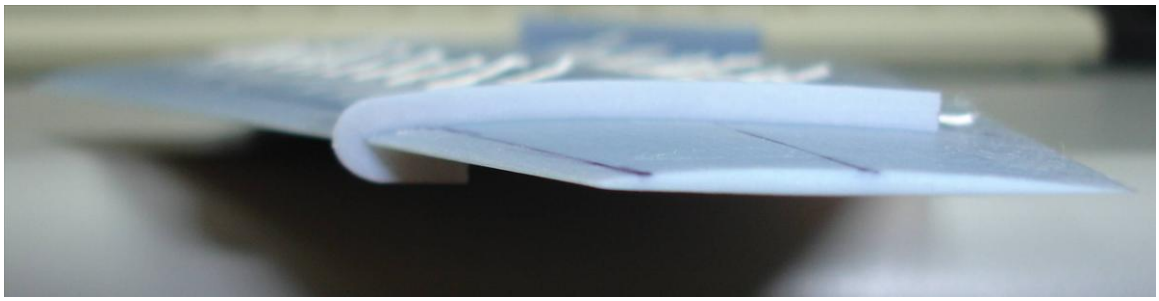

Figure 34. Model Fence 2

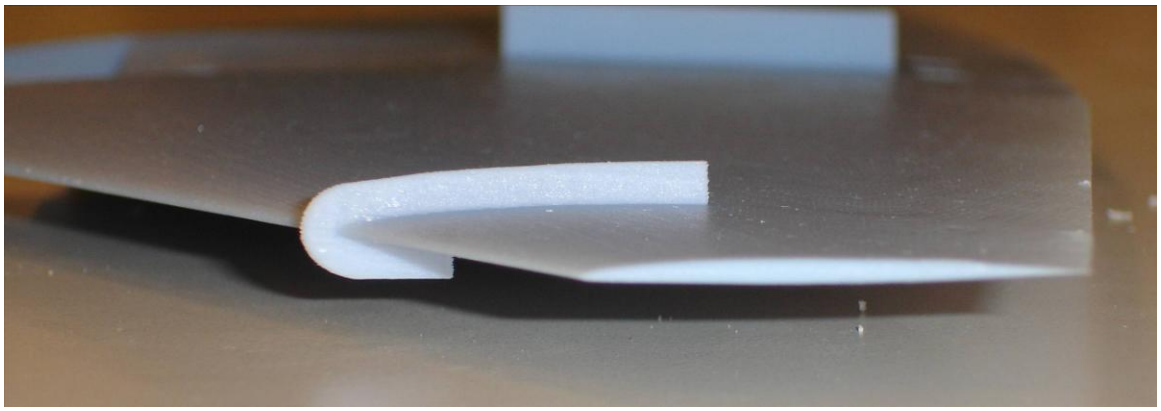

Figure 35. Model Fence 3

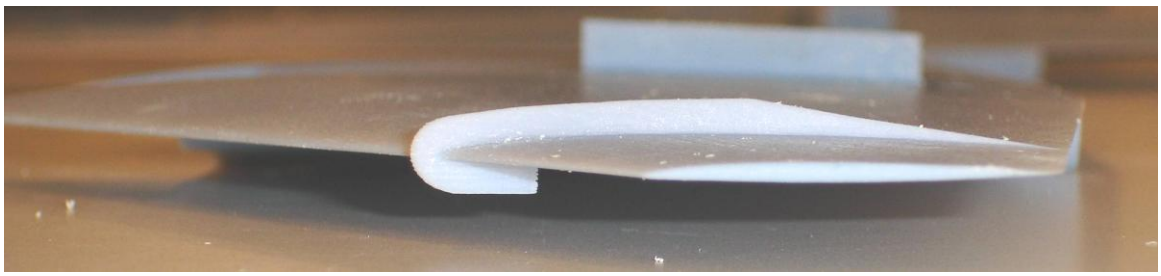

Figure 36. Model Fence 4

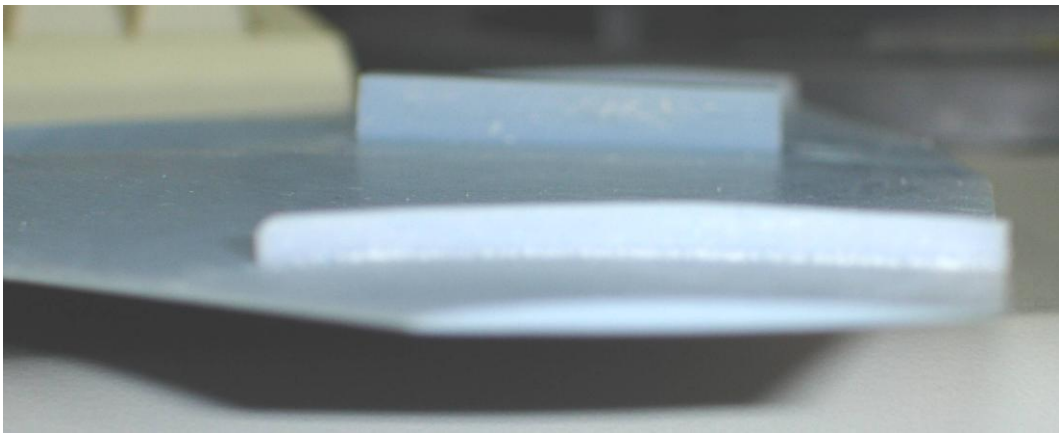

Figure 37. Model Fence 5

3.3.3 Model Trip Tape.

3.3.3.1 Reynolds Number Effects.

Reynolds number has a significant impact on aerodynamic results. Therefore, tests would ideally be conducted with the same Reynolds number. Because the model was constrained by the low-speed wind tunnel's size and airspeed limitations, tests were accomplished at Reynolds numbers based upon mean aerodynamic chord (Re_{mac}) of up to 0.3×10^6 whereas the flight test aircraft was operating at approximately 10×10^6. Reynolds number impacts the AOA at which the flow transitions from laminar to turbulent, and, in turn, impacts the skin-friction drag. Figure 38 depicts different transition points on a wing. However, the more important consequence can be on the stall AOA. If the model's boundary layer is not becoming turbulent at the same point as the real wing, separation will tend to occur earlier. If flow behavior like this happens, the lift curve slope and C_{Lmax} will drop off earlier than they would for the larger Reynolds number. One other effect here is that the stall will generally become more abrupt with a larger Reynolds number. The extent to which this occurs may not be easily measured. See Figure 39 for a plot of general Reynolds effects on the lift curve.

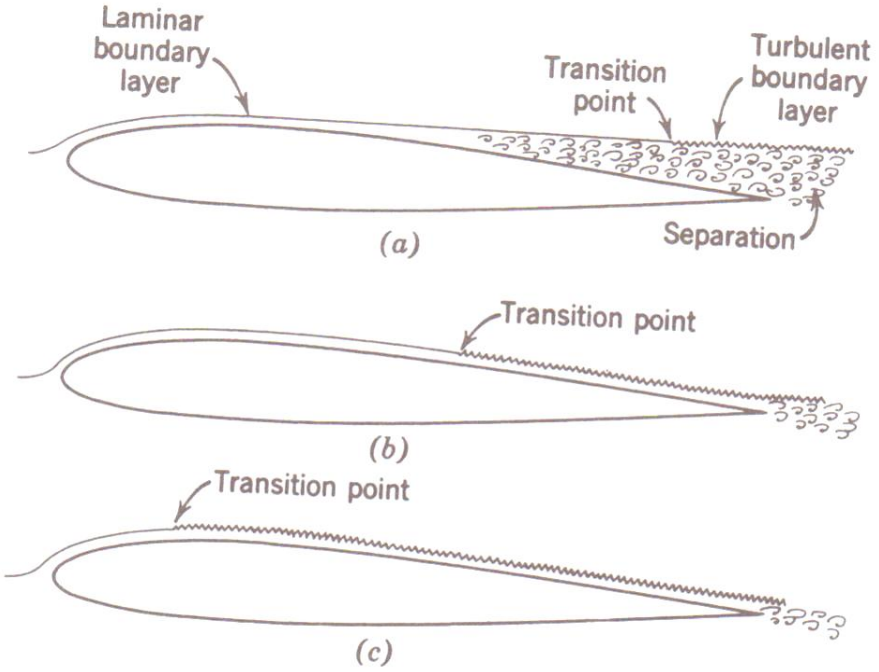

Figure 38. Aerodynamic Effect of Transition Point (3)

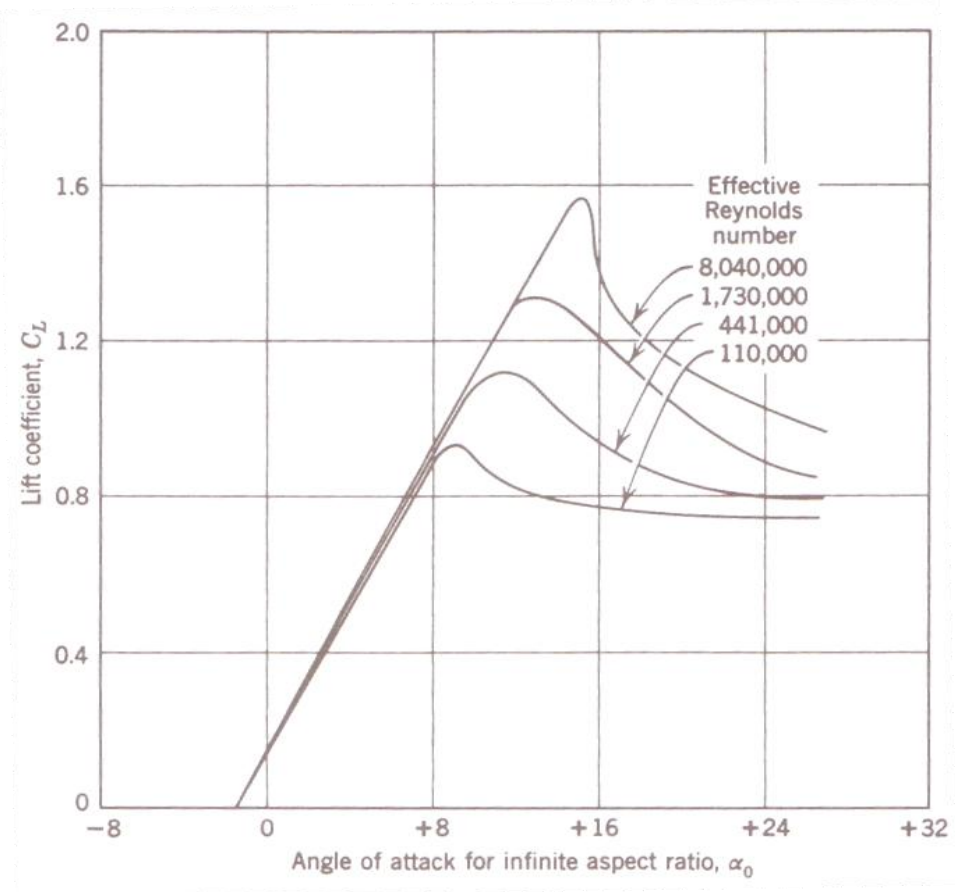

Figure 39. Generic Reynolds Effects on Lift Curve (3)

The wing's thickness ratio also plays an important role here. Because the T-38's thickness ratio was 4.8 percent, it could be considered a low-drag airfoil. Comments regarding the impact of this came from Reference 3:

> The angle of zero lift and the lift curve slope are virtually unaffected by scale…For thickness ratios of 12 percent or less, there is little effect over the lower Reynolds number range (up to Re = 6 x 10^6). Increasing Reynolds number beyond this area produces a rapid increase in C_{Lmax} to a more or less constant value, which then begins to decrease slowly on up to around Re = 25 x 10^6. Turbulent separation beginning at the edge seems to be responsible for this.

3.3.3.2 Technique and Calculations.

There is interest in modeling these Reynolds effects. One way to accomplish that is to use a trip strip. A trip strip is placed on the surface at a desired location to fix the position of transition from laminar to turbulent (3). One of the challenges is to not create a stall strip and actually make the situation worse. There are several techniques possible, including grit, 2-D tape, wire, 3-D tape, triangles and epoxy dots. The method of choice here was 2-D tape. The next decision was the location and height of the trip tape.

For most airfoils and conventional wing construction, full-scale transition occurs at about 10 percent of the chord (3). This rule-of-thumb was used for this analysis for cases where a trip strip was applied. The height (h) of the strip (in inches) can be estimated with the following equation provided in Reference 3:

$$h = \frac{12K}{R_{eft}} \tag{1}$$

where R_{eft} is Reynolds number per foot. K is a constant, and the value is 600 for Reynolds numbers greater than 100,000 based on free-stream speed and distance from the leading edge to the trip strip. If it is less than 100,000, the value of K increases to 1000. At the wing-fuselage intersection, 10 percent chord on the model was approximately 0.53

inches. Using this number and 90 miles per hour, the Reynolds number was found to be 36,000. That implied a K equal to 1000 for this scenario. Finally, the height was calculated, again using 90 miles per hour and equation 1. The desired height was found to be 0.0147 inches.

3.3.3.3 Implementation.

The clean wing and fence 2 were chosen for this analysis. Scotch® tape with a width of 0.5 inches was used. It was stacked in 6 layers, which measured 0.013 inches. This was short of the calculated height of 0.0147 inches, but one more layer exceeded the calculated height. This is a common problem with using tape as the technique of choice. The shorter height was chosen to avoid potentially creating a stall strip. The leading edge of the tape was placed along the 10 percent chord line of the wing. At the root, this was 0.53 inches aft of the leading edge, and at the tip, this was 0.13 inches aft of the leading edge. See Figures 40-44 for photographs of the wings with trip tape attached.

Figure 40. Model Clean Wing with Trip Tape (Top View)

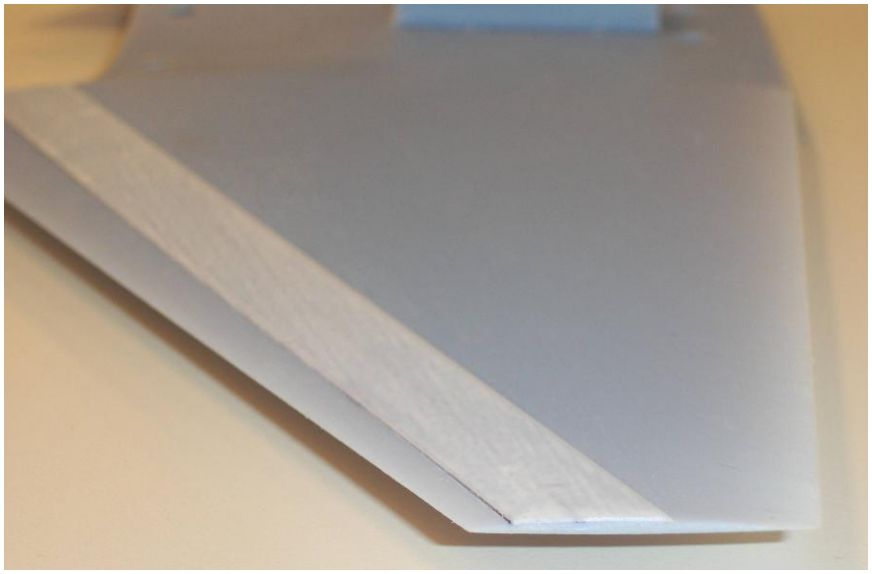

Figure 41. Model Clean Wing with Trip Tape (Side View)

Figure 42. Model Fence 2 with Trip Tape (Top View)

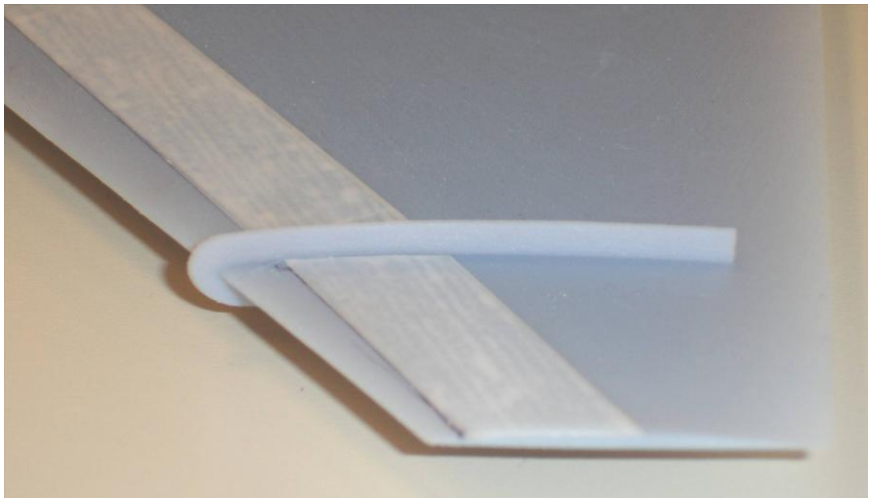

Figure 43. Model Fence 2 with Trip Tape (Side View)

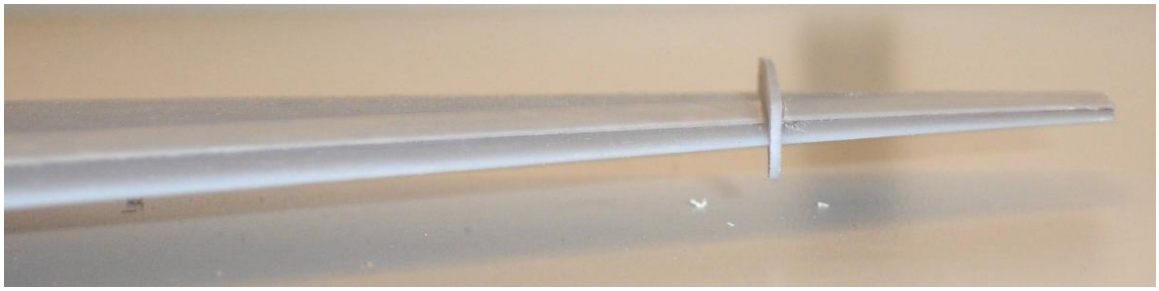

Figure 44. Model Fence 2 with Trip Tape (Front View)

3.3.4 Model Tufts.

Flow visualization was desired to aid in the understanding of fence effects on the flow field. Tufts were the technique of choice here and were applied to the clean and fence 2 configurations. Scotch® tape and small filaments of yarn were used at a length of 0.5 inches. Two rows were positioned on the upper surface. The first row covered (start of tuft to end of tuft) 19 percent to 29 percent chord at the root and 49 percent to 88 percent chord at the tip. The second row covered 58 percent to 68 percent chord at the root and 88 percent to 127 percent chord at the tip. Pictures of tufting can be seen in Figures 45-46.

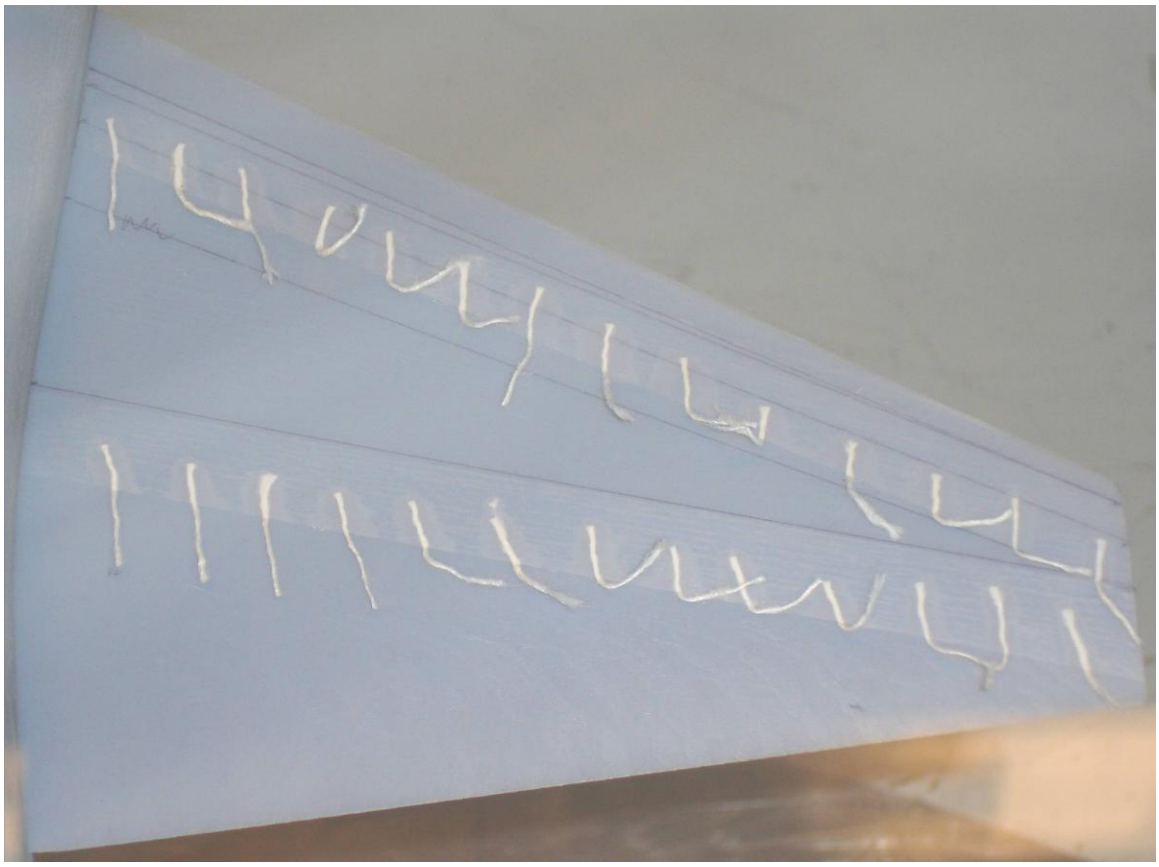

Figure 45. Model Clean Wing Tufting (During Tunnel Run)

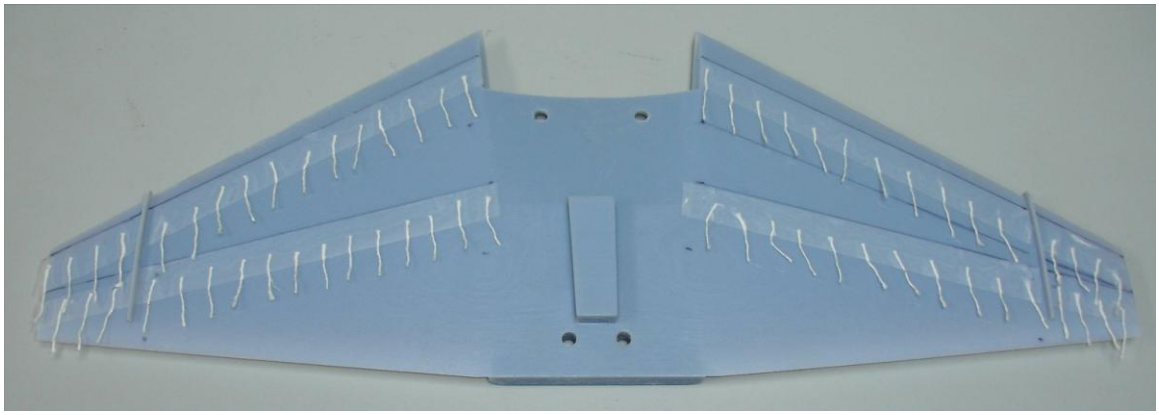

Figure 46. Model Wing Tufting with Fence 2

3.3.5 Model - Fuselage Only.

Determining the relative impacts of the fuselage to the entire aircraft was desired. Attaching this to the model and running the tunnel at the same conditions as other runs allowed for the necessary insight. See Figure 47 for a photograph.

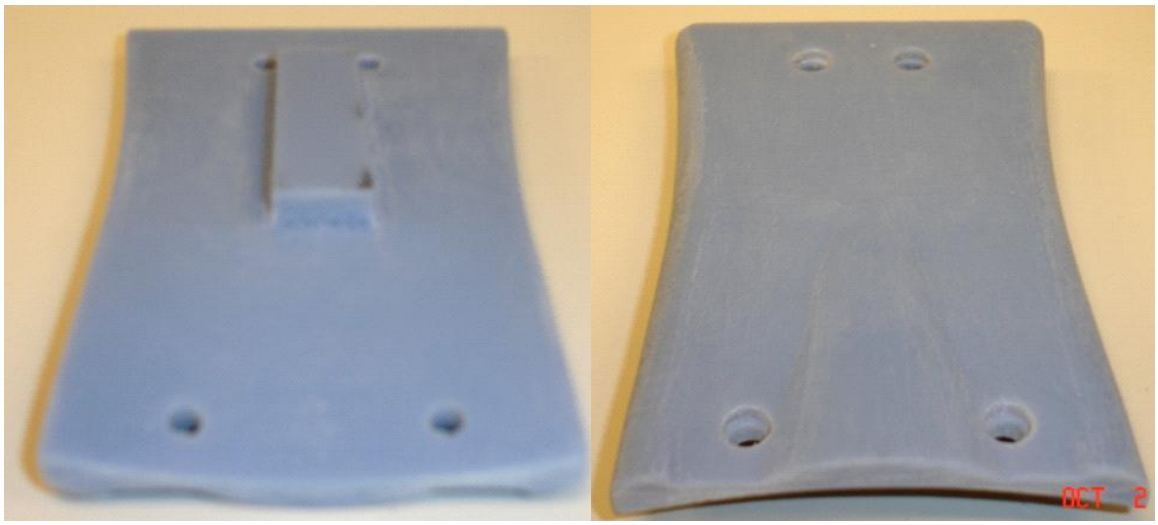

Figure 47. Fuselage Bottom Piece for Fuselage Only Runs

3.4 Experimental Equipment

3.4.1 AFIT Low-Speed Wind Tunnel.

The tests completed in this study utilized the Air Force Institute of Technology's low-speed, open-circuit wind tunnel. The schematic for the low-speed wind tunnel is Figure 48.

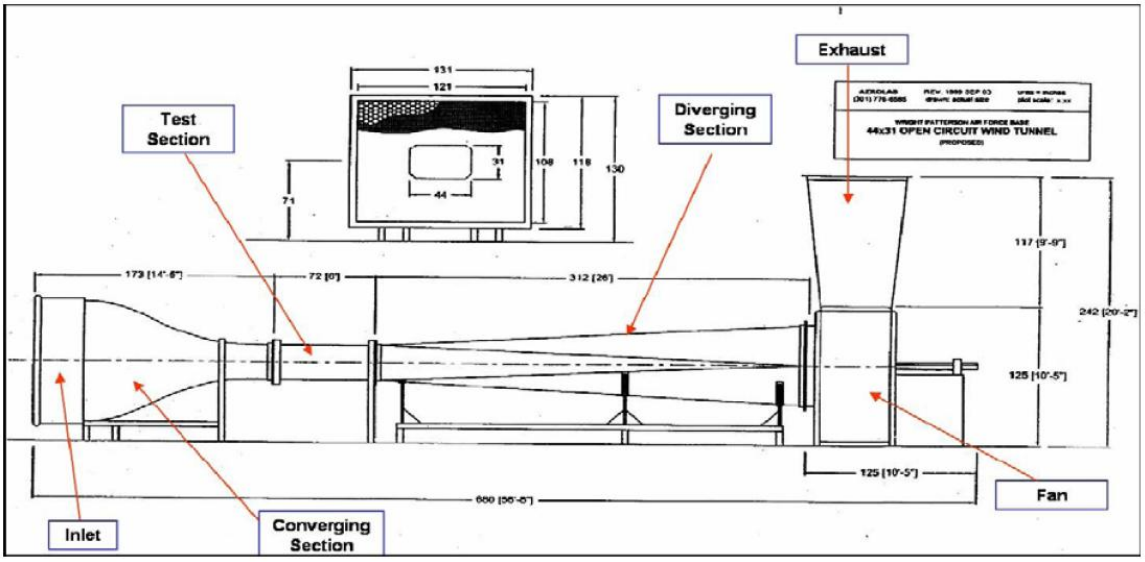

Figure 48. Schematic of the Low-Speed Wind Tunnel (13)

Ambient air was drawn through the intake plenum of the wind tunnel by the fan. Next, the air passed through an aluminum honeycomb flow-straightener and steel mesh anti-turbulence screens. Once through the last anti-turbulence screen, the flow entered the convergent section of the tunnel. The intake and convergent section of the tunnel are shown in Figure 49.

Figure 49. Intake and Convergent Section of the Wind Tunnel

The convergent section of the wind tunnel accelerated the flow into the octagon-shaped test section. The test section has a width of 44 inches and height of 31 inches. After leaving the test section, the flow entered the diffuser section of the wind tunnel, which decelerated the airflow. It was then exhausted vertically back into the room.

Models were mounted to an internal balance that was attached to a movable sting in the test section of the tunnel. The sting was adjusted by a movable control table and a pitch control device. The wind tunnel test section, balance, sting mechanism, and moveable table for sideslip, β, measurements are shown in Figure 50.

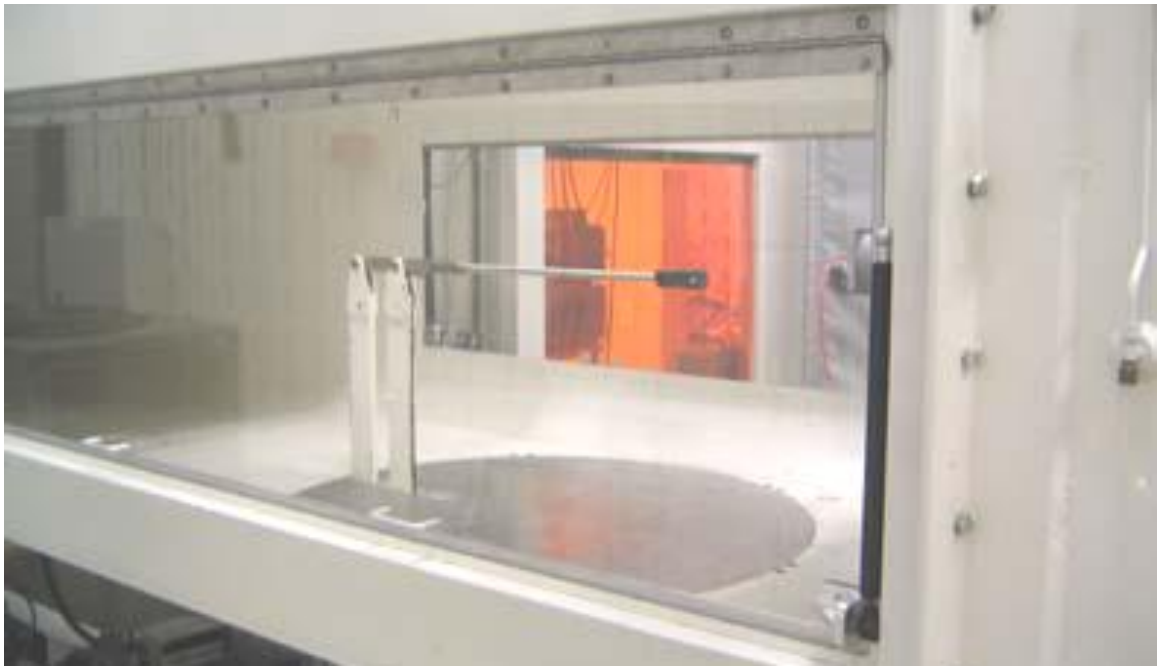

Figure 50. Test Section, Balance, Sting, and Moveable Table (13)

Force and moment measurements were taken by the balance once the wind tunnel reached the desired velocity. Angle of attack sweeps (α sweeps) were accomplished by pitching the balance and model via the stepper motor, accessed through the data acquisition program using National Instruments™ LabVIEW. This motor and linkage were located underneath the tunnel (Figure 51).

Figure 51. Sting Angle Control Device (13)

Data was acquired through the use of a computerized data acquisition system (Figure 52). It was operated by AFIT lab technician, John Hixenbaugh, who was trained and proficient with the system.

Figure 52. Computerized Data Acquisition System (13)

All data files for each test run were stored on the hard drive of the acquisition system and were retrieved for data reduction. The acquisition recorded the following

values: α, β, tunnel speed, unresolved normal force, unresolved axial force, side force, pitch moment, yaw moment, and roll moment. All forces and moments were measured about the balance center. The balance recorded the force data by comparing voltage measurements to the calibrated voltage measurements. The strain gage bridge on the balance was excited with a DC supply voltage (note: thermal equilibrium was reached).

A tare run, at zero velocity, was first completed with the model on the balance for the identical α sweep that was to be used for the test at speed. This information was ultimately necessary for data reduction and used to subtract the weight of the model from the data at all angles of attack. Between each change of tunnel velocity, it was brought back to zero to ensure that the balance was still calibrated correctly.

3.4.2 AFIT 10 Pound Strain Gage Balance.

A 10 pound, strain gage balance was used in the AFIT low-speed wind tunnel to record the force and moment measurements on all model configurations. The balance was manufactured by Modern Machine and Tool Company, Incorporated. Figure 53 shows the balance mounted in the sting and in test section of the wind tunnel.

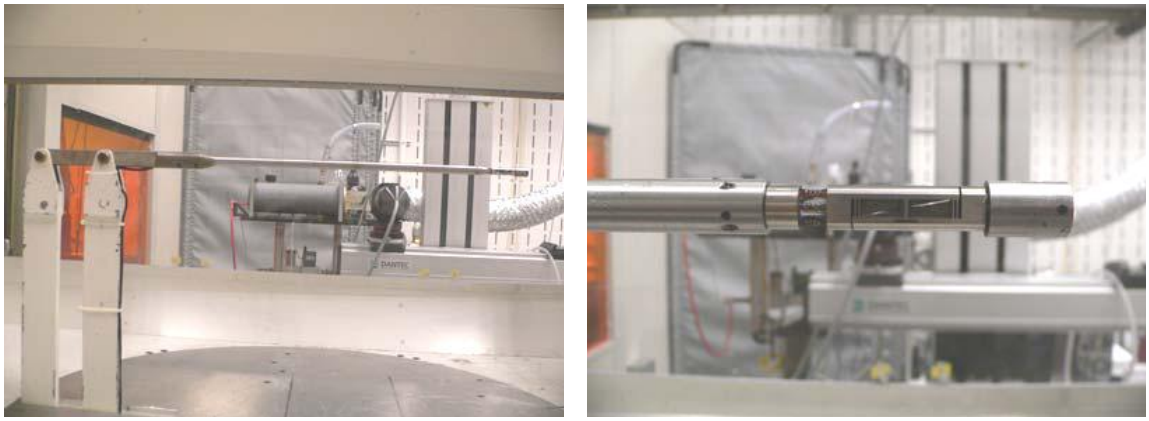

Figure 53. 10 Pound Balance Mounted in Test Section of the Wind Tunnel (13)

Maximum allowable forces and moments are listed in Table 2. If forces or moments exceed the allowable range, the balance could be damaged and thus invalidate the

calibration. The balance's moment center was located 1.4335 inches aft of the balance nose. The other dimensions of the balance can be seen in Figure 19.

Table 2. Maximum Allowable Forces and Moments for the 10 Pound Balance (13)

Component	**Max Force or Max Moment**
Normal Force	10 pounds
Axial Force	5 pounds
Side Force	5 pounds
Pitch Moment	10 inch-pounds
Roll Moment	4 inch-pounds
Yaw Moment	5 inch-pounds

3.4.2.1 Checking Balance Calibration.

Confirming the balance's calibration was desired and necessary. This was accomplished prior to testing by an AFIT lab technician, John Hixenbaugh, who used a system provided by Modern Machine and Tool Company, Incorporated. During this check, all force and moment measurements were tested. A correction to the calibration factor for the balance was performed for the axial measurement and linearity of the sensors was confirmed. The calibration constants were applied within the LabVIEW program and were used throughout the experiment.

Once the model was placed on the balance in the tunnel and testing began, some slow drift in force measurements in the axial direction was observed. This was further investigated with several separate tunnel runs, accomplished prior to recoding actual test data. Fortunately, the drift behaved linearly for at least 10 minutes, about the amount of time necessary for test runs. With this in mind, the full matrix of tests was completed. After that, the raw data was evaluated for each and every run to determine drift effects.

This behavior was not seen in past tests with the balance and was believed to be the result of mishandling of the balance prior to the initiation of testing.

Therefore, the way forward was determined to be: find the slope of the drift for each run and apply an individual correction to each run based on the drift observed in the raw data. This applied to both the tare and data files.

In order to validate this technique, one case was chosen to illustrate the effects of the correction on the raw data file. *Adjusted* refers to the data that has had the slope correction applied. The premise was that axial forces should start the test and end the test at zero. Additionally, at a steady AOA, the slope of the axial forces with respect to time should be zero. The process for data collection began with the balance sensors being nulled. The drive motor for the wind tunnel was brought up to speed, and then the test commenced (α sweep). Once the test was complete and the model was brought back to zero AOA, the wind tunnel was brought back to zero velocity and then data collection stopped. The tare and data files for a run at 30 miles per hour (mph) are shown below in Figures 54-55. The reason for showing both is to depict that two different drift rates and even in two different directions occurred. Two different corrections were applied, and both resulted in the improved measurements. Repeatability in static tests with the balance fostered confidence in using it for this study.

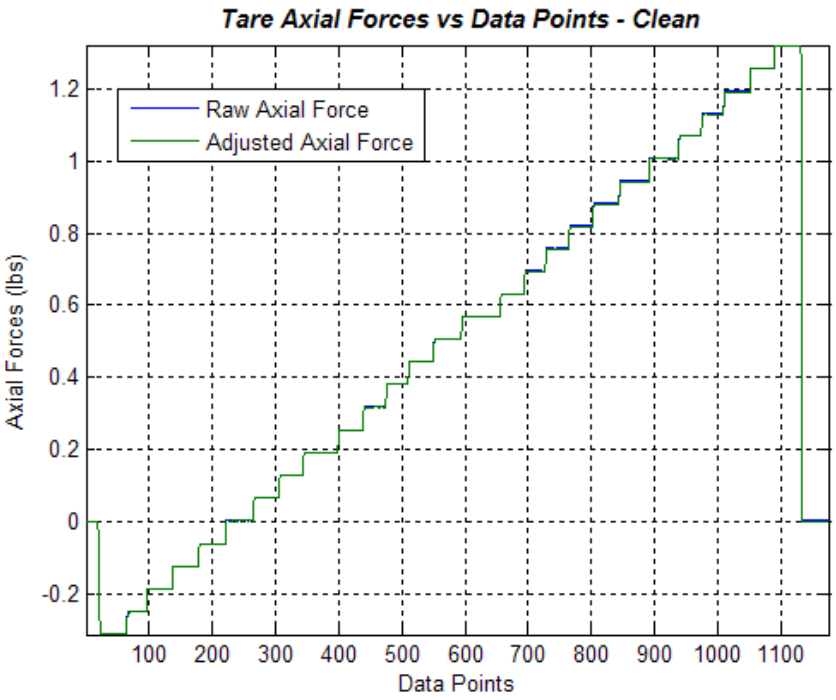

(a)

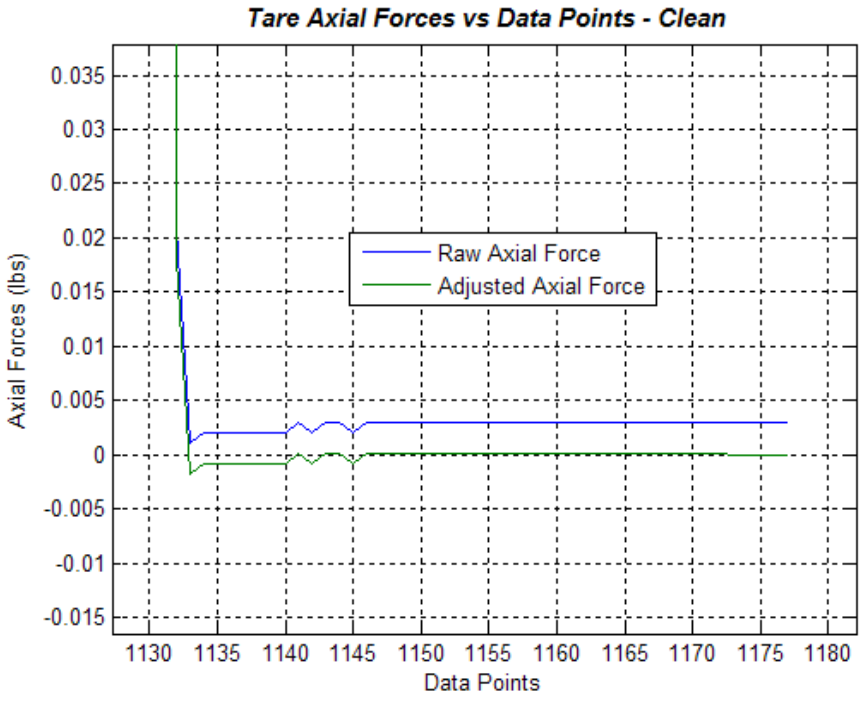

(b)

Figure 54. Balance Axial Forces Drift (Clean Configuration – Tare)
(a) Entire Data Set (b) End of Data Set

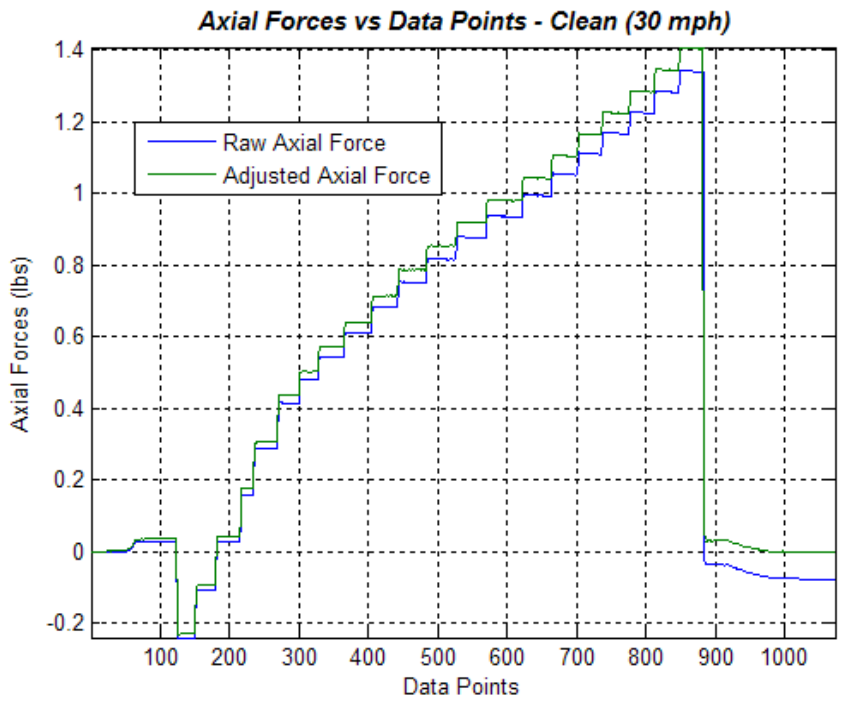
Axial Forces vs Data Points - Clean (30 mph)
Raw Axial Force
Adjusted Axial Force
Axial Forces (lbs)
Data Points
1.4
1.2
1
0.8
0.6
0.4
0.2
0
-0.2
100
200
300
400
500
600
700
800
900
1000

(a)

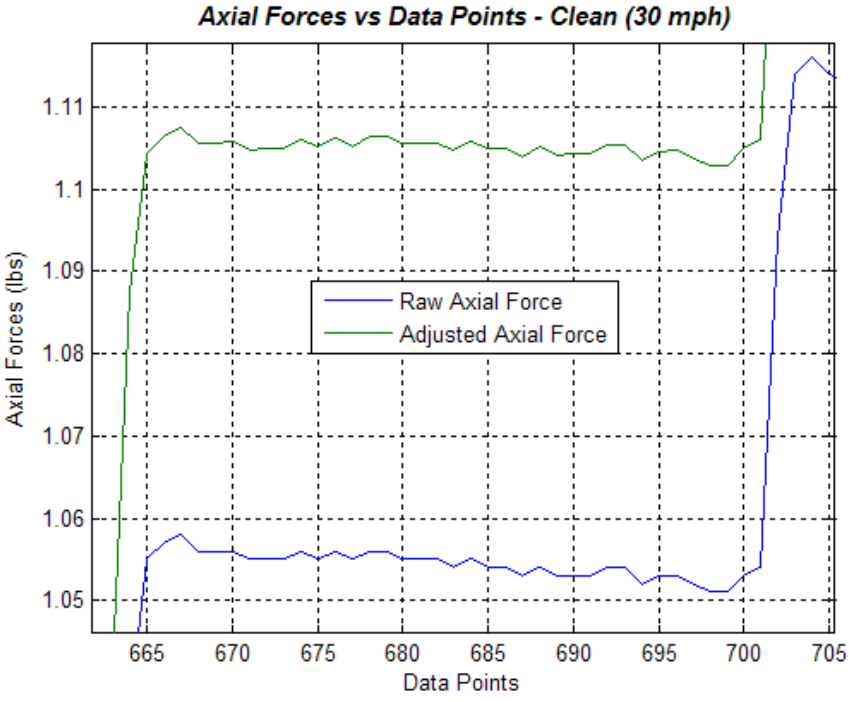
Axial Forces vs Data Points - Clean (30 mph)
Raw Axial Force
Adjusted Axial Force
Axial Forces (lbs)
Data Points
1.11
1.1
1.09
1.08
1.07
1.06
1.05
665
670
675
680
685
690
695
700
705

(b)

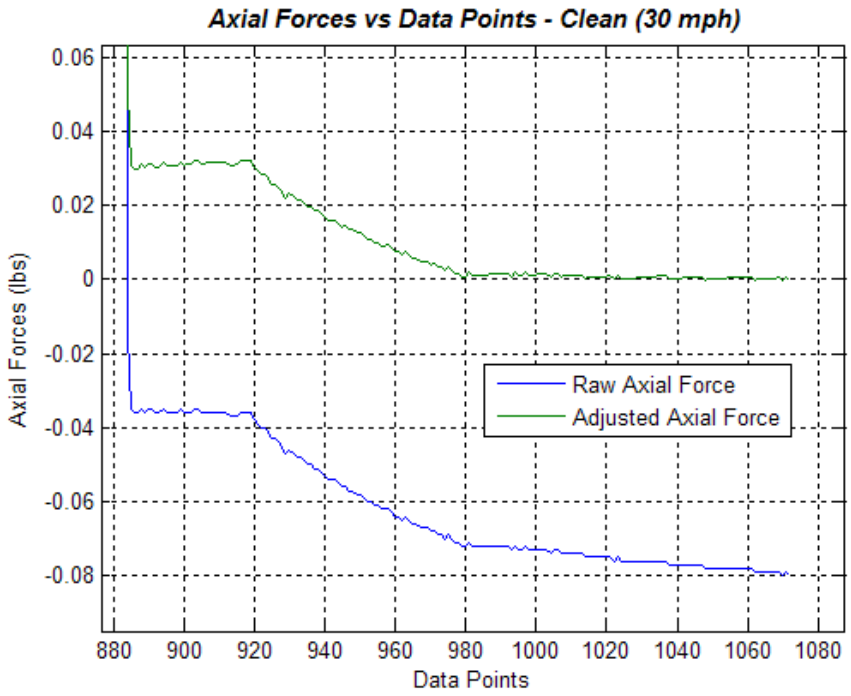

(c)

Figure 55. Balance Axial Forces Drift (Clean Configuration – 30 mph)
(a) Entire Data Set (b) Stable AOA (c) End of Data Set

For the tare run, the drift was only approximately 0.003 pounds and for the 30 mph run depicted, the drift was 0.07 pounds. It is important to note that the balance measurements were in the body axis and had to be converted to the wind axis through an Euler angle sequence (3). Because lift and drag both have axial and normal body force components, lift and drag were both affected by the drift. Additionally, lower speeds required more accurate load measurements. These effects are illustrated in Figure 56 and Figure 57. As expected, the impact on drag was much more significant than on lift. For example, at 10 degrees AOA and 30 mph, drag's magnitude was changed by a factor of 5.75 times more than lift's magnitude was changed.

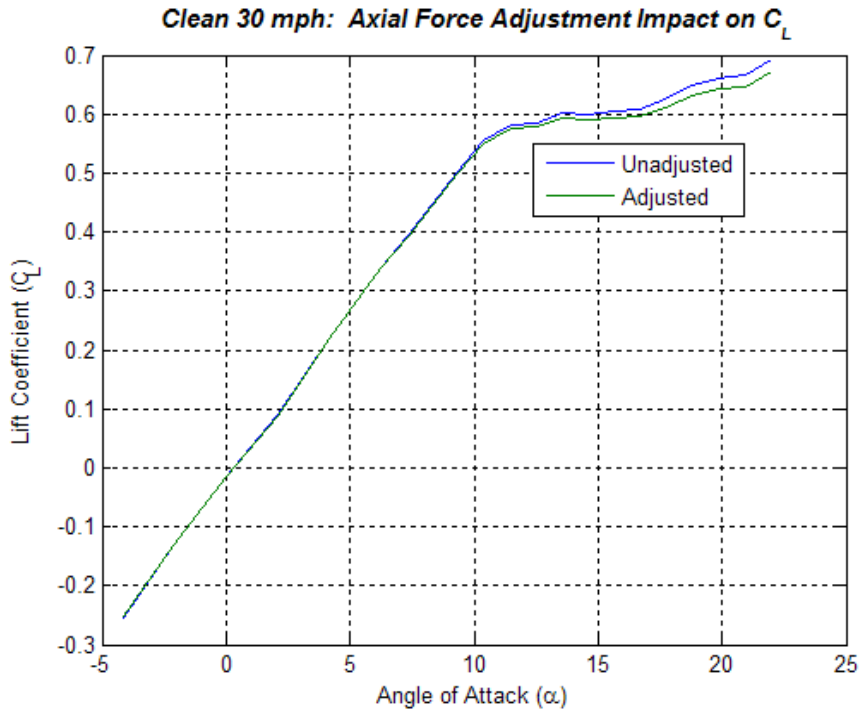

Figure 56. Axial Force Adjustment Impact on C_L (Clean Configuration – 30 mph)

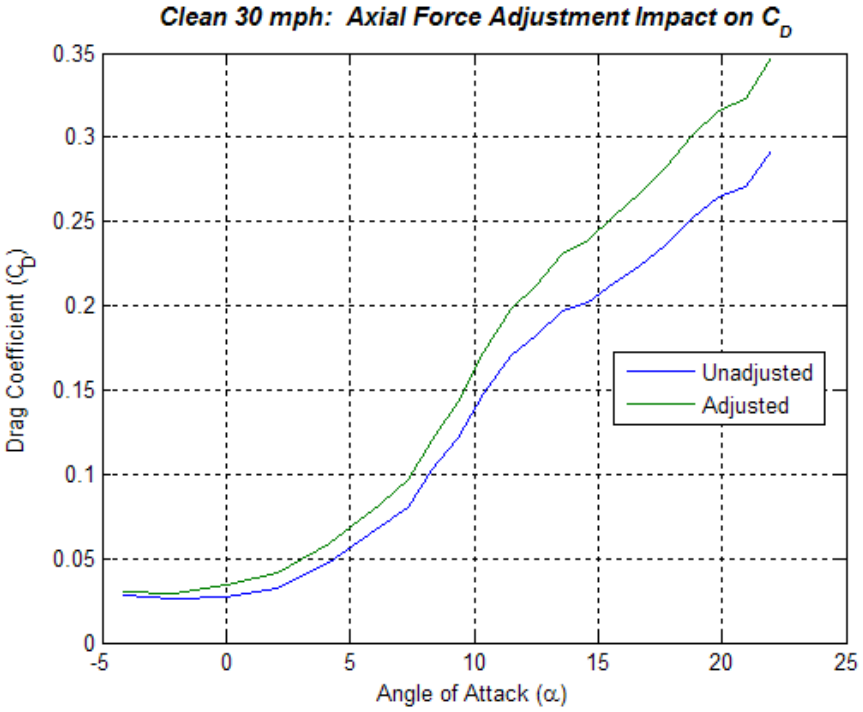

Figure 57. Axial Force Adjustment Impact on C_D (Clean Configuration – 30 mph)

3.5 Collecting and Processing Wind Tunnel Data

3.5.1 Correction of Balance Data Using MATLAB 10 Pound Balance Code.

Once the wind tunnel tests were completed, the data had to be processed in order to have results. This reduction was done using a MATLAB m-file that performed a series of operations and calculations on the tunnel output data file. The MATLAB 10 pound balance code was adapted from previous research conducted by former AFIT students Parga, Deluca, Walker, and Killian (13). The modified MATLAB 10 pound balance code can be found in Appendix B.

The code required multiple inputs regarding the model and ambient conditions at the time of testing (e.g., room temperature, barometric pressure). It also required the tare and wind tunnel data for each model configuration. This information as well as file names can be located in Appendix D. When the aircraft model was mounted on the balance, it was at the reference 0 AOA. When the balance was at the 0 degree position, the model was at 0 degrees aircraft AOA. The axial drift correction was also included at the beginning of the code and was applied in a loop to each data point in the tare and data files. The correction factors were changed for each test.

In order to obtain the moment data from the wind tunnel results, a reference center of gravity (CG) for the aircraft was determined. Although there was no tail included in any of the test configurations, a reference CG of 19.1 percent mean aerodynamic chord (MAC) was used. The aircraft had a CG limit of 14 percent to 25 percent MAC. According to the T-38 Systems Group, an average landing CG was 19.1 percent MAC. Because this investigation was specifically considering a reduction in landing speed, this reference CG was chosen. Using Figure 58 and coordinates for the balance moment center in the model, the result was a difference between reference CG

and balance moment center of 1.5339 inches in the longitudinal axis and -0.5664 inches in the vertical axis. The difference was zero in the lateral axis. These distances were used within the code for the moment coefficient calculations. The pitching moment about this reference CG is denoted C_{mcg}.

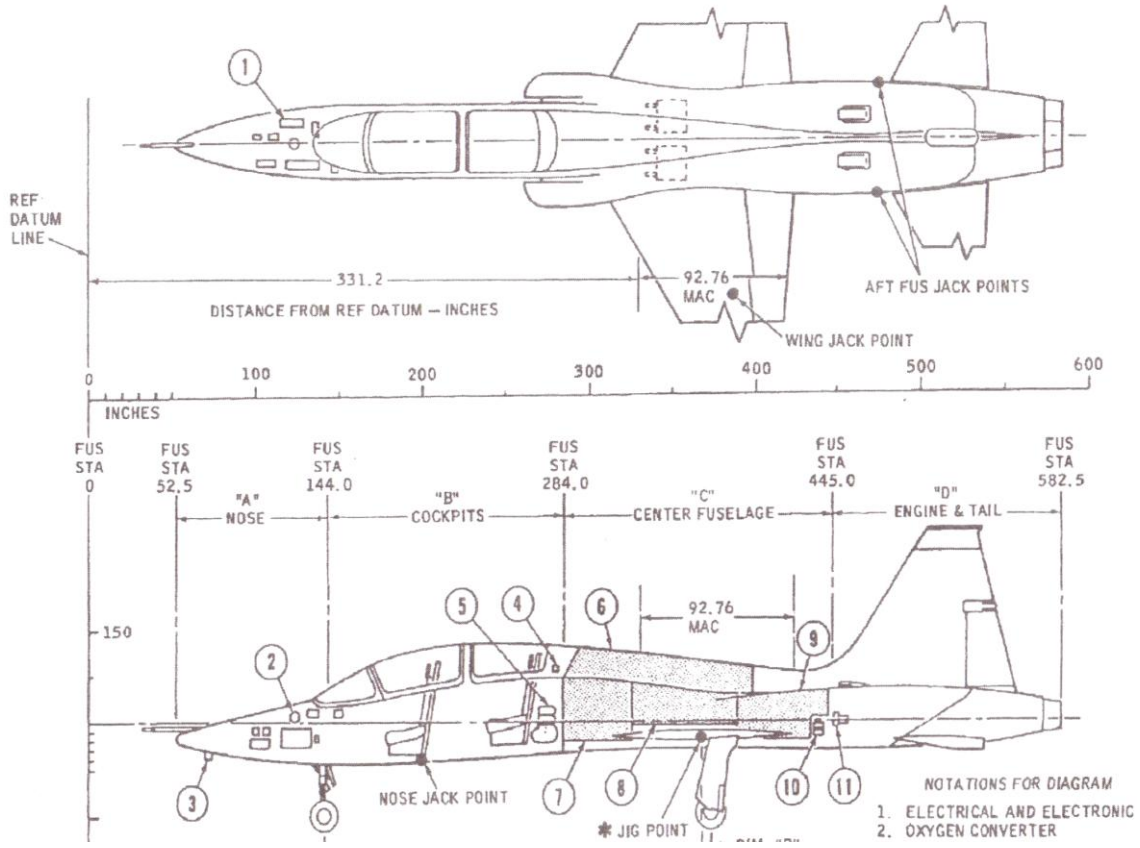

Figure 58. Aircraft Diagram and Reference Datum (28)

The code for data reduction began with the subtraction of the tare data from the test data. Next, a few corrections to the data were made. The first correction was to account for the solid blockage of flow in the wind tunnel by the model. This adjustment was done by determining the blockage correction factor. The blockage correction factor accounted for the change in speed of the airflow due to the reduction in the available cross-sectional area of the tunnel near the model. The techniques, graphs, and equations outlined in Barlow, Rae, and Pope were used (3).

In order to determine the blockage correction factor, several numbers were required. The dimensions of the test section, wing and body volumes (assumed constant for all configurations), wing span, and constants K_1, K_3, and τ_1 were necessary. These constants were determined from graphs in the text after the other numbers were found. The test section was 44 inches by 31 inches. The model's wing volume found with Magics was 9 cubic inches, and the body volume found with Magics was 66 cubic inches. The span was 14.43 inches. With these numbers, K_1 was found to be 0.97, K_3 was found to be 0.89, and τ_1 was found to be 0.87. Equations 2 and 3 yielded the solid-blockage correction factors (ε_{sb}). They were separated into wing (W) and body (B) factors for simplicity. The sum of the wing and body factors equaled the total. C is the tunnel cross-sectional area (3).

$$\varepsilon_{sb,W} = \frac{K_1 \tau_1 (wingvolume)}{C^{\frac{3}{2}}} \tag{2}$$

$$\varepsilon_{sb,B} = \frac{K_3 \tau_1 (bodyvolume)}{C^{\frac{3}{2}}} \tag{3}$$

The next correction was for downwash. This correction was required due to the finite boundaries of the wind tunnel and the vortices caused by wing loading. These vortices, often called image vortices, make the lift too large and the drag too small at a given AOA for a closed jet (3). The downwash correction factor (δ) was the same for all the model configurations due to their spans being equivalent. δ was found by first calculating the wind tunnel aspect ratio (λ):

$$\lambda = \frac{height_{tunnel}}{width_{tunnel}} \tag{4}$$

Where $height_{tunnel}$ is the height of the wind tunnel cross-section and $width_{tunnel}$ is the width of the wind tunnel cross-section. The AFIT low-speed wind tunnel λ was 0.705. The next calculation that was needed was the ratio (k) of the model's wingspan (b) to the width of the wind tunnel:

$$k = \frac{b}{width_{tunnel}} \tag{5}$$

For this test k was 0.33. Finally, the values for λ and k were used to find δ via the figures in Barlow et al (3). The δ term was found to be 0.1177.

The third correction to the data involved transferring the normal and axial balance data into the proper frame of reference with respect to the flow. This correction was necessary to translate the lift and force data so it was with respect to the free stream and not the AOA of the balance or model. The equations for the lift and drag coefficients found from the normal and axial forces acting on the balance are shown in equations 6 and 7.

$$C_L = \frac{N \cdot \cos\alpha - A \cdot \sin\alpha}{\frac{1}{2}\rho \cdot V^2 \cdot S} \tag{6}$$

$$C_D = \frac{N \cdot \sin\alpha + A \cdot \cos\alpha}{\frac{1}{2}\rho \cdot V^2 \cdot S} \tag{7}$$

Where C_L is the lift coefficient, C_D is the drag coefficient, N (pounds) is the unresolved normal force acting on the balance, A (pounds) is the unresolved axial force acting on the balance, α (degrees) is the AOA of the balance, ρ (slug per cubic foot) is the air density, V (feet per second) is the tunnel wind velocity, and S (square feet) is the reference wing planform area of the model (170 square feet for the T-38 or 0.3853 square feet for the model).

3.5.2 Wind Tunnel Uncertainty Analysis.

3.5.2.1 Using Clean Repeatability Runs.

Using the techniques in Barlow et al (3), confidence probabilities (β_{cp}) were used in conjunction with the standard deviations (s) and sample size (n) for the calculated C_L, C_D, C_{mcg}, and lift-to-drag ratio (L/D) values to determine percent error at each AOA. This was done for all three velocities (30, 60, and 90 mph) and was accomplished with the following equations:

$$\beta_{cp} = \{\bar{x} - \Delta x < \mu < \bar{x} + \Delta x\} \tag{8}$$

$$\Delta x = k_3 * s \tag{9}$$

Where μ is the mean, $\bar{x}$ is the sample mean, and k_3 is a constant from the table in Barlow et al (3). For a sample size of three, k_3 is 2.4841 for 95 percent confidence probability and 5.7301 for 99 percent confidence probability.

3.5.2.2 Using Raw Data.

The second uncertainty analysis methodology followed Killian's (13). This was performed on the lift-to-drag ratio for the clean model configuration. The uncertainty analysis was done by taking the equation for lift-to-drag and breaking it into a form consisting only of measurements from the wind tunnel results:

$$L/D = \frac{C_L}{C_D} = \frac{N \cdot \cos\alpha - A \cdot \sin\alpha}{N \cdot \cos\alpha + A \cdot \sin\alpha} \tag{10}$$

where C_L is the lift coefficient, C_D is the drag coefficient, N (pounds) is the unresolved normal force measurements on the balance, A (pounds) is the unresolved axial force measurement on the balance, and α (degrees) is the angle of the balance to the free stream velocity.

Then the partial of equation 10 was taken with respect to both *N* and *A*, yielding the following equations:

$$\frac{\partial(L/D)}{\partial N} = \frac{A}{(N \cdot \sin\alpha + A \cdot \cos\alpha)^2} \tag{11}$$

$$\frac{\partial(L/D)}{\partial A} = \frac{-N}{(N \cdot \sin\alpha + A \cdot \cos\alpha)^2} \tag{12}$$

Where $\frac{\partial(L/D)}{\partial N}$ is the partial of the lift-to-drag ratio with respect to the unresolved normal force, and $\frac{\partial(L/D)}{\partial A}$ is the partial of the lift-to-drag ratio with respect to the unresolved axial force.

Next, a worst case possible error and a realistic case possible error in lift-to-drag can be calculated:

$$\Delta(L/D)_{worst} = \left|\frac{\partial(L/D)}{\partial N} \cdot \Delta N\right| + \left|\frac{\partial(L/D)}{\partial A} \cdot \Delta A\right| \tag{13}$$

$$\Delta(L/D)_{realistic} = \sqrt{(\frac{\partial(L/D)}{\partial N} \cdot \Delta N)^2 + (\frac{\partial(L/D)}{\partial A} \cdot \Delta A)^2} \tag{14}$$

Where $\Delta(L/D)_{worst}$ is a worst-case error value in lift-to-drag ratio, $\Delta(L/D)_{realistic}$ is a more realistic error value in lift-to-drag ratio, ΔN is the possible error in the normal force measurement, and ΔA is the possible error in the axial force measurement. The worst case scenario is the case where each possible case of error occurs in the same direction. The realistic case scenario is the geometric mean of the possible errors and is a more probable occurrence.

For the 10 pound balance, the uncertainty in the normal force measurement, ΔN, was specified by the manufacturer to be more than 0.025 pounds. The uncertainty in the axial force measurement, ΔA, was specified by the manufacturer to be more than 0.0125 pounds. These values were considered to be too conservative for actual data acquisition. Therefore, the average standard deviation of N and A at each AOA for ΔN and ΔA were used. During the test, multiple data points were logged for each AOA. Therefore, the actual sample variance and standard deviation were computed. This may not be appropriate for accuracy. However, this provided good information for precision.

The range for the possible lift-to-drag ratio was then determined by:

$$L/D_{range} = L/D \pm \Delta(L/D) \tag{15}$$

Where $(L/D)_{range}$ is the possible range of the lift-to-drag ratio given uncertainty in the measurements taken, L/D is the measured lift-to-drag ratio, and Δ(L/D) is the possible error in the L/D measurement (in one direction).

3.6 Wind Tunnel Test Plan

A summary of tests performed on the various model configurations can be found in Table 3. All tests for balance data were run at 30, 60, and 90 mph for Reynolds number variation and results consistency. These speeds were equivalent to Reynolds numbers of approximately 0.1×10^6, 0.2×10^6, and 0.3×10^6 respectively. All α sweeps were from -4 to 22 degrees. Flow visualization with the tufts was only accomplished at 10 and 15 degrees AOA at 90 mph. Again, to see dates, temperatures, pressures and file names for each test run, refer to Appendix D.

Table 3. Summary of Wind Tunnel Runs Performed

α	Clean	Fence 1	Fence 2	Fence 3	Fence 4	Fence 5
-4	B ; R ; TT	B	B ; TT	B	B	B
-2	B ; R ; TT	B	B ; TT	B	B	B
0	B ; R ; TT	B	B ; TT	B	B	B
2	B ; R ; TT	B	B ; TT	B	B	B
4	B ; R ; TT	B	B ; TT	B	B	B
6	B ; R ; TT	B	B ; TT	B	B	B
7	B ; R ; TT	B	B ; TT	B	B	B
8	B ; R ; TT	B	B ; TT	B	B	B
9	B ; R ; TT	B	B ; TT	B	B	B
10	B ; R ; TT ; T	B	B ; TT ; T	B	B	B
11	B ; R ; TT	B	B ; TT	B	B	B
12	B ; R ; TT	B	B ; TT	B	B	B
13	B ; R ; TT	B	B ; TT	B	B	B
14	B ; R ; TT	B	B ; TT	B	B	B
15	B ; R ; TT ; T	B	B ; TT ; T	B	B	B
16	B ; R ; TT	B	B ; TT	B	B	B
17	B ; R ; TT	B	B ; TT	B	B	B
18	B ; R ; TT	B	B ; TT	B	B	B
19	B ; R ; TT	B	B ; TT	B	B	B
20	B ; R ; TT	B	B ; TT	B	B	B
21	B ; R ; TT	B	B ; TT	B	B	B
22	B ; R ; TT	B	B ; TT	B	B	B

B = Balance	T = Tufts	TT = Trip Tape	R = Repeatability (3 times)

3.7 Flight Test

3.7.1 Overview.

This section will cover the flight test item description, objectives, methodology, data reduction, and overall test plan (36; 34). Normalized AOA was primarily used for flight test discussions due to pilot familiarity with those numbers. True AOA has been put in parentheses next to normalized AOA numbers for ease of reference. Appendix J includes a plot of normalized AOA versus true AOA as calibrated on the flight test aircraft and a plot of normalized AOA versus true AOA as is normal to production T-38 aircraft.

3.7.2 Flight Test Item Description.

3.7.2.1 Flight Test Aircraft.

The T-38A was a two seat (tandem), supersonic trainer built by the Northrop Corporation, as shown in Figure 59. It had a wing reference area of 170 square feet and was powered by two General Electric J85-GE-5M afterburning turbojet engines. Further information about the T-38 aircraft and systems can be found in the flight manual, Reference 30. The test aircraft was tail number 68-8205.

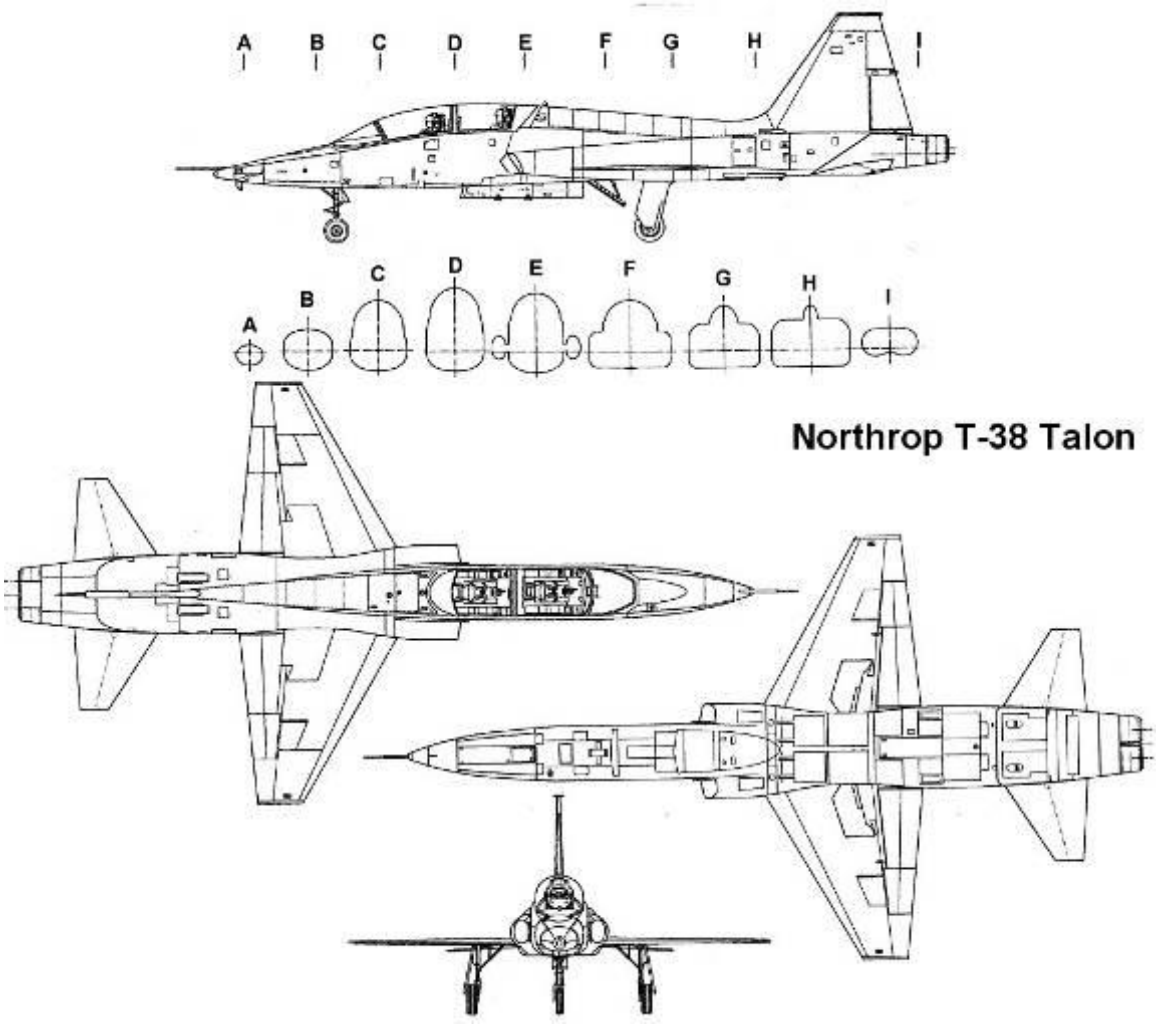

Figure 59. T-38 3-view (36)

The replacement of the production nose boom with a flight test nose boom and the addition of sensitive instruments used to gather performance data were assumed to have negligible effects on the aerodynamic and thrust characteristics of the aircraft. Therefore, the performance and stall characteristics of the test aircraft, without the wing fence, were considered production representative. The production normalized AOA gauge was inoperative. Previous flight test data and data obtained during a calibration flight on the test aircraft were used to convert normalized AOA to true AOA for test purposes and may be found in Reference 37. A description of the modifications to the test aircraft may be found in the modified flight manual (29).

3.7.2.2 Flight Test Wing Fence.

The test article was a wing fence that was attached to the T-38 at wing station 125 or 26.5 inches inboard from the wing tip on both wings. The pre-existing attachment line at this wing station was used to attach the fence to the top and bottom surfaces of the wing. The aircraft's wing span was not increased by the addition of the fences. The wing fence extended from the leading edge to 84.6 percent of the local chord length on the upper wing surface. The wing fence wrapped the leading edge and extended from the leading edge to 24.2 percent of the local chord length on the lower wing surface. This was greater than the 15 percent on the wind tunnel model. This extension was required for fence attachment purposes. It had a constant height of 2.5 inches above the wing's surface. Figure 60 shows a drawing of the fence. Each wing fence was made from two pieces of 6061-T6 aluminum. Both pieces were 0.25 inches thick and were welded together. The wing fence was attached to the wing using 18 of the existing wing tip fastener locations.

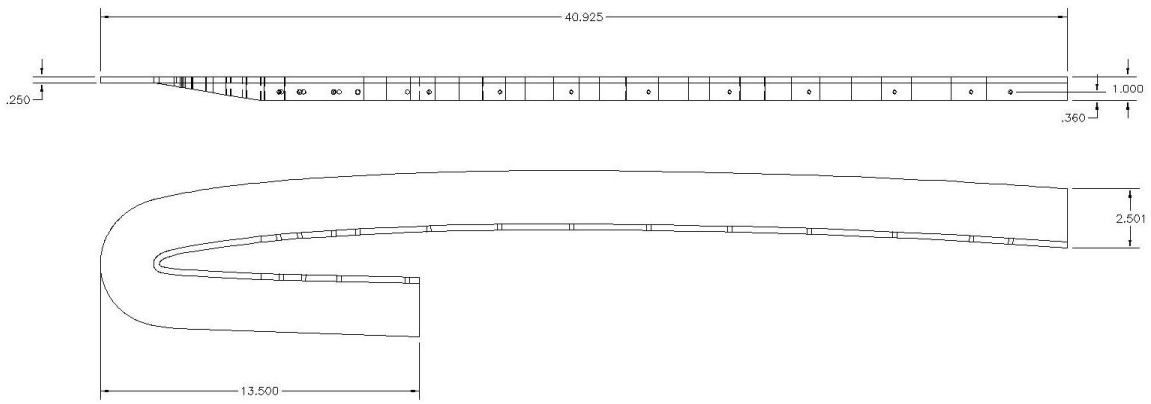

Figure 60. Top and Side Views of Flight Test Wing Fence (in inches) (1)

The Instrumentation Division of the 412th Test Wing was responsible for the design implementation and structural analysis for flight test. Structurally, the critical case was considered to be a side loading from either the spanwise flow of air over the wing or with the aircraft in a side slip. An extremely conservative, maximum load of 7.65 pounds per square inch was used, and an analysis for the fence and fasteners was accomplished to include stress and displacement. Figure 61 shows the finite element mesh used in the analysis. Lastly, an analysis on the weld was accomplished. All analyses showed the design to be adequate, and the fence was fabricated and installed. Figure 62 shows the installed wing fence on the left wing. More details on the structural analysis may be found in the AFFTC modification package, *T-38 Wing Fence*, M08A205A (1).

Figure 61. Finite Element Mesh for Flight Test Wing Fence (1)

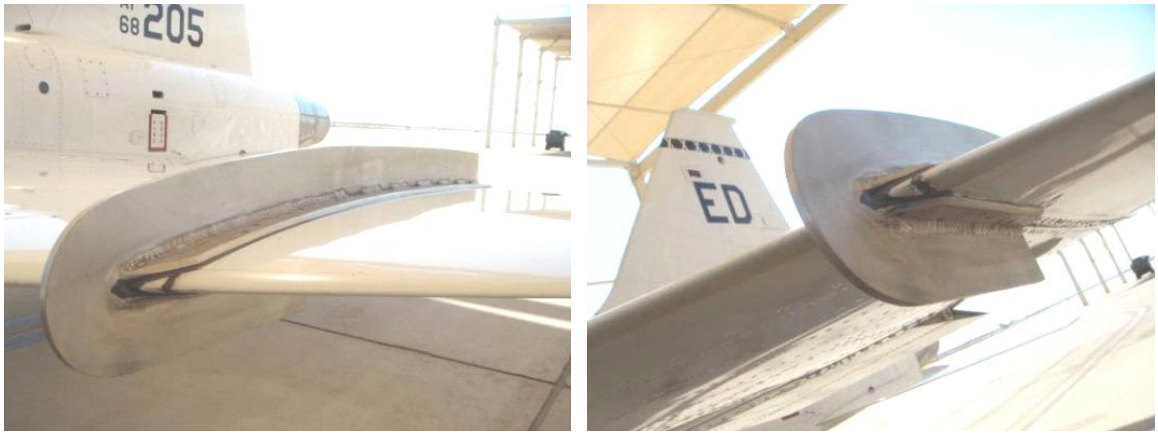

Figure 62. Top and Bottom Photographs of the Installed Left Wing Fence (36)

3.7.2.3 Flight Test Wing Tufting.

The right wing was tufted for two sorties, one in the clean (baseline) configuration and one in the fence (modified) configuration. Tuft rows were in the streamwise direction and tuft columns were in the spanwise direction. There were four rows of tufts

that extended from the wingtip (WS 151.5) inboard to approximately WS 98. The four rows were located at 11.1, 33.4, 55.7, and 78.0 percent of the local chord. The tufts were separated by a minimum of two times the tuft length, approximately 6 inches, to prevent entanglement. Figure 63 is a drawing of the planned tuft layout, and Figure 64 is a drawing of the planned tuft attachment technique. Figure 65-67 shows a front and side view photograph of the installed tufts.

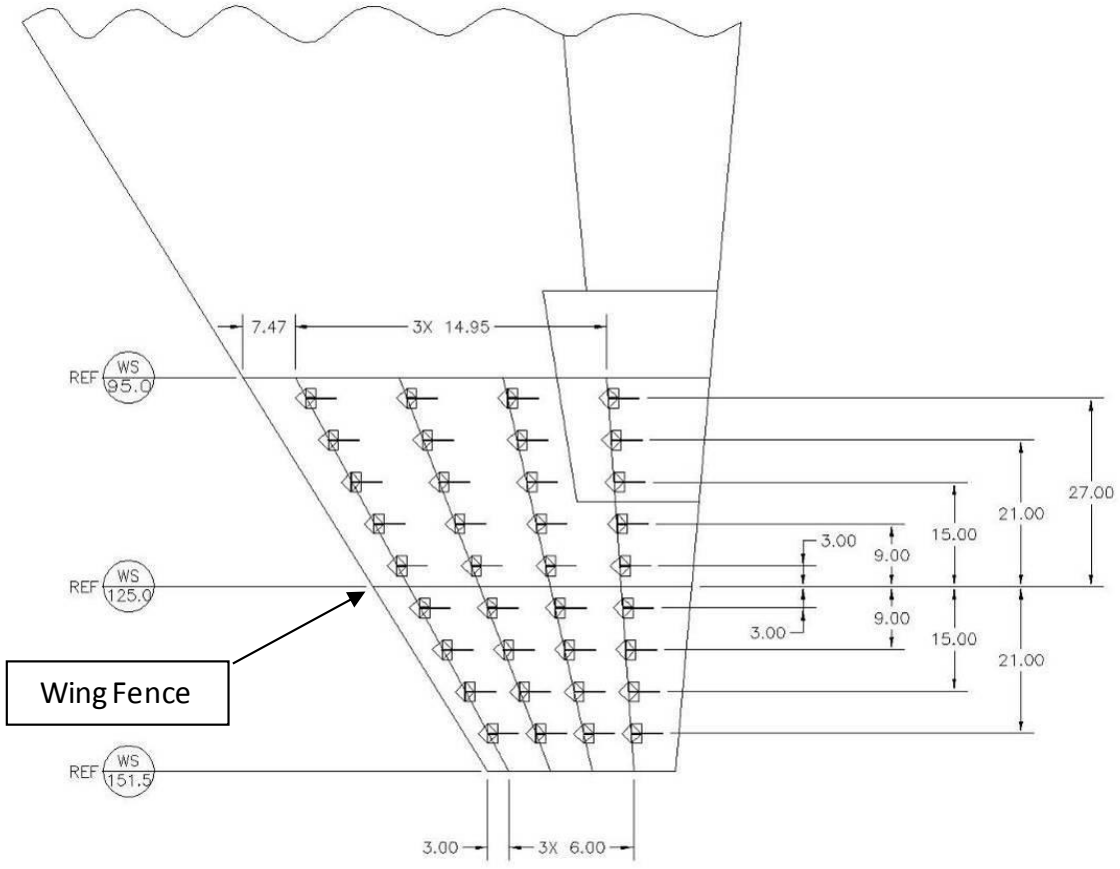

Figure 63. Flight Test Wing Tuft Layout (in inches) (1)

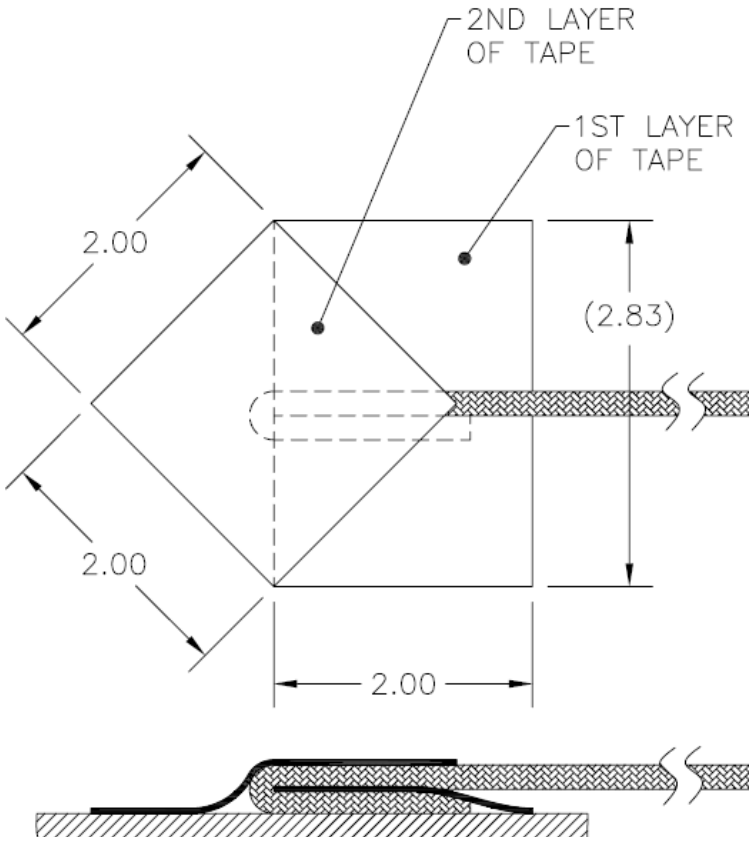

Figure 64. Flight Test Wing Tuft Attachment Methodology (in inches) (1)

Figure 65. Flight Test Installed Tufts (Front View)

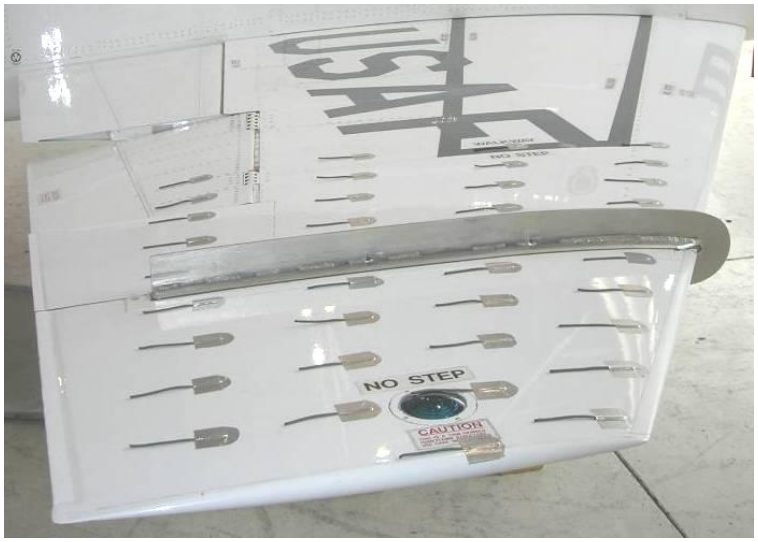

Figure 66. Flight Test Installed Tufts (Side View)

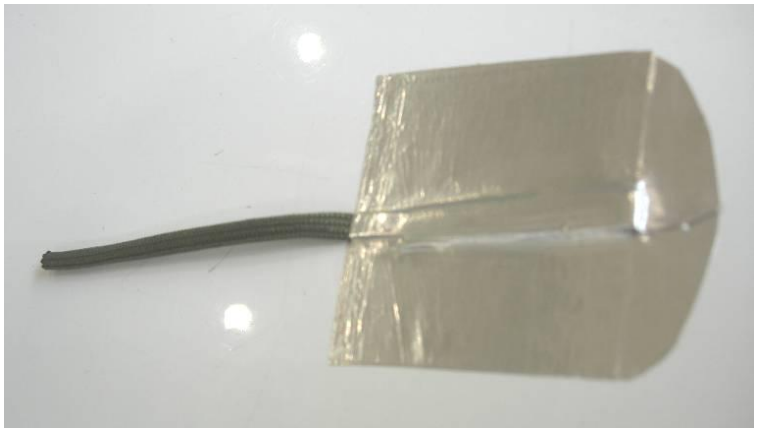

Figure 67. Flight Test Individual Installed Tuft (Top View)

3.7.3 Flight Test Objectives.

The flight test objectives were as follows:

Objective 1 – Compare the lift curve and drag polar of the baseline T-38 to those of the modified T-38 above 0.3 normalized angle of attack.

Objective 2 – Compare the approach-to-stall characteristics of the baseline T-38 to those of the modified T-38.

Objective 3 – Compare the upper wing surface flow characteristics of the baseline T-38 to the modified T-38 through inflight photography.

3.7.4 Flight Test Methodology.

3.7.4.1 Objective 1.

The team collected data from three flight test techniques (FTT): Level Deceleration, Sawtooth Descent, and Sawtooth Climb. Each FTT is defined below.

Level Deceleration: The level decelerations were performed at 18,000 feet pressure altitude (PA) in the cruise (gear and flaps retracted, speed brakes closed) configuration. For these test points, the pilot started at 0.65 Mach number and decelerated to 1.0 normalized AOA (15 degrees AOA) by snapping both throttles to idle. The following procedures were performed:

1. The aircraft was stabilized at Mach 0.65, 18,000 feet PA.
2. Throttles were pulled to idle power for deceleration.
3. Level flight was maintained while decelerating.
4. The aircraft was recovered prior to 1.1 normalized AOA (16.5 degrees AOA), uncommanded bank angles greater than 30 degrees, or 17,000 feet PA by releasing back pressure on stick and increasing throttles to military power (MIL). Lateral stick inputs were limited to less than 1/3 stick deflection and only small rudder inputs were used to keep wings level.

Sawtooth Descent: The sawtooth descents were performed from 19,000-17,000 feet PA, or for one minute (whichever occurred first) in the cruise configuration. These points were used to validate level deceleration data. The pilot trimmed the aircraft at a normalized AOA between 0.6 (9 degrees) and 1.0 (15 degrees). Once the aircraft was stabilized, an idle/MIL or idle/idle descent was performed while maintaining AOA. Aircrew alternated the idle engine for the idle/MIL descents to minimize fuel imbalances. The following procedures were performed:

1. The aircraft was setup above the data band on a heading perpendicular to the forecasted wind and on the speed corresponding to the test matrix AOA with throttles set as described in the test matrix.
2. The aircraft descended through the altitude data band (or for one minute) while maintaining the speed corresponding to the target AOA ± 2 KCAS.

Sawtooth Climb: The sawtooth climbs were performed from 17,000-19,000 feet PA, or for one minute (whichever came first) in the cruise configuration. These points were used to validate the level deceleration data. The pilot trimmed the aircraft between 0.3 (5 degrees) normalized AOA up to a normalized 0.8 (12 degrees) normalized AOA as depicted in the test matrix in section 3.7.6. Once the aircraft was stabilized, military power was used to climb through the data band or for one minute. Setup occurred below the altitude band to allow the engines to thermally stabilize for 30 seconds. For the 0.7 (10.5 degrees) through 0.8 (12 degrees) normalized AOA points, a starting altitude in the data band was used due to the fact that the aircraft did not climb well at that AOA. The following procedures were performed:

1. The aircraft was flown on the speed corresponding to test matrix AOA below the floor of the data band.
2. Engines were allowed to stabilize for 30 seconds in military power.
3. The aircraft was flown through the altitude data band (or for one minute) perpendicular to the forecasted winds while maintaining the speed corresponding to the target AOA ± 2 KCAS.

3.7.4.2 Objective 2.

Pilots qualitatively evaluated approach to stall in the cruise configuration for the modified and baseline aircraft. The maneuver began at the no-flap final approach speed,

and increased AOA in one degree increments. At each AOA, comments regarding pitch, roll, and yaw authority as well as buffet, wing rock, and other notable characteristics were made. The maneuvers were terminated at full aft stick, significant uncommanded motions, intolerable buffet or 17,000 feet PA. The following procedures were performed for wings-level stalls:

Test Point 1: No lateral stick inputs

1. Trimmed for wings-level flight at 18,000 feet PA (+1000/-1000) and 0.7 (10.5 degrees) normalized AOA. Throttles as required (Military power and below).
2. Reduced airspeed to increase AOA by 1 degree and stabilized. Buffet and wing rock noted.
3. Recovered at or before:
    a. Full aft stick
    b. Wing rock exceeded 45 degrees of bank
    c. 17,000 feet PA
    d. Prior to 1.1 (16.5 degrees) normalized AOA.

Test Point 2: Normal lateral stick inputs to maintain wings level

1. Trimmed for wings-level flight at 18,000 feet PA (+1000/-1000) and 0.7 (10.5 degrees) normalized AOA. Throttles as required (Military power and below).
2. Reduced airspeed to increase AOA by 1 degree and stabilize. Buffet and wing rock noted.
3. Lateral stick inputs were limited to less than 1/3 stick deflection.
4. Recovered at or before:
    a. Full aft stick
    b. Wing rock exceeded 30 degrees of bank

c. 17,000 feet PA

d. Prior to 1.1 (16.5 degrees) normalized AOA.

3.7.4.3 Objective 3.

An F-16 photo chase was used within the data band of 17,000-19,000 feet PA. The test aircraft was flown wings level and stabilized at 1 degree increments from 9-15 degrees AOA to allow the photo chase to capture the behavior of the wing tufts. A wings-level deceleration was also flown from 0.3 to 1.0 normalized AOA (5-15 degrees AOA). The aircraft was recovered prior to 1.1 normalized AOA (16.5 degrees), when wing rock exceeded 20 degrees of bank, or the aircraft descended below 17,000 feet PA. The deceleration rate was no greater than 1 KCAS per second. The photo chase recorded high definition video of the wing tuft behavior throughout the deceleration. Test team comments focused on comparisons of spanwise flow, vortex flow, and areas of flow reversal/separation.

3.7.5 Flight Test Data Reduction.

Data were recorded by either telemetry (TM) or onboard PCMCIA. The data was analyzed using Instrumentation Loading Integration Analysis and Decommutation (ILIAD), MATLAB, and Excel software. The data parameter list is provided in Appendix K. Data analysis methods regarding gross weight and CG, Pitot-statics, AOA, accelerometer corrections, the engine model, and test day lift and drag coefficients are discussed below.

3.7.5.1 Gross Weight and Center of Gravity.

Gross weights were calculated by subtracting the instrumented left and right fuel quantities used from the starting gross weight. Starting gross weight was determined by adding the empty (zero usable fuel) weight to the fuel weight indicated (on the front seat

cockpit gauge) at the time the data acquisition system (DAS) was initially turned on. The center of gravity change was assumed negligible throughout the flight provided the two fuel gauges were within 200 pounds.

3.7.5.2 Pitot-static Data.

Indicated Mach number was converted to true airspeed (V_t) using ambient temperature. Ambient temperature was calculated from total temperature, using a temperature recovery factor of 0.96. This temperature recovery factor was empirically derived as part of the USAF Test Pilot School curriculum T-38A Performance Phase. Instrument corrections, ΔH_{ic}, and position corrections, ΔH_{pc}, were assumed zero.

3.7.5.3 Angle of Attack.

The AOA vane was calibrated and evaluated in flight. The resulting calibration curve is shown in Appendix J. The AOA sensed by the vane on the nose boom was affected by pitch rate. The following procedure was used to calculate a correction for this. However, the resulting calculation increased scatter in the data. Based on engineering judgment, the pitch rate correction was not used.

$$\alpha_t = \tan^{-1}\left(\tan\alpha_v + \frac{qL_{x\alpha}}{V_t \cos\alpha_t}\right) + \alpha_u \qquad (16)$$

where

α_t = true AOA (radians)

α_v = vane AOA (radians)

α_u = upwash correction (degrees)

q = pitch rate (radians per second)

$L_{x\alpha}$ = distance from center of gravity to AOA vane (feet) – 29.98 feet

V_t = true airspeed (feet per second)

AOA for the airplane was measured relative to the fuselage reference line. While the upwash correction was not used (see Appendix I), a 1.8 degree bias was added to AOA data such that baseline lift coefficient followed the historical model at low angles of attack. The distance from the CG to the AOA vane was assumed constant and was measured using takeoff CG.

3.7.5.4 Accelerometer Corrections.

Accelerometers measured acceleration at their location and not the acceleration at the aircraft CG. This set of corrections pertained to the CG accelerometers which were part of the flight test instrumentation. The corrections in this section were made but not included in the final results because the noise in the pitch rate parameter made the associated accelerometer calculation noisy (to the point where lift coefficient data scatter was visibly higher). However, a 6 percent correction factor was added to normal acceleration and a 0.04 bias was subtracted from longitudinal acceleration based on ground block results and is explained more in section 4.6.4. Table 4 shows the accelerometer positions on the aircraft.

Table 4. DAS Accelerometer Positions

Reference	**x-accelerometer**	**z-accelerometer**
Fuselage Station (inches)	p_{xx}= 281	p_{xz}= 281
Buttock Line (inches)	p_{yx}= 0	p_{yz}= 0
Water Line (inches)	p_{zx}= -5.6	p_{zz}= -5.6

p_{xz}, for example, was the fuselage station (x) position of the accelerometer measuring acceleration in the z-direction. The equations used for the unused, position correction calculations can be found in Appendix G.

3.7.5.5 J85-GE-5M Engine Model.

Net thrust, $F_{N,}$ and propulsive drag, F_e, were predicted using the thrust model provided by the 445 FLTS, Edwards AFB, CA. Details of the MIL power thrust model can be found in the *T-38A Aircraft Single Engine Takeoff Speed (SETOS) Performance Spot-Check,* AFFTC-TR-05-57 (32). The IDLE power thrust model was obtained from AFFTC-TR-03-18 (37). Engine test cell trim measurements for each engine obtained during engine calibration runs can be found in Appendix H. Additionally, the line maintenance trim cards obtained during ground engine trim runs with the engines installed in aircraft tail 68-8205 can be found in Appendix H.

3.7.5.6 Test Day Lift Coefficient.

The summation of forces on the aircraft perpendicular to the velocity vector produced the equations:

$$L + F_g \sin(\alpha + i_T) - W\cos(\gamma) = \left(\frac{W}{g}\right)V_t^2 \Big/ R \tag{17}$$

or solving for lift:

$$L = W\cos(\gamma) - F_g \sin(\alpha + i_T) + \left(\frac{W}{g}\right)V_t^2 \Big/ R \tag{18}$$

where:

L = aerodynamic lift force, pounds

W = gross weight, pounds

γ = flight path angle, degrees

F_g = gross thrust, pounds

α = AOA, degrees

i_T = thrust incidence angle (equal to 0.5 degrees for the T-38), degrees

g = acceleration due to gravity, 32.174 feet per second squared

V_t = true airspeed, feet per second

R = turn radius, feet

where:

$$W\cos(\gamma) \approx \frac{W}{g}(a_{x_B}\sin(\alpha) - a_{z_B}\cos(\alpha)) \tag{19}$$

The assumptions for equation 17 were wings level and zero sideslip. Assuming constant flight path angle (either level flight or constant-flight-path-angle climbs and descents), then R = infinity and 1/R = 0, where R was the radius of a turn in the vertical plane. Reducing and substituting equation 19 into equation 18 yields:

$$L = \frac{W}{g}(a_{x_B}\sin(\alpha) - a_{z_B}\cos(\alpha)) - F_g\sin(\alpha + i_T) \tag{20}$$

Lift coefficient was calculated by:

$$C_L = \frac{L}{qS} = \frac{2L}{\rho V_t^2 S} \tag{21}$$

where:

C_L = lift coefficient, dimensionless

q = incompressible dynamic pressure, pounds per square foot

S = aerodynamic reference area, 170 square feet

ρ = ambient air density, pounds seconds squared per foot to the fourth power

3.7.5.7 Test Day Drag Coefficient.

The summation of forces on the aircraft along the velocity vector produced the equations:

$$[F_g \cos(\alpha + i_T) - F_e] - D - W \sin(\gamma) = \left(\frac{W}{g}\right)\frac{d}{dt}(V_T) \quad (22)$$

or:

$$D = [F_g \cos(\alpha + i_T) - F_e] - W \sin\gamma - \left(\frac{W}{g}\right)\frac{d}{dt}(V_T) \quad (23)$$

where:

F_g = gross thrust, pounds

α = AOA, degrees

i_T = thrust incidence angle (equal to 0.5 degrees for the T-38), degrees

F_e = propulsive drag, pounds

D = aerodynamic drag, pounds

W = gross weight, pounds

γ = flight path angle, degrees

g = acceleration due to gravity, 32.174 feet per second squared

$\frac{d}{dt}(V_T)$ = flight path acceleration, feet per second squared

where:

$$W \sin(\gamma) + \left(\frac{W}{g}\right)\frac{d}{dt}(V_T) = W\left[\sin(\gamma) + \left(\frac{1}{g}\right)\frac{d}{dt}(V_T)\right] \approx \frac{W}{g}(a_{x_B}\cos(\alpha) + a_{z_B}\sin(\alpha)) \quad (24)$$

The assumptions in equation 24 were that the aircraft's wings were level with no sideslip, and the velocity vector was in the plane of the aircraft centerline. Net thrust was calculated using:

$$F_N = F_g \cos(\alpha + i_T) - F_e \quad (25)$$

where:

F_N = net thrust, pounds

Substituting equations 24 into equation 23 yields:

$$D = F_N - \frac{W}{g}(a_{x_B}\cos(\alpha) + a_{z_B}\sin(\alpha)) \tag{26}$$

Drag coefficient is calculated by:

$$C_D = \frac{D}{qS} = \frac{2D}{\rho V_t^2 S} \tag{27}$$

where:

C_D = drag coefficient, dimensionless

q = incompressible dynamic pressure, pounds per square foot

S = aerodynamic reference area, 170 square feet

ρ = ambient air density, pounds seconds squared per foot to the fourth power

3.7.6 Flight Test Plan

The plan included flight test of baseline (clean) aircraft and modified (wing fence) aircraft to meet the requirements of the *compare* objectives in section 3.7.3. The complete test plan that this flight test was executed under can be found in Reference 34. The significance of changing the upper surface of an aircraft's wing drove first flight requirements which included extra considerations and safety precautions. Additionally, the first student test pilot sortie in the modified aircraft was a check out sortie, flown with a T-38 instructor test pilot (IP). In Table 5, the maneuvers associated with these sorties are in the dual maneuvers column. Following the completion of this supervised sortie, the student test pilot was cleared crew solo, implying that the data collection sorties were flown by a student test pilot in the front seat and a student flight test engineer in the back seat. Table 6 shows the sortie matrix with 16 test sorties planned and their associated events. Table 7 shows the test point summary and their associated parameters. Flight

test was limited to less than 4 g and below 0.65 Mach due to limited structural and transonic effects analyses.

Table 5. Maneuver Matrix

Point	Maneuver	Dual Flight Maneuvers (qty)	Crew Solo Flight Maneuvers (qty)	Prerequisites:
	Takeoffs[1]			
TO1*	Reduce Fuel Takeoff Approx 3200lbs	1	0	
TO2	Full Fuel Takeoff	1	16	TO1
	Open Loop FQ[2]			
OL1	Gear Up, Flaps Up	1	0	
OL2	Gear Up, Flaps 60	1	0	
OL3	Gear Up, Flaps Full	1	0	
OL4*	Gear Down, Flaps Up	1	0	
OL5*	Gear Down, Flaps 60	1	0	
OL6	Gear Down, Flaps Full	1	0	
	Closed Loop HQ (Formation)[3]			
CL1	Gear Down, Flaps Up	1	0	OL4
CL2	Gear Down, Flaps 60	1	0	OL5
CL3	Gear Down, Flaps Full	1	0	OL6
	Stalls/TP Stalls[4]			
TP1	Gear Up, Flaps Up -- wings level	1	0	OL1
TP2	Gear Up, Flaps 60 -- wings level	1	0	OL2
TP3	Gear Up, Flaps Full -- wings level	1	0	OL3
TP4	Gear Up, Flaps Up, final turn setup	1	0	TP1
TP5	Gear Up, Flaps 60, final turn setup	1	0	TP2
TP6	Gear Up, Flaps Full, final turn setup	1	0	TP3
TP7*	Gear Down, Flaps Up -- wings level	1	0	OL4
TP8*	Gear Down, Flaps 60 -- wings level	1	0	OL5
TP9	Gear Down, Flaps Full -- wings level	1	0	OL6
TP10	Gear Down, Flaps Up, final turn setup	1	0	TP7
TP11	Gear Down, Flaps 60, final turn setup	1	0	TP8
TP12	Gear Down, Flaps Full, final turn setup	1	0	TP9
T*	**Trim Shot at 0.63 to 0.65 Mach**	1	0	
WUT*	**Windup Turn (WUT) to first of 4g or 0.8 AoA, Cruise[5]**	1	0	T
	Performance/Stall FTTs[6]			
SC*	Sawtooth Climbs	1	48	IP must see each FTT once before students are cleared crew solo
SD*	Sawtooth Descents	1	48	
LD*	Level Decel	1	24	
S*	Approach to Stall Characteristics	1	12	
	Touch and Go Landings[7]			
L1*	Flaps 60, straight in	1	0	TP8
L2*	Flaps Up, straight in	1	0	TP7
L3	Flaps 60, overhead	1	0	TP11
L4	Flaps Full, overhead	1	0	TP12
L5*	**Sim SE Approach and Go Around[8]**	1	0	L1
L6*	**Full Stop Landings (flaps 60, straight in)[9]**	1	16	TP8

The asterisked points above were required to be accomplished with an IP on board prior to the data sorties. Prior to any student flying crew solo (student test pilot and student flight test engineer) on a wing-fence-modified sortie, the student had to fly at least one traffic pattern stall set at 60 percent flaps.

Notes for Table 5**:**

1. The initial takeoff utilized a partial fuel load (approximately 3200 pounds) to achieve a takeoff gross weight of approximately 12,000 pounds and the maximum temperature allowed was be 80 degrees Fahrenheit or 30 degrees Celsius. This provided a larger performance margin in case of an engine or handling qualities problem on the first takeoff. All other wing fence sorties utilized the takeoff and landing data (TOLD) margins stated in the general minimizing considerations (GMCs) of the safety package (35).
2. Open loop flying qualities (FQ) consisted of standard pitch and rudder doublets and step inputs. This was intended to allow the pilot a controlled build up in preparation for the closed loop handling qualities (HQ) evaluation.
3. Closed loop handling qualities consisted of low and high bandwidth tracking tasks against the chase/target aircraft from a route formation position.
4. Traffic pattern (TP) stalls with the gear down were accomplished to ensure the wing fence modification did not create any significant differences from a baseline T-38. The stalls also allowed the pilots to become familiar with the approach-to-stall indications for the actual FTTs and for familiarity with aircraft handling in the traffic pattern. The normal recovery AOA for traffic pattern stalls is approximately 0.8 normalized AOA.

5. Maximum desired load factor for the wind-up turn (WUT) was 4 g if allowed by aircraft performance and aerodynamic buffet. The maximum load factor until the WUT was accomplished was 2 g. All other limits were stated in the safety package (35).
6. FTTs were flown in accordance with section 3.7.4.
7. Touch and go landings were only accomplished with an IP on the aircraft and in accordance with the weather limits listed in the safety package (35).
8. Simulated single-engine (SE) patterns were only accomplished with an IP on the aircraft.

Crew solo students planned on straight-in full stop landings. Approaches and landings to a full stop were made with 60 percent or full flaps at the pilot's discretion. A 60 percent flap approach and landing placed the aircraft in the desired configuration for an engine out scenario. A full flap landing would decrease stopping distance if landing distance was critical.

Table 6. Sortie Matrix

Sortie	Activity / Config	1	2	3	4	5	6	7	8	9	10	11	12
1	Modified	First Flight / Student Checkout with IP*											
2	Modified	First Flight / Student Checkout with IP*											
3	Modified	SC3	SD8	SC5	SD85	SC7	SD9	SC75	SD95	LD	LD	S1	S2
4	Modified	SC4	SD8	SC6	SD85	SC7	SD9	SC75	SD95	LD	LD	S1	S2
5	Modified	SC3	SD8	SC5	SD85	SC7	SD9	SC75	SD95	LD	LD	S1	S2
6	Modified	SC4	SD8	SC6	SD85	SC7	SD9	SC75	SD95	LD	LD	S1	S2
7	Modified	SC3	SD8	SC5	SD85	SC7	SD9	SC75	SD95	LD	LD	S1	S2
8	Modified	SC4	SD8	SC6	SD85	SC7	SD9	SC75	SD95	LD	LD	S1	S2
9	Modified	SC3	SD8	SC5	SD85	SC7	SD9	SC75	SD95	LD	LD	S1	S2
10	Modified	Tufted Wing Photo Chase*											
11	Baseline	Tufted Wing Photo Chase*											
12	Baseline	SC3	SD8	SC5	SD85	SC7	SD9	SC75	SD95	LD	LD	S1	S2
13	Baseline	SC4	SD8	SC6	SD85	SC7	SD9	SC75	SD95	LD	LD	S1	S2
14	Baseline	SC3	SD8	SC5	SD85	SC7	SD9	SC75	SD95	LD	LD	S1	S2
15	Baseline	SC4	SD8	SC6	SD85	SC7	SD9	SC75	SD95	LD	LD	S1	S2
16	Baseline	SC3	SD8	SC5	SD85	SC7	SD9	SC75	SD95	LD	LD	S1	S2

*See appendix A for more information

where SC is sawtooth climb, SD is sawtooth descent, LD is level deceleration, and S is approach-to-stall characteristics. The number indicates normalized AOA to fly except for

S. For example, SC3 means sawtooth climb at 0.3 normalized AOA. Also, S1 and S2 mean stick-fixed and stick-controlled conditions respectively.

Table 7. Test Point Summary

Maneuver	**Altitude**	**Power**	**AOA (normalized)**
Sawtooth Climbs	17K-19K	MIL-MIL	0.30
Sawtooth Climbs	17K-19K	MIL-MIL	0.40
Sawtooth Descents	19K-17K	IDLE-IDLE	0.80
Sawtooth Climbs	17K-19K	MIL-MIL	0.50
Sawtooth Climbs	17K-19K	MIL-MIL	0.60
Sawtooth Descents	19K-17K	IDLE-IDLE	0.85
Sawtooth Climbs	17K-19K	MIL-MIL	0.70
Sawtooth Descents	19K-17K	MIL-IDLE	0.90
Sawtooth Climbs	17K-19K	MIL-MIL	0.75
Sawtooth Descents	19K-17K	MIL-IDLE	0.95
Level Decel	18K	IDLE-IDLE	0.65M - 1.0 AOA
Stall Characteristics 1 Stick-Fixed	18K	As Required	0.7 - 1.0
Stall Characteristics 2 Stick-Controlled	18K	As Required	0.7 - 1.0

All test points in Table 7 were flown with the gear up, flaps up, and speed brake retracted. Table 7 does not include the photo sorties. Altitude was pressure altitude where K means thousands of feet and M is Mach.

IV. Results and Analysis

4.1 Chapter Overview

In this chapter, results are shown for wind tunnel tests conducted on all configurations. In addition to the balance results, there is an analysis of flow visualization as accomplished with model tufting. All data presented here was adjusted by the axial force correction discussed in section 3.4.2.1. In the AFIT low-speed wind tunnel, an angle of attack (AOA) sweep from -4 degrees to 6 degrees in steps of 2 degrees and then from 6 degrees to 22 degrees in steps of 1 degree was performed on all configurations at three different speeds: 30, 60, and 90 miles per hour (mph). These speeds correlated to approximate Reynolds numbers (Re) of 1 x 10^5 (100K), 2 x 10^5 (200K), and 3 x 10^5 (300K) based upon the model's mean aerodynamic chord (MAC) of 0.3681 feet. When considering this data in comparison to the actual aircraft, it is important to recall that the last 7.79 feet of aircraft were not modeled here. Therefore, the differences caused by configuration and speed are focused on over comparisons to the actual aircraft.

The results are divided into five main sections. The first four are based on the wind tunnel and the fifth is based on flight test. The first section presents the clean (no wing fence) configuration's runs. The second section includes the results of each of the fence configurations as compared to the clean configuration. Here, the better performer was chosen to continue with the results section. Plots of the fuselage-only results show its contribution to the parameters of interest and can be found in Appendix O. The third section covers Re comparisons and the results of the trip tape runs. The fourth section describes flow visualization. The fifth section shows the flight test results and analysis.

4.2 Wind Tunnel Balance Data – Clean Configuration

4.2.1 Overview.

The clean configuration was run on two separate days for a total of three individual times at each wind tunnel velocity of 30, 60, and 90 mph. The three different runs were labeled Clean A, Clean B, and Clean C. Establishing baseline data, determining test repeatability, and accomplishing an uncertainty analysis were the primary objectives here. Each of these runs included the removal and reattachment of the wing. Specifically, the first run was accomplished at the beginning of the day. Following that run, three fence configurations were tested prior to the second clean run. The third clean run was accomplished the following day. The three runs at each velocity were averaged to create Clean Average, which was the basis for comparison to the fence configurations. A summary of the resulting aerodynamic performance is in Table 8.

For the lift column, 10.4 degrees was chosen because that is the point where the lift-curve slope ($C_{L\alpha}$) began to change, and 15.6 degrees was chosen because that was an approximate maximum usable AOA in the clean configuration. Additionally, both of these angles of attack fell right on data points. For $C_{L\alpha}$ and the slope of the pitching moment curve ($C_{m\alpha}$), the same range in AOA was used for consistency. This range was 0 degrees to 10.4 degrees. Minimum total drag and zero-lift drag occurred at different angles of attack and are included in Table 8.

Table 8. Aerodynamic Performance of the Clean Configuration

		Drag		Zero Lift	Slopes		Lift (C_L)		L/D max (-)	
Model	**Re (-)**	**C_{Dmin} (-)**	**C_{D0} (-)**	**$\alpha_{0\ Lift}$ (°)**	**$C_{L\alpha}$ (/°)**	**$C_{m\alpha}$ (/°)**	**α=10.4°**	**α=15.6°**	**α (°)**	**Value**
Clean A	100K	0.0290	0.0337	0.28	0.0544	-0.0256	0.5509	0.5959	6.27	4.217
Clean B	100K	0.0316	0.0348	0.43	0.0537	-0.0275	0.5357	0.6034	6.27	4.143
Clean C	100K	0.0338	0.0368	0.35	0.0543	-0.0265	0.5458	0.6100	6.27	4.060
Clean Average	100K	0.0314	0.0351	0.35	0.0541	-0.0265	0.5441	0.6031	6.27	4.140
Clean A	200K	0.0220	0.0244	0.26	0.0554	-0.0265	0.5622	0.6527	6.27	5.115
Clean B	200K	0.0219	0.0244	0.46	0.0560	-0.0264	0.5564	0.6619	6.27	5.175
Clean C	200K	0.0233	0.0255	0.39	0.0558	-0.0265	0.5587	0.6573	6.27	5.077
Clean Average	200K	0.0224	0.0248	0.36	0.0557	-0.0265	0.5591	0.6573	6.27	5.122
Clean A	300K	0.0228	0.0264	0.26	0.0569	-0.0276	0.5773	0.6717	6.27	5.063
Clean B	300K	0.0226	0.0262	0.43	0.0580	-0.0276	0.5786	0.6607	6.27	5.087
Clean C	300K	0.0232	0.0264	0.40	0.0580	-0.0277	0.5797	0.6617	6.27	5.102
Clean Average	300K	0.0229	0.0263	0.36	0.0576	-0.0277	0.5785	0.6647	6.27	5.084

4.2.2 Drag Polar.

The drag polar plots, lift coefficient (C_L) versus drag coefficient (C_D), for all clean configuration runs are shown in Figures 68, 69, and 70. As seen below, the repeatability between runs was satisfactory and fostered confidence in the methodology and resulting balance data. One valuable aspect of the drag polar plot is that the impact of AOA is essentially reduced as a possible variable between runs. The zero-lift drag can also be found with this plot. The drag polar results were an important evaluator for the best performer among wing fence configurations in the following sections.

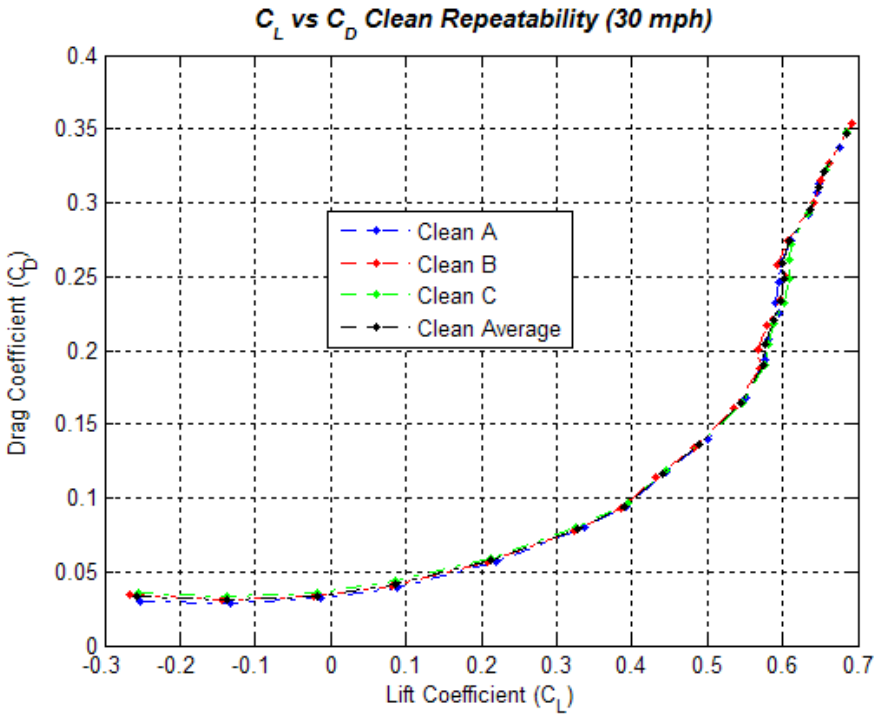

Figure 68. Clean Lift Coefficient vs. Drag Coefficient (30 mph)

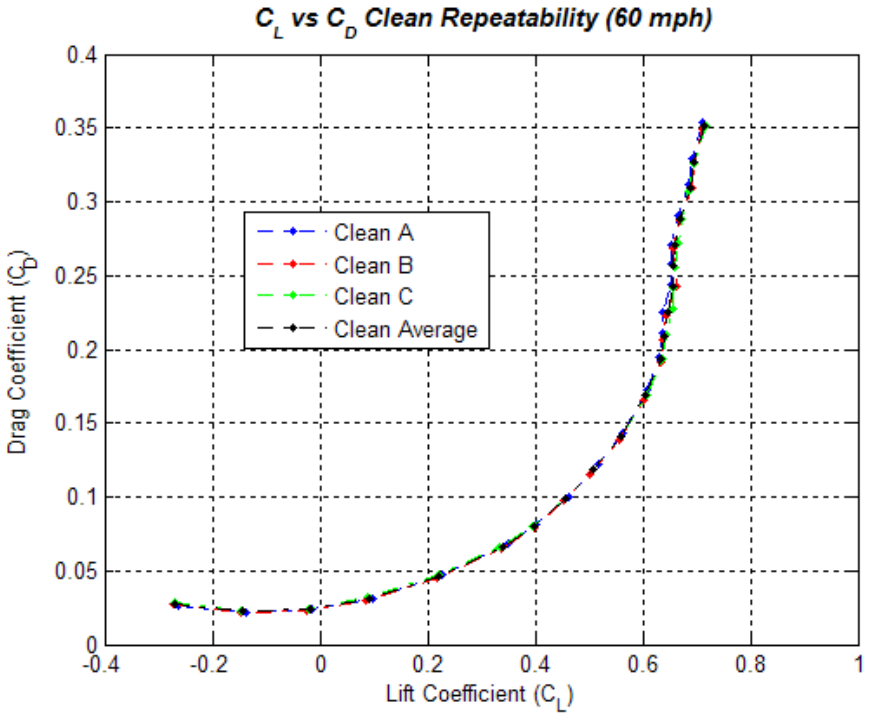

Figure 69. Clean Lift Coefficient vs. Drag Coefficient (60 mph)

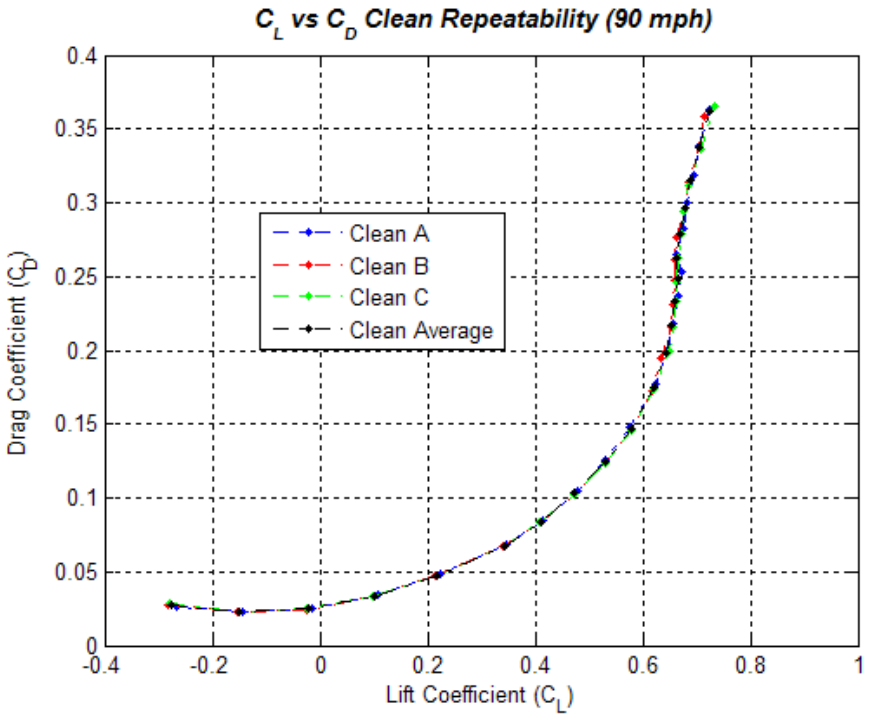

Figure 70. Clean - Lift Coefficient vs. Drag Coefficient (90 mph)

4.2.3 Lift Curve.

Figures 71, 72, and 73 plot C_L vs. AOA for clean configuration runs. From the lift curve, a number of important aerodynamic values can be attained. C_{Lmax} is the maximum lift coefficient of the aircraft, or model. C_{Lmax} usually occurs right before stall. As seen in the figures below, the model exhibited a gradual or "mushy" stall at the test conditions. This was expected as previously discussed in the Chapter I. $C_{L\alpha}$ gives an amount of change in C_L with respect to AOA for the linear region of the lift curve. $\alpha_{0\ Lift}$ is the AOA where the aircraft produces zero lift. Again, repeatability between the runs was satisfactory.

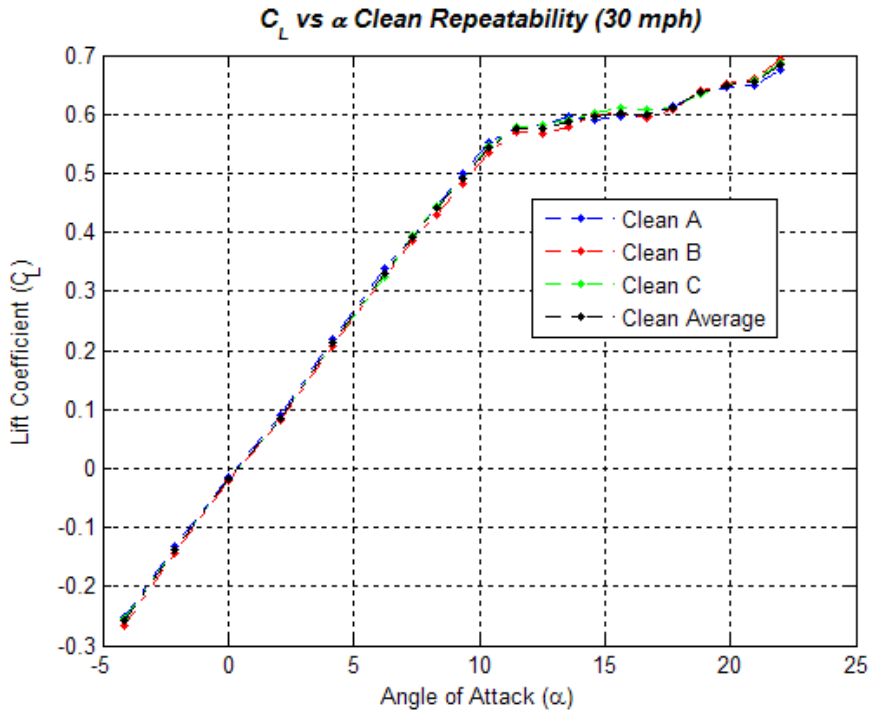

Figure 71. Clean Lift Coefficient vs. Angle of Attack (30 mph)

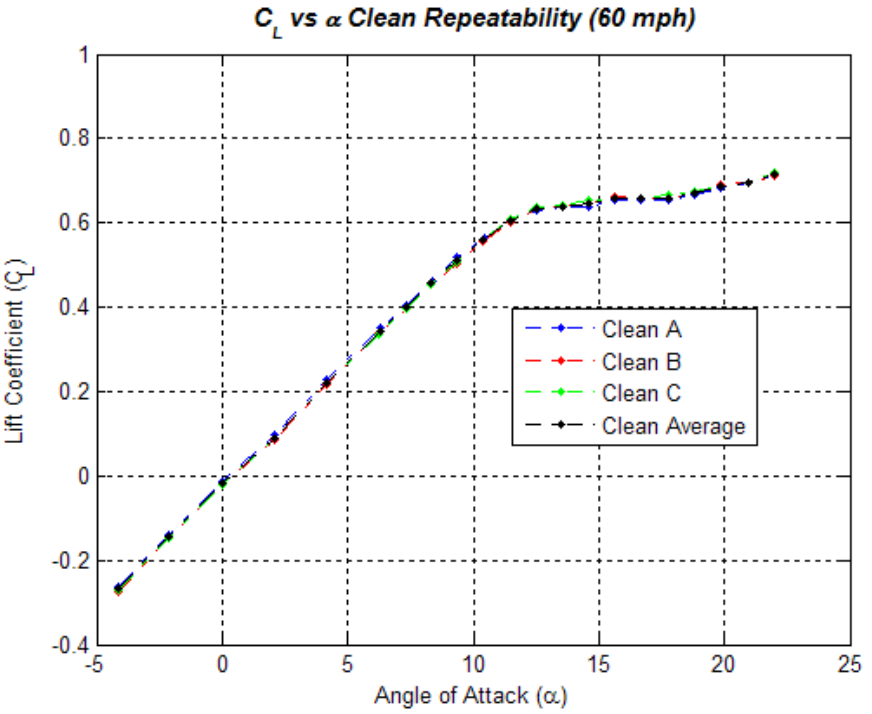

Figure 72. Clean Lift Coefficient vs. Angle of Attack (60 mph)

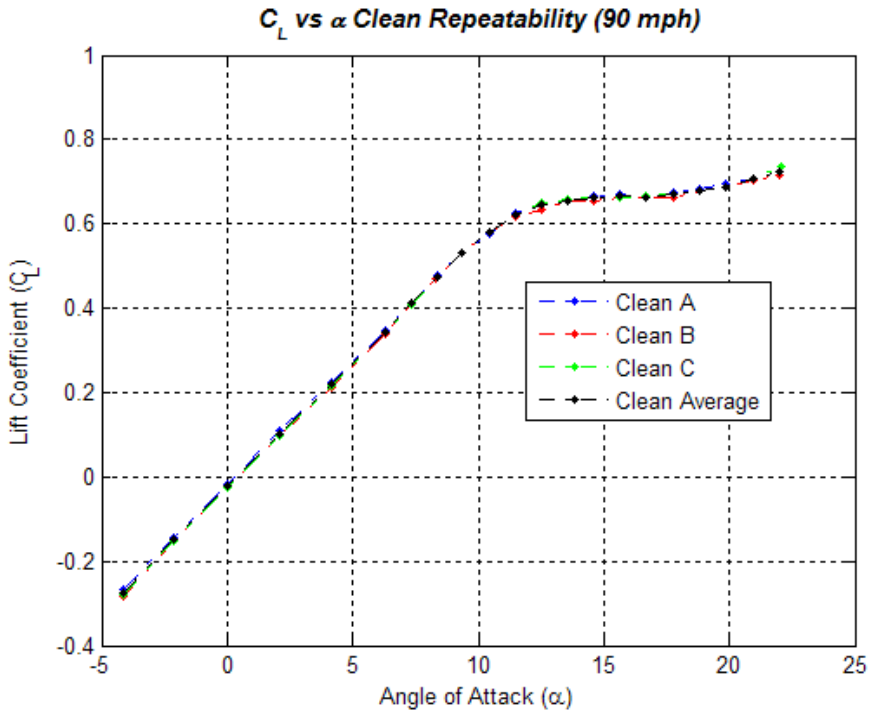

Figure 73. Clean Lift Coefficient vs. Angle of Attack (90 mph)

4.2.4 Drag Curve.

Figures 74, 75, and 76 plot C_D vs. AOA for clean configuration runs. From the drag curve, a number of important aerodynamic values can be attained, one of which is minimum drag, C_{Dmin}. The difference between the three different Reynolds numbers studied is of note here. At Re equal to approximately 1 x 10^5 (30 mph), C_{Dmin} was 0.0314. At Re equal to approximately 2 x 10^5 (60 mph), C_{Dmin} was 0.0224. Lastly, at Re equal to approximately 3 x 10^5 (90 mph), C_{Dmin} was 0.0229. While the values for Re equal to 2 x 10^5 and 3 x 10^5 were very close, the value for 1 x 10^5 was significantly higher. As discussed in Barlow, this was expected because C_{Dmin} decreases with an increase in Re (3).

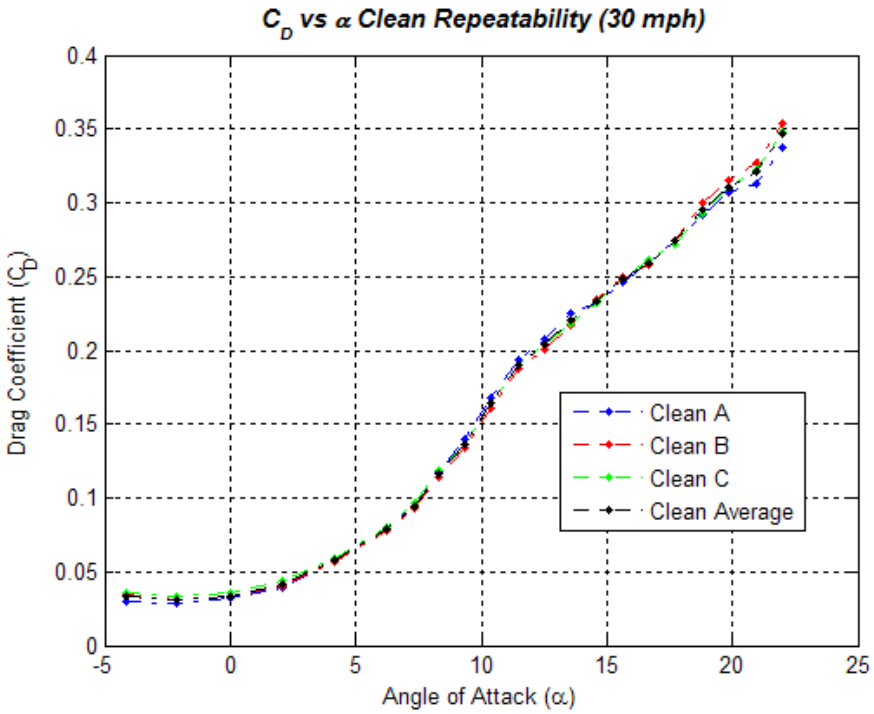

Figure 74. Clean Drag Coefficient vs. Angle of Attack (30 mph)

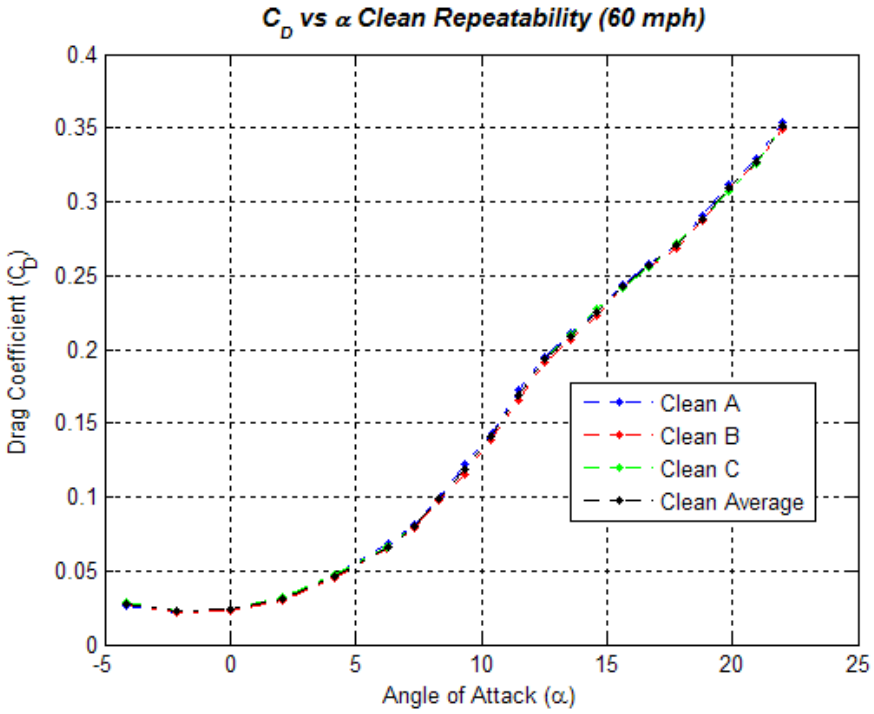

Figure 75. Clean Drag Coefficient vs. Angle of Attack (60 mph)

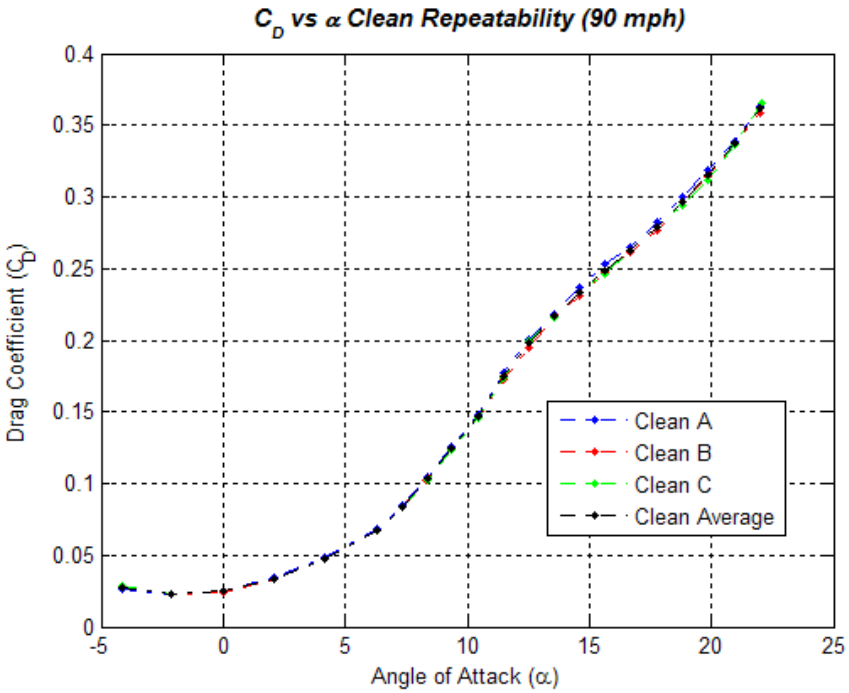

Figure 76. Clean Drag Coefficient vs. Angle of Attack (90 mph)

4.2.5 Pitching Moment Curve.

Figures 77, 78, and 79 plot the pitching moment coefficient, C_{mcg}, vs. AOA for all clean runs. These plots used the reference CG discussed in section 3.5.1. Again, it is important to recall that there was no tail on the model. The longitudinal static stability derivative, $C_{m\alpha}$, can be attained from the linear portion of this plot. It is desirable to have a negative value for $C_{m\alpha}$ for positive angles of attack. A negative $C_{m\alpha}$ value will return the aircraft to trim state ($C_m = 0$) when it is perturbed.

The clean configuration, as expected, was longitudinally stable. As anticipated, the only time there was a positive $C_{m\alpha}$ value was when AOA was negative. Additionally, there were no points at high AOA where the pitching moment showed a sudden positive slope. This would have indicated an undesirable pitch-up in the stall.

At approximately 12 degrees AOA, a break in pitching moment occurred at about the same AOA as the $C_{L\alpha}$ curves. Also noteworthy, the pitching moment significantly

varied after the break between the three different clean runs at 90 mph. This was likely due to model oscillations observed during the runs at that speed and at the higher AOAs.

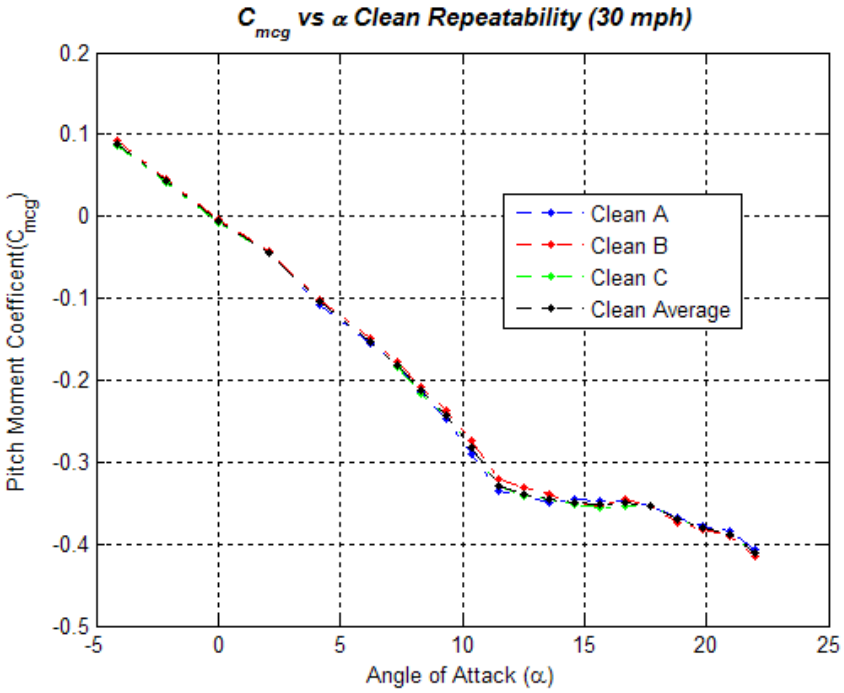

Figure 77. Clean Pitching Moment Coefficient vs. Angle of Attack (30 mph)

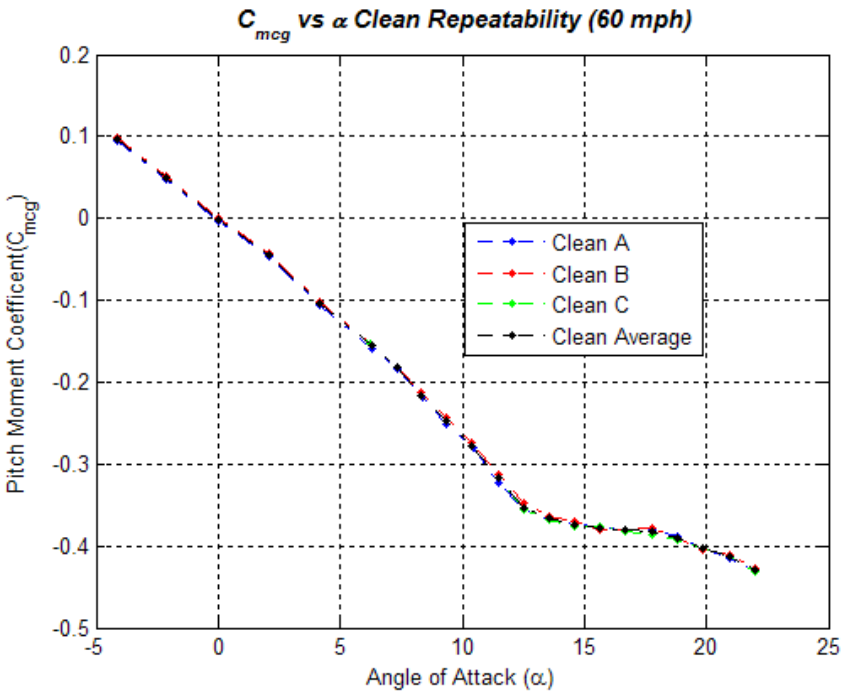

Figure 78. Clean Pitching Moment Coefficient vs. Angle of Attack (60 mph)

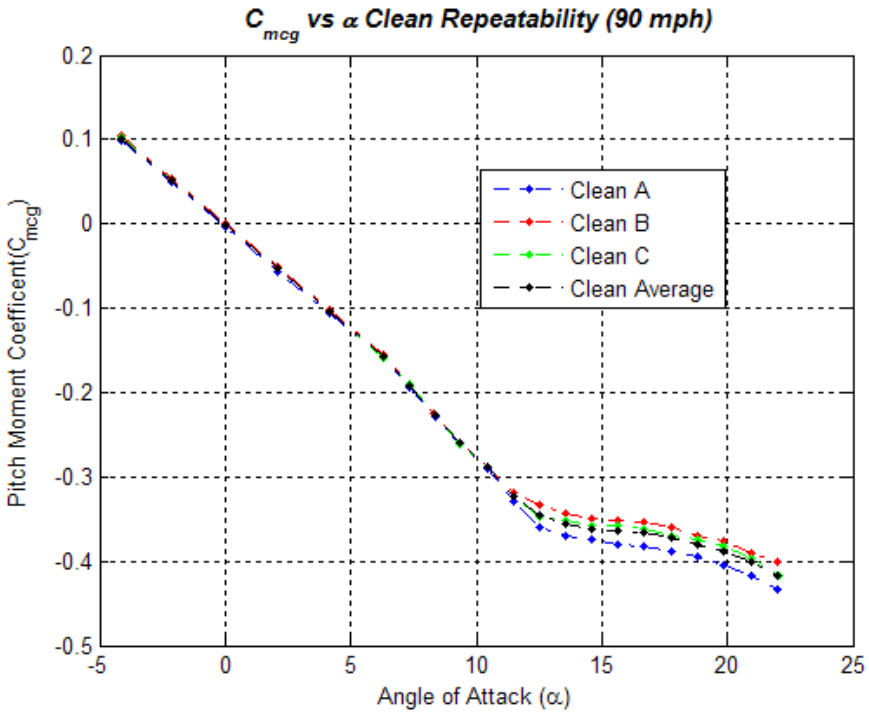

Figure 79. Clean Pitching Moment Coefficient vs. Angle of Attack (90 mph)

4.2.6 Lift-to-Drag Curve.

Figures 80, 81, and 82 show the lift-to-drag ratio, L/D, vs. AOA for all clean configurations run. L/D is one measure of aircraft efficiency. A powered aircraft that flies at the AOA corresponding to the maximum L/D is maximizing its endurance. There is a strong correlation between an increase in Re and an increase in L/D values (3). Repeatability at each velocity was again satisfactory.

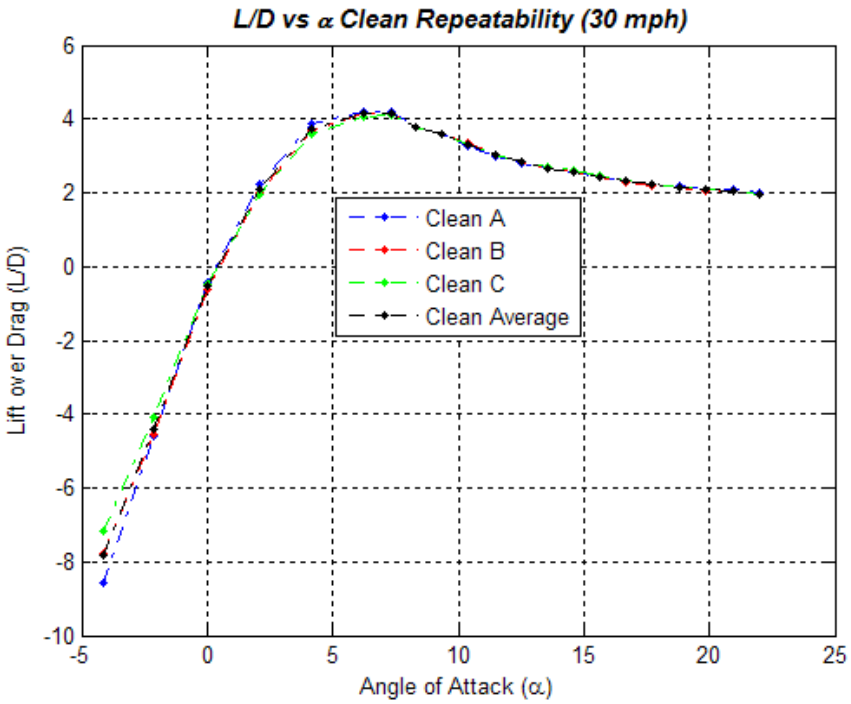

Figure 80. Clean Lift-to-Drag vs. Angle of Attack (30 mph)

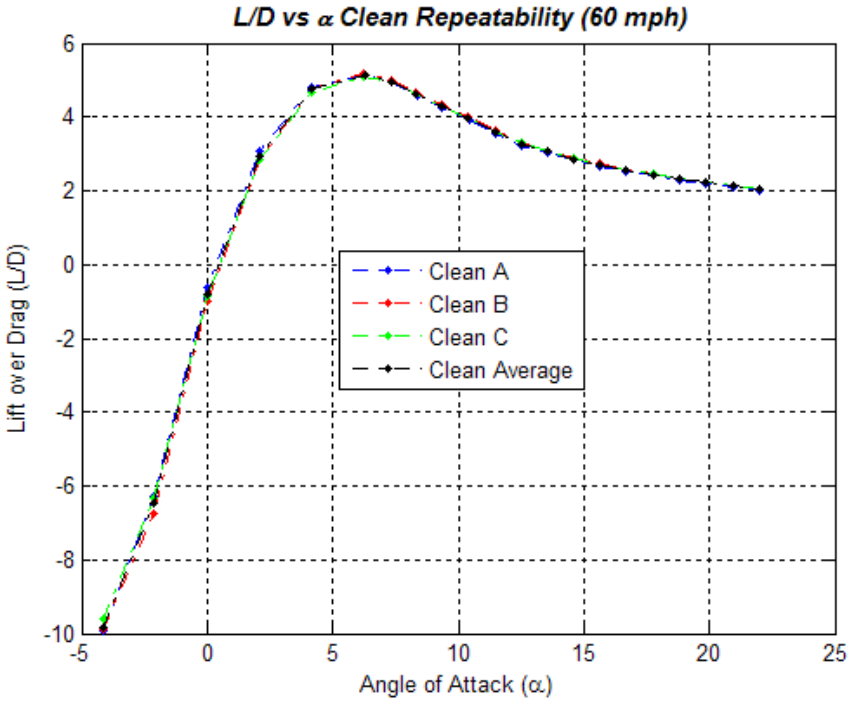

Figure 81. Clean Lift-to-Drag vs. Angle of Attack (60 mph)

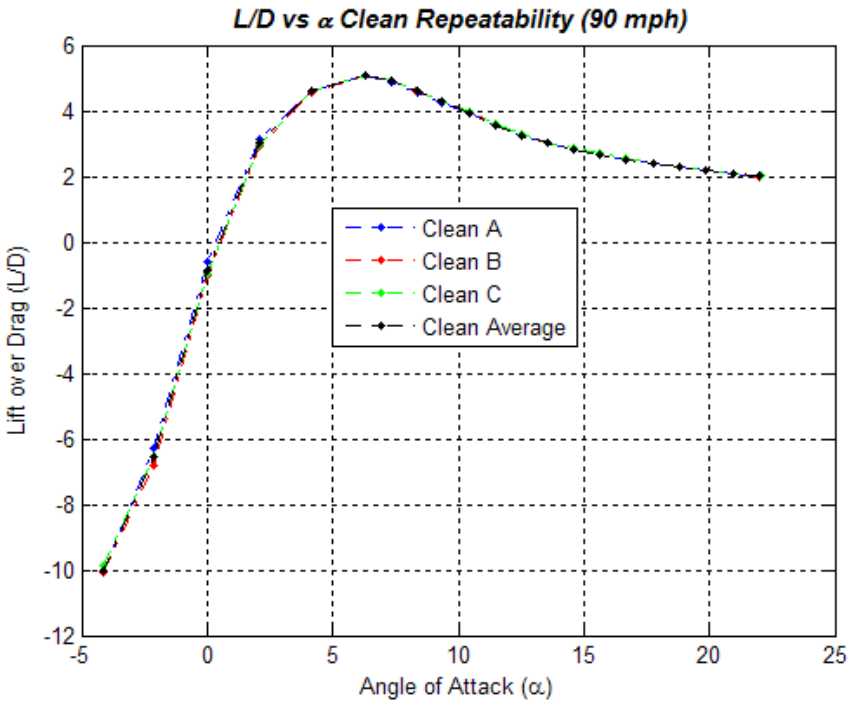

Figure 82. Clean Lift-to-Drag vs. Angle of Attack (90 mph)

4.2.7 Uncertainty Analysis.

First, the standard deviations of C_L, C_D, C_m, and L/D between the three clean repeatability runs (i.e. Clean A, Clean B, and Clean C) at each of the speeds were computed. Additionally, the standard deviation of forces and moments for each AOA within each run was computed in the code and saved. These values were used later for the second analysis discussed in section 3.5.2.2.

4.2.7.1 Based Upon Repeatability Runs.

Utilizing the first technique described in section 3.5.2.1, percent errors were calculated for both 95 percent and 99 percent confidence probabilities. This was accomplished for C_L, C_D, C_{mcg}, and L/D. However, only the results of L/D (using error bars) are shown in Figures 83 and 84 for brevity. Table 9 only includes the percent error values for 90 mph, also for brevity. These results were representative of C_L, C_D, and C_{mcg}. It is important to note that C_L, C_D, C_{mcg}, and L/D are all small numbers near zero

AOA. That artificially resulted in large percent errors near zero AOA and was not representative of the data quality. The average percent error was determined by excluding the zero AOA points. The results, rounded to the nearest tenth, are in the last row of Table 9. Lastly, it is noteworthy that looking at an AOA range of interest from 9.4 to 15.7 degrees reduced the average percent error between 0.6 and 4.1 percent.

Table 9. Uncertainty Analysis Using Calculated Data - Clean Average 90 mph

Percent Error 95 Percent Confidence Probability					**Percent Error 99 Percent Confidence Probability**			
α (º)	**C_L**	**C_D**	**C_{mcg}**	**L/D**	**C_L**	**C_D**	**C_{mcg}**	**L/D**
-4.2	7.3	8.7	7.0	2.6	16.9	20.1	16.1	6.0
-2.1	8.9	3.2	11.2	9.5	20.6	7.3	25.8	21.8
0	59.7	4.1	469.2	63.1	137.8	9.4	1082.3	145.6
2.1	15.0	5.4	12.5	9.7	34.6	12.4	28.8	22.3
4.1	5.9	4.4	5.2	1.5	13.6	10.2	12.0	3.4
6.3	2.7	3.4	3.0	1.0	6.3	7.9	6.8	2.2
7.3	1.6	3.5	2.4	1.9	3.7	8.1	5.6	4.4
8.4	2.0	3.8	2.0	1.8	4.6	8.8	4.5	4.2
9.4	0.5	2.2	0.7	1.7	1.1	5.2	1.7	4.0
10.4	0.5	1.4	1.0	1.8	1.2	3.1	2.3	4.2
11.5	1.0	3.0	4.5	2.0	2.4	6.9	10.5	4.6
12.5	3.1	3.8	9.4	1.8	7.0	8.7	21.6	4.1
13.6	0.7	1.7	9.7	1.5	1.6	3.9	22.4	3.4
14.6	1.8	2.7	8.8	1.3	4.2	6.3	20.4	3.1
15.7	2.3	3.5	10.7	1.3	5.2	8.0	24.7	3.1
16.7	1.2	1.4	9.7	1.4	2.7	3.2	22.4	3.2
17.7	2.4	3.0	9.9	1.2	5.6	6.8	22.9	2.8
18.8	1.1	2.2	8.4	1.2	2.5	5.1	19.3	2.7
19.8	1.8	2.7	9.5	1.2	4.2	6.3	21.9	2.7
21.0	0.5	0.9	8.6	1.1	1.2	2.2	19.8	2.5
22.0	3.3	2.6	9.6	1.0	7.6	5.9	22.1	2.3
Avg	3.2	3.2	7.2	2.3	7.3	7.3	16.6	5.4

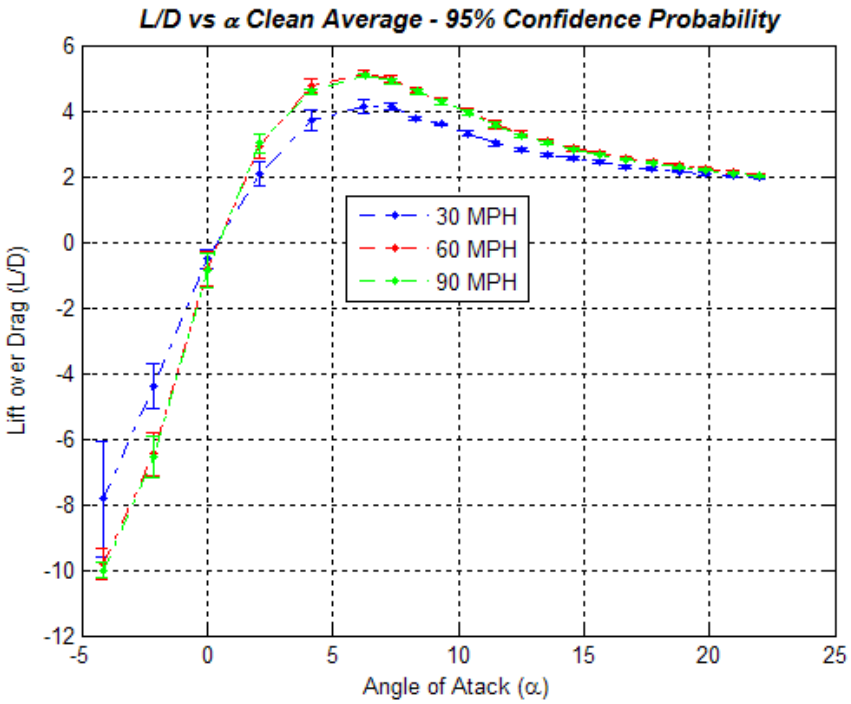

Figure 83. Lift-to-Drag with Error Bars – 95 Percent Confidence Probability

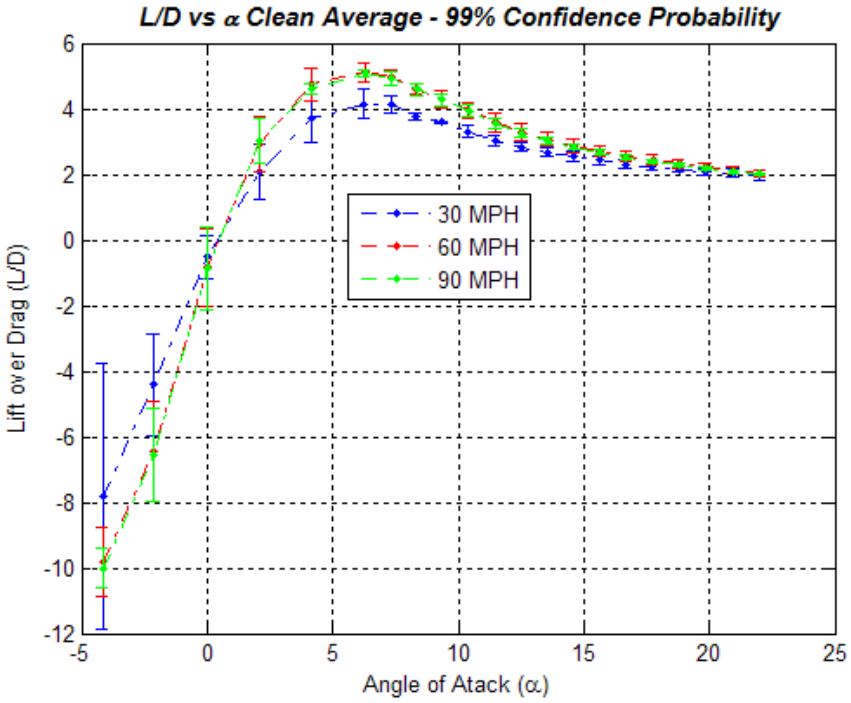

Figure 84. Lift-to-Drag with Error Bars – 99 Percent Confidence Probability

4.2.7.2 Based Upon Raw Data.

This analysis was accomplished in accordance with section 3.5.2.2. The average standard deviation of the normal force and axial force at each wind tunnel run speed for a given α were used as the Δ*N* and Δ*A* values from section 3.5.2.2. Table 10 shows the percent error data for 30, 60, and 90 mph in L/D. The second method produced results that had significantly less error percentages, reported to two decimal places, than the previous analysis. The average was again computed without zero AOA and is shown in the bottom row of Table 10. Figures 85 and 86 depict the results as well.

Table 10. Uncertainty Analysis Using Raw Data - Percent Error in L/D

	30 Mph		**60 Mph**		**90 Mph**	
α (º)	**Worst Case**	**Realistic**	**Worst Case**	**Realistic**	**Worst Case**	**Realistic**
-4.2	2.69	2.07	0.74	0.67	0.54	0.48
-2.1	8.03	6.64	1.59	1.13	1.08	0.76
0	60.37	58.56	10.42	9.73	4.28	3.97
2.1	3.40	2.59	2.11	1.71	0.90	0.69
4.1	2.70	2.12	0.61	0.43	0.37	0.26
6.3	1.96	1.52	0.31	0.24	0.28	0.20
7.3	1.08	0.79	0.25	0.20	0.21	0.15
8.4	1.01	0.73	0.29	0.21	0.19	0.14
9.4	0.93	0.70	0.34	0.24	0.18	0.13
10.4	0.73	0.53	0.36	0.25	0.19	0.13
11.5	0.85	0.64	0.45	0.32	0.35	0.24
12.5	0.75	0.55	0.63	0.48	0.40	0.28
13.6	0.84	0.64	0.58	0.44	0.41	0.29
14.6	1.01	0.75	0.60	0.46	0.49	0.35
15.7	0.98	0.70	0.58	0.43	0.51	0.36
16.7	0.93	0.67	0.61	0.45	0.53	0.37
17.7	0.75	0.53	0.45	0.32	0.42	0.30
18.8	0.75	0.53	0.44	0.32	0.37	0.26
19.8	0.64	0.47	0.38	0.27	0.32	0.23
21.0	0.61	0.46	0.30	0.22	0.27	0.19
22.0	0.60	0.46	0.28	0.20	0.27	0.19
Avg	1.56	1.20	0.60	0.45	0.41	0.30

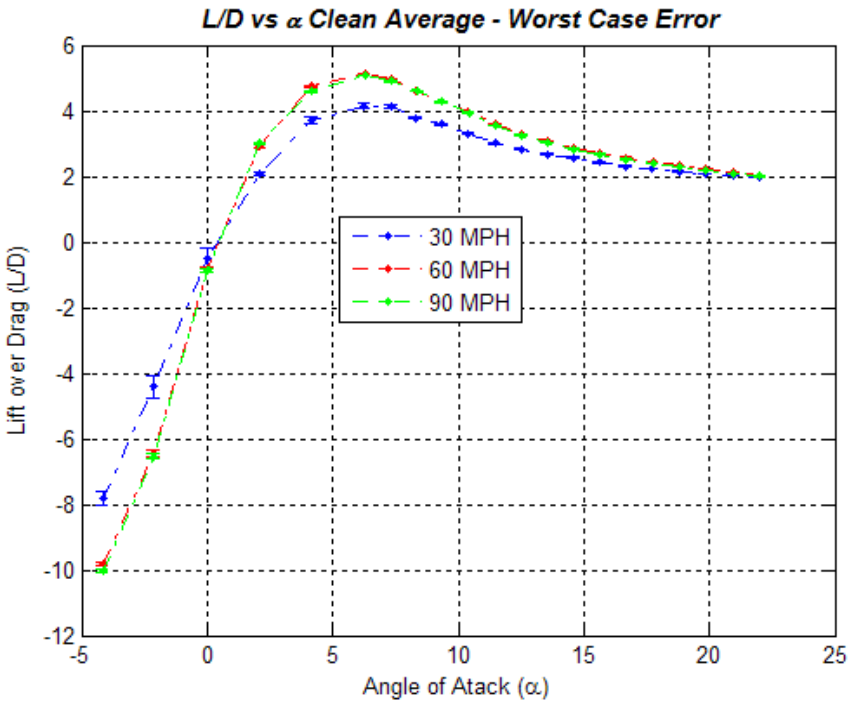

Figure 85. Lift-to-Drag with Error Bars – Worst Case

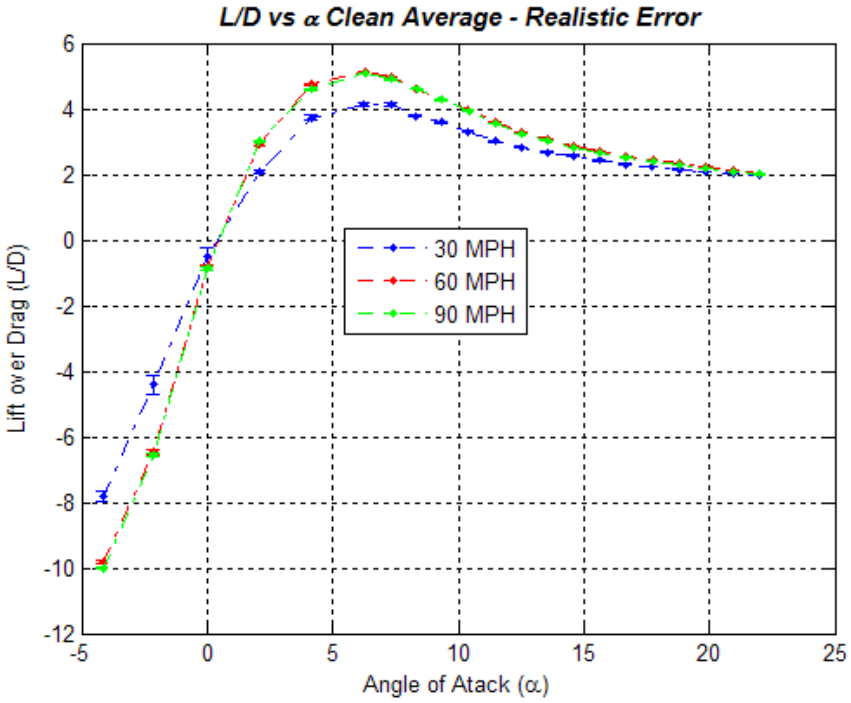

Figure 86. Lift-to-Drag with Error Bars – Realistic Case

4.2.7.3 Uncertainty Analysis Discussion.

This discussion is specific to L/D at Re_{mac} of approximately 3 x 10^5 because that was the common parameter analyzed between the two techniques.

The first analysis found: The possible error ranged from 1.0 percent to 9.7 percent for 95 percent confidence probability. With 99 percent confidence probability, the possible error ranged from 2.3 percent to 22.3 percent. At $(L/D)_{max}$, the possible error was 1.0 percent for 95 percent confidence probability and 2.2 percent for 99 percent confidence probability. Overall, these results were large relative to the likely difference a wing fence could make.

The second analysis found: The worst case error ranged from 0.18 percent to 1.08 percent for L/D, and the realistic case ranged from 0.13 percent to 0.76 percent for L/D. At $(L/D)_{max}$, the possible error was 0.28 percent for the worst case scenario and 0.20 percent for the realistic case scenario. As a reminder, these results are indicative of precision more than accuracy due to the ΔN and ΔA values used.

The first analysis was based on data a small sample size of three runs by using the MATLAB output results for the various parameters. This technique did not take advantage of the true sample size of the raw data and was not considered indicative of this analysis' ability to compare clean and fence configurations. The second analysis was considered more indicative of this analysis' ability to compare clean and fence configurations and will be used to draw future conclusions in this report.

4.3 Wind Tunnel Fence Configurations Compared to Clean Average

4.3.1 Overview.

A summary of the resulting aerodynamic performance can be seen in Table 11. This section will follow the same flow as previous: drag polar, lift coefficient, drag coefficient, pitching moment coefficient, and lift-to-drag ratio. Following Section 4.3, the best performer will move forward with the clean wing for the remainder of Chapter IV's analysis. As a reminder, refer to Table 1 in section 3.3.2 for descriptions of the various fence designs. Amplifying plots for each of the sub-sections, not necessary for the current discussion, are found in Appendix C.

Table 11. Aerodynamic Performance of the Fence Configurations

		Drag		Zero Lift	Slopes		Lift (C_L)		L/D max (-)	
Model	**Re (-)**	**C_{Dmin} (-)**	**C_{D0} (-)**	**$\alpha_{0\ Lift}$ (°)**	**$C_{L\alpha}$ (/°)**	**$C_{m\alpha}$ (/°)**	**α=10.4°**	**α=15.6°**	**α (°)**	**Value**
Clean Average	100K	0.0314	0.0351	0.35	0.0541	-0.0265	0.5441	0.6031	6.27	4.140
Fence 1	100K	0.0345	0.0382	0.39	0.0555	-0.0278	0.5557	0.6028	7.32	4.101
Fence 2	100K	0.0327	0.0345	0.13	0.0560	-0.0288	0.5754	0.6269	6.27	4.385
Fence 3	100K	0.0330	0.0361	0.33	0.0536	-0.0261	0.5395	0.6056	6.27	4.055
Fence 4	100K	0.0353	0.0376	0.28	0.0554	-0.0278	0.5609	0.6179	7.32	4.111
Fence 5	100K	0.0361	0.0395	0.47	0.0547	-0.0265	0.5428	0.6069	7.32	3.931
Clean Average	200K	0.0224	0.0248	0.36	0.0557	-0.0265	0.5591	0.6573	6.27	5.122
Fence 1	200K	0.0247	0.0275	0.41	0.0568	-0.0271	0.5677	0.6560	6.27	4.867
Fence 2	200K	0.0257	0.0276	0.12	0.0573	-0.0281	0.5895	0.6843	6.27	4.964
Fence 3	200K	0.0235	0.0270	0.38	0.0559	-0.0267	0.5598	0.6517	6.27	4.842
Fence 4	200K	0.0257	0.0283	0.29	0.0564	-0.0272	0.5702	0.6660	6.27	4.830
Fence 5	200K	0.0247	0.0269	0.46	0.0567	-0.0270	0.5632	0.6575	6.27	4.935
Clean Average	300K	0.0229	0.0263	0.36	0.0576	-0.0277	0.5785	0.6647	6.27	5.084
Fence 1	300K	0.0247	0.0285	0.37	0.0576	-0.0280	0.5773	0.6615	6.27	4.829
Fence 2	300K	0.0240	0.0262	0.11	0.0594	-0.0290	0.6112	0.6802	6.27	5.251
Fence 3	300K	0.0216	0.0248	0.36	0.0583	-0.0280	0.5850	0.6513	6.27	5.241
Fence 4	300K	0.0240	0.0275	0.30	0.0585	-0.0283	0.5905	0.6647	6.27	5.038
Fence 5	300K	0.0243	0.0280	0.45	0.0577	-0.0278	0.5745	0.6581	6.27	4.926

4.3.2 Drag Polar.

The drag polar plot was critical in guiding the best choice of a wing fence design to go forward with. While most of the other plots are against AOA, this plot reduced AOA's impact as a variable and allowed for a better contrast. Figures 87 through 89

depict these comparisons at 30 and 60 mph. At zero lift, all configurations were very close, as they should be. As lift increased, there was a general trend for all fenced wings to have a greater C_L than the clean wing at the same C_D. Fences 2 and 4 clearly began to stand out at all three speeds. In particular, fence 2 was the best performer with an average (over all three velocities) maximum increase of approximately 0.04 in C_L for the same C_D when compared to the Clean Average data (denoted *Clean* in the plots). This equated to an average maximum increase in lift of 6.3 ± 0.6 percent for the same price in drag. The error of ±0.6 percent was based upon the average of the worst case errors at all three velocities evaluated. The error analysis can be found in section 4.2.7.2.

The lift coefficients were also compared between the clean and fence 2 configurations at the C_D corresponding to 13.6 degrees AOA for fence 2. The resulting C_D was between 0.22 and 0.23. Again, the reported errors were based on the worst case errors at each velocity as presented in the analysis of section 4.2.7.2. At 30 mph, the clean C_L was 0.597 ± 0.005, and the fence 2 C_L was 0.634 ± 0.005. At 60 mph, the clean C_L was 0.643 ± 0.004, and the fence 2 C_L was 0.665 ± 0.004. At 90 mph, the clean C_L was 0.657 ± 0.003, and the fence 2 C_L was 0.683 ± 0.003.

The drag polar also provided a good look at C_{D0}. Drag at zero lift should depict a reasonable order (low-drag to high-drag) based on configuration changes. However, in this case, it did not. The order was different for all three velocities. The clean configuration was lowest at only 60 mph. This was not completely unexpected because the fences only added a very small frontal area. The largest difference in C_{D0} at all three speeds was 0.005 at 30 mph. This was also expected since the lower velocity resulted in smaller forces and reduced balance sensitivity.

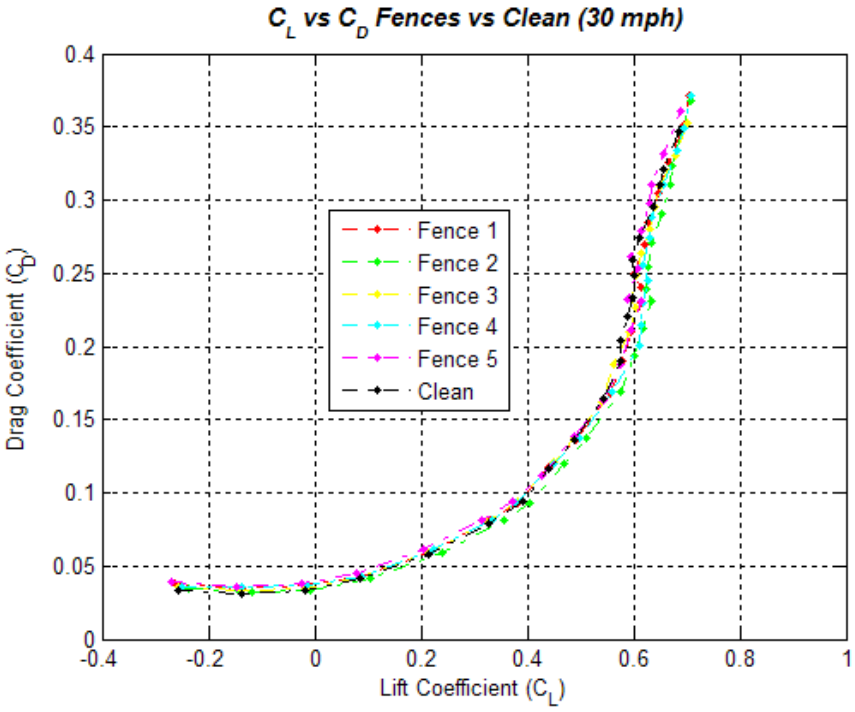

Figure 87. Drag Polar – Fence Comparisons (30 mph)

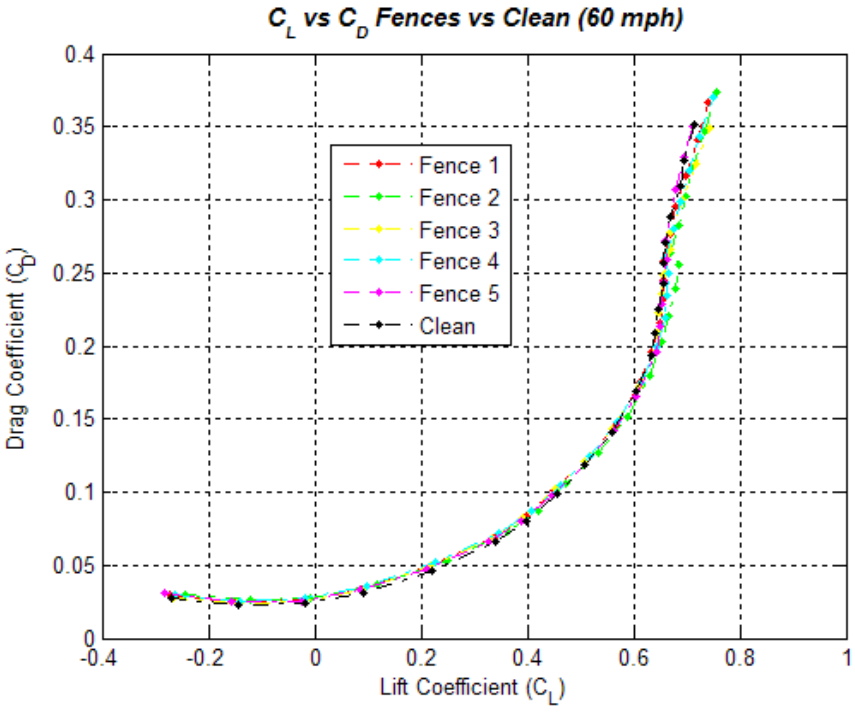

Figure 88. Drag Polar – Fence Comparisons (60 mph)

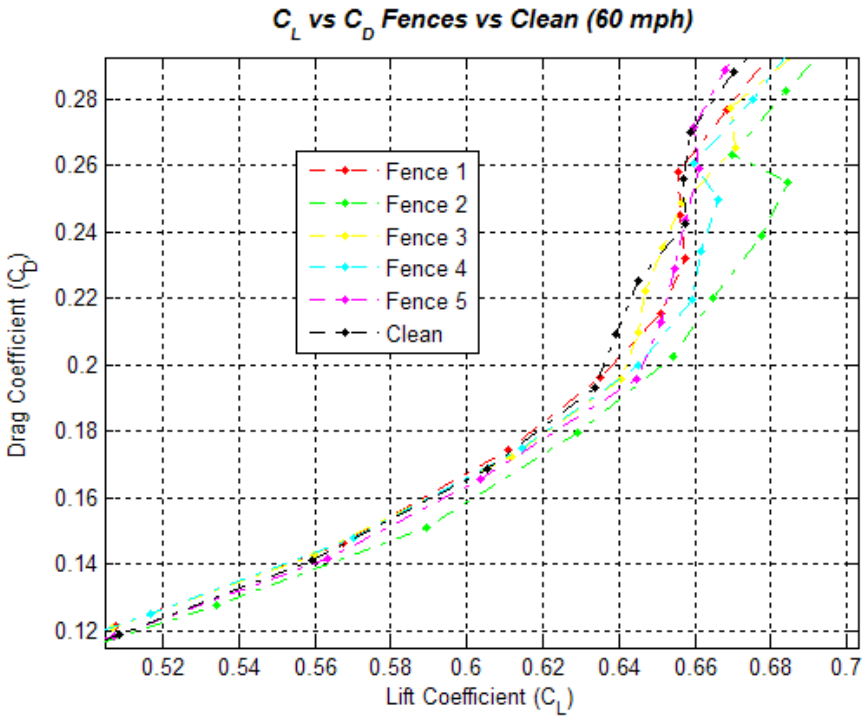

Figure 89. Drag Polar – Zoom-in Fence Comparisons (60 mph)

4.3.3 Lift Curve.

The lift curve provided insight into several important factors, one of which was C_{Lmax}. Again, fence 2 and 4 stood out with fence 2 showing the most improvement. Figures 90 and 91 show the comparisons at 90 mph. The maximum increase in C_L occurred between 12.5 and 14.5 degrees, dependent upon velocity. Based upon this data, the average maximum increase in C_L relative to the clean configuration was about 0.039, which equated to an increase of approximately 6.3 ± 0.6 percent. The reported error was based on the same analyses mentioned previously in the drag polar section.

The lift coefficients were also compared between the clean and fence 2 configurations at 13.6 degrees AOA. Again, the reported errors are based on the worst case errors at each velocity as presented in the analysis of section 4.2.7.2. At 30 mph, the clean C_L was 0.588 ± 0.005, and the fence 2 C_L was 0.634 ± 0.005. At 60 mph, the clean

C_L was 0.640 ± 0.004, and the fence 2 C_L was 0.665 ± 0.004. At 90 mph, the clean C_L was 0.655 ± 0.003, and the fence 2 C_L was 0.683 ± 0.003.

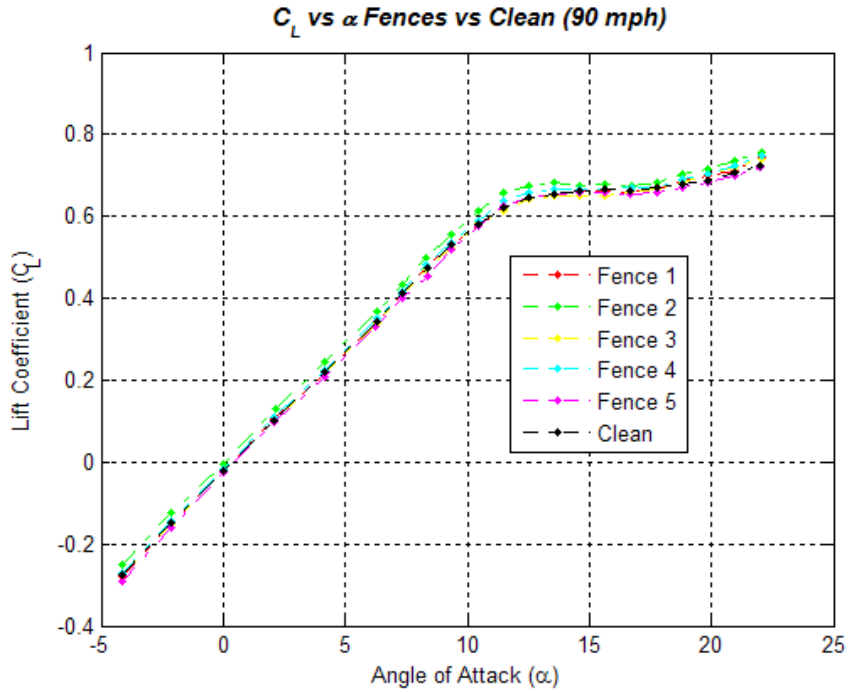

Figure 90. Lift Curve – Fence Comparisons (90 mph)

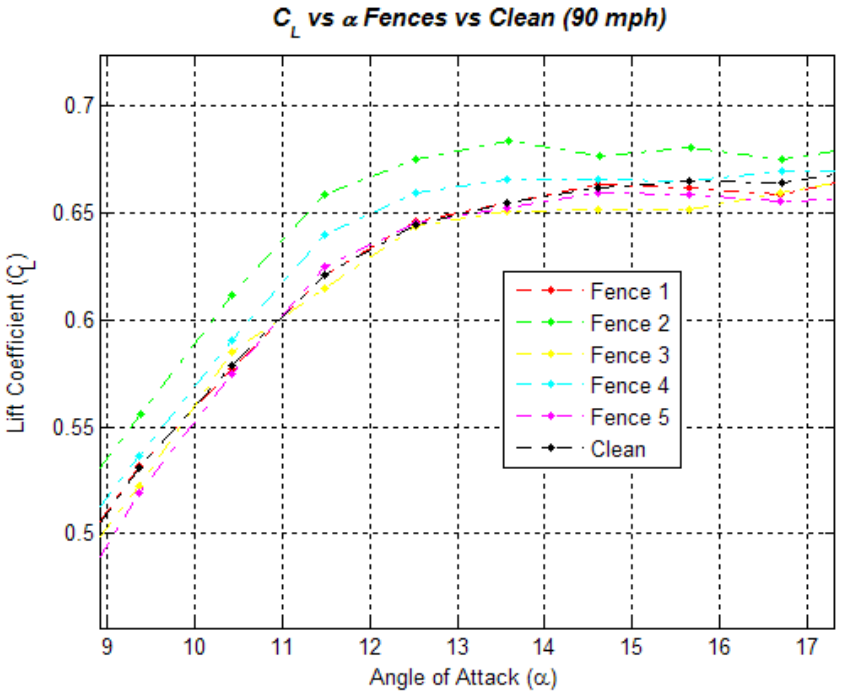

Figure 91. Lift Curve – Zoom-in Fence Comparisons (90 mph)

There was a small offset in AOA at zero lift (α_{0Lift}). The average offset for fence 2 to the clean wing for α_{0Lift} was approximately 0.24 degrees. While it cannot be known for sure, it may have been due to the way the wing was attached to bottom of the fuselage. Variations in the fastener tightness or other small changes may account for this.

Because of the offset, a manual adjustment was made for fence 2 at each speed. This was accomplished two ways. First, a manual adjustment was accomplished by reducing all C_L values by the amount required to force the α_{0Lift} to be identical with the clean configuration. For 30, 60, and 90 mph respectively, the corrections were to subtract 0.012, 0.015, and 0.017 from C_L. Once this was accomplished, the average maximum increase in C_L relative to the clean configuration became 0.024, which equated to an increase of approximately 3.9 percent. Second, a manual adjust was completed by adding the difference in α_{0Lift} to fence 2's angles of attack. For 30, 60, and 90 mph respectively, the increase was 0.22, 0.24, and 0.25 degrees. Once this was accomplished, the average maximum increase in C_L relative to the clean configuration became 0.039, which equated to an increase of approximately 6.3 percent. Both techniques are shown below in Figures 92, 93, and 94.

The AOA adjustment was plausible due to the way the wings were mounted on the model. Additionally, making and not making the angle adjustment yielded the same average maximum increase in lift. This also corresponded well with the drag polar results, which reduced AOA's role. Therefore, it was considered the most likely source of the error, and it was not considered necessary to propagate this adjustment throughout all of the data.

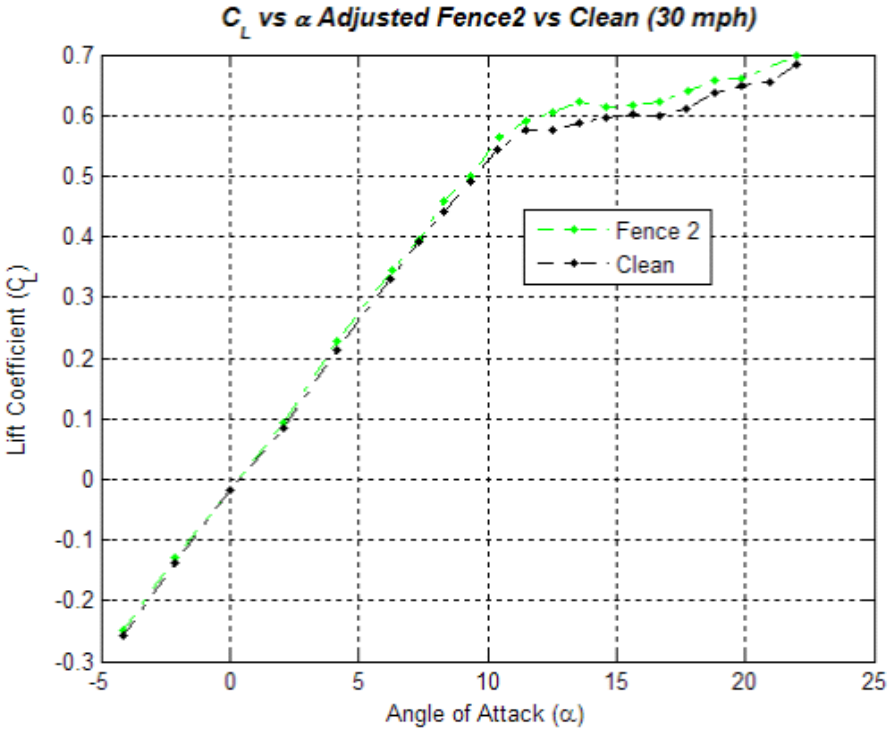

(a)

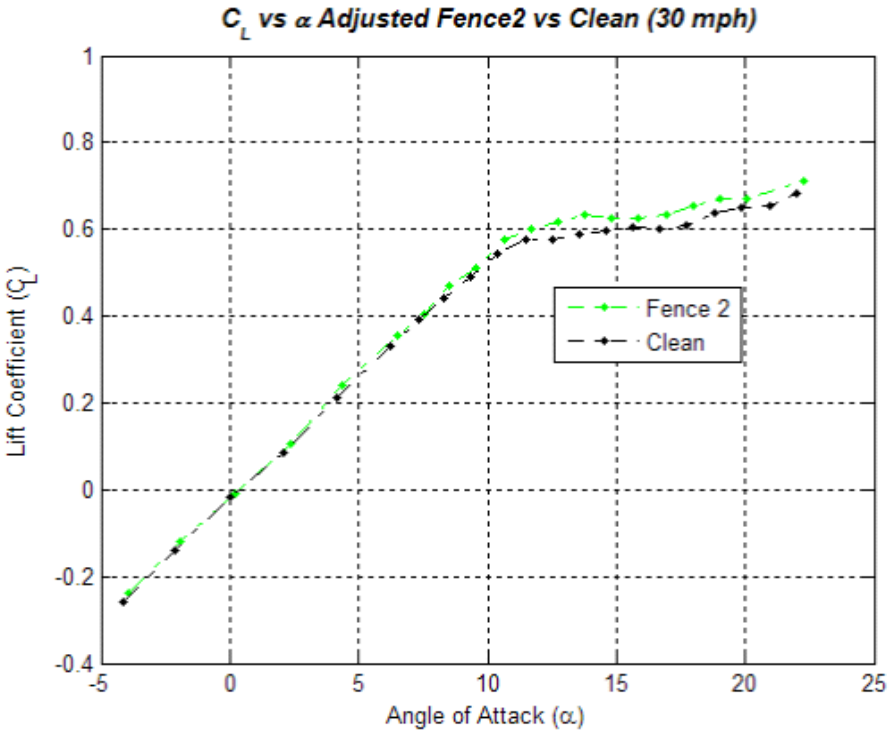

(b)

Figure 92. Lift Curve - Adjusted Fence 2 vs Clean (30 mph)
(a) C_L Adjusted (b) AOA Adjusted

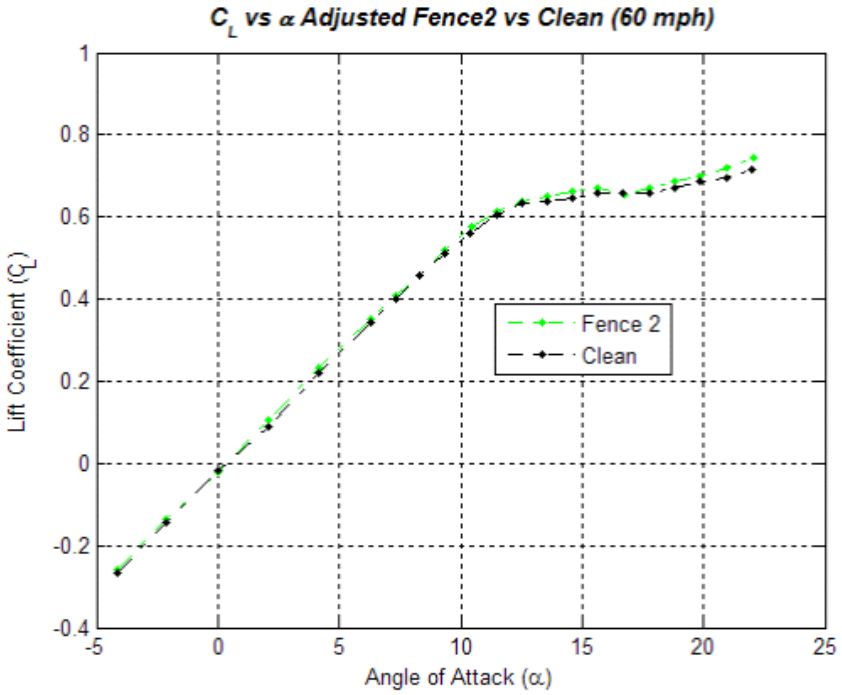

(a)

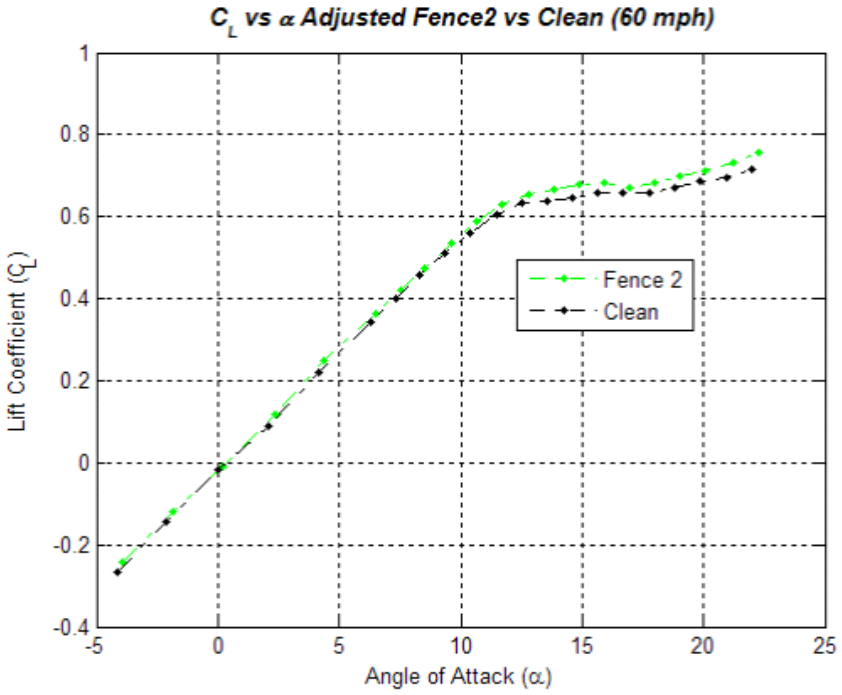

(b)

Figure 93. Lift Curve - Adjusted Fence 2 vs Clean (60 mph)
(a) C_L Adjusted (b) AOA Adjusted

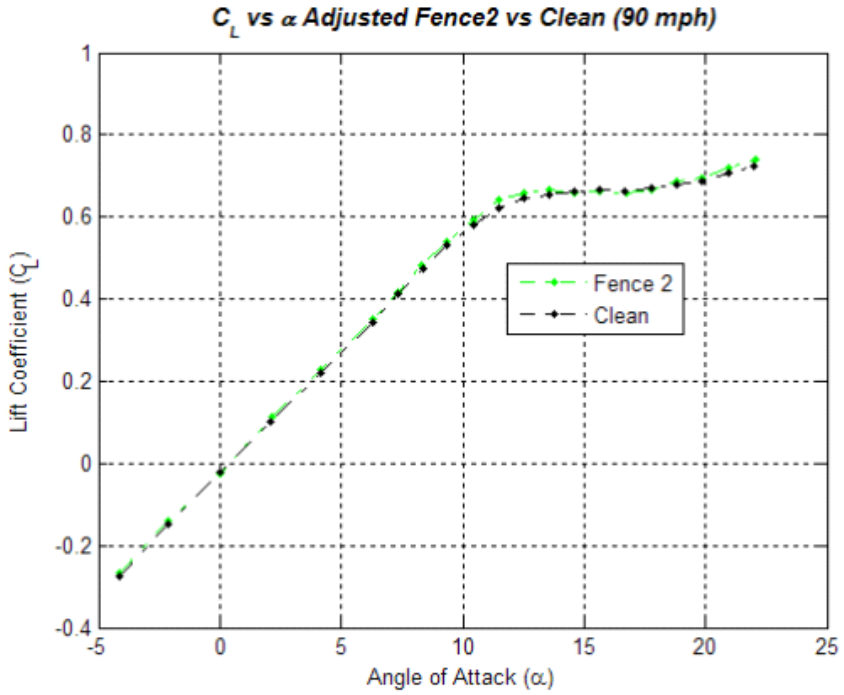

(a)

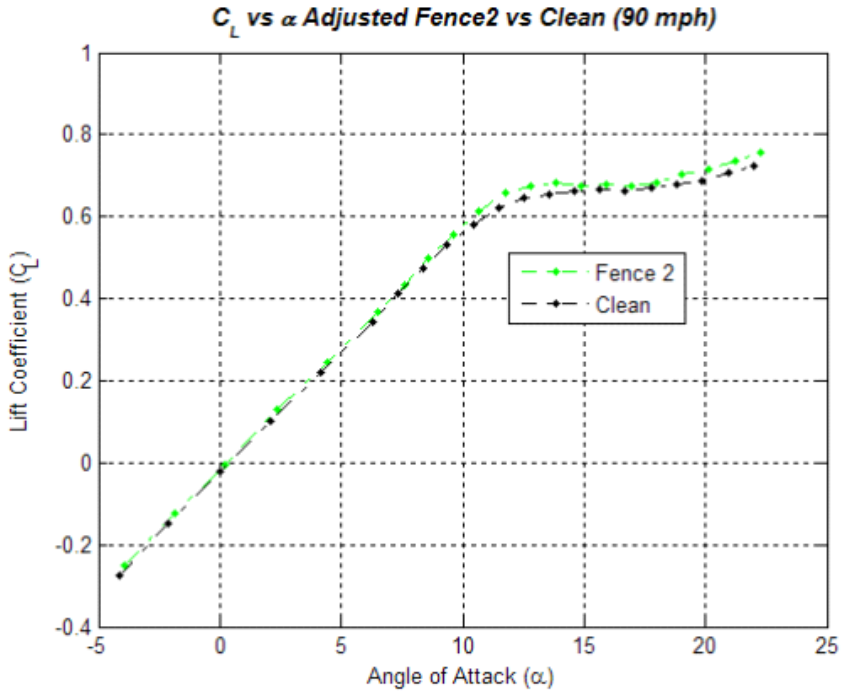

(b)

Figure 94. Lift Curve - Adjusted Fence 2 vs Clean (90 mph)
(a) C_L Adjusted (b) AOA Adjusted

4.3.4 Drag Curve.

The total drag coefficient plot allowed minimum drag, C_{Dmin}, to be investigated as well as total drag trends. Figures 95 through 97 show these plots. C_{Dmin} was found to consistently occur at -2.1 degrees. With only one exception at 90 mph, the clean configuration's C_{Dmin} values were consistently the lowest. Among the other configurations, there was no trend. Additionally, it was clear that the lift-curve slope began to drop off between 11 and 13 degrees. This was expected since total drag is a function of C_L^2, among other things. Therefore, the drag results correlated well with lift results.

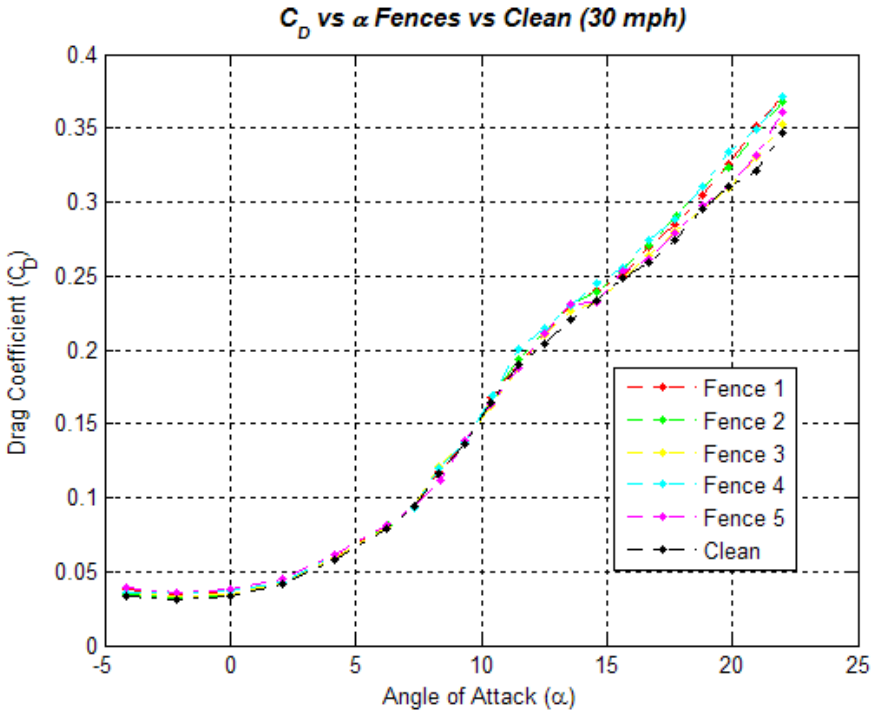

Figure 95. Drag – Fence Comparisons (30 mph)

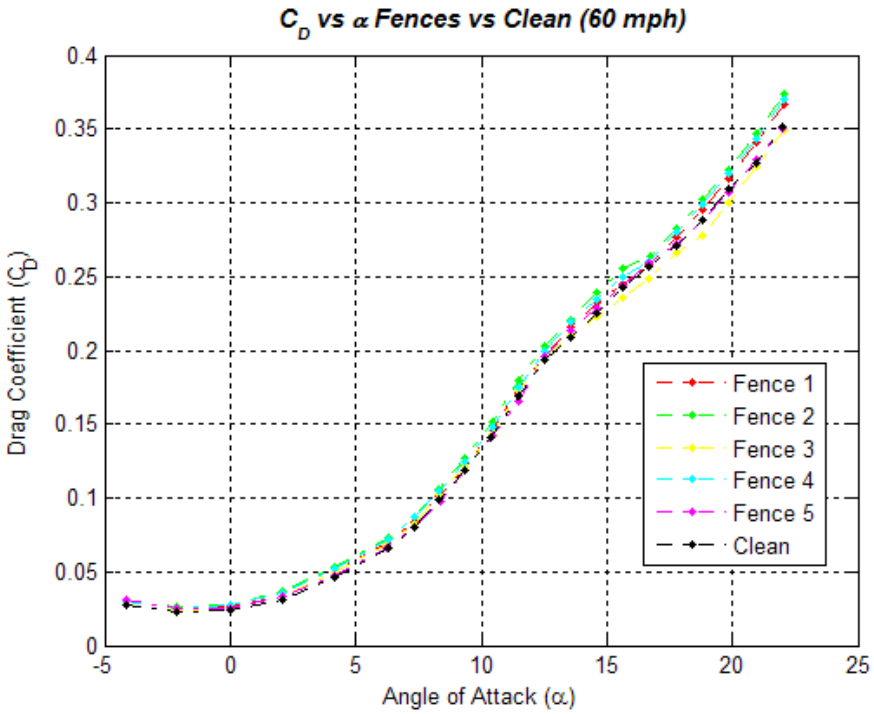

Figure 96. Drag – Fence Comparisons (60 mph)

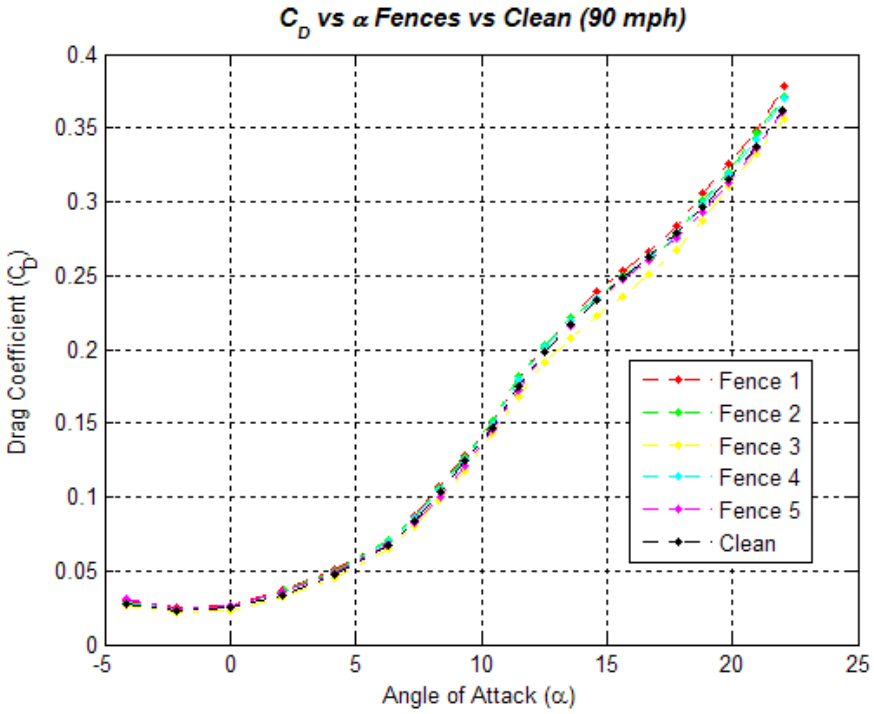

Figure 97. Drag – Fence Comparisons (90 mph)

4.3.5 Pitching Moment Curve.

The primary purpose of this portion of the analysis was to ensure safety for the planned flight test. The T-38 already had very good longitudinal static stability. There was no specific objective to increase that. However, as mentioned in Chapter II, wing fences have been used historically to improve longitudinal stability. Although there was no tail on the model, verification that the wing fences did not have a negative impact on stability was desired.

The longitudinal static stability derivative, $C_{m\alpha}$, can be attained from the linear portion of this plot. It was computed here by using the two endpoints of -4.2 and 9.4 degrees AOA and assuming linearity between these points. Additionally, any unstable or unfavorable pitching moments would be observed in these plots. Again, as a reminder, the model was tailless. The average $C_{m\alpha}$ was stable for all velocities and configurations at -0.0275 per degree. In the 30 mph plot (Figure 98), there are a few areas of slightly positive slope from 13 to 17 degrees. This indicated a pitch-up motion in the stall and is unfavorable. The areas of positive slope were reduced in the 60 mph run, and by the 90 mph run, there were no areas of positive slope. Figures 99 through 101 show the 60 and 90 mph runs below. Because there was no tail on the model and the positive slopes were not consistent or large, this was not considered a concern for flight test.

The largest $C_{m\alpha}$ (most negative) was consistently fence 2. The average increase over the clean configuration was -0.002. This was equivalent to about a 6.4 percent increase in restoring pitching moment.

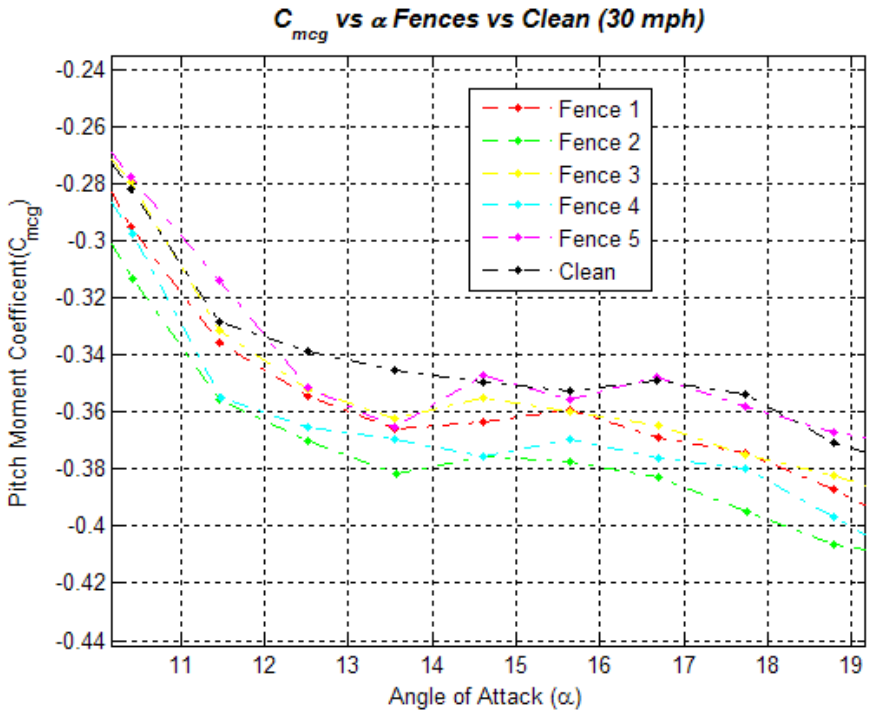

Figure 98. Pitching Moment Coefficient – Zoom-in Fence Comparisons (30 mph)

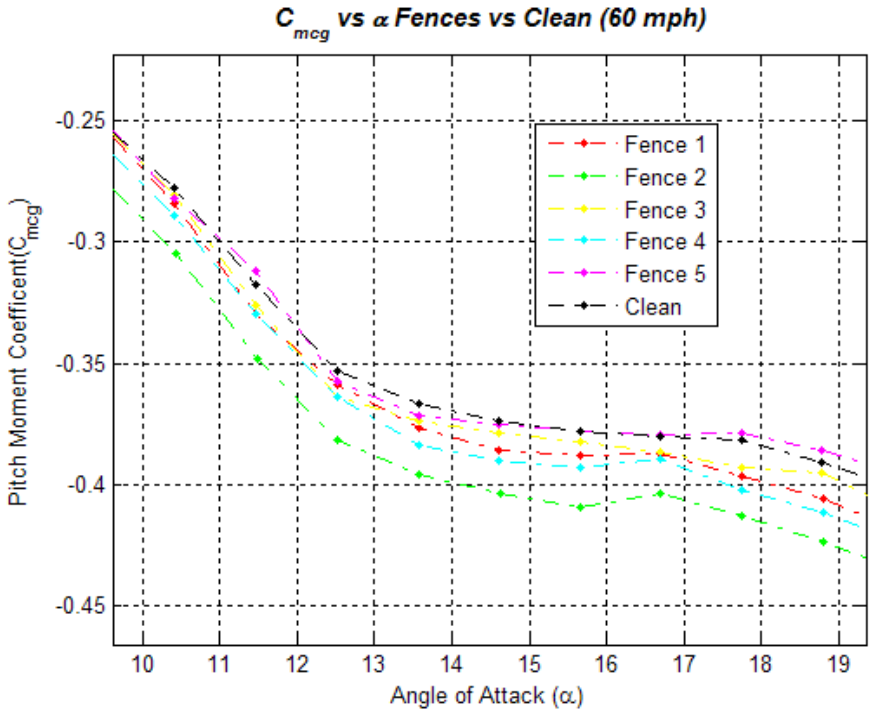

Figure 99. Pitching Moment Coefficient – Zoom-in Fence Comparisons (60 mph)

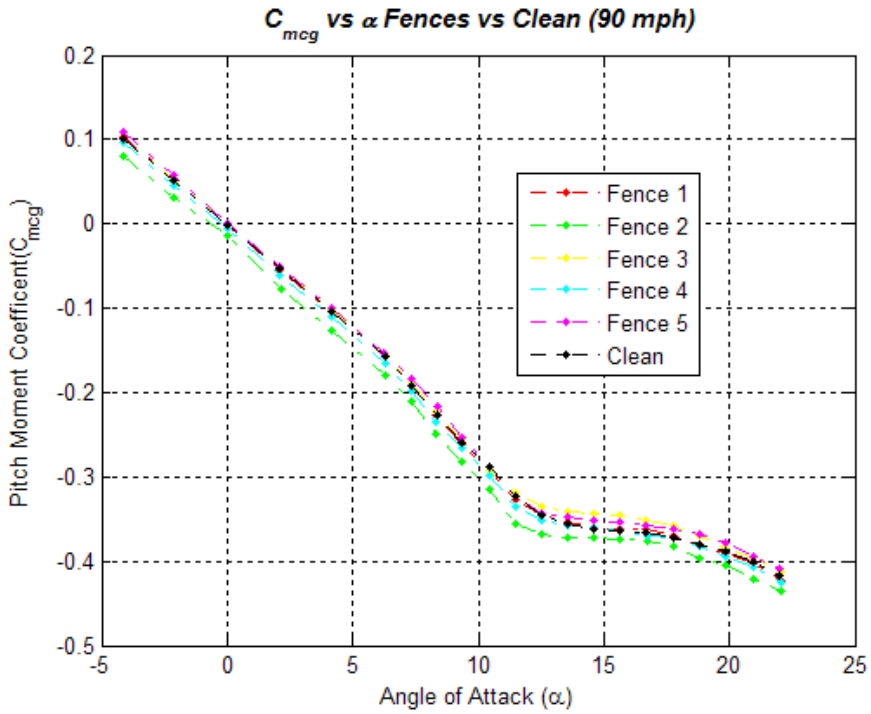

Figure 100. Pitching Moment Coefficient – Fence Comparisons (90 mph)

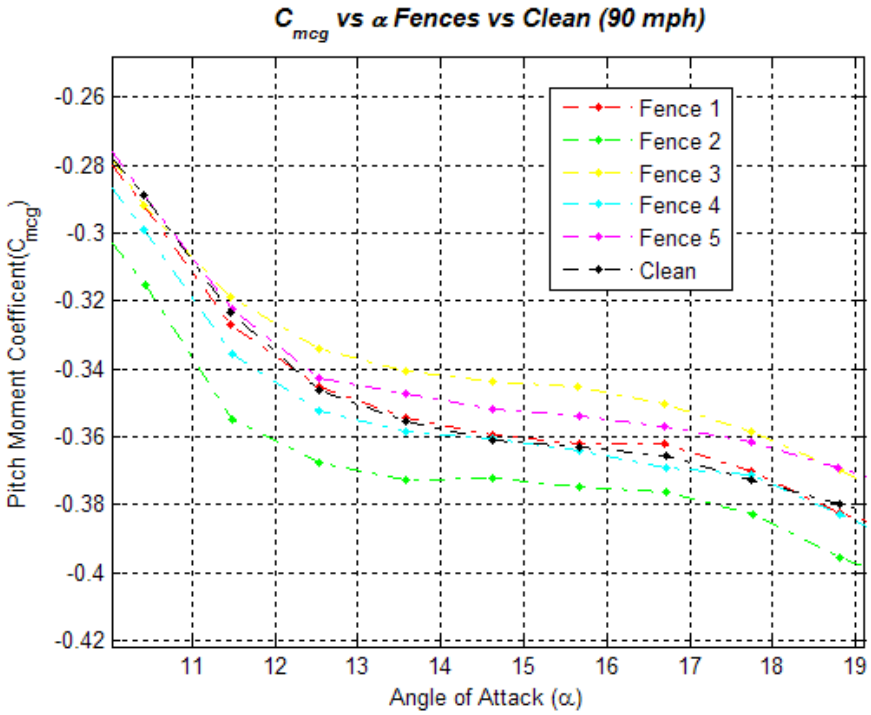

Figure 101. Pitching Moment Coefficient – Zoom-in Fence Comparisons (90 mph)

4.3.6 Lift-to-Drag Curve.

Lift-to-drag ratio is one measure of aircraft efficiency. This happens at a lower AOA than what has been discussed thus far. It has been shown that fence 2 increased lift at moderate and high angles of attack for no cost in drag. However, this was observed at the largest C_L values. Now, an AOA around 6 degrees is analyzed since a different configuration may perform better in this area. Figures 102 and 103 show the 30 mph case. Figures 104 and 105 show the 60 and 90 mph cases respectively.

In both the 30 and 90 mph cases, fence 2 outperformed all other configurations at $(L/D)_{max}$. In the 60 mph case, the clean configuration was the better performer. It also came in a close second and third for 30 and 90 mph runs respectively. This was expected because a wing fence generally does not start having significant effects until a higher AOA than $(L/D)_{max}$. The $(L/D)_{max}$ values for clean and fence 2 were averaged, and the result was fence 2 having an $(L/D)_{max}$ of 0.085 more than clean. This was approximately a 1.8 ± 0.85 percent increase. The reported error was based on the average worst case error at the associated AOA, presented in section 4.2.7.2. This increase was considered insignificant for the purposes of this study.

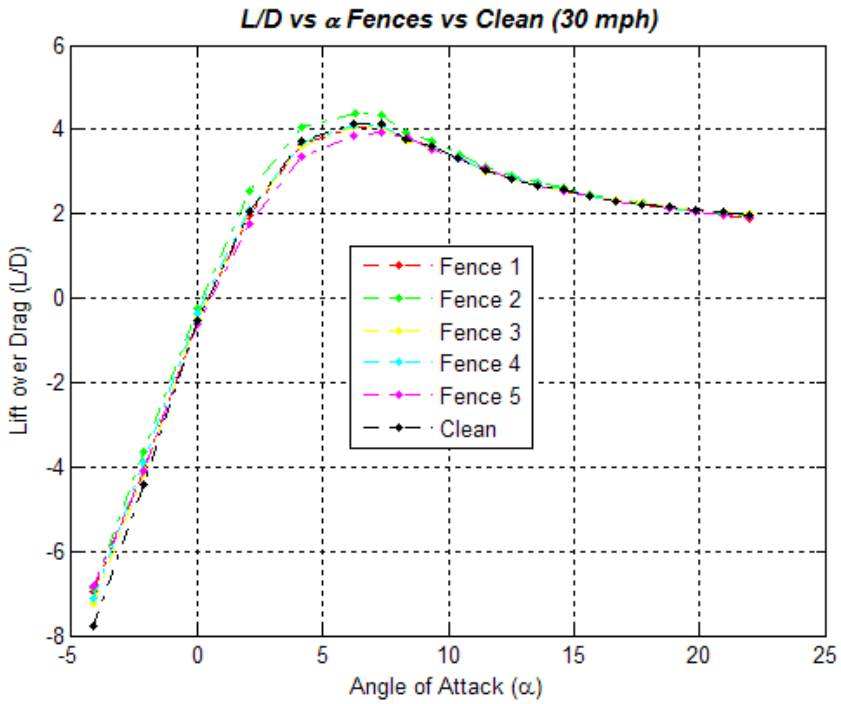

Figure 102. Lift-to-Drag – Fence Comparisons (30 mph)

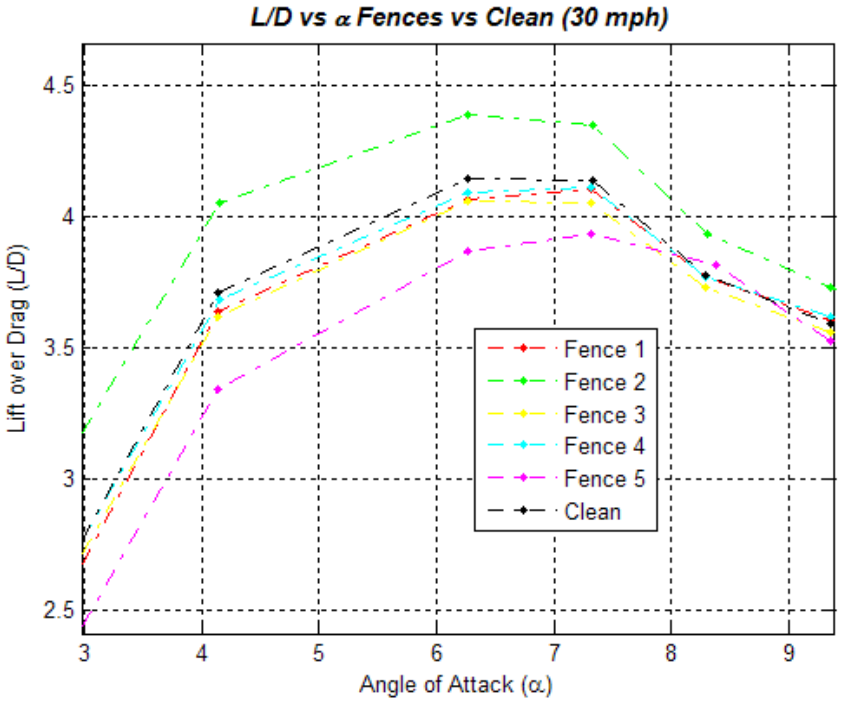

Figure 103. Lift-to-Drag – Zoom-in Fence Comparisons (30 mph)

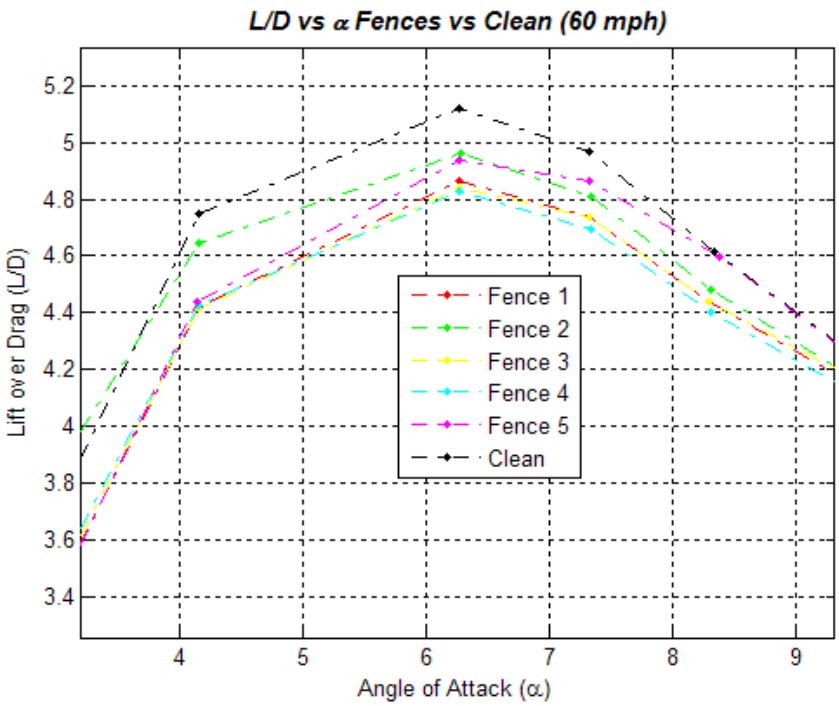

Figure 104. Lift-to-Drag – Zoom-in Fence Comparisons (60 mph)

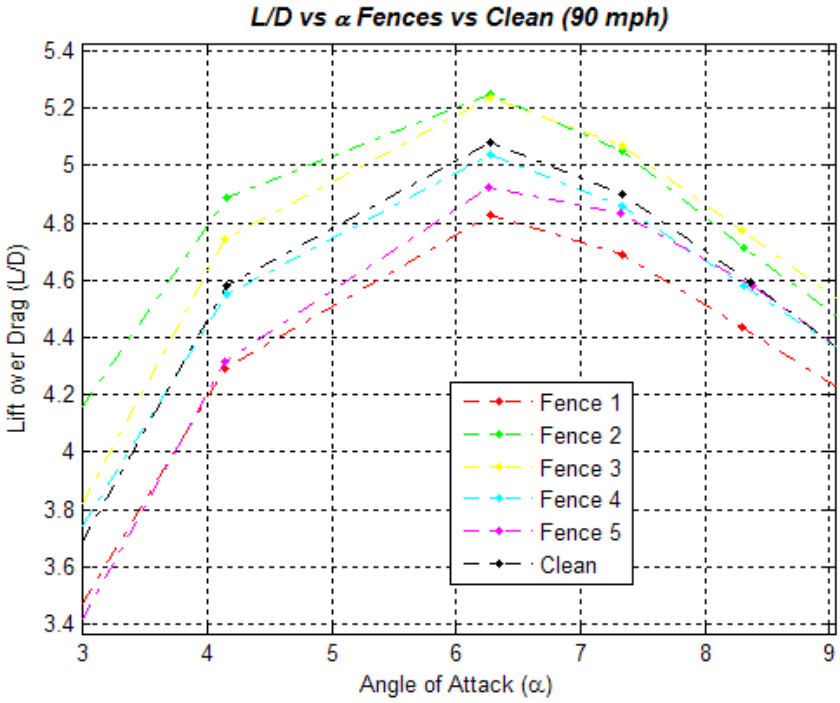

Figure 105. Lift-to-Drag – Zoom-in Fence Comparisons (90 mph)

4.4 Wind Tunnel Reynolds Number and Trip Tape Comparisons

4.4.1 Overview.

Reynolds number effects were investigated by running at the three velocities of 30, 60, and 90 mph. As mentioned previously, the resulting Re_{mac} were approximately 1 x 10^5 (100K), 2 x 10^5 (200K), and 3 x 10^5 (300K). Because the trip tape was intended to model the impact of increased Re, the results of those tests are covered here as well. Amplifying plots for each of the sub-sections, not necessary for the current discussion, are found in Appendix C.

Trip tape was only placed on the clean and Fence 2 configurations. Though previously presented, the results without trip tape are included for ease of reference and comparison. Table 12 summarizes these results. In this section, only the drag polar, lift curve, and drag curves are addressed.

Table 12. Aerodynamic Performance of the Trip Tape Configurations

		Drag		Zero Lift	Slopes		Lift (C_L)		L/D max (-)	
Model	**Re (-)**	**C_{Dmin} (-)**	**C_{D0} (-)**	**$\alpha_{0\ Lift}$ (°)**	**$C_{L\alpha}$ (/°)**	**$C_{m\alpha}$ (/°)**	**α=10.4°**	**α=15.6°**	**α (°)**	**Value**
Clean	100K	0.0314	0.0351	0.35	0.0541	-0.0265	0.5441	0.6031	6.27	4.140
Clean TT	100K	0.0341	0.0368	0.21	0.0539	-0.0260	0.5491	0.6125	6.27	4.167
Fence 2	100K	0.0327	0.0345	0.13	0.0560	-0.0288	0.5754	0.6269	6.27	4.385
Fence 2 TT	100K	0.0355	0.0378	-0.02	0.0554	-0.0284	0.5774	0.6099	6.27	4.237
Clean	200K	0.0224	0.0248	0.36	0.0557	-0.0265	0.5591	0.6573	6.27	5.122
Clean TT	200K	0.0243	0.0260	0.17	0.0560	-0.0268	0.5733	0.6623	6.27	5.162
Fence 2	200K	0.0257	0.0276	0.12	0.0573	-0.0281	0.5895	0.6843	6.27	4.964
Fence 2 TT	200K	0.0255	0.0271	-0.05	0.0564	-0.0273	0.5892	0.6737	6.27	5.176
Clean	300K	0.0229	0.0263	0.36	0.0576	-0.0277	0.5785	0.6647	6.27	5.084
Clean TT	300K	0.0247	0.0275	0.07	0.0572	-0.0271	0.5904	0.6623	6.27	5.088
Fence 2	300K	0.0240	0.0262	0.11	0.0594	-0.0290	0.6112	0.6802	6.27	5.251
Fence 2 TT	300K	0.0259	0.0289	-0.23	0.0573	-0.0264	0.6093	0.6723	6.27	5.139

4.4.2 Drag Polar.

There was a clear difference between the 100K runs and the others. The higher C_{Dmin} associated with lower Reynolds numbers played a key role as did the fact that the

lift curve was significantly affected by Reynolds number. Because these effects were coupled in the drag polar, the differences were magnified.

The jump from 100K to 200K had much more impact on the results than from 200K to 300K. Also, the models with trip tape had a trend for slightly better performance. The results are in the following plots (Figures 106-108). For these plots, trip tape is denoted TT.

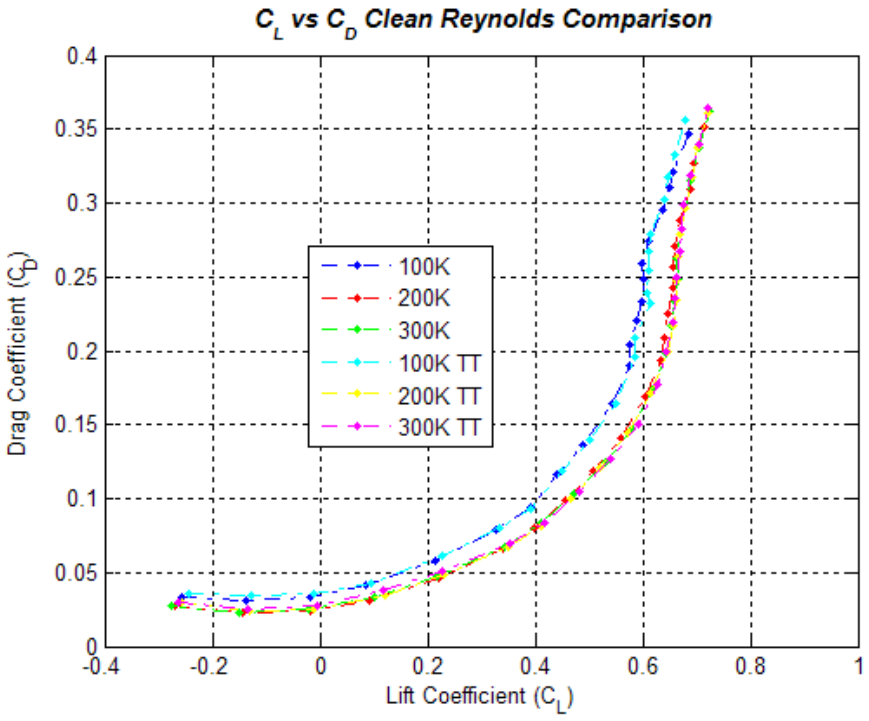

Figure 106. Clean Drag Polar – Reynolds and Trip Tape Comparisons

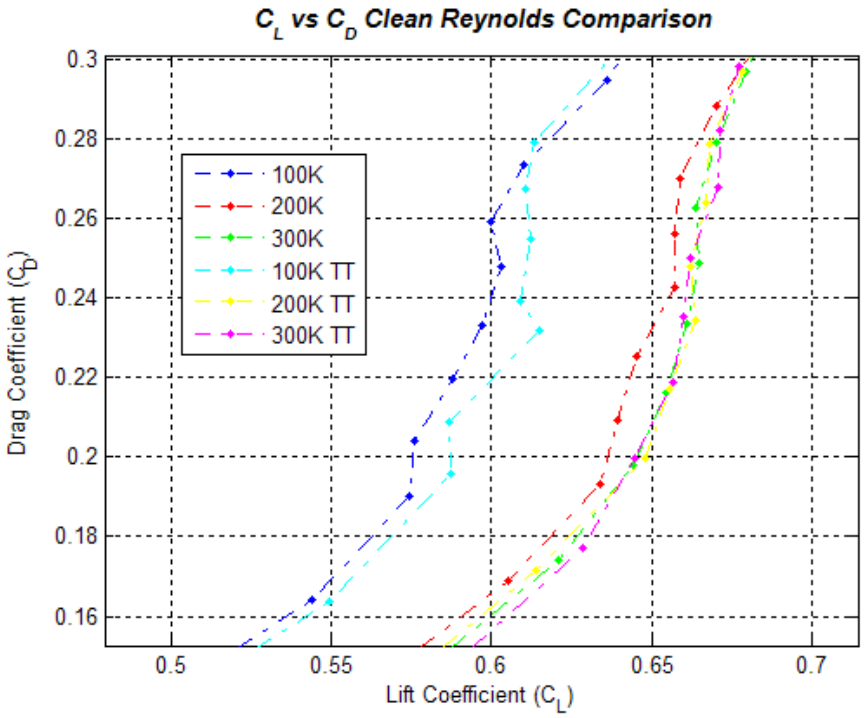

Figure 107. Clean Drag Polar – Zoom-in Reynolds and Trip Tape Comparisons

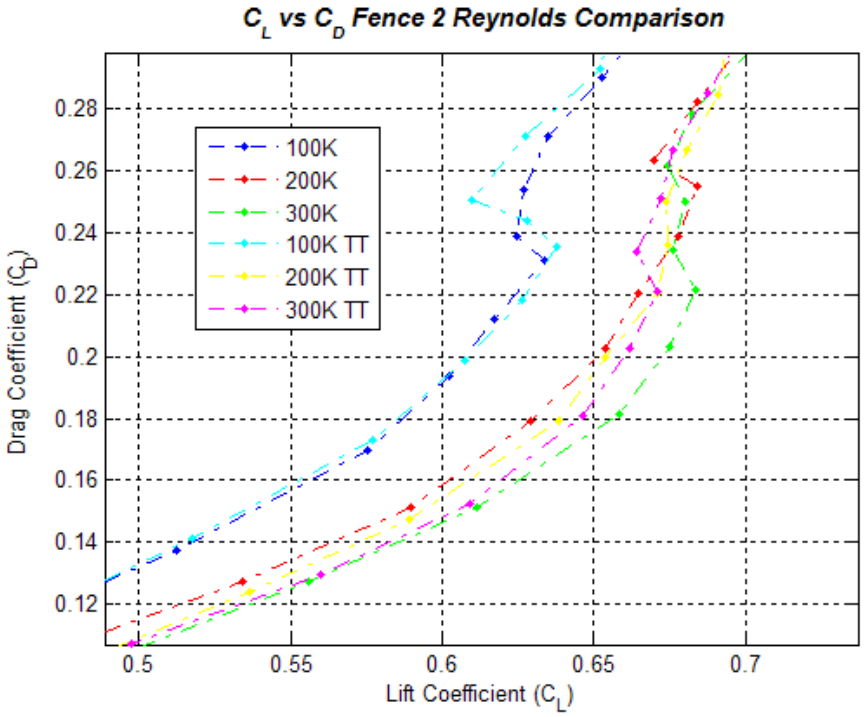

Figure 108. Fence 2 Drag Polar – Zoom-in Reynolds and Trip Tape Comparisons

4.4.3 Lift Curve.

As discussed in Chapter III, Re has a big impact on the lift curve. While its impact is low on the slope, its impact is large on C_{Lmax} and on the slope of the curve after C_{Lmax}, or stall (3). The effects that were expected are depicted well for the clean configuration (Figures 109-110). The curves are in the expected order. Again, the jump from 100K to 200K showed the most impact, particularly on C_{Lmax}. The stall was not any more abrupt from one Re to the next.

While this worked well for the clean configuration, it didn't work so clearly for fence 2. For example, at 15.5 degrees AOA on Figure 111, all three trip tape runs were under performing the fence alone. The reason for this result was unknown.

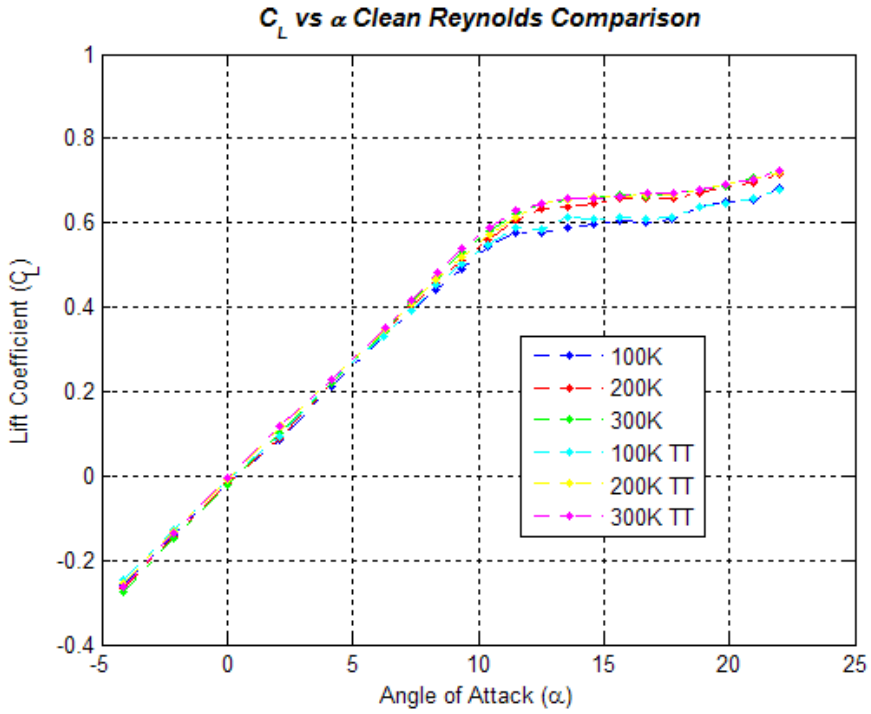

Figure 109. Clean Lift Curve – Reynolds and Trip Tape Comparisons

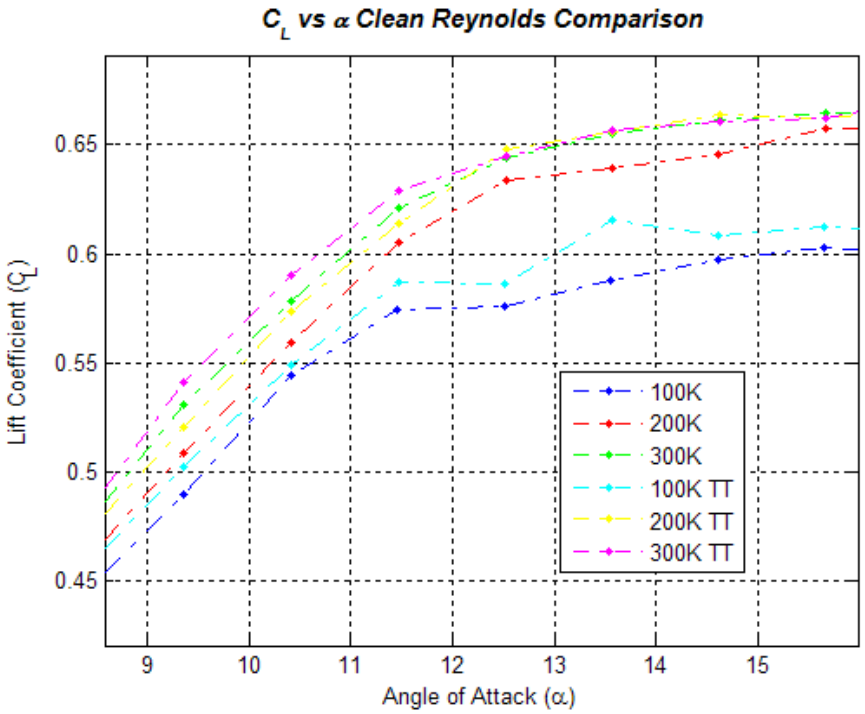

Figure 110. Clean Lift Curve – Zoom-in Reynolds and Trip Tape Comparisons

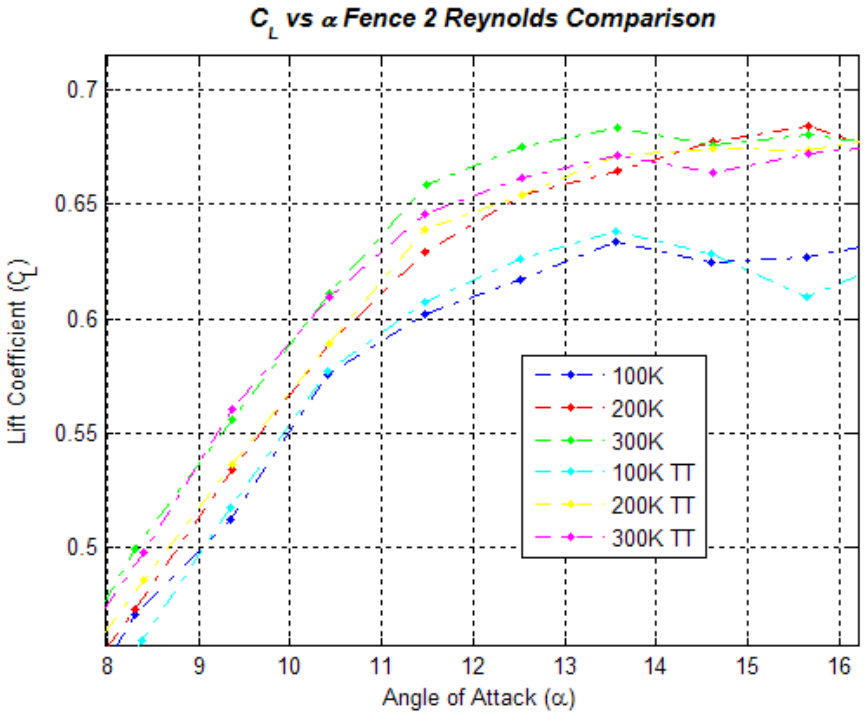

Figure 111. Fence 2 Lift Curve – Zoom-in Reynolds and Trip Tape Comparisons

4.4.4 Drag Curve.

C_{Dmin} typically decreases with increasing Re (3). Although trip tape models an increase in Re, its impact is far from a pure increase in Re. After all, the thickness of the tape acts as an obstruction to the flow, particularly at low AOA. In the case of trip tape, it was observed that C_{Dmin} increased approximately 0.002 for all cases. Refer to Figures 112 through 114.

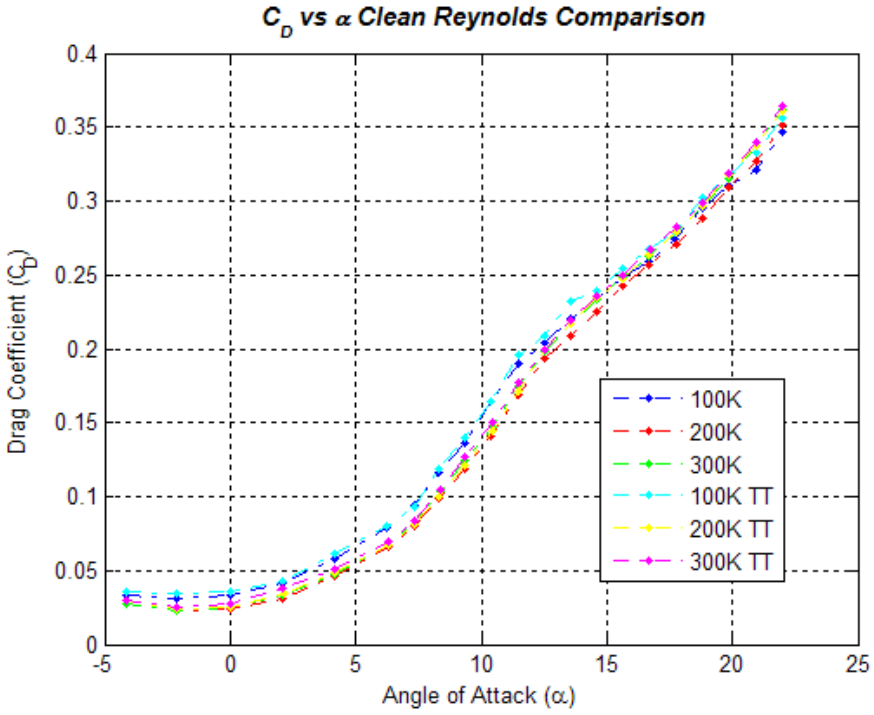

Figure 112. Clean Drag – Reynolds and Trip Tape Comparisons

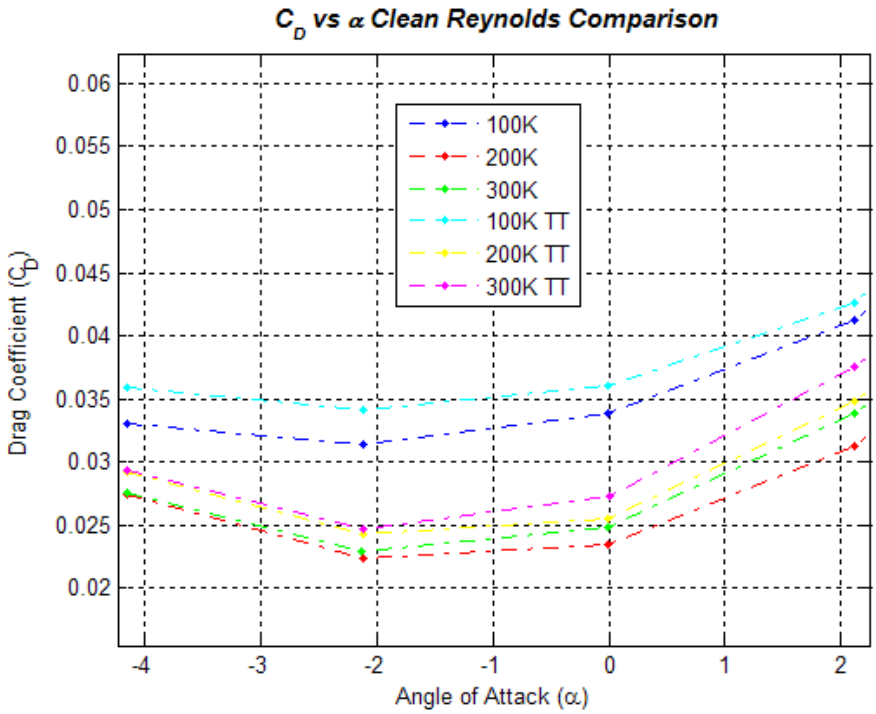

Figure 113. Clean Drag – Zoom-in Reynolds and Trip Tape Comparisons

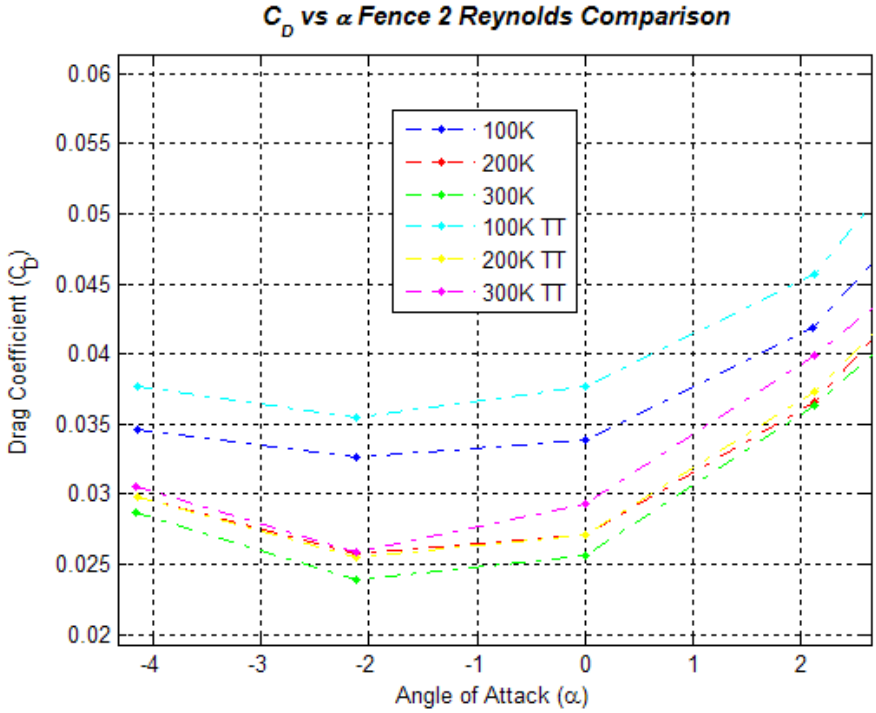

Figure 114. Fence 2 Drag – Zoom-in Reynolds and Trip Tape Comparisons

4.5 Wind Tunnel Flow Visualization

4.5.1 Overview.

Flow visualization was used to better understand the effects of the fence and improve the correlation of balance and CFD data. Again this focused on clean and fence 2 configurations. Tufts were the method of choice here. No balance data was taken on the flow visualization runs because of the aerodynamic interaction of the tape and tufts. After the results are discussed, there will be a brief section with some comparison of wind tunnel flow visualization and CFD flow visualization.

4.5.2 Tufts.

The tufts were applied per section 3.3.4. The observations were made at 10 and 15 degrees AOA, partly because they were the angles at which CFD had been previously run by Solfelt (23). Additionally, these runs were all accomplished at a Re_{mac} of approximately 300K. This section compares clean and fence 2 at each AOA with a side view presented first followed by a top view. There were two rows of tufts in the streamwise direction. The first row had 14 tufts in the spanwise direction, and the second row had 13 tufts in the spanwise direction.

4.5.2.1 Clean versus Fence 2 – 10 Degrees AOA.

In the side view, the clean wing (Figure 115) showed some significantly reversed flow in the second row on the outer two-thirds of the wing. The inboard one-third was attached in the second row. In the first row, there were areas of thick boundary layer as well as a few areas of reversed flow. In the case of fence 2 (Figure 116), the first row was very similar except that the flow just outside the fence was attached. Also, in the second row, the second through tenth tufts in from the wingtip showed much more streamlined, attached flow. The fence significantly altered the flow over the wing in its

vicinity. There was some effect inboard of the fence where the spanwise flow was directed in the streamwise direction. However, most of its impact was outboard of the fence.

Figure 115. Clean Tufts 10 Degrees – Right Wing Side View (90 mph)

(a)

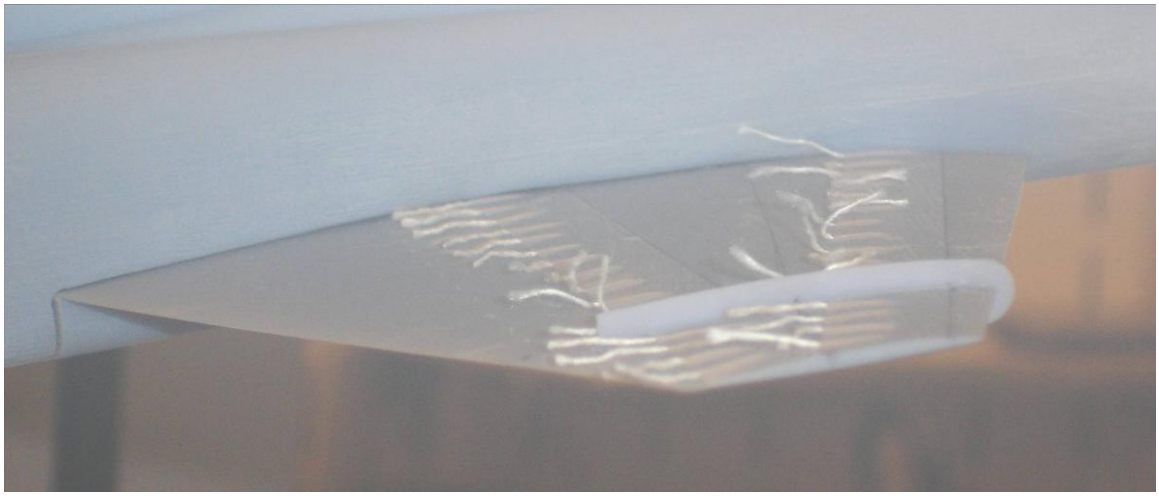

(b)

Figure 116. Fence 2 Tufts 10 Degrees – Right Wing Side View (90 mph)
(a) Forward Side View (b) Direct Side View

The top view shed further light on the side view. In the first row on the clean wing (Figures 117 and 118), significant spanwise flow existed for almost the entire semispan. In the second row, the middle-third showed spanwise flow toward the tip that transitioned into reversed flow and then to flow moving toward the fuselage. The spanwise flow was almost completely removed by fence 2 on the right wing (Figure 119a) except for the second tuft in from the wing tip on the first row. However, the left wing (Figure 119b) showed more spanwise flow near the wing tip. That was possibly an artifact of still photography of unsteady flow, especially with vortices in the vicinity. None the less, the fence clearly had some impact on the flow inboard of the fence and a significant impact on the flow outboard of the fence, particularly in arresting spanwise flow and increasing the amount of attached flow on the wing.

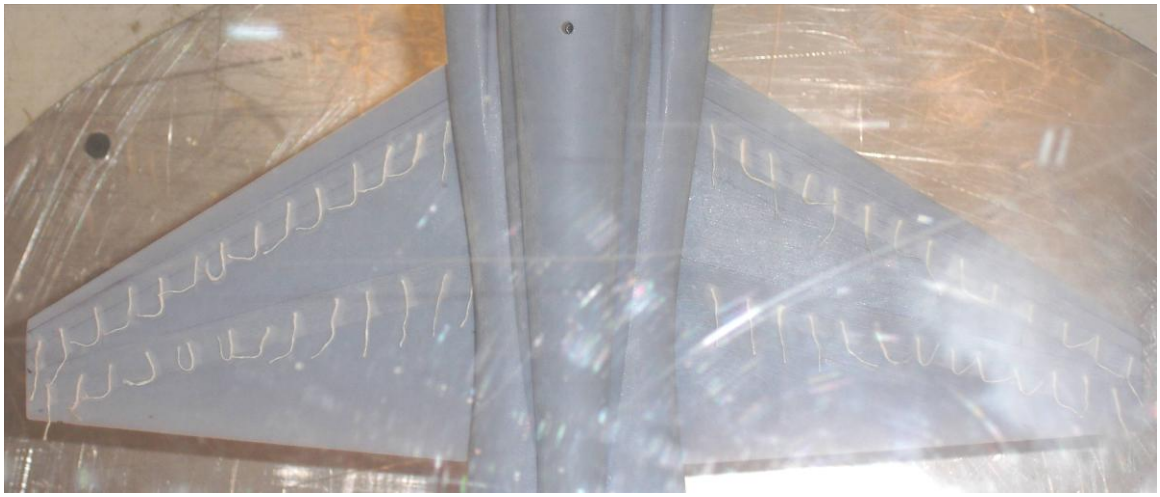

Figure 117. Clean Tufts 10 Degrees – Both Wings Top View (90 mph)

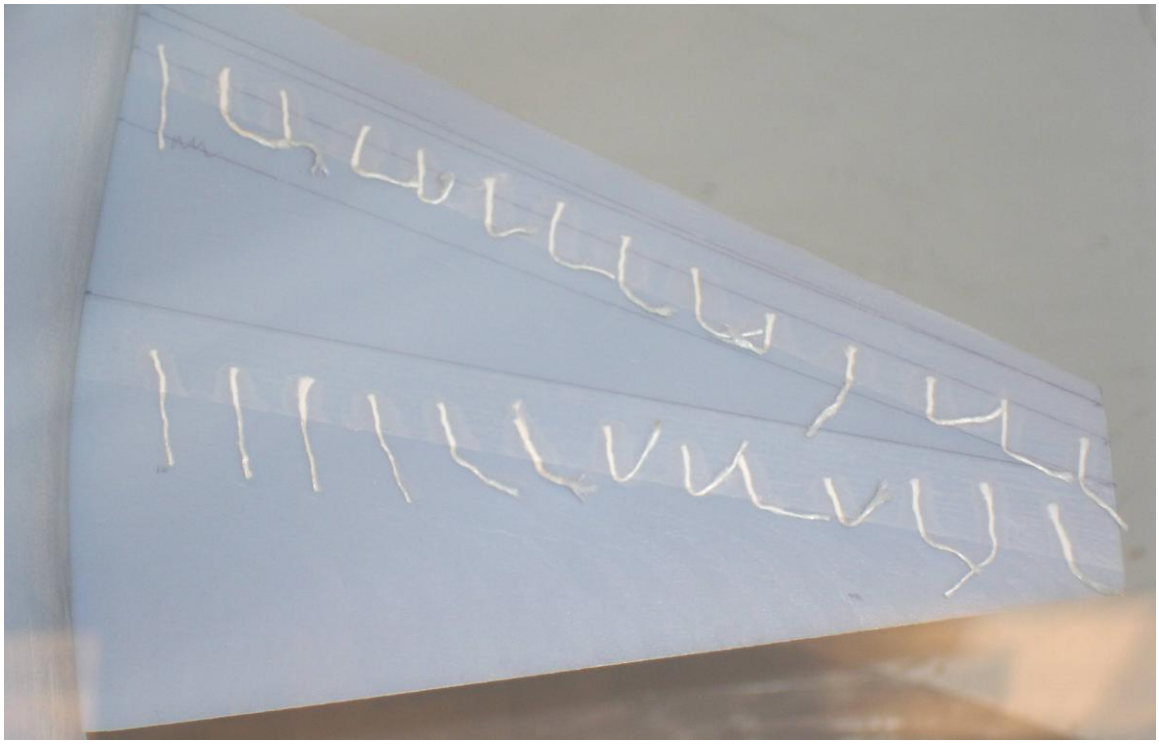

Figure 118. Clean Tufts 10 Degrees – Right Wing Top View (90 mph)

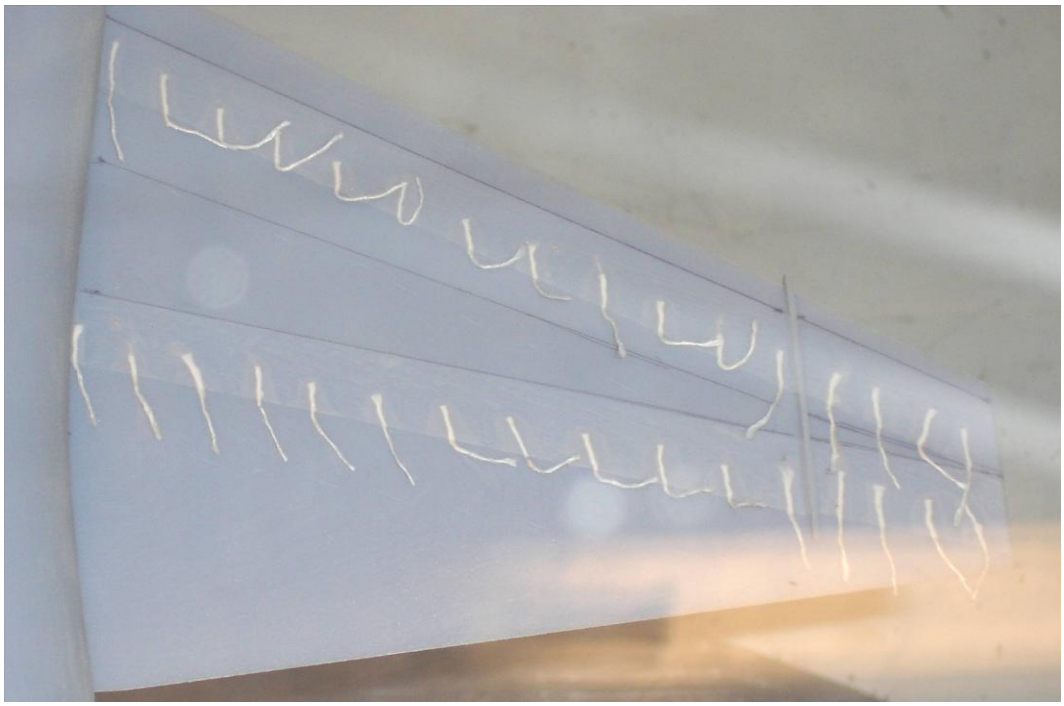

(a)

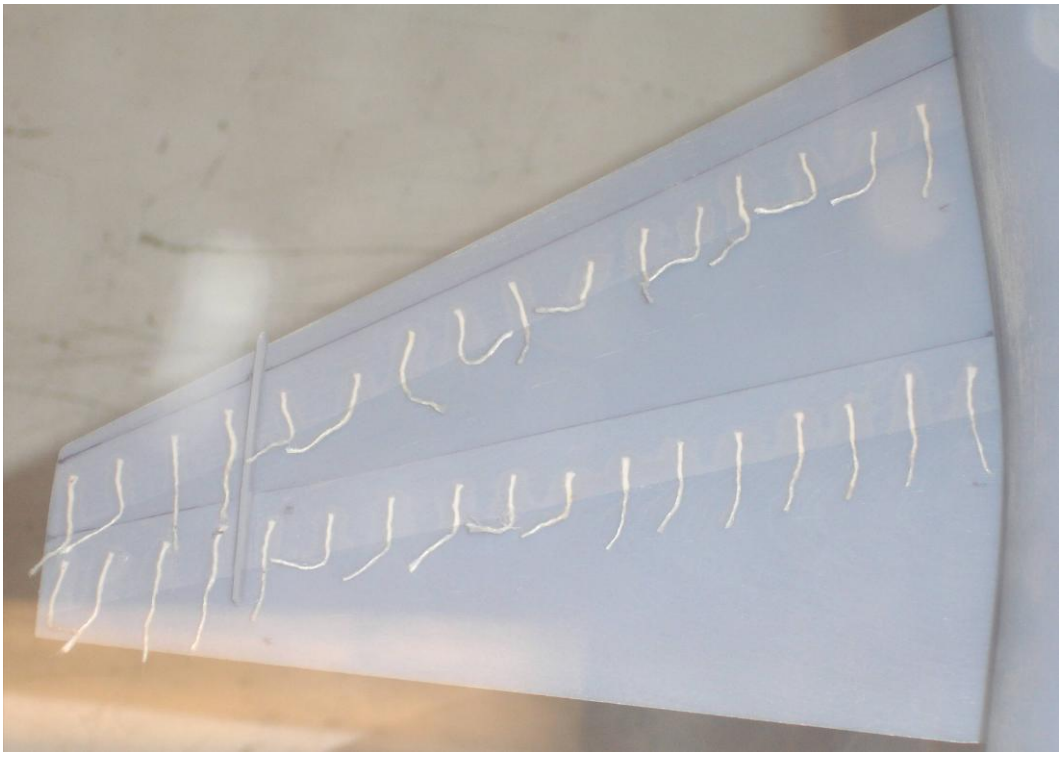

(b)

Figure 119. Fence 2 Tufts 10 Degrees –Wing Top View (90 mph)
(a) Right Wing (b) Left Wing

4.5.2.2 Clean versus Fence 2 – 15 Degrees AOA.

Here, the clean wing was almost entirely stalled. In the side view, the clean wing (Figure 120) showed significantly reversed flow in the entire second row. The first row was essentially the same but not as heavily reversed. In the case of fence 2 (Figure 121), the first and second rows were very similar to the clean wing except that just inboard and completely outboard of the fence was no longer detached. The fence had significantly altered the flow over the wing in its vicinity for the better.

Figure 120. Clean Tufts 15 Degrees – Right Wing Side View (90 mph)

(a)

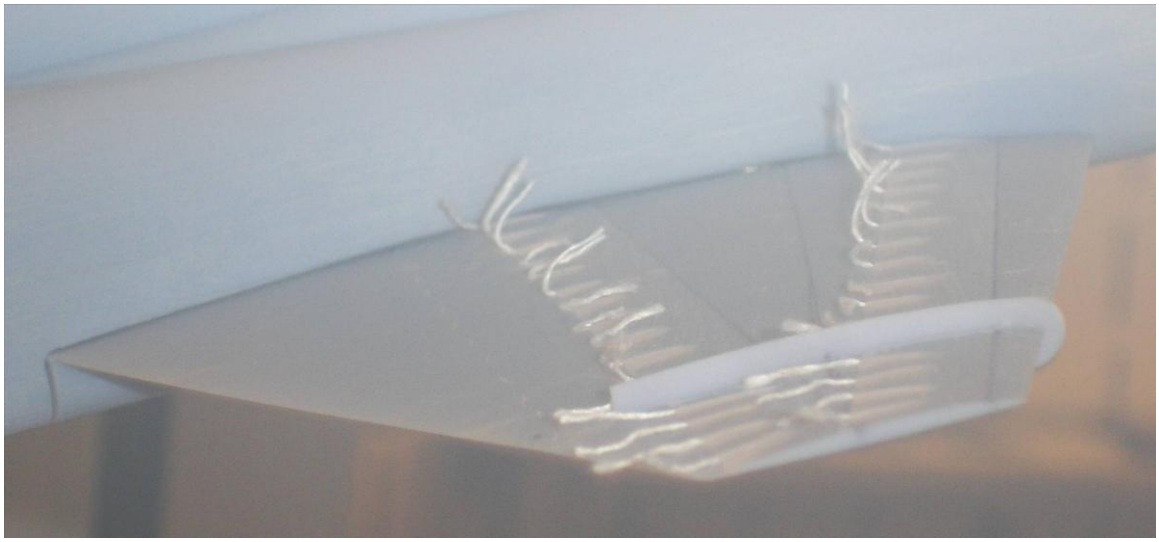

(b)

Figure 121. Fence 2 Tufts 15 Degrees – Right Wing Side View (90 mph)
(a) Forward Side View (b) Direct Side View

The top views shed further light on the results seen in the side view photographs. In the first row for the clean wing (Figure 122), significant spanwise flow existed for the entire semispan. In the second row for fence 2 (Figure 123), the spanwise flow of the outer five tufts in both rows was almost completely removed. The fence clearly had a significant impact on the flow both inboard and outboard of the fence, particularly in arresting spanwise flow as well as increasing the overall amount of attached flow on the wing.

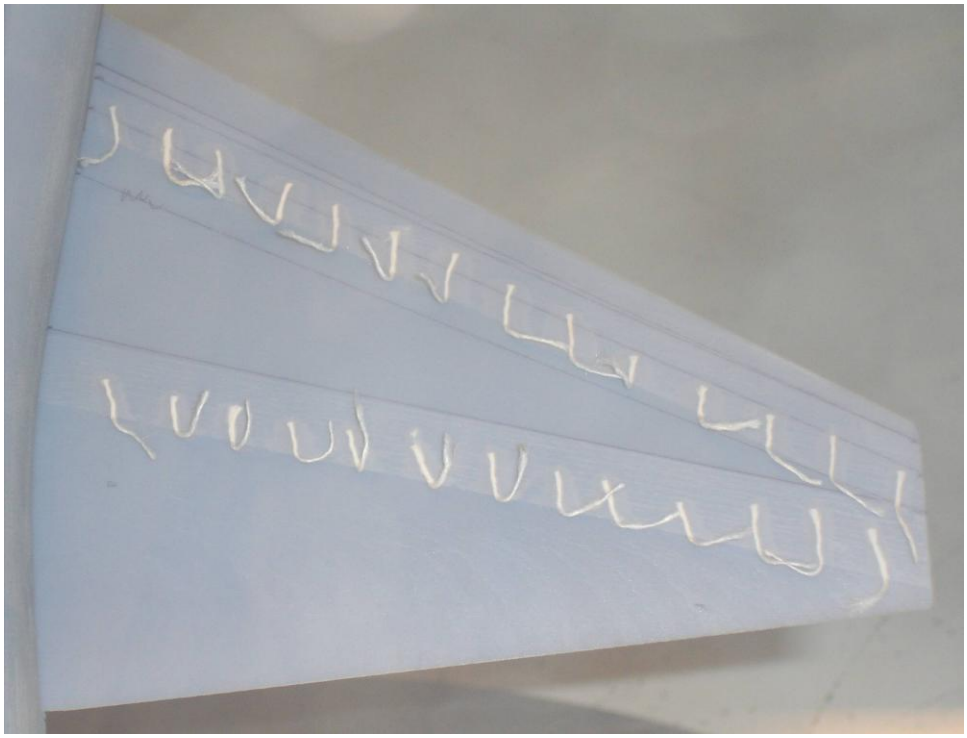

Figure 122. Clean Tufts 15 Degrees – Right Wing Top View (90 mph)

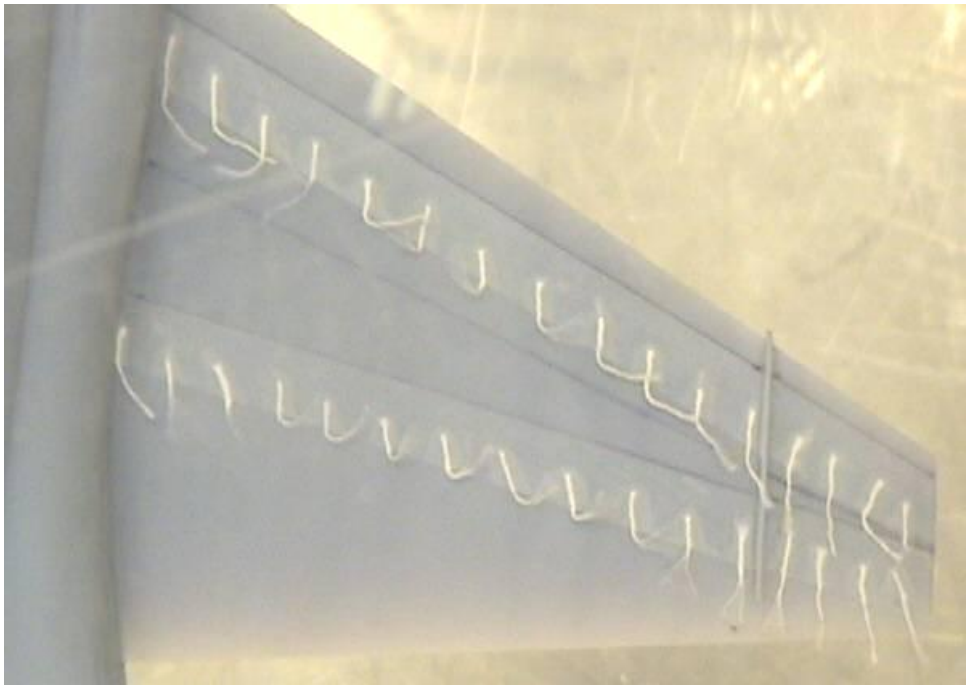

Figure 123. Fence 2 Tufts 15 Degrees – Right Wing Top View (90 mph)

4.5.3 Wind Tunnel and CFD Flow Visualization Compared

Utilizing Solfelt's CFD results and data, several flow visualizations were extracted for comparison to wind tunnel flow visualization. The work of Solfelt and Maple, Reference 24, was also used for Figure 124. Again, the CFD configurations included the flaps down at 100 percent. The Reynolds number associated with the CFD was 10 x 10^6, based on root chord, and 0.3 x 10^6, based on mean aerodynamic chord, for the wind tunnel. AOAs of interest here are 10 and 15 degrees. The velocity vectors in the *(a)* subparts of Figures 124 through 127 are two dimensional and came from cuts in the xz and yz planes, with the axes depicted in the lower left corner of each picture. Additionally, the plane of interest for these velocity vectors was coincident with the fence's location, 82.5 percent semispan. All figures depict the right wing. In all cases, the CFD and wind tunnel results correlated well with regards to the direction of surface flow.

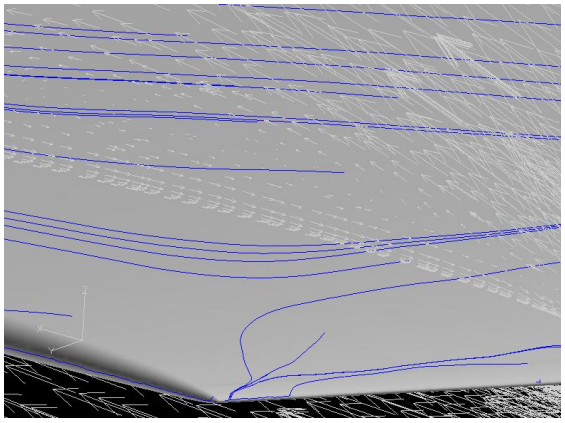

(a)

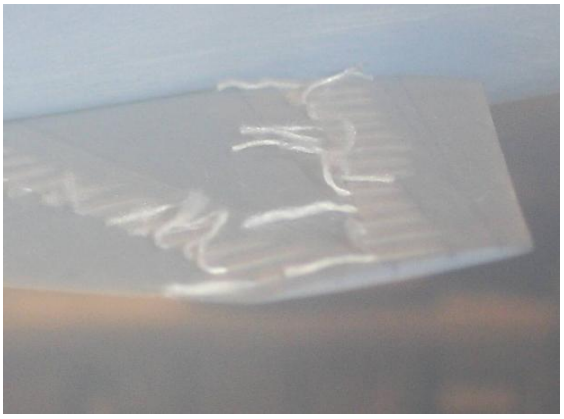

(b)

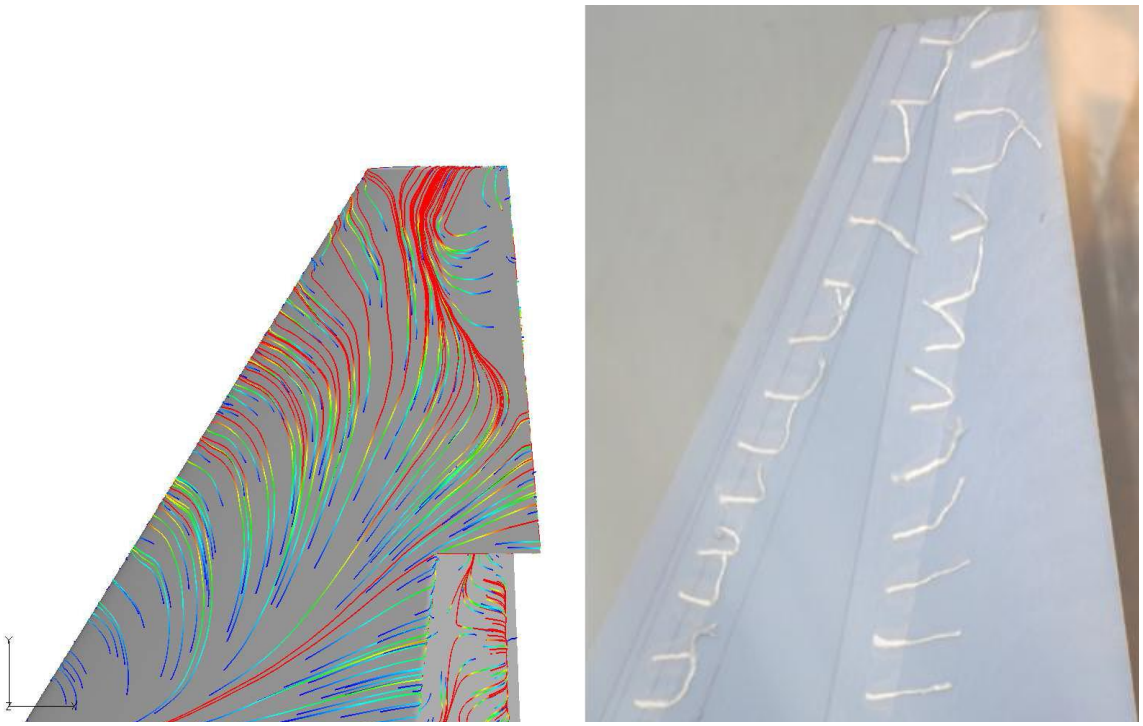

(c) (d)

Figure 124. Clean – 10 Degrees AOA – CFD and Wind Tunnel Tufts
(a) Extracted from Solfelt's Results (xz plane) (1) (b) Wind Tunnel Side View
(c) Solfelt/Maple (flow is blue to red) (24) (d) Wind Tunnel Top View

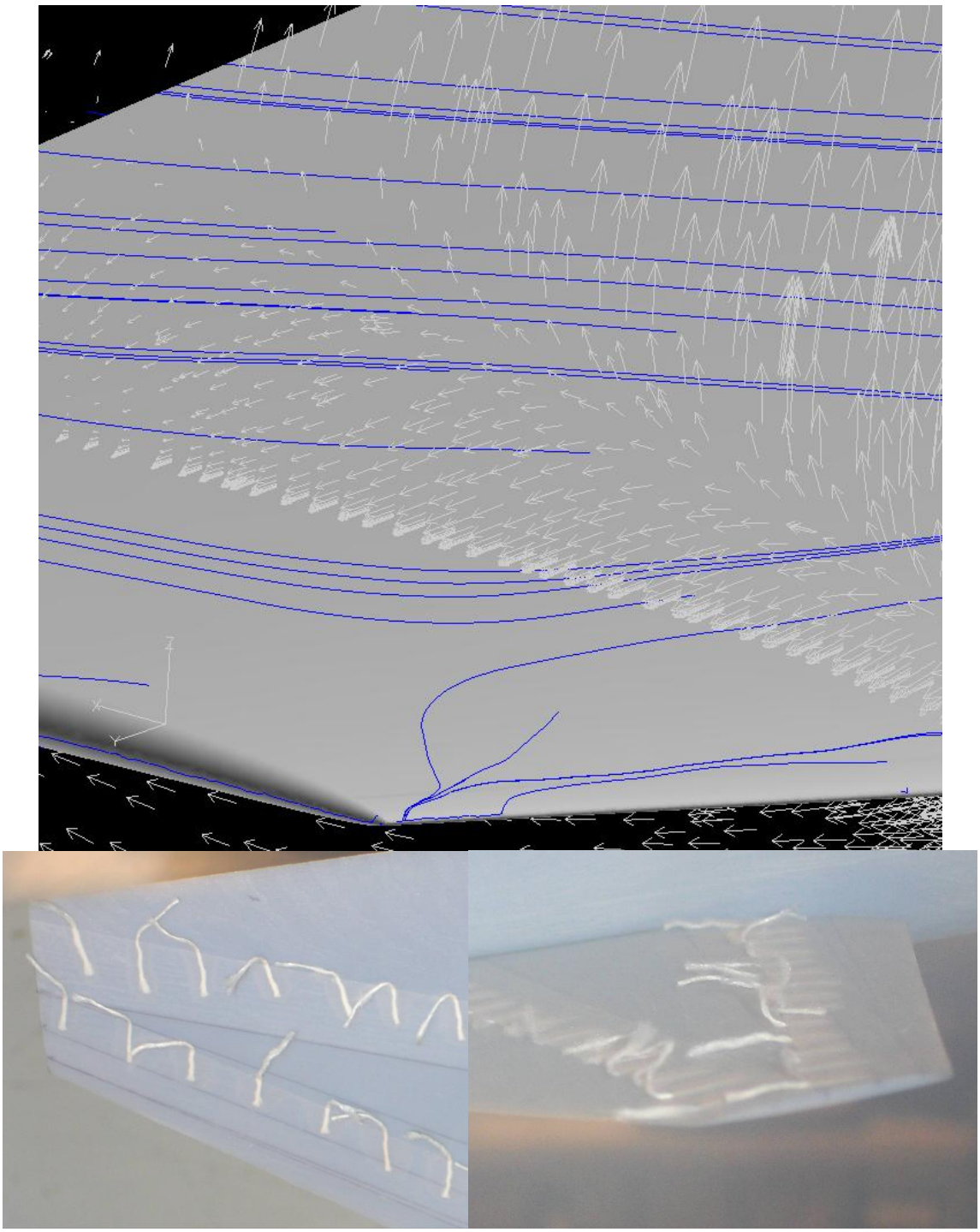

Figure 125. Clean – 10 Degrees AOA – CFD (yz plane) and Wind Tunnel Tufts

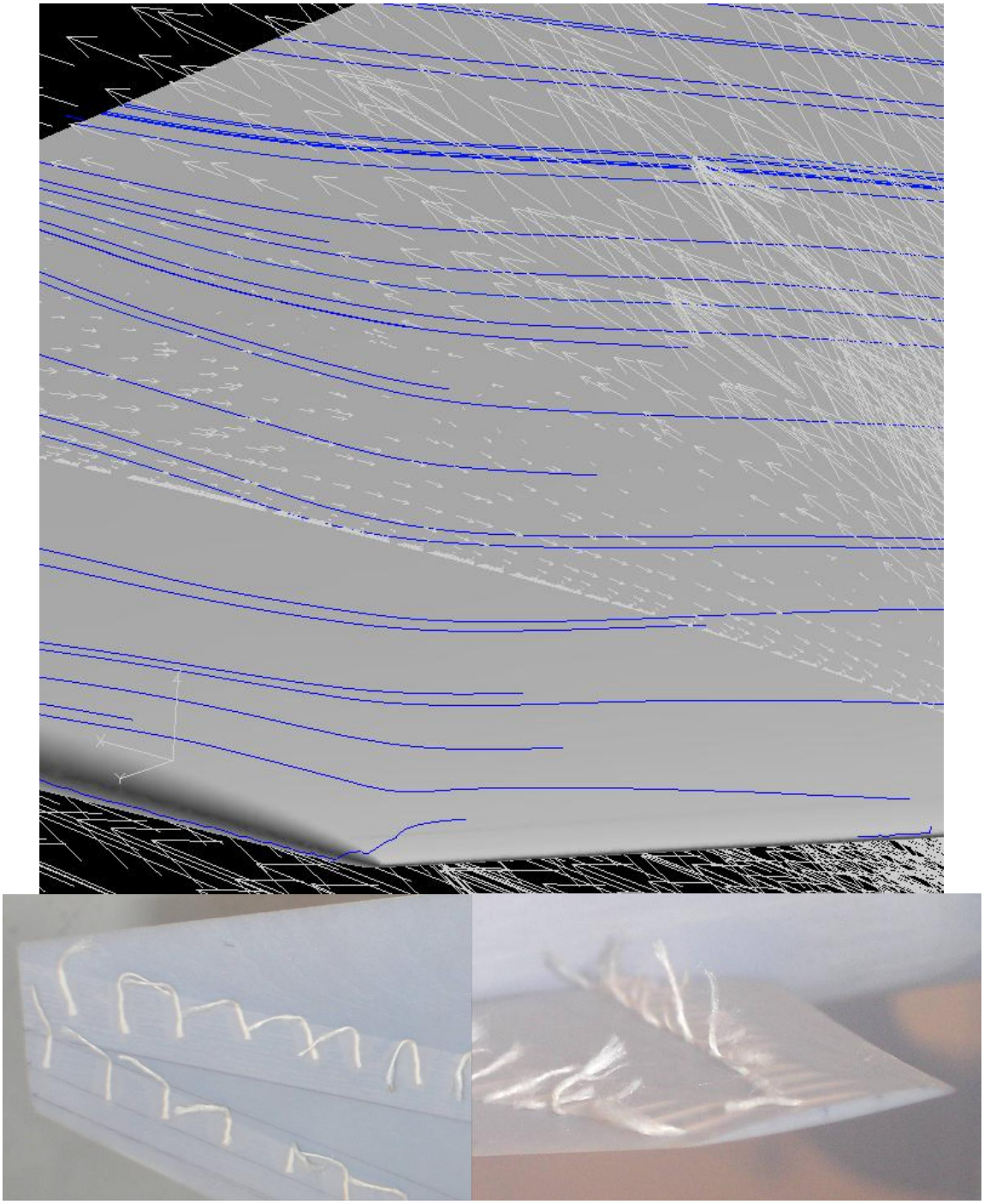

Figure 126. Clean – 15 Degrees AOA – CFD (xz plane) and Wind Tunnel Tufts

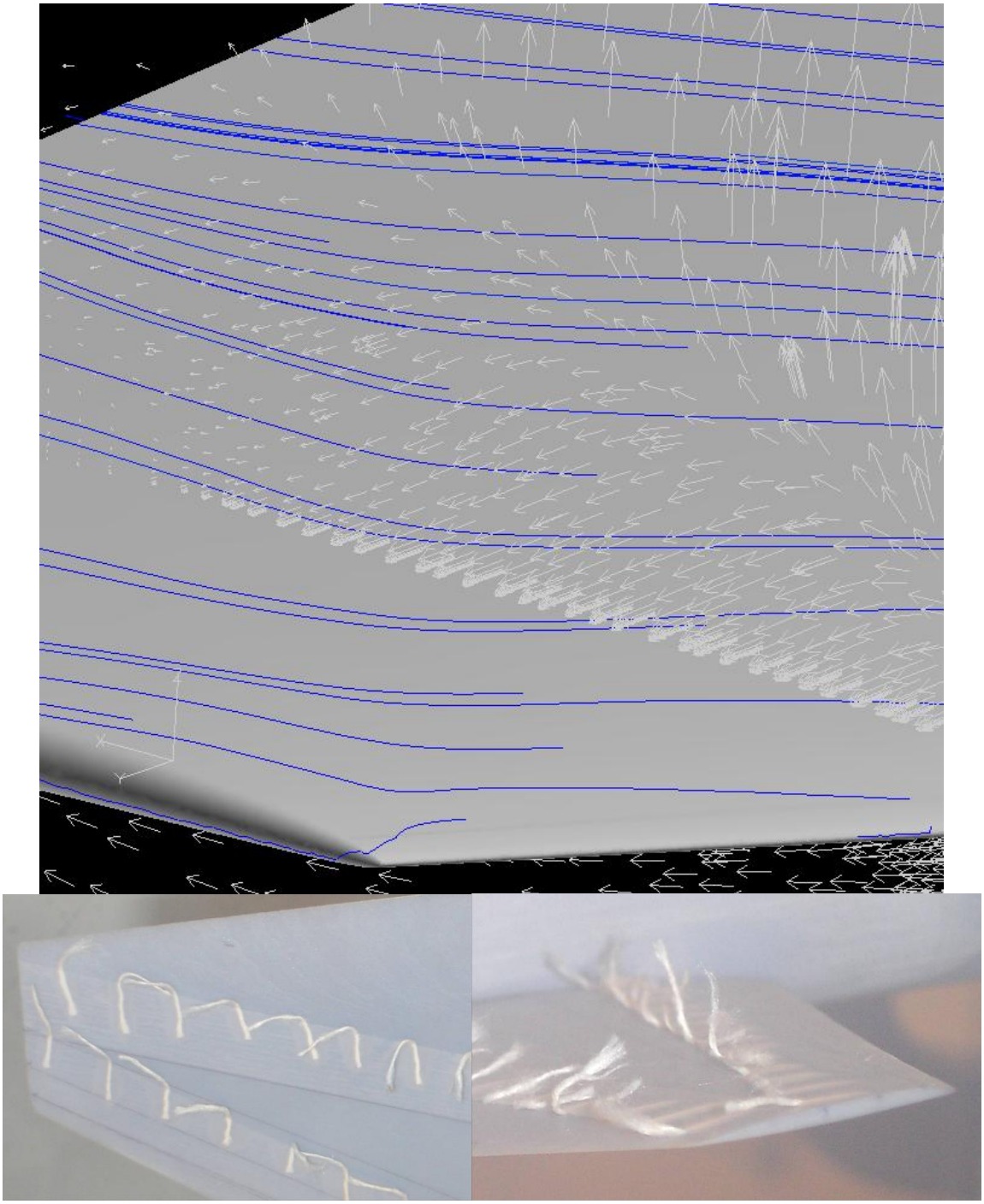

Figure 127. Clean – 15 Degrees AOA – CFD (yz plane) and Wind Tunnel Tufts

Lastly, Figure 128 compares CFD and wind tunnel flow visualization results with a wing fence installed. The CFD fence wrapped the leading edge and was nearly identical to fence 2 used in the wind tunnel. The colors on the CFD picture were

associated with specific values for pressure. Those specifics are not important here, but dark blue was the lowest pressure and green was the highest pressure. Figure 128 shows that the wind tunnel and CFD flow visualization results were very similar.

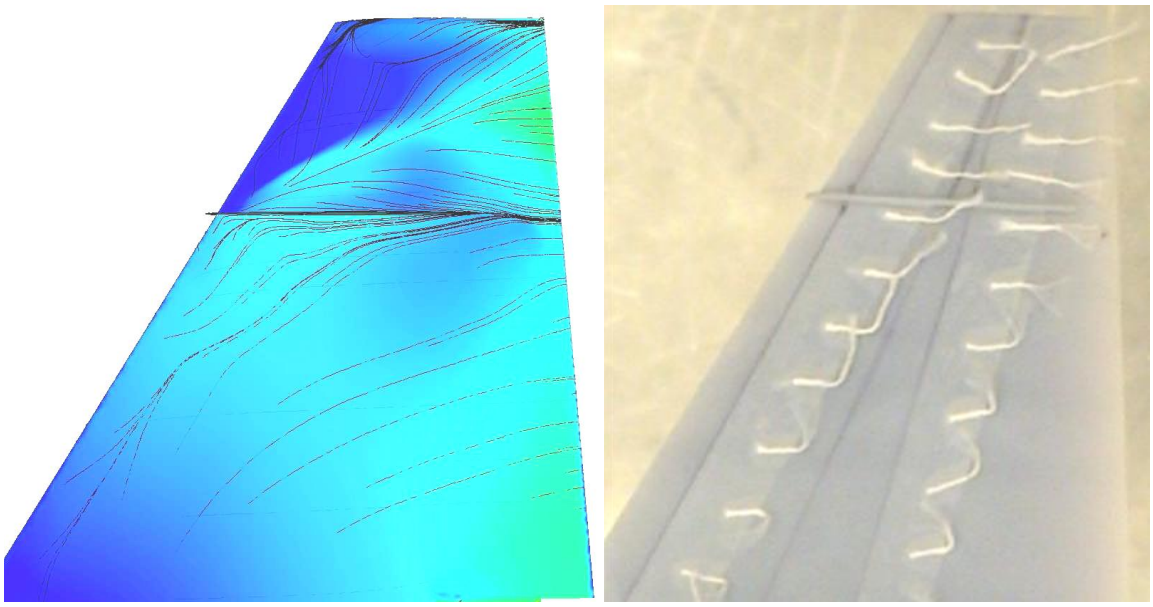

Figure 128. Fence – 15 Degrees AOA – CFD Oil Flow and Wind Tunnel Tufts (23)

4.6 Flight Test

4.6.1 Overview.

In this section, the flight test objectives, limitations, drag polar and lift curves, approach-to-stall characteristics, and flow visualization are covered (36). Again, these flight test results were the product of a five-member team as a part of the USAF TPS Class 08A test management project (TMP). The author of this thesis was the project manager for the TMP, and the separate report for the TMP is Reference 36. The aircraft without the fence installed is referred to as the baseline T-38, and the aircraft with the fence installed is referred to as modified T-38. Normalized AOA was primarily used for flight test discussions due to pilot familiarity with those numbers. True AOA has been put in parentheses next to normalized AOA numbers for ease of reference. Appendix J

includes a plot of normalized AOA versus true AOA as calibrated on the flight test aircraft and a plot of normalized AOA versus true AOA as is normal to production T-38 aircraft.

Ten flight test sorties, totaling 11.4 hours, were accomplished from 19 September to 10 October 2008 at Edwards AFB, California. The flight test techniques described in Chapter III were used. Table 13 shows the flight test sortie summary.

Table 13. Flight Test Sortie Summary

Date	Aircrew	Profile Flown	Flight Time
19-Sep	Dietrich, Wroten	Baseline Aircraft, AOA calibration	1.1
29-Sep	Williams, Schneider	Baseline Aircraft, standard profile	1.2
29-Sep	Dietrich, Wroten	Baseline Aircraft, standard profile	1.2
1-Oct	Williams, Tanner	Modified Aircraft, student checkout	1.0
2-Oct	Dietrich, Hsu	Modified Aircraft, student checkout	1.1
2-Oct	Dietrich, Schneider	Modified Aircraft, standard profile	1.1
6-Oct	Williams, Greco	Modified Aircraft, standard profile	1.1
6-Oct	Williams, Schneider	Modified Aircraft, standard profile	1.3
8-Oct	Dietrich, Greco	Modified Aircraft with tufts installed, photo sortie	1.2
10-Oct	Williams, Wroten	Baseline Aircraft with tufts installed, photo sortie	1.1

- AOA Calibration: This was flown in formation with a production T-38 to calibrate the cockpit AOA and data acquisition system (DAS) AOA versus normalized AOA.
- Standard Profile: This alternated between sawtooth climb and descents between 0.3 - 0.95 normalized AOA (5 degrees to 14.5 degrees) followed by two level decelerations, and ended with approach to stall stick-fixed and stick-controlled flight test techniques.
- Student Checkout: This profile was flown to checkout student pilots to fly the wing fence modified aircraft. This profile included open loop flying qualities, closed loop

handling qualities in the approach configuration, stalls, and landings. Table 5 depicts the first flight profiles.

4.6.2 Flight Test Objectives.

As a reminder the flight test objectives were:

Objective 1 – Compare the lift curve and drag polar of the baseline T-38 to those of the modified T-38 above 0.3 normalized angle of attack.

Objective 2 – Compare the approach-to-stall characteristics of the baseline T-38 to those of the modified T-38.

Objective 3 – Compare the upper wing surface flow characteristics of the baseline T-38 to the modified T-38 through inflight photography.

Objectives two and three were met. Some limitations were experienced as a result of data quality for objective one.

4.6.3 Flight Test Limitations.

Instrumentation calibration and accuracy issues limited the test team's ability to draw conclusions regarding the lift curve and drag polar of the baseline and modified aircraft for objective one. A more detailed discussion regarding these limitations may be found in Appendix L. Objectives two and three were not affected by these limitations.

4.6.4 Flight Test Lift Curve and Drag Polar.

The following analysis was accomplished despite the limitations previously discussed. The test methodology and descriptions of flight test techniques may be found in Chapter III. Sawtooth climbs and descents along with level decelerations were flown to determine the lift curve and drag polar of the baseline and modified aircraft. Level decelerations started at 18,000 feet pressure altitude (PA) and 0.64 Mach number and

were terminated prior to reaching 1.1 normalized AOA, or about 16.5 degrees AOA. Sawtooth climbs and descents were flown at AOAs ranging from 5 to 13.5 degrees.

The data reduction for lift coefficient, C_L, and drag coefficient, C_D, was accomplished in Microsoft® Office Excel 2007. Lift and drag coefficients were calculated using data from these maneuvers and the data reduction procedures outlined in section 3.7.5. The thrust deck used was provided by the 445th Flight Test Squadron at Edwards AFB, CA and is described in References 36 and 32.

Initial analyses revealed large scatter in lift and drag coefficients. A large portion of this scatter was due to noise in the AOA sensor as well as noise in the normal and longitudinal acceleration sensors. After examination of the noise, it was assessed to be essentially random or white and was commonly about ±1.2 degrees in just 0.1 seconds. As a result, a 0.2 second moving average filter was used to reduce data scatter from the AOA sensor, the normal accelerometer, and longitudinal accelerometer. The time of 0.2 seconds was chosen to reduce unrealistic changes in flight parameters and filter the small AOA oscillations observed in the 10 Hertz range.

Problems were noted with the accelerometer data. Ground block data recorded an average normal acceleration of 0.94. This was equivalent to the accelerometer being tilted 20 degrees relative to the horizon. The cause of this anomaly was unknown. To correct for this error, 6 percent was added to all normal acceleration data.

Also, ground block data indicated the average longitudinal acceleration was 0.04. At the time of data reduction, the assumption was that the longitudinal acceleration should have been zero based on a zero degree pitch attitude of the aircraft on the ramp. Therefore, the test team subtracted 0.04 from all longitudinal acceleration data. Upon further analysis, it was determined that the aircraft should have had approximately a one

degree nose up attitude on the ground, resulting in a longitudinal acceleration of 0.0175. Instead of 0.04, 0.0225 should have been subtracted from all longitudinal acceleration data. The effect of this discrepancy was considered minimal.

The corrections described above shifted the lift curve and drag polar. This shift more closely aligned the flight test lift curve and drag polar to models based on historical data. Again, the direct comparison to wind tunnel data is complicated since the model did not have a tail.

4.6.4.1 Lift Curve Validation.

Lift coefficient data from baseline aircraft sorties were plotted alongside the historical Air Force Flight Test Center (AFFTC) T-38 lift curve model to validate the data reduction process. It was noticed that a correction, possibly due to upwash and/or AOA calibration, was needed to align lift coefficient data with the model. It was not possible to calculate an upwash correction and/or AOA calibration error (Appendix I). To correct for the differences between the flight test data and AFFTC historical model, a positive bias of 1.8 degrees was selected. This bias more closely aligned the flight test data and historical data at lower AOA where the test team had the most confidence in their data. The bias was added to flight test AOA data immediately after the pitch rate correction prior to the calculation of lift and drag (Appendix J).

Figure 129 shows the AFFTC model along with data from two level decelerations, two sawtooth climbs, and two sawtooth descents after the additions of the moving average filter, the accelerometer correction, and the 1.8 degree bias. At lift coefficients below 0.4, baseline AOA was within about ±0.3 degrees of the historical model. At higher lift coefficients, baseline AOA was higher than predicted. At 0.7 lift coefficient as depicted in Figure 129, average baseline AOA was approximately 0.6

degrees higher than the historical model. All subsequent data included the 1.8 degree bias and the moving average filter for AOA and accelerometer data outputs. The colors on this plot (Figure 129) only delineate between the maneuvers used to collect the data in that region of the curve. The blue and black were based on level decelerations. All of the other colors were based on sawtooth climbs and descents at various angles of attack.

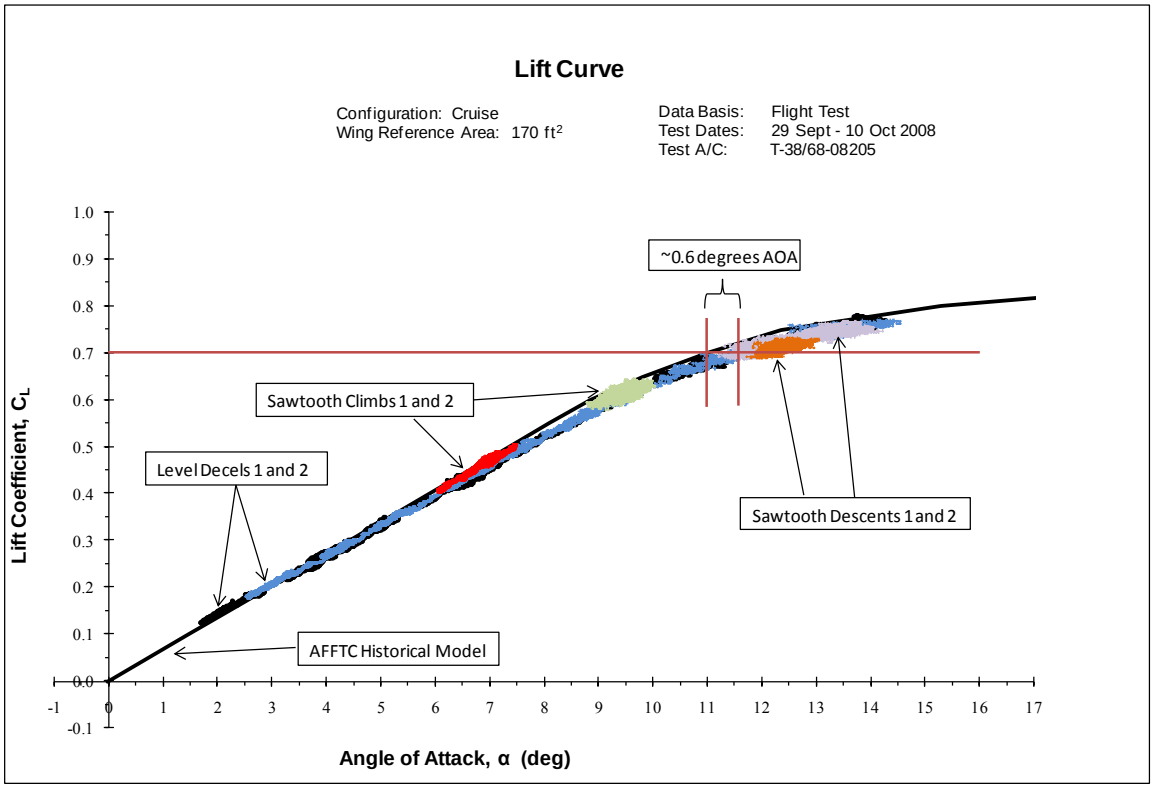

Figure 129. Baseline Aircraft Lift Curve Validation

Data from the sawtooth climbs and descents overlaid the level decelerations with similar values, slopes, and scatter as depicted in Figure 129. Scatter for each maneuver was approximately 0.01 lift coefficient (2.5 percent scatter) from 2 to 9 degrees AOA. Above 9 degrees AOA, the scatter was roughly 0.04 lift coefficient (5.7 percent scatter). Additionally, there was about a 7 percent reduction in lift curve slope.

4.6.4.2 Lift Curve Comparison.

To compare lift coefficients of the baseline and modified aircraft, level deceleration data of both baseline and modified aircraft were plotted together. Lift coefficient data of four baseline level decelerations and six modified level decelerations are shown in Appendix M. For the 10 maneuvers plotted in there, total data scatter at 0.72 lift coefficient was 2 degrees AOA. Based on this plot alone and due to this data scatter, there was no discernable difference in lift coefficient data of the modified versus baseline aircraft. Therefore, further analysis was necessary.

An expanded plot covering the range from 12 to 16 degrees AOA is shown in Figure 130 with the data sub-sampled down to 5 Hertz for ease of viewing. Data from four baseline and four modified aircraft level decelerations are shown. The subdued lines bound the data scatter. For instance, at 0.72 lift coefficient, AOA varied from approximately 12.5 degrees to 14 degrees. In addition to the data scatter, the data had a bias of approximately 2.5 degrees relative to the historical model. Although this portion of the lift curve was nonlinear, linearity was assumed for this small region of interest. This assumption was based on the shape of the historical model above 13.5 degrees AOA. Linear trend lines were fitted to the data using Excel and are displayed in Figure 130 as solid and dotted lines. The four modified aircraft trend lines lay above three of the four baseline trend lines. The exception was a baseline trend line for a data set that ended at 13.5 degrees AOA. Again, based on graphical evidence alone, it was difficult to conclude the effects of the wing fence on the lift curve.

In order to quantify this, 95 percent confidence intervals were calculated based on the sub-sampled (5 Hertz) data used to plot Figure 130. The same technique described in section 3.5.2.1 was used to accomplish this. Specifically, two areas were evaluated, 13.4

to 13.6 degrees and 14.4 to 14.6 degrees. In the range of 13.4 to 13.6 degrees AOA, the average AOA was 13.5 degrees with an average C_L of 0.719 ± 0.005 for the baseline aircraft and an average C_L of 0.728 ± 0.013 for the modified aircraft. In the range of 14.4 to 14.6 degrees AOA, the average AOA was 14.5 degrees with an average C_L of 0.735 ± 0.011 for the baseline aircraft and an average C_L of 0.749 ± 0.005 for the modified aircraft. In both cases, the 95 percent confidence intervals overlapped and prevented the conclusion that the wing fence made a difference in the lift curve.

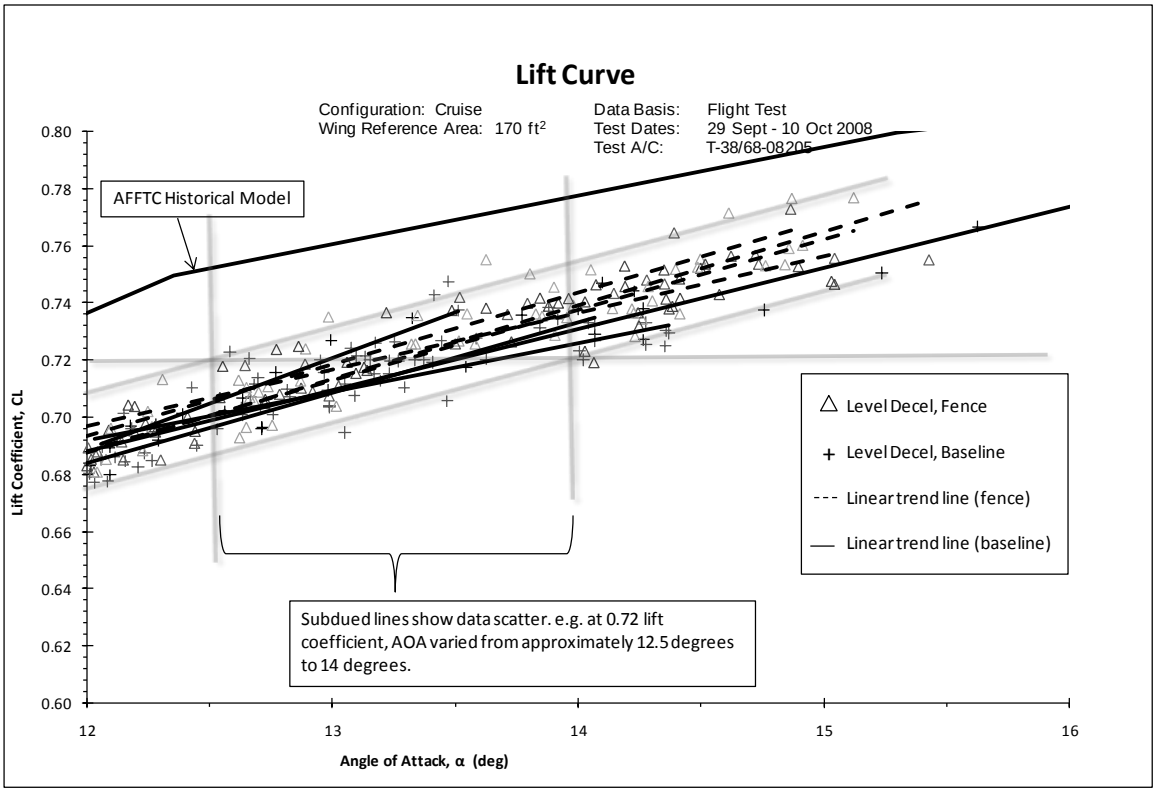

Figure 130. Expanded Baseline versus Modified Aircraft Lift Curve

Lastly, a general linear regression was run on the data using STATISTICA. Data included lift coefficients from all maneuvers in the 13.5 to 16 degrees AOA range. The same linear assumption was applied as discussed in the previous paragraph. Data were sub-sampled down to 5 Hertz in order to remove correlation caused by two sources. The first source would be the moving average filter, and the second would be AOA vane and

aircraft limits. In theory it would be impossible for the aircraft to produce an error off the regression line significantly different than the previous one over the course of approximately 1 millisecond. Independence in the residuals was verified graphically. The regression included lift coefficient as a dependent variable, the modification as a categorical variable, maneuver type as a categorical variable, and AOA as a continuous variable.

Analysis Of Variance (ANOVA) results revealed that the maneuver type variable was not significant (i.e. different types of maneuvers did not have different effects on lift coefficient) and was removed from the model. AOA was obviously significant since it had a direct correlation to lift coefficient. The wing fence modification was significant at the 95 percent confidence level. The word "significant" here means that, under the assumptions of the general linear regression model, the wing fence had an effect on the average lift coefficient at a particular AOA. Thus, while the scatter in the baseline and modified wing data did overlap, the wing fence data displayed an average lift coefficient that was statistically higher than the baseline data. This was evidenced graphically in Figure 130, where trend lines of the modified aircraft fell above trend lines of the baseline aircraft. The effect of the wing fence modification was estimated by the model to be a 1.8 percent increase in the lift coefficient, approximately 0.012 incremental lift coefficient, at 13.5 degrees AOA. The specific values were a C_L of 0.718 ± 0.002 for the clean aircraft and 0.730 ± 0.002 for the modified aircraft.

The regression was re-run with only sawtooth climb and descent data. Once again, the wing fence modification was found to be statistically significant. The estimated effect of the modification was a 3.8 percent increase in the lift coefficient, approximately 0.029 incremental lift coefficient, at 13.5 degrees AOA. The specific

values were a C_L of 0.711 ± 0.01 for the clean aircraft and 0.737 ± 0.01 for the modified aircraft. However, these data included only one sawtooth maneuver with the modified aircraft because only one was flown in the AOA range above 13.5 degrees.

While the general linear regression took into account data scatter (such that confidence increased with an increase in sample size), it did not take into account the relatively few numbers of maneuvers. Indeed, the high sample size was due to the high sample rate of the DAS, although it was not so high as to cause correlation in the residuals. The regression also did not take into account the lack of an upwash correction for AOA and the low confidence in the DAS parameters of AOA, pitch rate, and normal and longitudinal acceleration.

While statistical analysis pointed to a small increase in lift coefficient (1.8 to 3.8 percent) with the wing fence, it was difficult to verify this graphically. Graphical evidence did not discount the possibility of an increase, but the data scatter was wider than the estimated increase. For example, at 13.5 degrees AOA, there was a 6 percent difference in C_L between two baseline data points. Therefore, it was inconclusive whether the fence caused an increase in lift coefficient or not.

An additional way the sub-sampled data set, seen in Figure 130, was analyzed is shown in Figure 131. All of the data in each 0.5 degree group (12-12.5, 12.5-13, 13-13.5, 13.4-14, 14-14.5 degrees) was averaged to create one data point of AOA and C_L for that group. This was accomplished for both the baseline (clean) and modified (fence) configurations. The error bars are 95 percent confidence intervals for each separate data set. The average lift coefficient was increased by the fence over the clean configuration in each group. However, because the confidence intervals overlap in all cases, except 14-14.5 degrees, this increase cannot be reported with 95 percent confidence.

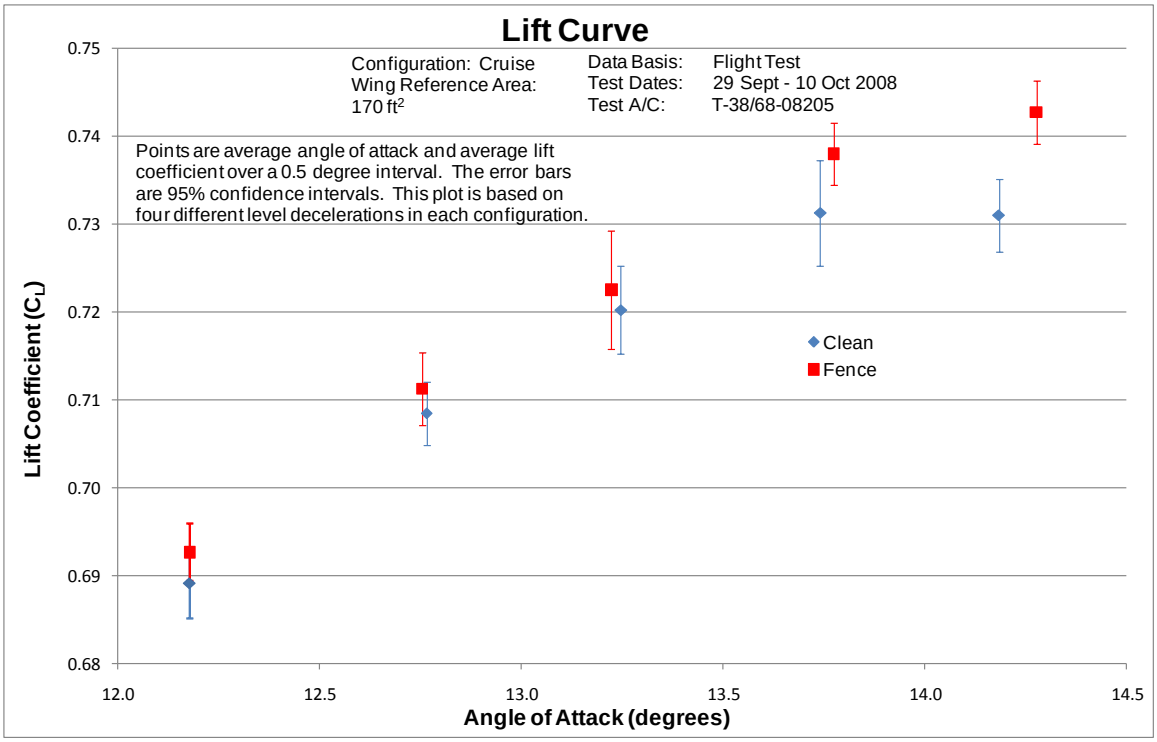

Figure 131. Expanded Baseline versus Modified Aircraft Lift Curve (Binned Data)

An important point, when considering these results as compared to the wind-tunnel results, is the absence of the wind-tunnel model's tail. The reference area for the T-38's tail is 59 square feet and 170 square feet for the wing. A simple area analysis, ignoring fuselage contribution, shows that the wind-tunnel results (fence's impact on overall lift coefficient) could be as much as 25 percent greater than flight-test results. Assuming that the fence's impact on lift coefficient was the same in the wind tunnel and flight test, its contribution would be a lower percentage of the overall lift coefficient.

4.6.4.3 Drag Polar Validation.

Drag coefficient data from baseline aircraft sorties were plotted alongside the historical AFFTC T-38 drag polar model to validate the data reduction process. The corrections used for lift coefficient data reduction, moving average filter, accelerometer correction, and 1.8 degree bias in AOA, were also applied to drag coefficient data

reduction. Figure 132 shows data from two level decelerations, two sawtooth climbs, and two sawtooth descents, along with the AFFTC T-38 drag polar model. Baseline drag polar data followed the historical drag polar model to within about ±0.0060 drag coefficient (or 60 drag counts) below a lift coefficient of 0.35. The flight test results were greater than the model predicted drag coefficient at higher lift coefficients. For instance, at 0.7 lift coefficient, as depicted in Figure 132, the average drag coefficient, based on a level deceleration, was approximately 0.1750, while the model predicted 0.1500. It was unknown why this 17 percent difference existed. The colors in Figure 132 again represent the different maneuvers used to collect the data.

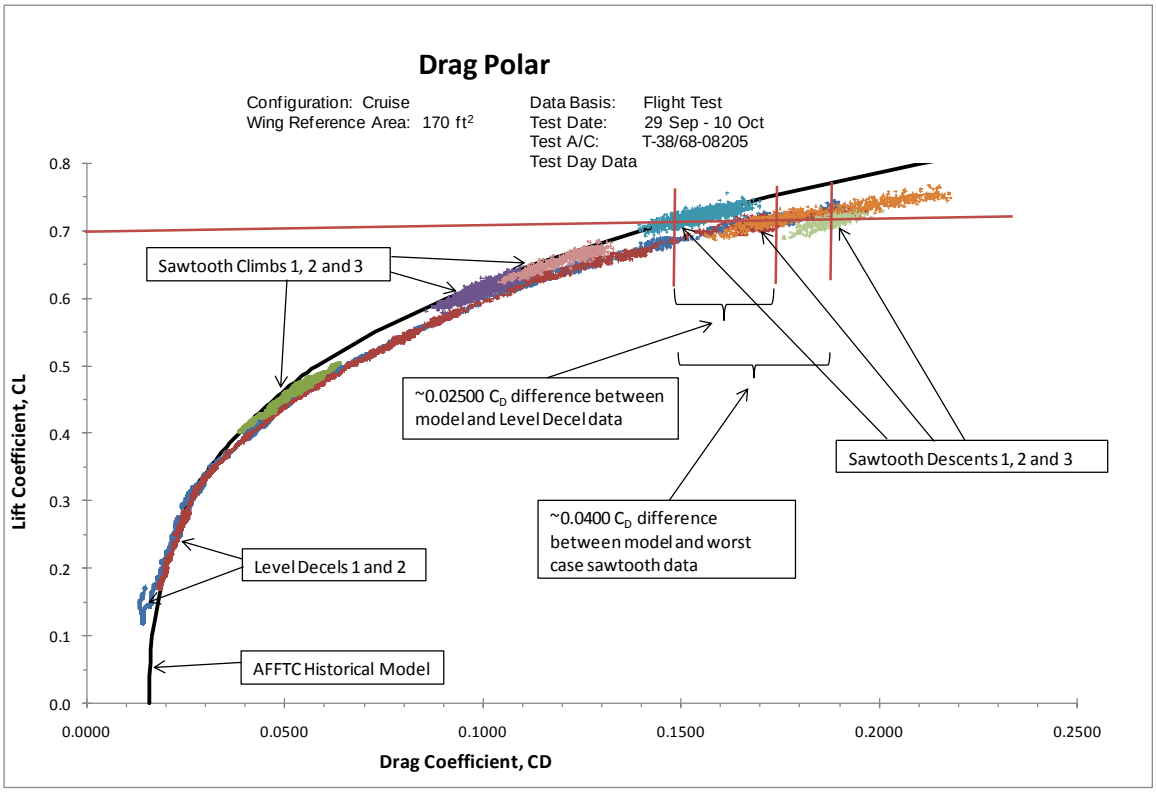

Figure 132. Baseline Aircraft Drag Polar Validation

4.6.4.4 Drag Polar Comparison.

Level deceleration data were plotted to compare the drag polar of the baseline and modified aircraft. Lift and drag coefficient data of four baseline level decelerations and

six modified aircraft level decelerations are shown in Appendix M. Similar to the lift curve comparison plot, there was no discernable difference in the drag polar of modified versus baseline aircraft in this plot. At 0.72 lift coefficient, the data scatter was about 350 drag counts, or ±8.9 percent.

An expanded plot covering the range above 0.7 lift coefficient is shown in Figure 133, with the data sub-sampled down to 5 Hertz for ease of viewing. Data from three baseline and four modified aircraft level decelerations are shown. The subdued lines bound the data scatter. For instance, at 0.74 lift coefficient, drag coefficient varied from approximately 0.1800 to 0.2060. Although this portion of the drag polar was nonlinear, linearity was assumed for this small region of interest. Linear trend lines were fitted to the data using Excel and are displayed in the figure as solid and dotted lines. Unlike the expanded lift curve plot, the trend lines were interspersed, and there was no graphical evidence of a difference in drag polar. Therefore, a statistical analysis was not accomplished for the drag polar. There was no discernable difference in drag polar for the modified versus baseline aircraft.

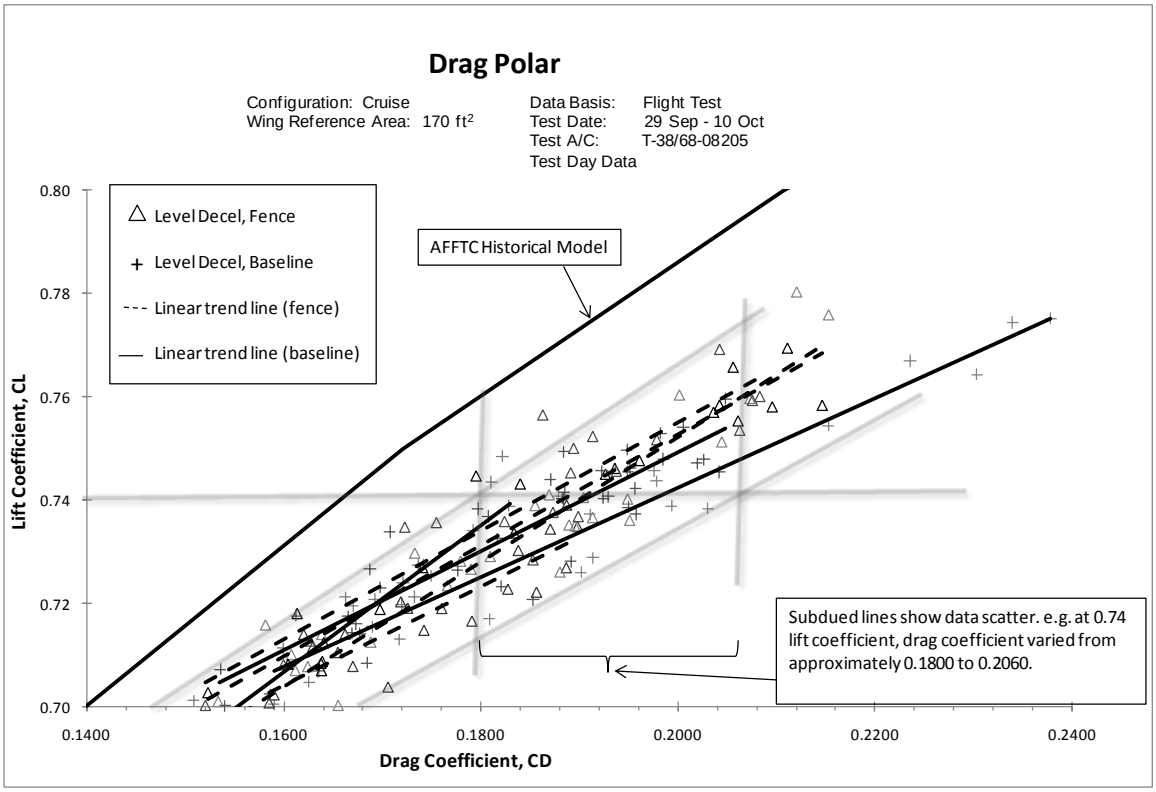

Figure 133. Expanded Baseline versus Modified Aircraft Drag Polar

4.6.5 Flight Test Approach-to-Stall Characteristics.

The approach-to-stall characteristics were investigated qualitatively through pilot observations and comments and quantitatively through simple measurements of AOA, lateral stick position, and bank angle. The approach-to-stall characteristics of each configuration were evaluated through two separate techniques. In the first method, the pilot attempted to maintain the control stick centered laterally (stick-fixed) while stabilizing at successively higher AOA. The second method allowed the pilot to attempt to maintain a wings level attitude at successively higher AOA using ailerons only (stick-controlled). Pilot comments about controllability, buffet onset and intensity, uncommanded rolls, and stick deflection were noted. The DAS recorded AOA, lateral stick deflection, and bank angle.

In the baseline and wing fence, modified aircraft, the approach to stall was characterized by moderate buffet, wing rock (observed high frequency oscillation), and bank angle oscillations (observed low frequency oscillations). Full page figures that show the DAS acquired data are in Appendix M. This section includes figures of one baseline and one modified sortie with both stick-fixed and stick-controlled scenarios.

The stick-fixed, clean configuration (Figure 134) showed bank angle oscillations of up to ±11 degrees with a period of approximately 25 seconds. Wing rock overlaid the bank angle oscillations and was characterized by quick, shallow, alternating wing dips with a period of approximately 2 seconds. The wing rock magnitude was as much as ±9 degrees. The aircraft started the approach to stall wings level but then rolled left to about 20 degrees of bank, where the bank angle oscillations and wing rock were then centered around. This occurred even though there was 3 degrees of right stick deflection during the left roll-off.

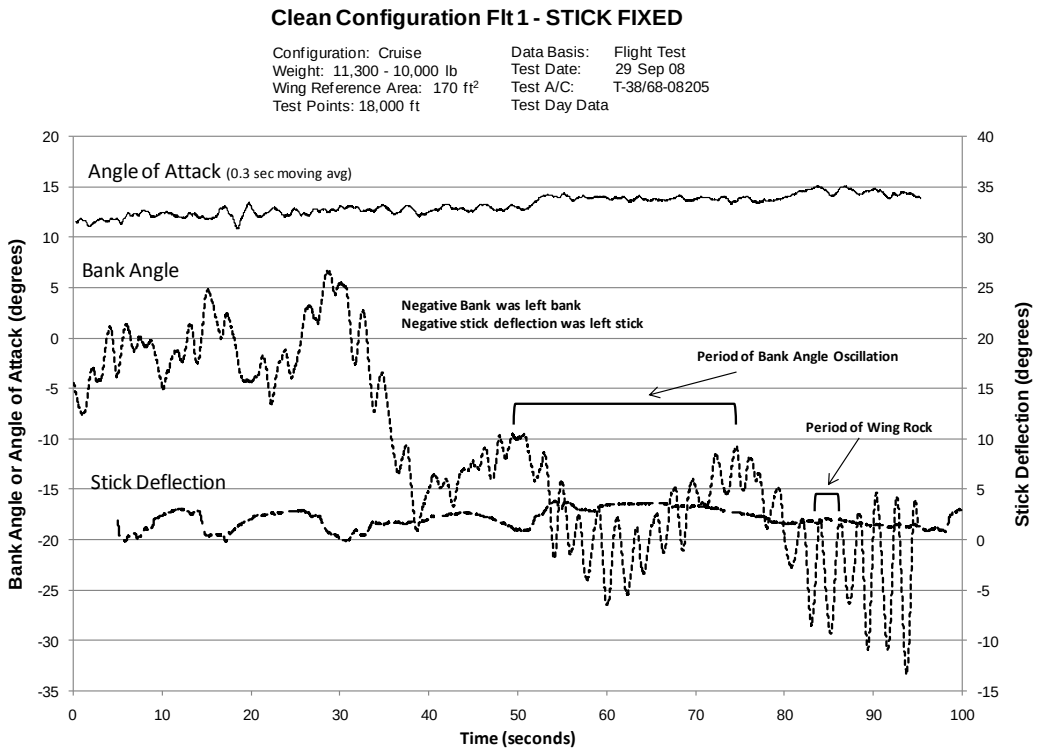

Figure 134. Baseline Stick-Fixed Approach to Stall, Flight 1

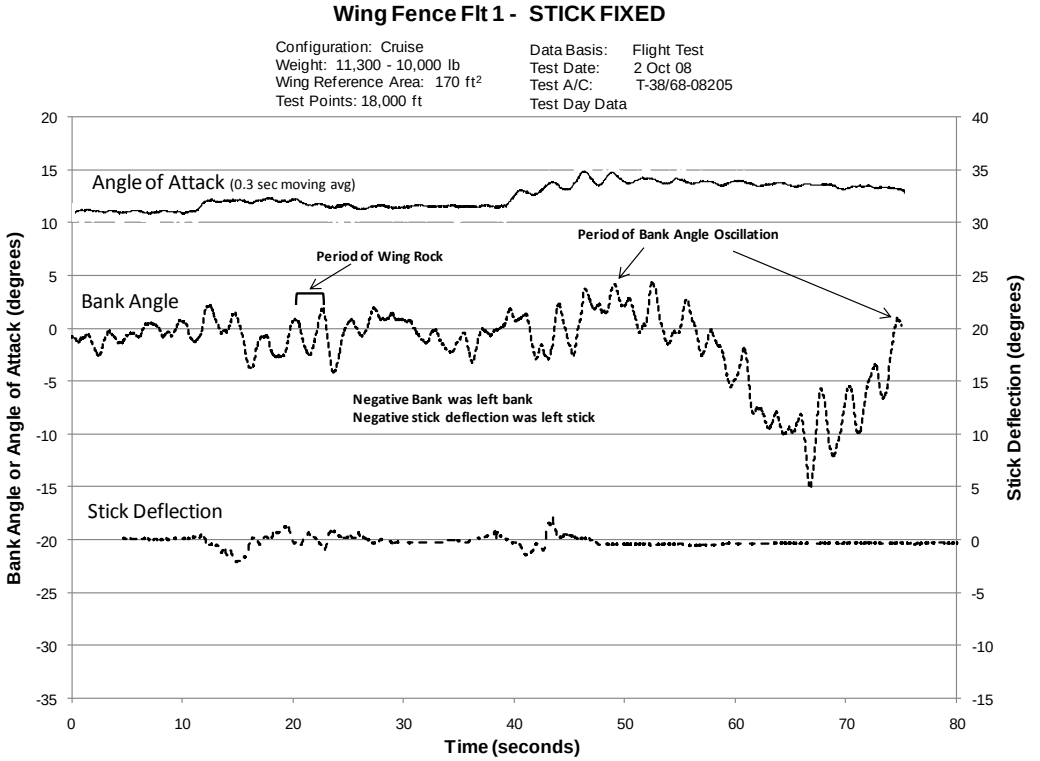

Figure 135. Wing Fence Stick-Fixed Approach to Stall, Flight 1

The stick-fixed, modified configuration (Figure 135) showed bank angle oscillations of up to ±8 degrees with a period of approximately 20 seconds. Wing rock had a period of approximately 2 seconds and a magnitude of up to ±4 degrees. The aircraft started the approach to stall wings level and rolled left to only about 5 degrees of bank, where wing rock and bank angle oscillations were centered around. This occurred with about 0.5 degrees of left stick deflection.

The wing fence improved the approach-to-stall characteristics. The bank angle oscillations were decreased from 22 degrees to 16 degrees. Wing rock oscillations were decreased from 18 degrees to 8 degrees. Considering that the wing rock periods were about the same, the difference in amplitudes made a significant difference in the roll rates experienced by the pilot during the approach to stall. This was qualitatively observed and noted by one pilot in a daily flight report. Additionally, a pilot comment was that addition of the wing fence slightly reduced buffet intensity. According to the pilot, the buffet for both configurations was moderate but the random, aperiodic spikes, characteristic of a T-38, were not as severe with the wing fence installed (36). Lastly, the wing fence modified aircraft did not experience the large left roll-off experienced by the clean aircraft.

The stick-controlled, clean configuration (Figure 136) showed that when the pilot used the ailerons to level the wings, the aircraft still favored left bank. With up to 10 degrees of right stick deflection and up to 5 degrees of left stick deflection, the aircraft bank oscillations could be countered and centered on about 5 degrees of left bank. As the AOA increased above 12 degrees, pilot comments were that stick inputs aggravated the oscillations due to the sluggish aircraft response at high AOA.

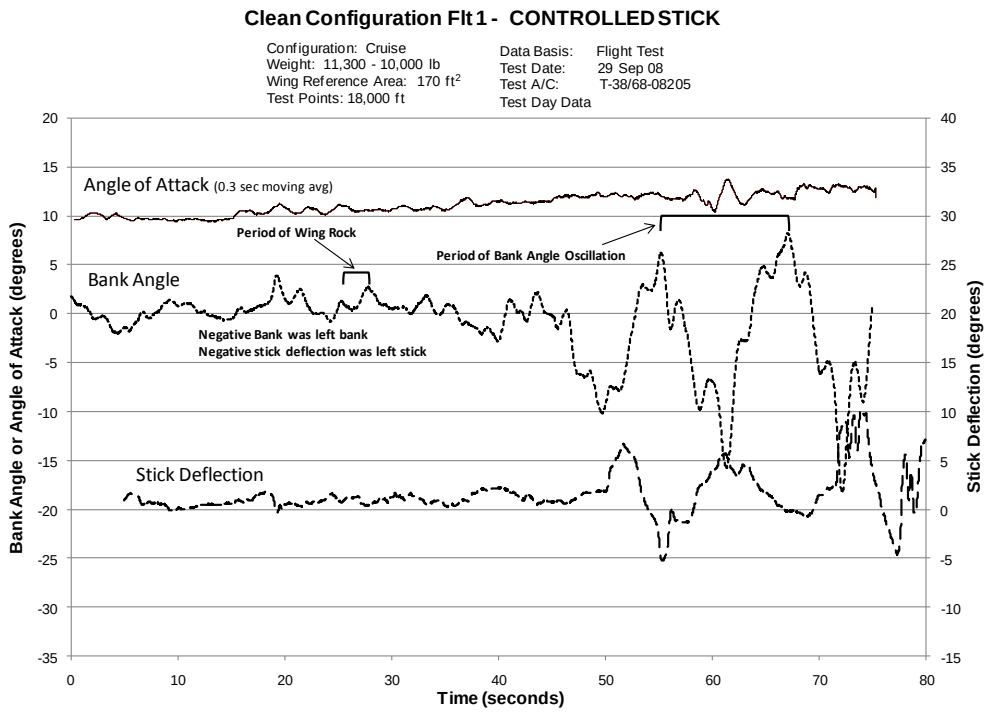

Figure 136. Baseline Stick-Controlled Approach to Stall, Flight 1

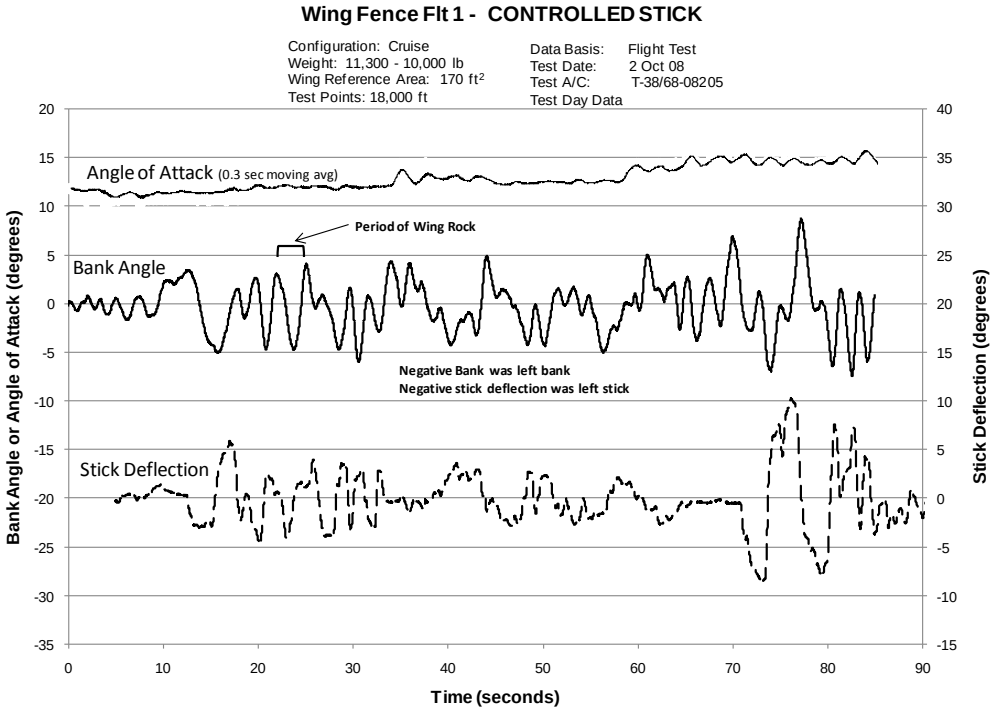

Figure 137. Wing Fence Stick-Controlled Approach to Stall, Flight 1

The stick-controlled, modified configuration (Figure 137) showed that when the pilot used the ailerons to level the wings, the aircraft oscillations could be maintained about wings level with up to 10 degrees of right stick deflection and up to 8 degrees of left stick deflection. In this case, the pilot did not comment that stick inputs aggravated the oscillations. When the pilot used ailerons to keep the wings level, the bank oscillations were smaller and centered on wings level with the fence installed as compared to the baseline aircraft. The wing fence modification reduced the roll rates experienced during wing rock and provided more time for pilot inputs to take effect. The improved ability to keep the wings level during an approach to stall is highly desirable and an excellent result of the wing fence modification.

After the conclusions of this section were made, the wind-tunnel's roll moment data was analyzed to determine if the same results were evident there. Specifically, the raw data (approximately 20 data points per AOA), computed roll moment, and the standard deviation of roll moment at each AOA we evaluated. No difference between the fence and no-fence configurations was apparent in the data.

4.6.6 Flight Test Flow Characteristics.

The third test objective was to compare the upper wing surface flow characteristics of the baseline T-38 to the modified T-38 through inflight photography. This comparison was accomplished using wing tufts and high definition video taken by a member of AFFTC's aerial photo team. The video was recorded from the back seat of an F-16 chase aircraft.

Two sorties were flown with a wing tufted. One sortie was flown with the wing fence installed and one sortie was flown in the baseline configuration. The right wing

was tufted for both sorties in accordance with section 3.7.2.3. Tuft rows were in the spanwise direction and tuft columns were in the streamwise direction.

The test aircraft was flown wings level and stable at approximately 1 degree increments from 8 to 15 degrees AOA to allow the photo-chase to capture the tufts behavior. Additionally, a wings level deceleration was also flown from approximately 3 degrees to 15 degrees AOA. The aircraft was recovered prior to 1.1 normalized AOA (16.5 degrees). The deceleration rate was no greater than 1 KCAS per second. The photo-chase recorded video of the wing tuft behavior throughout the deceleration. The video camera used was a Sony high definition camera recording at a resolution of 1440 x 1080 pixels at a rate of 30 frames per second.

Still shots of the baseline and modified wing were compared and qualitatively evaluated. Specifically, areas of spanwise flow and flow reversal/separation were compared. Top and near-level perspectives were used for this comparison. To maximize the correlation of DAS data to inflight video, the camera was synchronized to Inter-Range Instrumentation Group (IRIG) time before data recording took place. This allowed DAS data to be used to describe the flight conditions for each photograph. DAS AOA was increased by 1.8 degrees, the same bias used in the lift curve and drag polar section.

Re_{mac} ranged from 7.61×10^6 to 9.98×10^6 based on 18,000 feet pressure altitude and the associated airspeeds. The most important conditions are covered in this section for point illustration, but all still shot comparisons for AOAs from 8.1 degrees to 14.9 degrees are found in Appendix N.

The wing fence generally impacted the flow field as theory and models predicted. The impact was less apparent at reduced AOA and greater at increased AOA. The

spanwise flow outboard of the wing fence was reduced as were areas of flow separation/reversal. The effects inboard of the fence were minimal. The effects primarily addressed here are outboard of the wing fence.

As seen in Figure 138 and Figure 139, at 8.4 degrees and 12.4 degrees, the flow outboard of the wing fence / seam (location on the clean wing where the fence was installed) was similar for both configurations. Specifically, the outer three columns of tufts were nearly identical between configurations. The exception was the column of tufts immediately outboard of the fence / seam. On the clean wing, this column of tufts showed separated and reversed flow for nearly the full chord length. However, with the fence installed, the same column of tufts was streamlined and indicated attached flow.

(a) (b)

Figure 138. Fence and Clean Tufted Wings at 8.4 degrees AOA (0.56 normalized)
(a) 185 KCAS (b) 188 KCAS

(a) (b)

Figure 139. Fence and Clean Tufted Wings at 12.4 degrees AOA (0.83 normalized)
(a) 159 KCAS (b) 159 KCAS

At 13.9 degrees, a significant change in the flow on the clean wing was observed as seen in Figure 140. The entire area outboard of the seam was characterized by strong spanwise, separated, and reversed flow. The fence effects were much more significant here and clearly reduced spanwise flow and separation outboard of the fence. The overall reduction in spanwise flow facilitated the decrease in flow separation. This was expected as the flow maintained a higher velocity in the streamwise direction, reducing its tendency to separate and reverse in the presence of an adverse pressure gradient.

(a) (b)

Figure 140. Fence and Clean Tufted Wings at 13.9 degrees AOA (0.92 normalized)
(a) 149 KCAS (b) 153 KCAS

At 14.9 degrees, the flow outboard of the seam on the clean wing was completely separated. The tufts were all standing straight up or reversed as evident in Figure 141. The impact of the fence was even more apparent at this AOA. Contrary to the clean wing, the flow over the wing area outboard of the fence was primarily attached and in the streamwise direction.

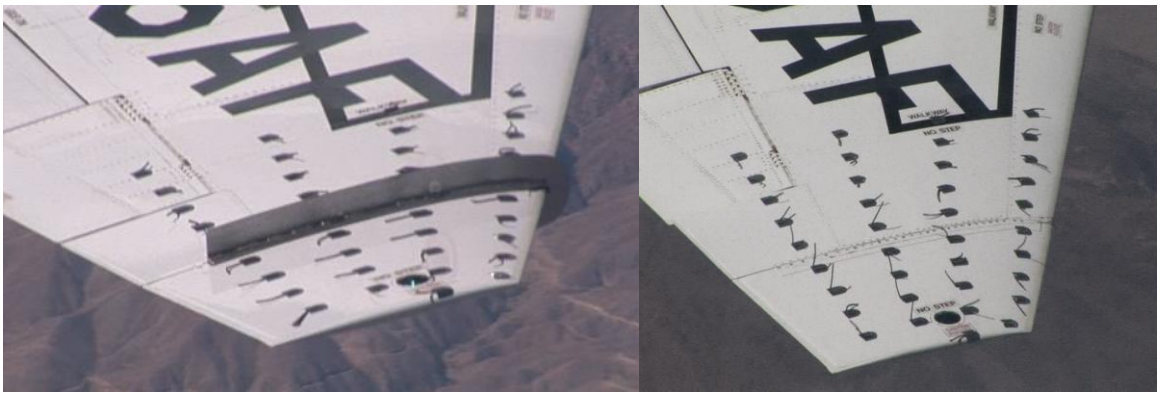

(a) (b)

Figure 141. Fence and Clean Tufted Wings at 14.9 degrees AOA (1.0 normalized)
(a) 153 KCAS (b) 152 KCAS

V. Conclusions and Recommendations

5.1 Conclusions of Research

It was found that the addition of a wing fence, placed at 0.825 semispan, increased the lift coefficient (C_L) by up to 6.3 ± 0.6 percent based upon both drag polar and lift curve analyses from the wind tunnel study. Drag, pitching moment, and lift-to-drag ratio curves provided consistent and expected results. Reynolds effects were evaluated through three different tunnel velocities and trip tape. The most significant Reynolds effect was observed by increasing from 1 x 10^5 to 2 x 10^5, based on mean aerodynamic chord. Although the expected trends continued for a Reynolds number of 3 x 10^5, the variations were much smaller. Trip tape results trended as expected but had an overall small impact. Flow visualization with tufts confirmed expected behaviors based upon previous studies and CFD work accomplished by Solfelt (23) and Solfelt/Maple (24). The wing fence increased the areas of streamlined/attached flow, primarily outboard of the fence.

Fence length and whether or not it wrapped the leading edge directly impacted performance in the wind tunnel. The data showed that extending past 50 percent chord was important, but so was not having the full height of the fence extend all the way to 100 percent chord. Fences that wrapped the leading edge were generally better performers than the one that did not, supporting the conclusion drawn by Solfelt (23).

From flight test data analysis, no lift or drag differences between the baseline and modified aircraft were determined because of data scatter. However, the wing fence did improve the approach-to-stall characteristics. The wing fence modification reduced the roll-off tendency above 9 degrees AOA (0.60 normalized) during the approach to stall

and reduced the wing rock magnitude from 18 degrees to 8 degrees of bank angle. Additionally, with the fence, the aircraft was essentially less sluggish in roll, allowing the pilot to keep the aircraft's wings level more easily. Only small differences in flow characteristics were noted at AOAs below 12.4 degrees (0.83 normalized). However, observed flow characteristics indicated that the wing fence significantly decreased separated flow at AOAs above 13.9 degrees (0.92 normalized).

The following discussion specifically addresses the metrics for success for this study from section 1.3. An increase in lift was reported by Solfelt (4.9 percent at 15 degrees AOA) and Solfelt/Maple (7 percent at 13 degrees AOA) (23; 24). An increase in lift was found via wind tunnel analysis, but the results were inconclusive from flight test (36). The 6.3 percent increase found in the wind tunnel came at no price in drag. A reduced approach speed cannot be recommended for two reasons. First, the flight test results were inconclusive. Second, the effects of the wing fence were not large enough at the AOAs associated with approach and touchdown (approximately 9 to 12 degrees) to allow even a 5 knot decrease in speeds. Lastly, flight test clearly showed an improvement in approach-to-stall characteristics associated with the wing fence modification while buffet intensity was only slightly reduced.

5.2 Recommendations for Future Research

It is recommended that there be continued testing of the T-38 with wing fences. There clearly are benefits. However, there are several aspects of the fence design that would need to be optimized. Spanwise location would likely have a significant impact on performance and should be studied in the future. Fence length as a function of spanwise location should also be considered. As the fence moves inboard, effects on ailerons and

the horizontal stabilizer would have to be evaluated. Additionally, high speed drag and Mach effects should be investigated as well as the impact on range. Because of the increased lift outboard of the fence found by Solfelt, a more thorough study of the forces involved and structural analysis must be made before a flight test for maneuverability could be accomplished. Lastly, a two-fence per wing configuration should be evaluated. Consideration of section 2.6.5's discussion of spanwise location, the location of the F-5F's wing fence (wing station 80.7), Solfelt (23) and Solfelt and Maple's work (24), and this thesis should be given in a two-fence study.

Appendix A: AFIT 10 Pound Balance Schematic

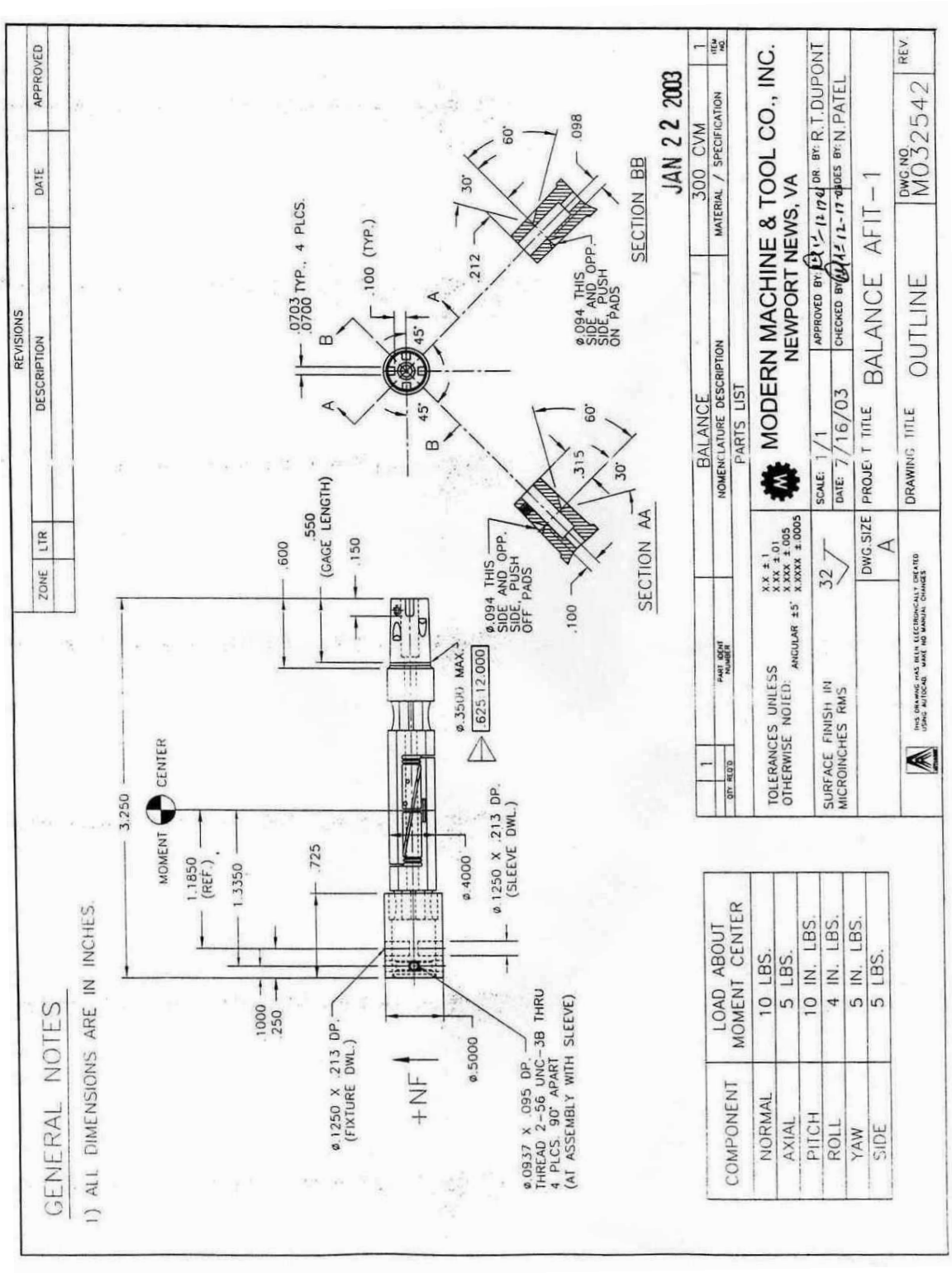

Figure 142. AFIT 10 Pound Balance Schematic

Appendix B: MATLAB 10 Pound Balance Code

```
%************************************************************************
%************************************************************************
%**********         Lt. Gebbie & Capt Anthony DeLuca    ******************
%******   Adapted for the Balance AFIT 1 by Lt. Rivera Parga **************
%*********     re-adapted by Troy Leveron, ENS, USNR    ******************
%**********     Calculation of Lift, Drag, Moments      ******************
%**********     FLEX WING, Prop OFF, ALPHA SWEEPS       ******************
%************************************************************************
%***********  re-adapted by 1Lt Michael Walker, ENY, USAF  ****************
%***********  re-adapted by ENS Dermot Killian, ENY, USN   ****************
%***********  re-adapted by Maj Michael Williams, ENY, USAF  **************
%************************************************************************
% This Code will transfer measured Forces and Moments on the AFIT 1 balance to Wind
% (earth) centered frame of reference by correcting for tare effects, balance
% interactions, and wind tunnel irregularities, then gives a file with all the
% corrected data

clear; clc; close all;
format long

%#########################################################################
%                                INPUT DECK
% FIRST, FILL THE FOLLOWING INFORMATION (modified by Mike Williams on 26 Sep, 2007)

Masskg = 1.5;                           % kgs - Mass of Fuselage + Wings
T_room = mean([75.8]) + 459.67;         % deg R  ****Room Temperature on 26 Sep 2007****
P_barro = mean([29.0254]) * 0.4911541; % Psi    ****Pressure on ____ 2007****
%P_barro = 14.21;                        % Psi    ****Pressure on 26 Sep 2007****

load Williams_T38_tare_AOAmin5to22_fence2.txt;           % tarefile tare.txt - CHANGE FOR
EACH TEST RUN
TareFile = Williams_T38_tare_AOAmin5to22_fence2(:,1:9);

load Williams_T38_90MPH_AOAmin4to22_fence2.txt;          % datafile .txt - CHANGE FOR
EACH TEST RUN
DataFile = Williams_T38_90MPH_AOAmin4to22_fence2(:,1:9);

% insert linear adjustment for axial force drift for Tare File

ctr1 = 1;
adjust1 = -2.27671e-6;
for ctr1 = 1:length(TareFile)
    TareFile(ctr1,6) = TareFile(ctr1,6) + (adjust1*ctr1);
end

dlmwrite('adj_Williams_T38_tare_AOAmin5to22_fence2',TareFile(:,1:9),'\t')

% insert linear adjustment for axial force drift for Data File

ctr = 1;
adjust = 2.79146e-5;
for ctr = 1:length(DataFile)
    DataFile(ctr,6) = DataFile(ctr,6) + (adjust*ctr);
end

dlmwrite('adj_Williams_T38_90MPH_AOAmin4to22_fence2',DataFile(:,1:9),'\t')

% Offset distances from balance moment center to aircraft reference c.g. in inches
% If they are all zero, we're not adjusting the moment data from the
% balance moment center to the reference point.
% Using 19.1% MAC as Std CG for Landing CG
% Note this ref cg is aft of the balance moment center location
% Consider using Actual model CG...or just zeros...if use zeros, use .001
% for Xcmb

X_cmb = -1.5339;            % inches  (from origin @ balance center w/ + forward)
Y_cmb = 0;                  % inches  (zero for symmetry)
Z_cmb = .5664;              % inches  (from origin @ balance center w/ + down)
```

```
% Required for the solid body blockage corrections due to wing and fuselage
% The number below is from Magics and is fuselage only

Body_Volume = 66/(12^3);            % (ft^3)
Wing_Area = .3853;                  % (ft^2)
c_bar = .3681;                      % (ft)
span = 1.2024;                      % (ft)
root_chord = 6.412/12;              % (ft)

%**************************************************************************
% Required for the Pitching Moment Correction (NOT USED - NO TAIL ON MODEL)
% l_t =  9/12;                      % ft = length from tail MAC to aircraft CG
% Span_t = (4+(6/16)) / 12;         % ft = horizontal span
% Tail_Area = (9.42962435) / 144;   % ft^2 =  horizontal tail area
%**************************************************************************
 %########################################################################
% II.-   Room Conditions and Model Specifics :
%       UNITS are in Ft, Sec, lbm, Psf, Rankine, fps
%########################################################################

Mass = (Masskg * 1000) * 0.0022046226;              % lbm
Gas_Const = 1716.16;                                % ft-lbf/Slug-R
Density = (P_barro * 144)/(Gas_Const * T_room);     % lbm/ft^3 or lbf-s^2/ft^4
Root_Chord = root_chord;                            % ft
Span = span;                                        % ft
Aspect_Ratio = Span^2 / Wing_Area;
Dynamic_Viscosity = 3.84e-7;                        % slug/ft-s (@ 75 deg F)
Speed_of_Sound = sqrt(1.4 * T_room * Gas_Const);    % ft/s

%########################################################################
% III.-     Solid body blockage corrections due to wing and fuselage
%           Barlow pg 368-370
%########################################################################

K_1 = 0.97;                         % Barlow page 369 Figure 10.2
K_3 = 0.89;                         % Barlow page 369 Figure 10.2
delta = 0.1177;                     % Barlow page 385 Figure 10.16/17
Tau_1 = 0.87;                       % Barlow page 369 Figure 10.3
X_Section = (31/12)*(44/12);        % ft^2
Wing_Volume = 9/(12^3);             % ft^3

Epsilon_sb_w = (K_1*Tau_1*Wing_Volume) / X_Section^(3/2);
Epsilon_sb_b = (K_3*Tau_1*Body_Volume) / X_Section^(3/2);
Epsilon_tot = Epsilon_sb_w + Epsilon_sb_b;

%########################################################################
% III.-  Load the static tare data for the alpha sweep w/o the wind,
%        separate each force from the file, and fit a 4th order poly
%        as an x-y plot (AoA vs. Force) for each of the 6 force sensors.
%########################################################################

FILE = TareFile(:,:);                   % Pulls in tare data file
j = 1;
k = 1;
L = length(FILE);

for i = 1:L                             % Run for all data points # of rows
    if i ~= L                           % if current row is not last row, go to next
        NEXT = i+1;                     % set next equal to the value of the next row
        VALUE2 = FILE(NEXT,1);          % set value2 as next row column 1
    else if i == L                      % unless the it is the last value
        VALUE2 = 50;                    % value2 set to 50 to end the sequence
    end
    end
    A(j,:) = FILE(i,:);                 % set row j of A equal to row i of FILE
    VALUE1 = FILE(i,1);                 % set value1 equal to row i column 1 of FILE
    if VALUE1 == VALUE2                 % if value1 equals value2, go to next row
        j = j+1;
    else if VALUE1 ~= VALUE2            % if value1 and value2 are different check
        if length(A(:,1)) < 5        % if less than 5 values, ignored due to angle change
            j = 1;
            clear A;
```

```
        else if length(A(:,1)) > 5            % if more than 5 values
                C = length(A(:,1));           % find length of A
                for m = 1:9                   % Average all rows of the like values in A
                    B(k,m) = mean(A(4:C,m));  % disregarding first 3 for vibrations
                end
                j = 1;
                k = k+1;
                clear A
        end
        end
    end
    end
end

if B(k-1,1) < B((k-2),1)
    B = B(1:(k-2),:)
end

tare = [B];
[row,col] = size(tare);

for k = 1:row;

theta_tare(k,:,:)   = tare(k,1).* (pi/180);
NF_tare(k,:,:)      = tare(k,4);
PM_tare(k,:,:)      = tare(k,5);
AF_tare(k,:,:)      = tare(k,6);
SF_tare(k,:,:)      = tare(k,7);
YM_tare(k,:,:)      = tare(k,8);
RM_tare(k,:,:)      = tare(k,9);

end

NF_poly = polyfit(theta_tare,NF_tare,4);
PM_poly = polyfit(theta_tare,PM_tare,4);
AF_poly = polyfit(theta_tare,AF_tare,4);
SF_poly = polyfit(theta_tare,SF_tare,4);
YM_poly = polyfit(theta_tare,YM_tare,4);
RM_poly = polyfit(theta_tare,RM_tare,4);

%#########################################################################
% IV.- Load the specific test run files,
%#########################################################################

clear ('AA','B','C','L')

FILE = DataFile(:,:);                     % Pulls in test data file

j = 1;
k = 1;
L = length(FILE);

for i = 1:L                               % Run for all data points # of rows
    if i ~= L                             % if current row is not last row, go to next
        NEXT = i+1;                       % set next equal to the value of the next row
        VALUE2 = FILE(NEXT,1);            % set value2 as next row column 1
    else if i == L                        % unless the it is the last value
        VALUE2 = 50;                      % value2 set to 50 to end the sequence
    end
    end
    A(j,:) = FILE(i,:);                   % set row j of A equal to row i of FILE
    VALUE1 = FILE(i,1);                   % set value1 equal to row i column 1 of FILE
    if VALUE1 == VALUE2                   % if value1 equals value2, go to next row
        j = j+1;
    else if VALUE1 ~= VALUE2              % if value1 and value2 are different check
        if length(A(:,1)) < 5       % if less than 5 values, ignored due to angle change
            j = 1;
            clear A;
        else if length(A(:,1)) > 5              % if more than 5 values
                C = length(A(:,1));             % find length of A
                for m = 1:9                   % Average all rows of the like values in A
                    B(k,m) = mean(A(4:C,m));  % disregarding first 3 for vibrations
```

```
                    B(k,m+9) = std(A(4:C,m));    % finding std dev of raw data
                end
                j = 1;
                k = k+1;
                clear A
        end
        end
    end
    end
end

%  if B(k-1,1)<B((k-2),1)
%     B=B(1:(k-2),:)
%  end

sample_data = [B];

dlmwrite('stddev_Williams_T38_90MPH_AOAmin4to22_fence2',B(:,10:18),'\t')

[row2,col2] = size(sample_data);

for i = 1:row2;

% Angles of the model during test runs (Roll, Pitch {AoA}, Yaw {Beta}):

phi               = 0;
theta(i,:)        = sample_data(i,1) .* (pi/180)-(0*pi/180);    % radians
si(i,:)           = sample_data(i,2) .* (pi/180);               % radians
Wind_Speed(i,:)   = sample_data(i,3) .* (5280/3600);            % fps

% Flight Parameters (Re#, Ma#, Dynamic Pressure):

q = (.5 * Density) .* Wind_Speed.^2;                                    % lbf/ft^2
q_Corrected = q .* (1 + Epsilon_tot)^2;                                 % lbf/ft^2
Wind_Speed_Corrected = Wind_Speed .* (1 + Epsilon_tot);                 % fps
Mach_Number = Wind_Speed_Corrected ./ Speed_of_Sound;                   % NonDimensional

% RE # based on MAC length

Reynolds_Number = ((Density * c_bar) .* Wind_Speed_Corrected) ...
    ./ Dynamic_Viscosity;                                           % NonDimensional

Flight_Parameters = [Mach_Number Reynolds_Number q_Corrected]

% Individual forces and moments for each sensor:

% NEW NOTATION

NF_test(i,:,:) = sample_data(i,4);
PM_test(i,:,:) = sample_data(i,5);
AF_test(i,:,:) = sample_data(i,6);
SF_test(i,:,:) = sample_data(i,7);
YM_test(i,:,:) = sample_data(i,8);
RM_test(i,:,:) = sample_data(i,9);

%%%%%%%%%%%%%%%%%%%%%%%%%%%%%%%%%%%%%%%%%%%%%%%%%%%%%%%%%%%%%%%%%%%%%%%
% V.-   Subtract the effect of the static
%       weight with the tare polynominals above
%%%%%%%%%%%%%%%%%%%%%%%%%%%%%%%%%%%%%%%%%%%%%%%%%%%%%%%%%%%%%%%%%%%%%%%
% Evaluating the actual test theta angle (AoA) in the tare polynominal to
% determine the tare values for the angles tested in each run

NF_eval = polyval(NF_poly,theta);
PM_eval = polyval(PM_poly,theta);
AF_eval = polyval(AF_poly,theta);
SF_eval = polyval(SF_poly,theta);
YM_eval = polyval(YM_poly,theta);
RM_eval = polyval(RM_poly,theta);

% The Time-Averaged (raw) forces and momentums NF,AF,SF,PM,YM AND RM measured
% in the wind tunnel (body axis) with the tare effect of the weight subtracted off.
```

```
NF_resolved = NF_test - (NF_eval);
PM_resolved = PM_test - (PM_eval);
AF_resolved = AF_test - (AF_eval);
SF_resolved = SF_test - (SF_eval);
YM_resolved = YM_test - (YM_eval);
RM_resolved = RM_test - (RM_eval);

Forces_minus_tare = [NF_resolved, AF_resolved, PM_resolved, RM_resolved, YM_resolved,
SF_resolved]';

%#########################################################################
% VI.- CORRECT FORCES AND MOMENTS FOR BALANCE INTERATIONS (body axis)
%#########################################################################
% USING THE REDUCTION EQUATIONS
% LET US SET A MAXIMUN NUMBER OF INTERATIONS (FOR AVOIDING AN INFINIT LOOP)

MAXIT = 100;

% SET THE LIMIT FOR THE DIFFERENCE BETWEEN INTERATIONS(CRITERIA FOR FINISH THE
INTERATIONS)

LIMIT = 10E-14;

% MATCHING EACH NAME WITH THE DATA
% Prof. Reeder added :i

MNF = NF_resolved(i);
MAF = AF_resolved(i);
MPM = PM_resolved(i);
MRM = RM_resolved(i);
MYM = YM_resolved(i);
MSF = SF_resolved(i);

% INPUT OF THE CONSTANTS VALUES FROM THE MATRIX FOR SENSITIVITIES AND INTERATIONS

K = [     0      -1.3567E-03  -3.8021E-03  -4.2814E-03  -1.6966E-03   1.7567E-03 ...
     5.3167E-05  -1.3867E-04  -5.5629E-05   3.5181E-05   1.0601E-05  -2.5271E-04 ...
     5.6693E-05  -1.9537E-04   1.7908E-05  -3.6606E-05  -4.9934E-05   4.1205E-05 ...
     2.5648E-05  -1.9289E-05   8.9661E-05  -1.9594E-05  -4.9859E-04  -1.1599E-03 ...
     5.7163E-05   8.9798E-05  -7.8591E-05   9.3187E-03       0       -3.8421E-03 ...
     3.5740E-03   9.7714E-05  -2.7776E-03  -1.3552E-04   5.1538E-04   2.2082E-04 ...
    -1.2706E-05  -2.3637E-05   1.3686E-05   1.1085E-04  -3.6557E-06   4.9876E-06 ...
     8.1085E-06   3.7381E-05   1.2791E-04  -9.4527E-06  -2.3083E-06  -1.2046E-06 ...
     7.8161E-04  -1.1997E-03  -3.0560E-05  -6.6202E-05   3.7227E-04  -2.1469E-04 ...
     4.8386E-03  -3.7387E-03       0       -1.8479E-02   3.9077E-03   9.9165E-04 ...
    -1.4825E-05  -1.4830E-06   6.0845E-05   8.0667E-05   1.8547E-05  -5.0212E-05 ...
     1.0539E-04  -2.2676E-04   4.3793E-05  -1.0456E-05  -8.1186E-06  -2.1653E-05 ...
    -3.3070E-05   1.7280E-05  -7.4509E-05  -3.4399E-05  -8.2999E-04  -6.7962E-04 ...
     4.0521E-05  -5.1604E-05   9.1132E-06  -5.7360E-03  -2.2213E-04   9.9131E-04 ...
          0      -9.5790E-03   6.7114E-03   3.6824E-05   1.0056E-04  -3.7105E-05 ...
    -9.0295E-05  -7.4580E-05   1.4814E-04   7.2634E-05  -8.4778E-06   6.3486E-05 ...
     5.6328E-05  -1.3617E-04   2.2196E-05   1.3606E-05  -3.6689E-05   8.3283E-05 ...
     1.1865E-04   1.8544E-05  -1.9831E-05   1.7894E-05  -6.8164E-05  -7.0892E-05 ...
     1.2378E-03   1.6961E-03  -6.5102E-03  -9.3202E-03       0        5.1349E-03 ...
     1.3612E-05  -1.3175E-04   7.2442E-06   5.6705E-04  -1.4723E-05  -4.8656E-05 ...
    -1.4282E-04   5.9711E-05   5.9046E-05  -3.6490E-04   7.4881E-05   5.4601E-06 ...
     1.0129E-03  -1.3867E-04   8.1617E-05   6.6053E-05  -1.3417E-05   9.0025E-05 ...
    -4.5362E-05  -4.4672E-06   9.5087E-05  -3.4077E-02   7.9142E-04   1.6667E-03 ...
    -6.6512E-03   8.1538E-03       0       -1.4185E-05   7.3209E-05  -2.5849E-05 ...
     1.2325E-03  -4.1696E-05   4.6266E-05   8.6146E-05   2.1436E-05   5.0874E-05 ...
    -3.2738E-04   2.2218E-04   8.6478E-06   7.3395E-04  -4.1453E-05   3.5719E-05 ...
     2.5313E-05   1.5182E-04   3.6007E-05  -2.8844E-05   8.9741E-05  -7.3257E-05 ];

% COMPUTE THE UNCORRECTED FORCES AND MOMENTS BY
% CONSIDERING THAT THE PRIME SENSITIVITY CONSTANTS ARE ALREADY APPLIED:

NF1 = MNF;
AF1 = MAF;
PM1 = MPM;
RM1 = MRM;
YM1 = MYM;
SF1 = MSF;
```

```
% FOR THE FIRST INTERACTION, LET US INITIALIZE THE VALUES OF FORCES AND
% MOMENTS WITH THE VALUES OF THE UNCORRECTED FORCES AND MOMENTS

NF(1) = NF1;
AF(1) = AF1;
PM(1) = PM1;
RM(1) = RM1;
YM(1) = YM1;
SF(1) = SF1;

% DOING THE INTERACTION EQUATIONS:

for n = 2:MAXIT;

NF(n) = NF1-((K(2)*AF(n-1))+(K(3)*PM(n-1))+(K(4)*RM(n-1))+(K(5)*YM(n-1))+(K(6)*SF(n-
1))+(K(7)*NF(n-1)^2)+...
        (K(8)*(NF(n-1)*AF(n-1)))+(K(9)*(NF(n-1)*PM(n-1)))+(K(10)*(NF(n-1)*RM(n-
1)))+(K(11)*(NF(n-1)*YM(n-1)))+...
        (K(12)*(NF(n-1)*SF(n-1)))+(K(13)*(AF(n-1)^2))+(K(14)*(AF(n-1)*PM(n-
1)))+(K(15)*(AF(n-1)*RM(n-1)))+...
        (K(16)*(AF(n-1)*YM(n-1)))+(K(17)*(AF(n-1)*SF(n-1)))+(K(18)*(PM(n-
1)^2))+(K(19)*(PM(n-1)*RM(n-1)))+...
        (K(20)*(PM(n-1)*YM(n-1)))+(K(21)*(PM(n-1)*SF(n-1)))+(K(22)*(RM(n-
1)^2))+(K(23)*(RM(n-1)*YM(n-1)))+...
        (K(24)*(RM(n-1)*SF(n-1)))+(K(25)*(YM(n-1)^2))+(K(26)*(YM(n-1)*SF(n-
1)))+(K(27)*(SF(n-1)^2)));

AF(n) = AF1-((K(28)*NF(n-1))+(K(30)*PM(n-1))+(K(31)*RM(n-1))+(K(32)*YM(n-1))+(K(33)*SF(n-
1))+(K(34)*NF(n-1)^2)+...
        (K(35)*(NF(n-1)*AF(n-1)))+(K(36)*(NF(n-1)*PM(n-1)))+(K(37)*(NF(n-1)*RM(n-
1)))+(K(38)*(NF(n-1)*YM(n-1)))+...
        (K(39)*(NF(n-1)*SF(n-1)))+(K(40)*(AF(n-1)^2))+(K(41)*(AF(n-1)*PM(n-
1)))+(K(42)*(AF(n-1)*RM(n-1)))+...
        (K(43)*(AF(n-1)*YM(n-1)))+(K(44)*(AF(n-1)*SF(n-1)))+(K(45)*(PM(n-
1)^2))+(K(46)*(PM(n-1)*RM(n-1)))+...
        (K(47)*(PM(n-1)*YM(n-1)))+(K(48)*(PM(n-1)*SF(n-1)))+(K(49)*(RM(n-
1)^2))+(K(50)*(RM(n-1)*YM(n-1)))+...
        (K(51)*(RM(n-1)*SF(n-1)))+(K(52)*(YM(n-1)^2))+(K(53)*(YM(n-1)*SF(n-
1)))+(K(54)*(SF(n-1)^2)));

PM(n) = PM1-((K(55)*NF(n-1))+(K(56)*AF(n-1))+(K(58)*RM(n-1))+(K(59)*YM(n-1))+(K(60)*SF(n-
1))+(K(61)*NF(n-1)^2)+...
        (K(62)*(NF(n-1)*AF(n-1)))+(K(63)*(NF(n-1)*PM(n-1)))+(K(64)*(NF(n-1)*RM(n-
1)))+(K(65)*(NF(n-1)*YM(n-1)))+...
        (K(66)*(NF(n-1)*SF(n-1)))+(K(67)*(AF(n-1)^2))+(K(68)*(AF(n-1)*PM(n-
1)))+(K(69)*(AF(n-1)*RM(n-1)))+...
        (K(70)*(AF(n-1)*YM(n-1)))+(K(71)*(AF(n-1)*SF(n-1)))+(K(72)*(PM(n-
1)^2))+(K(73)*(PM(n-1)*RM(n-1)))+...
        (K(74)*(PM(n-1)*YM(n-1)))+(K(75)*(PM(n-1)*SF(n-1)))+(K(76)*(RM(n-
1)^2))+(K(77)*(RM(n-1)*YM(n-1)))+...
        (K(78)*(RM(n-1)*SF(n-1)))+(K(79)*(YM(n-1)^2))+(K(80)*(YM(n-1)*SF(n-
1)))+(K(81)*(SF(n-1)^2)));

RM(n) = RM1-((K(82)*NF(n-1))+(K(83)*AF(n-1))+(K(84)*PM(n-1))+(K(86)*YM(n-1))+(K(87)*SF(n-
1))+(K(88)*NF(n-1)^2)+...
        (K(89)*(NF(n-1)*AF(n-1)))+(K(90)*(NF(n-1)*PM(n-1)))+(K(91)*(NF(n-1)*RM(n-
1)))+(K(92)*(NF(n-1)*YM(n-1)))+...
        (K(93)*(NF(n-1)*SF(n-1)))+(K(94)*(AF(n-1)^2))+(K(95)*(AF(n-1)*PM(n-
1)))+(K(96)*(AF(n-1)*RM(n-1)))+...
        (K(97)*(AF(n-1)*YM(n-1)))+(K(98)*(AF(n-1)*SF(n-1)))+(K(99)*(PM(n-
1)^2))+(K(100)*(PM(n-1)*RM(n-1)))+...
        (K(101)*(PM(n-1)*YM(n-1)))+(K(102)*(PM(n-1)*SF(n-1)))+(K(103)*(RM(n-
1)^2))+(K(104)*(RM(n-1)*YM(n-1)))+...
        (K(105)*(RM(n-1)*SF(n-1)))+(K(106)*(YM(n-1)^2))+(K(107)*(YM(n-1)*SF(n-
1)))+(K(108)*(SF(n-1)^2)));

YM(n) = YM1-((K(109)*NF(n-1))+(K(110)*AF(n-1))+(K(111)*PM(n-1))+(K(112)*RM(n-
1))+(K(114)*SF(n-1))+(K(115)*NF(n-1)^2)+...
        (K(116)*(NF(n-1)*AF(n-1)))+(K(117)*(NF(n-1)*PM(n-1)))+(K(118)*(NF(n-1)*RM(n-
1)))+(K(119)*(NF(n-1)*YM(n-1)))+...
```

```
        (K(120)*(NF(n-1)*SF(n-1)))+(K(121)*(AF(n-1)^2))+(K(122)*(AF(n-1)*PM(n-
1)))+(K(123)*(AF(n-1)*RM(n-1)))+...
        (K(124)*(AF(n-1)*YM(n-1)))+(K(125)*(AF(n-1)*SF(n-1)))+(K(126)*(PM(n-
1)^2))+(K(127)*(PM(n-1)*RM(n-1)))+...
        (K(128)*(PM(n-1)*YM(n-1)))+(K(129)*(PM(n-1)*SF(n-1)))+(K(130)*(RM(n-
1)^2))+(K(131)*(RM(n-1)*YM(n-1)))+...
        (K(132)*(RM(n-1)*SF(n-1)))+(K(133)*(YM(n-1)^2))+(K(134)*(YM(n-1)*SF(n-
1)))+(K(135)*(SF(n-1)^2)));

SF(n) = SF1-((K(136)*NF(n-1))+(K(137)*AF(n-1))+(K(138)*PM(n-1))+(K(139)*RM(n-
1))+(K(140)*YM(n-1))+(K(142)*NF(n-1)^2)+...
        (K(143)*(NF(n-1)*AF(n-1)))+(K(144)*(NF(n-1)*PM(n-1)))+(K(145)*(NF(n-1)*RM(n-
1)))+(K(146)*(NF(n-1)*YM(n-1)))+...
        (K(147)*(NF(n-1)*SF(n-1)))+(K(148)*(AF(n-1)^2))+(K(149)*(AF(n-1)*PM(n-
1)))+(K(150)*(AF(n-1)*RM(n-1)))+...
        (K(151)*(AF(n-1)*YM(n-1)))+(K(152)*(AF(n-1)*SF(n-1)))+(K(153)*(PM(n-
1)^2))+(K(154)*(PM(n-1)*RM(n-1)))+...
        (K(155)*(PM(n-1)*YM(n-1)))+(K(156)*(PM(n-1)*SF(n-1)))+(K(157)*(RM(n-
1)^2))+(K(158)*(RM(n-1)*YM(n-1)))+...
        (K(159)*(RM(n-1)*SF(n-1)))+(K(160)*(YM(n-1)^2))+(K(161)*(YM(n-1)*SF(n-
1)))+(K(162)*(SF(n-1)^2)));

% SET THE LIMIT FOR THE DIFFERENCE BETWEEN INTERATIONS(CRITERIA FOR FINISH THE
INTERATIONS)

DIFFNF(n) = abs(NF(n)-NF(n-1));
DIFFAF(n) = abs(AF(n)-AF(n-1));
DIFFPM(n) = abs(PM(n)-PM(n-1));
DIFFRM(n) = abs(RM(n)-RM(n-1));
DIFFYM(n) = abs(YM(n)-YM(n-1));
DIFFSF(n) = abs(SF(n)-SF(n-1));

if DIFFNF(n) & DIFFAF(n) & DIFFPM(n) & DIFFRM(n) & DIFFYM(n) & DIFFSF(n) < LIMIT
 break

end

end

% disp('THE FINAL VALUES ARE (NF,AF,PM,RM,YM,SF):');
Corrected_Data(:,i) = [NF(n);AF(n);PM(n);RM(n);YM(n);SF(n)];

% disp('THE FINAL DIFFERENCE BETWEEN INTERATIONS ARE(FOR NF,AF,PM,RM,YM,SF) :');
FINAL_DIFFERENCE = [DIFFNF(n),DIFFAF(n),DIFFPM(n),DIFFRM(n),DIFFYM(n),DIFFSF(n)];

% disp('THE NUMBER OF INTERATIONS USED WAS:')
n;

%#########################################################################
% VII.- Calculation of the Axial, Side, & Normal Forces from the corrected balance
%       forces in the Body Axis reference frame
%#########################################################################

Forces_b(:,i) = [Corrected_Data(2,i); Corrected_Data(6,i); Corrected_Data(1,i)];

% Calculation of the Drag, Side, & Lift Forces in the Wind Axis reference frame

Forces_w =
[Forces_b(1,:).*cos(theta').*cos(si')+Forces_b(2,:).*sin(si')+Forces_b(3,:).*sin(theta').
*cos(si');
          -Forces_b(1,:).*sin(si').*cos(theta')+Forces_b(2,:).*cos(si')-
Forces_b(3,:).*sin(theta').*sin(si');
          -Forces_b(1,:).*sin(theta')+Forces_b(3,:).*cos(theta')];  % in radians

% First entry is the moments calculated by the balance or direct calculation
% in the Body Reference Frame.  Balance measures Roll (l), Yaw is about the
% z-axis (n), and Pitch is about the y-axis (m).  Distances from strain
% gages to C.G. are in INCHES.  Moments are in-lbf. See pp. 236-238 of
% Barlow et. al., 3rd ed.

m = Corrected_Data(3,i);
```

```
n = Corrected_Data(5,i);

l = Corrected_Data(4,i);

Moments_b(:,i) = [l ; m ; n];

% Second entry is the conversion from the "Balance Centeric" moments to the
% Wind Reference monments with respect to the Balance Center (bc)

Moments_w_bc = [Moments_b(1,:).*cos(theta').*cos(si')-
Moments_b(2,:).*sin(si')+Moments_b(3,:).*sin(theta').*cos(si');

Moments_b(1,:).*sin(si').*cos(theta')+Moments_b(2,:).*cos(si')+Moments_b(3,:).*sin(theta'
).*sin(si');
               -Moments_b(1,:).*sin(theta')+Moments_b(3,:).*cos(theta')];

% Finally, the balance centered moments are converted to moments about the
% Model's Center of Mass (cm) or Center of Gravity (CG)

cgdist = sqrt((X_cmb)^2+(Z_cmb)^2); % Obtaining the direct distance between the
                                    % center of the balance and the center of mass
w = atan(-Z_cmb/X_cmb);             % Obtaining the angle between cgdist and the x
                                    % axes at zero angle of attack

X_cm(i,:) = cos(theta(i,:)+w)*cos(si(i,:))*(cgdist);
Y_cm(i,:) = Y_cmb + X_cm(i,:)*tan(si(i,:));  % Appropriate for very small y_cmb and
reasonable si
Z_cm(i,:) = -sin(theta(i,:)+w)*(cgdist);

Moments_w_cg_u = [Moments_w_bc(1,:) + Z_cm(i,:)*Forces_w(2,:)  + Forces_w(3,:)*
Y_cm(i,:);
                  Moments_w_bc(2,:) - Forces_w(3,:)* X_cm(i,:) + Forces_w(1,:)*
Z_cm(i,:);
                  Moments_w_bc(3,:) - Forces_w(1,:)* Y_cm(i,:) - Forces_w(2,:)*
X_cm(i,:)];

%#########################################################################
% VIII.- Calculation of the actual Lift and Drag nondimensional Coefficients,
%        uncorrected for tunnel effects, (Cl and Cd)
%#########################################################################

C_D_u = Forces_w(1,:) ./ (q_Corrected' .* Wing_Area);
C_Y_u = Forces_w(2,:) ./ (q_Corrected' .* Wing_Area);
C_L_u = Forces_w(3,:) ./ (q_Corrected' .* Wing_Area);  %Keuthe & Chow pg 178
Coefficients = [C_L_u; C_D_u; C_Y_u]';
Ave_Cl = mean(Coefficients(:,1));
Ave_Cd = mean(Coefficients(:,2));

end

%#########################################################################
% IX          Drag Coefficient Correction
%#########################################################################

C_D_o = min(Coefficients(:,2));
C_L_u_sqrd = Coefficients(:,1).^2;
Delta_C_D_w = ((delta * Wing_Area) / X_Section) .* C_L_u_sqrd;
C_D_Corrected = C_D_u' + Delta_C_D_w;

%#########################################################################
% X.-  Angle of Attack due to upwash Correction
%#########################################################################

alpha_before = sample_data(:,1);

% ***18APR05 change to 5 for sting block angle, then back to 0 for Aero 517
% SU 2005***

alpha = [alpha_before]-[0];
Delta_alpha_w = ((delta * Wing_Area) / X_Section) .* (57.3 * C_L_u);
alpha_Corrected = alpha + Delta_alpha_w';
```

```
%#########################################################################
% XI.-  Pitching Moment Correction
%#########################################################################

% tau2 = 0.65;
c_bar = c_bar;                                  % ft = Mean Chord of wing
% V_bar =  0/ (Wing_Area * c_bar);              % Horizontal tail volume ratio
% eta_t = 1.0;
% epsilon_o = 0;
% i_t = pi/4;                                   % radians
% i_w = 0;
% Aspect_Ratio_t = Span_t^2 / Tail_Area;
%
% D_epslion_D_alpha = ((2 .* C_L_u) ./ (pi* Aspect_Ratio))';
% epsilon = epsilon_o + (D_epslion_D_alpha .* alpha_Corrected );
% alpha_t = alpha_Corrected - i_w - epsilon + i_t;
% C_L_alpha_t = 0 %((0.1* Aspect_Ratio) / (Aspect_Ratio_t +2)) * 0.8;
% D_Cm_cg_t_D_alpha_t = -C_L_alpha_t* V_bar * eta_t;
% Delta_C_m_cg_t = ((D_Cm_cg_t_D_alpha_t) * (delta*tau2) * (Wing_Area / X_Section) .*
(C_L_u * 57.3))';

Cl_w_cg =   Moments_w_cg_u(1,:) ./ (q_Corrected' .* (Wing_Area * Span*12));
Cm_w_cg_u = Moments_w_cg_u(2,:) ./ (q_Corrected' .* (Wing_Area * c_bar*12));
Cn_w_cg =   Moments_w_cg_u(3,:) ./ (q_Corrected' .* (Wing_Area * Span*12));

Cm_w_cg_corrected = Cm_w_cg_u     %-Delta_C_m_cg_t';  % no tail
Corrected_Moment_Coefficients = [Cl_w_cg' Cm_w_cg_corrected' Cn_w_cg'];

% OBTAINING THE MOMENT COEFFICIENTS CORRECTED ABOUT THE CENTER OF THE BALANCE

Cl_w_bc =   Moments_w_bc(1,:) ./ (q_Corrected' .* (Wing_Area * Span*12));
Cm_w_bc_u = Moments_w_bc(2,:) ./ (q_Corrected' .* (Wing_Area * c_bar*12));
Cn_w_bc =   Moments_w_bc(3,:) ./ (q_Corrected' .* (Wing_Area * Span*12));

Cm_w_bc_corrected = Cm_w_bc_u ;  %no tail
Corrected_Moment_Coefficients_bc = [Cl_w_bc' Cm_w_bc_corrected' Cn_w_bc'];

%#########################################################################
% XII.- OUTPUT VARIABLES FORMATING
%#########################################################################

alpha = sample_data(:,1);

fprintf('   Mach Number Reynolds Number Dynamic Pressure(Psf)\r')
% Flight_Parameters
fprintf(' \r');
fprintf(' Loads are in lbf and arranged [D S L] across the top and increments of alpha
down the side \r')
Forces_w'
fprintf(' \r')
fprintf(' Moments are in in-lbf and arranged [L M N] down the side and increments of
alpha along the top \r')
% Moments_w_cg_u
fprintf(' \r')
fprintf('       Cl_u           Cd_u             CY_u \r');
% Coefficients
fprintf(' \r')
fprintf('    Del_CD_w       CD_u     CD_Corrected \r');
Compare_CD = [Delta_C_D_w C_D_u' C_D_Corrected]
fprintf(' \r')
fprintf('    Del_alpha_w    alpha_g     alpha_Corrected \r');
Compare_alpha = [Delta_alpha_w' alpha alpha_Corrected ]
fprintf(' \r')
fprintf('    Cl_cg_wind    Cm_cg_corrected_w     Cn_cg_wind \r');
% Corrected_Moment_Coefficients
fprintf(' \r')
fprintf('       M#           Re#          q_c           Uoo        alpha_c        C_L
C_D_c      Cl_cg_w       Cm_cg_c_w    Cn_cg_w       C_Y\r');
YY = [Flight_Parameters (Wind_Speed_Corrected .* (3600/5280)) alpha_Corrected C_L_u'
C_D_Corrected Corrected_Moment_Coefficients C_Y_u' NF_resolved AF_resolved]
```

```
% XX=['M#', 'Re#', 'q_c',  'Uoo', 'alpha_c', 'C_L', 'C_D_c', 'Cl_cg_w', 'Cm_cg_c_w',
'Cn_cg_w', 'C_Y_u'];
% ZZ=[XX; YY];
% wk1write('output.xls',YY,2,1)
% Max_Cl = max(Coefficients(:,1))

L_over_D = YY(:,6) ./ YY(:,7);

% SAVE TOTAL DATA IN A EXTERNAL FILE

dlmwrite('adj_output_Williams_T38_90MPH_AOAmin4to22_fence2',YY,'\t')

%%%%%%%%%%%%%%%%%%%%%%%%%%%%%%%%%%%%%%%%%%%%%%%%%%%%%%%%%%%%%%%%%%%%%%%
% XIII.- PLOTS
%%%%%%%%%%%%%%%%%%%%%%%%%%%%%%%%%%%%%%%%%%%%%%%%%%%%%%%%%%%%%%%%%%%%%%%

%***************1.- C_L VS C_D PLOT************************************

figure(1);
plot(C_D_Corrected,Coefficients(:,1),'b.-.');
legend('90 mph (Re_c\approx 300K)','\beta \approx 0\circ');
grid on;
title('\it C_L vs C_D Fence 2 (90 mph)','FontWeight','bold','FontSize',11); xlabel('Drag
Coefficient (C_D)'); ylabel('Lift Coefficient (C_L)');

subplot ('position',[.15 .6 .3 .3]);
plot(alpha_Corrected,Coefficients(:,1),'b-'); grid on
legend('90 mph');
title('\it Fence 2: C_L_u vs \alpha '); xlabel('Angle of Attack (\alpha)'); ylabel('Lift
Coefficient (C_L_u)');

subplot ('position',[.65 .6 .3 .3]);
plot(alpha_Corrected,Coefficients(:,2),'b',alpha_Corrected,C_D_Corrected,'r'); grid on
legend('C_D_u', 'C_D_c');
title('\it Fence 2: C_D vs \alpha'); xlabel('Angle of Attack (\alpha)'); ylabel('Drag
Coefficient (C_D)');

subplot('position',[.15 .1 .3 .3]);
plot(Coefficients(:,2),Coefficients(:,1),'b',C_D_Corrected,Coefficients(:,1),'r'); grid
on
legend('C_D_u', 'C_D_c');
title('\it Fence 2: C_L_u vs C_D'); xlabel('Drag Coefficient (C_D)'); ylabel('Lift
Coefficient (C_L_u )');

subplot ('position',[.65 .1 .3 .3])
plot(Coefficients(:,2),Coefficients(:,1).^2,'b',C_D_Corrected,Coefficients(:,1).^2,'r');
grid on
legend('C_D_u', 'C_D_c');
title('\it Fence 2: C_L_u ^2 vs C_D'); xlabel('Drag Coefficient (C_D)'); ylabel('Lift
Coefficient (C_L_u ^2)');
print -djpeg POLAR_PLOTS_90MPH_Fence2

%***************2.- C_L VS ALPHA PLOT************************************

figure(2);
plot(alpha_Corrected,Coefficients(:,1),'b.-.');
legend('90 mph (Re_c\approx 300K)','\beta \approx 0\circ');
grid on;
title('\it C_L vs \alpha Fence 2 (90 mph)','FontWeight','bold','FontSize',11);
xlabel('Angle of Attack (\alpha)'); ylabel('Lift Coefficient (C_L)');
print -djpeg C_L_VS_ALPHA_90MPH_Fence2

%***************3.- C_D VS ALPHA PLOT************************************

figure(3);
plot(alpha_Corrected,C_D_Corrected,'b.-.');
grid on;
legend('90 mph (Re_c\approx 300K)','\beta \approx 0\circ');
title('\it C_D vs \alpha Fence 2 (90 mph)','FontWeight','bold','FontSize',11);
xlabel('Angle of Attack (\alpha)'); ylabel('Drag Coefficient (C_D)');
print -djpeg C_D_VS_ALPHA_90MPH_Fence2
```

```
%***************4.- C_D AND C_L VS ALPHA PLOT*********************************

figure(4);
plot(alpha_Corrected,C_D_Corrected,'b.-.',alpha_Corrected,Coefficients(:,1),'r');
legend('C_D (90 mph)', 'C_L(90 mph)')
grid on;
title('\it C_D and C_L vs \alpha Fence 2 (90 mph)','FontWeight','bold','FontSize',11);
xlabel('Angle of Attack (\alpha)'); ylabel('Drag Coefficient (C_D) or Lift Coefficient
(C_L)');
print -djpeg C_L_AND_CD_VS_ALPHA_90MPH_Fence2

%***************4.- Lift, Drag and Side Forces VS ALPHA
PLOT**********************************

figure(5);
plot(alpha_Corrected,Forces_w(1,:),'b.-
.',alpha_Corrected,Forces_w(2,:),'r',alpha_Corrected,Forces_w(3,:),'*');
legend('Drag','Side force','Lift')
grid on;
title('\it Lift, Drag and side Forces VS \alpha Fence 2 (90
mph)','FontWeight','bold','FontSize',11); xlabel('Angle of Attack (\alpha)');
ylabel('Lift, Drag or Side Force');
print -djpeg FORCES_VS_ALPHA_90MPH_Fence2

%***************5.- Side Force Coefficient C_y VS ALPHA
PLOT**********************************

figure(7);
plot(alpha_Corrected,Coefficients(:,3),'b.-.');
grid on;
title('\it C_Y vs \alpha Fence 2 (90 mph)','FontWeight','bold','FontSize',11);
xlabel('Angle of Attack (\alpha)'); ylabel('Side Force Coefficient (C_Y)');
print -djpeg SIDEFORCE_COEFF_VS_ALPHA_90MPH_Fence2

%***************6.- Rolling moment (Cl cg) VS ALPHA
PLOT**********************************

figure(8);
plot(alpha_Corrected,Corrected_Moment_Coefficients(:,1),'b.-.');
grid on;
title('\it C_l (roll moment)vs \alpha Fence 2 (90
mph)','FontWeight','bold','FontSize',11); xlabel('Angle of Attack (\alpha)');
ylabel('Rolling Moment Coefficent(C_l_c_g)');
print -djpeg ROLLING_MOMENT_VS_ALPHA_90MPH_Fence2

%***************7.- YAW moment (Cn cg) VS ALPHA PLOT*********************************

figure(9);
plot(alpha_Corrected,Corrected_Moment_Coefficients(:,3),'b.-.');
grid on;
title('\it C_n_c_g vs \alpha Fence 2 (90 mph)','FontWeight','bold','FontSize',11);
xlabel('Angle of Attack (\alpha)'); ylabel('Yaw Moment Coefficent(C_n_c_g)');
print -djpeg YAW_MOMENT_VS_ALPHA_90MPH_Fence2

%***************8.- Pitching moment (Cm cg) VS ALPHA
PLOT**********************************

figure(10);
plot(alpha_Corrected,Corrected_Moment_Coefficients(:,2),'b.-.');
grid on;
title('\it C_m_c_g vs \alpha Fence 2 (90 mph)','FontWeight','bold','FontSize',11);
xlabel('Angle of Attack (\alpha)'); ylabel('Pitch Moment Coefficent(C_m_c_g)');
print -djpeg PITCHING_MOMENT_VS_ALPHA_90MPH_Fence2

%***************9.- L/D VS ALPHA PLOT*********************************

figure(11);
plot(alpha_Corrected,L_over_D,'b.-.'); grid on;
title('\it L/D vs \alpha Fence 2 (90 mph)','FontWeight','bold','FontSize',11);
xlabel('Angle of Attack (\alpha)'); ylabel('L/D');
print -djpeg L_over_D_VS_ALPHA_90MPH_Fence2
```

Appendix C: Additional Supporting Wind Tunnel Plots

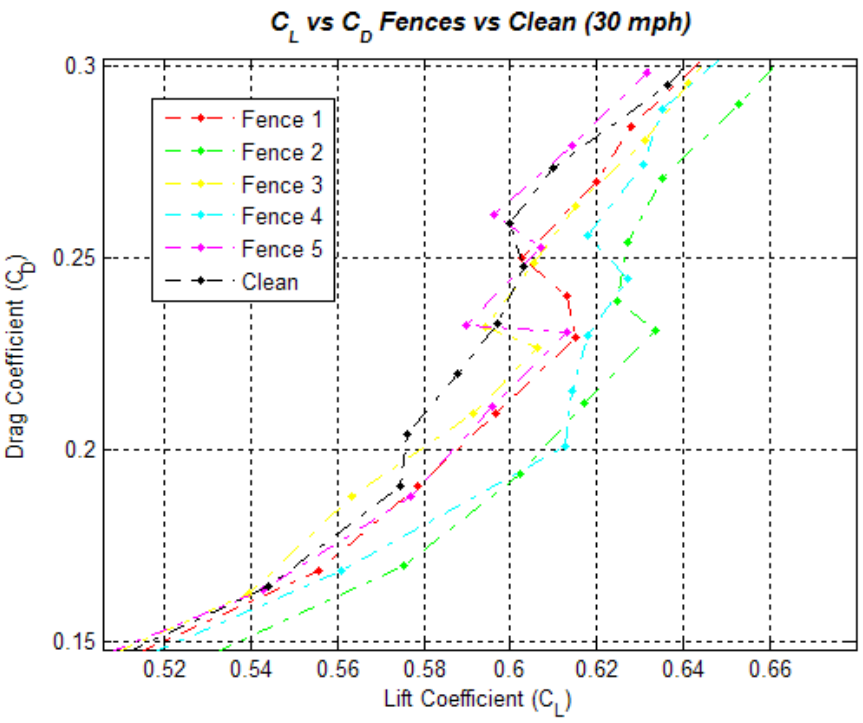

Figure 143. Drag Polar – Zoom-in Fence Comparisons (30 mph)

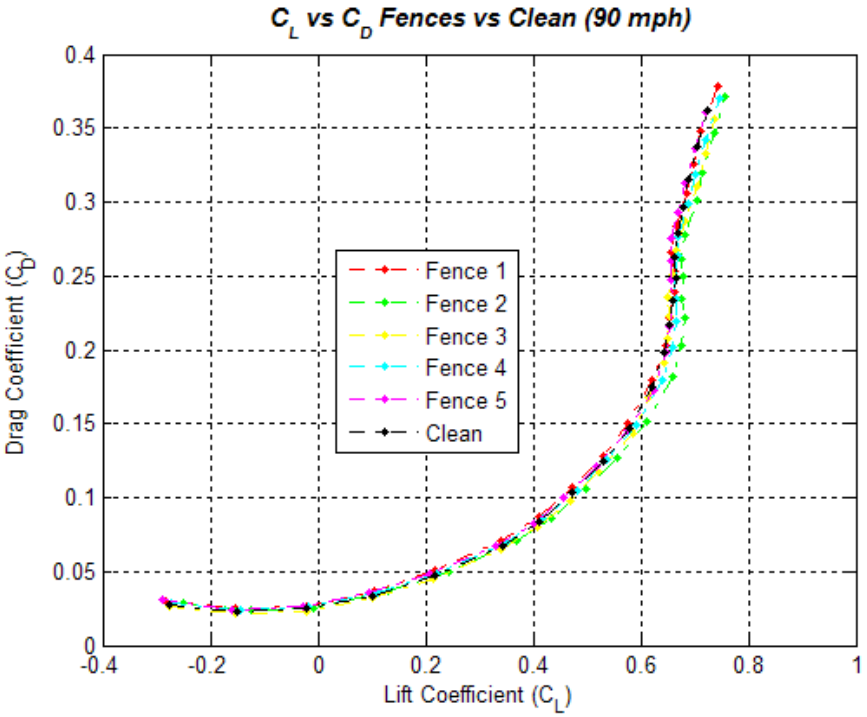

Figure 144. Drag Polar – Fence Comparisons (90 mph)

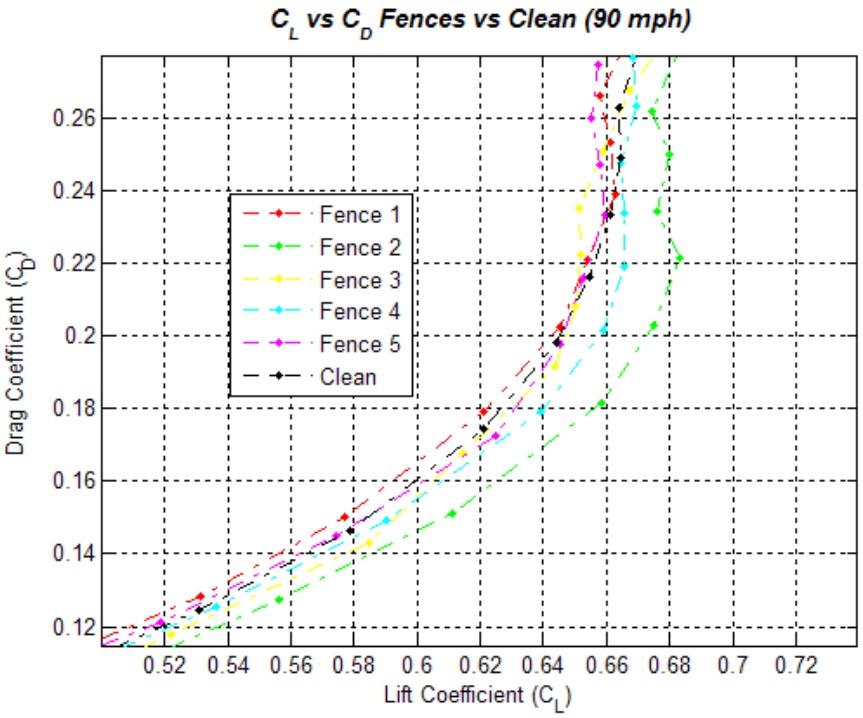

Figure 145. Drag Polar – Zoom-in Fence Comparisons (90 mph)

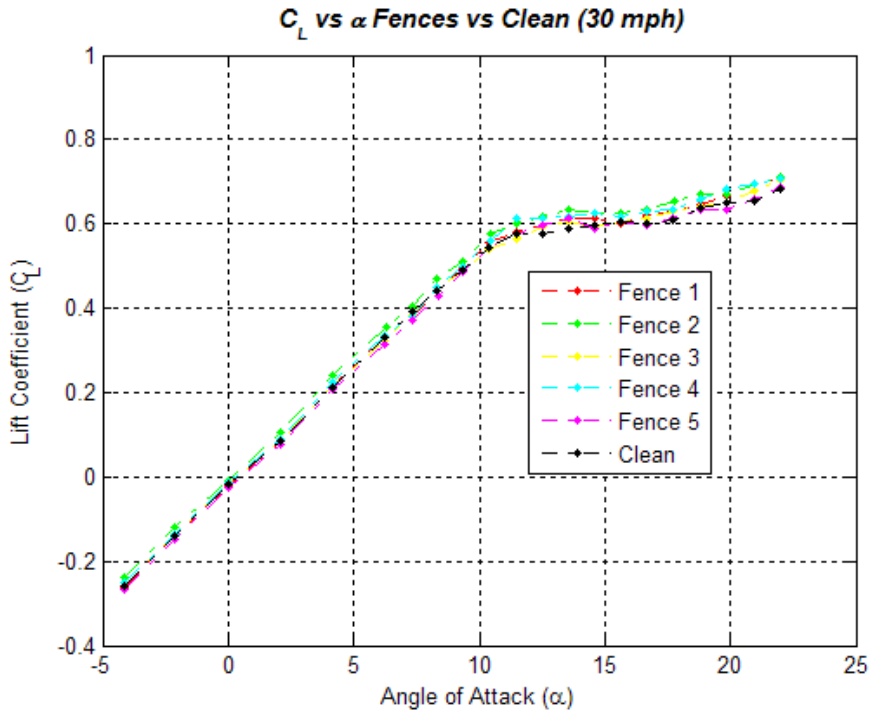

Figure 146. Lift Curve –Fence Comparisons (30 mph)

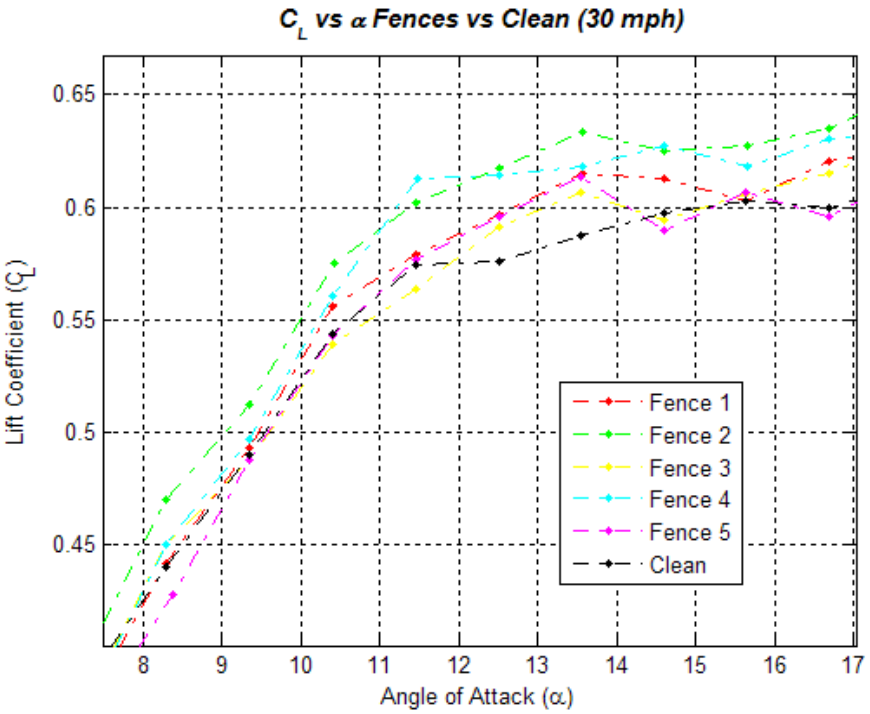

Figure 147. Lift Curve – Zoom-in Fence Comparisons (30 mph)

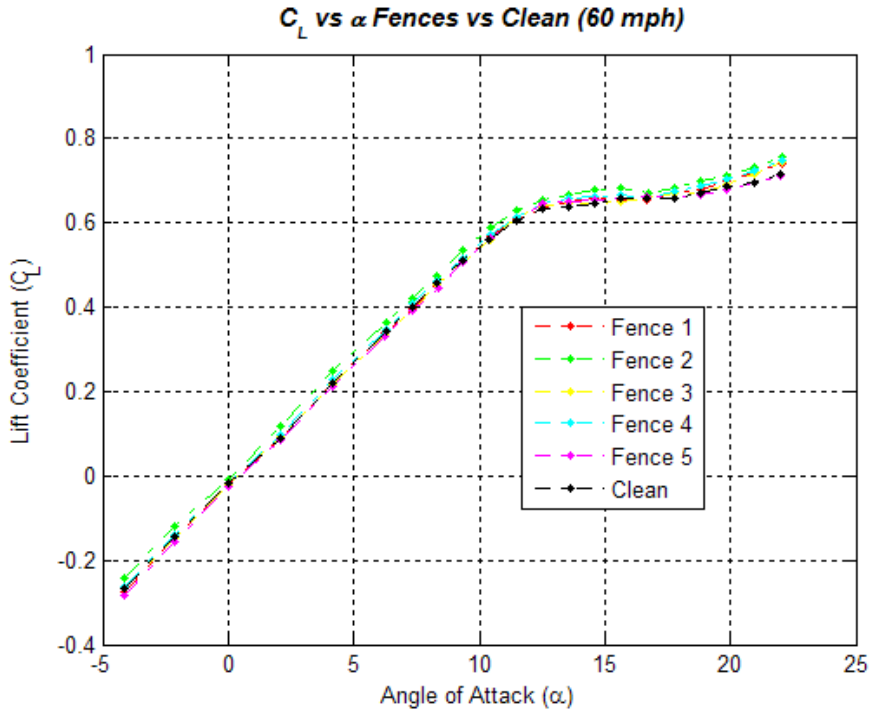

Figure 148. Lift Curve –Fence Comparisons (60 mph)

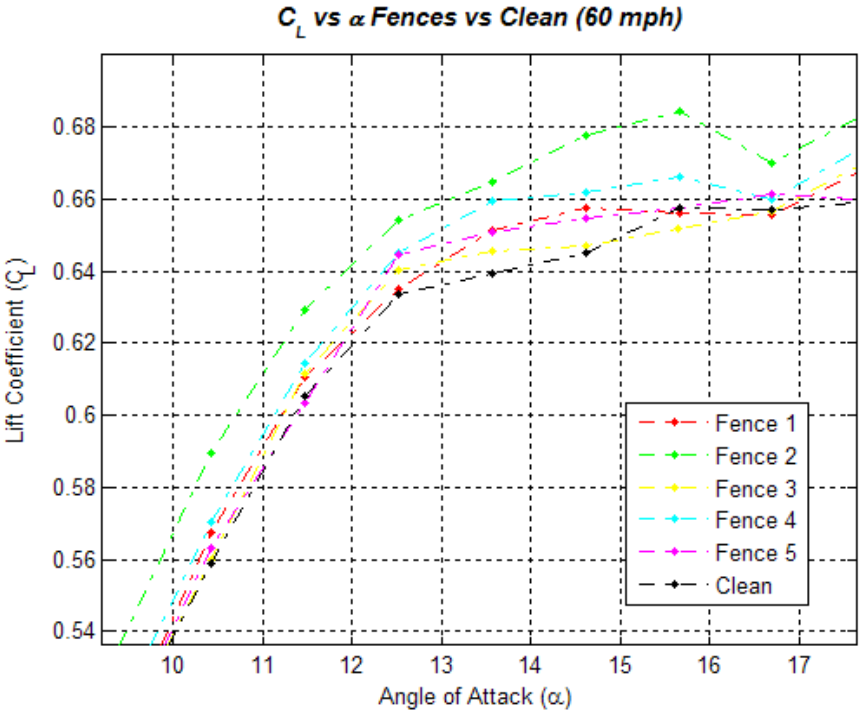

Figure 149. Lift Curve – Zoom-in Fence Comparisons (60 mph)

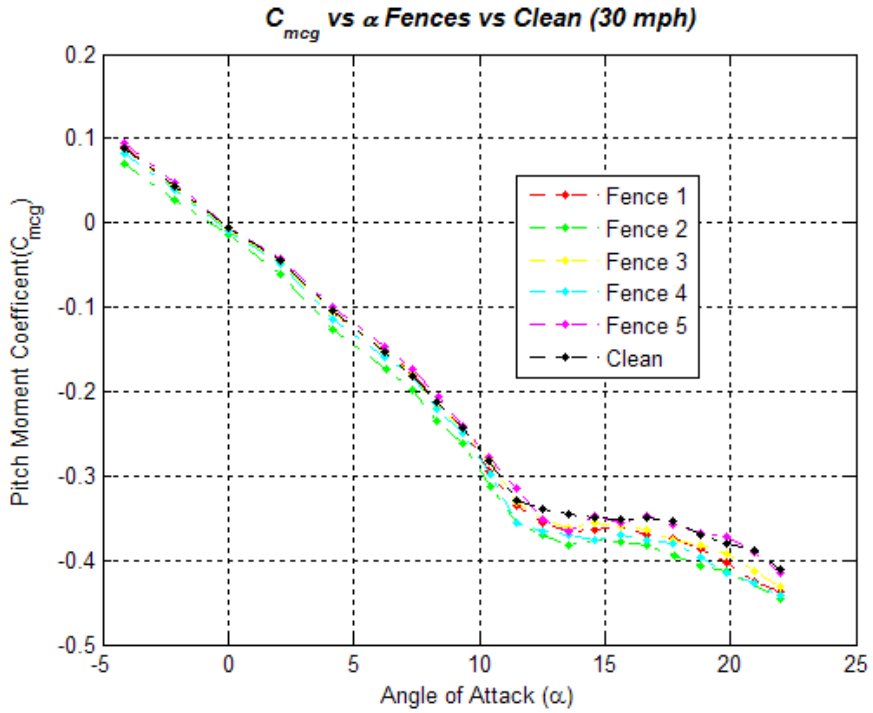

Figure 150. Pitching Moment Coefficient – Fence Comparisons (30 mph)

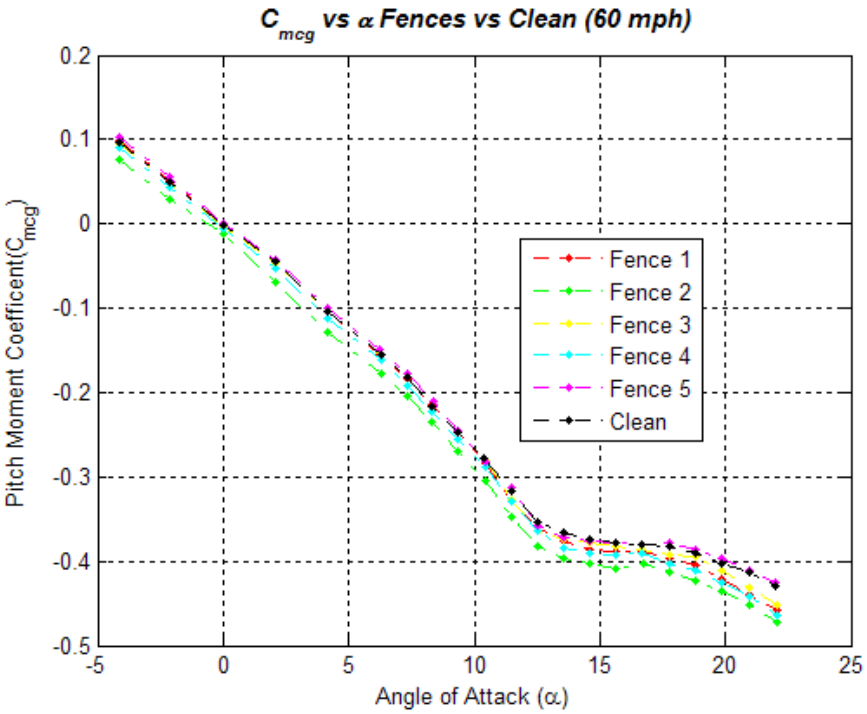

Figure 151. Pitching Moment Coefficient – Fence Comparisons (60 mph)

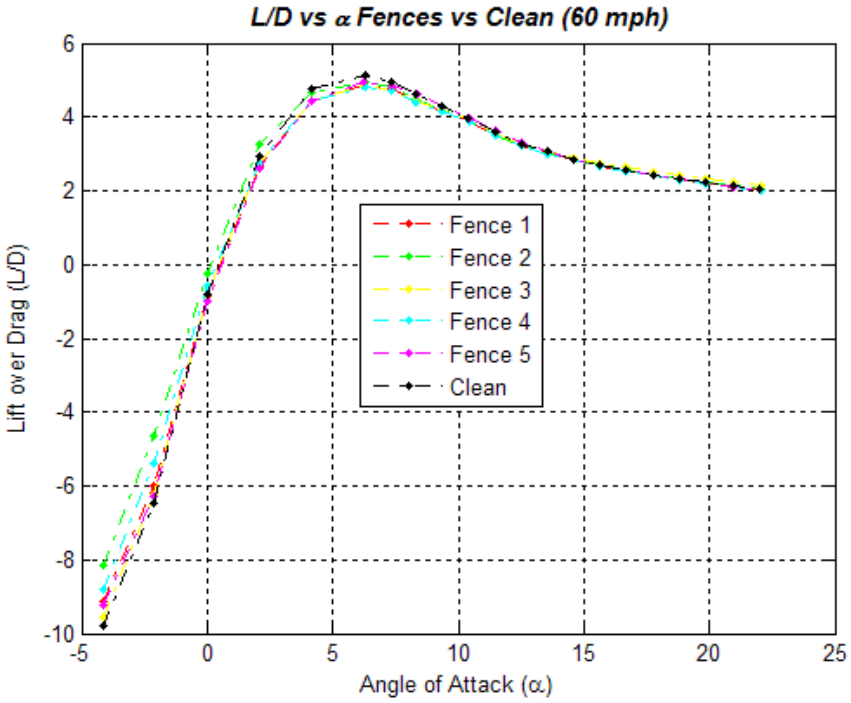

Figure 152. Lift-to-Drag – Fence Comparisons (60 mph)

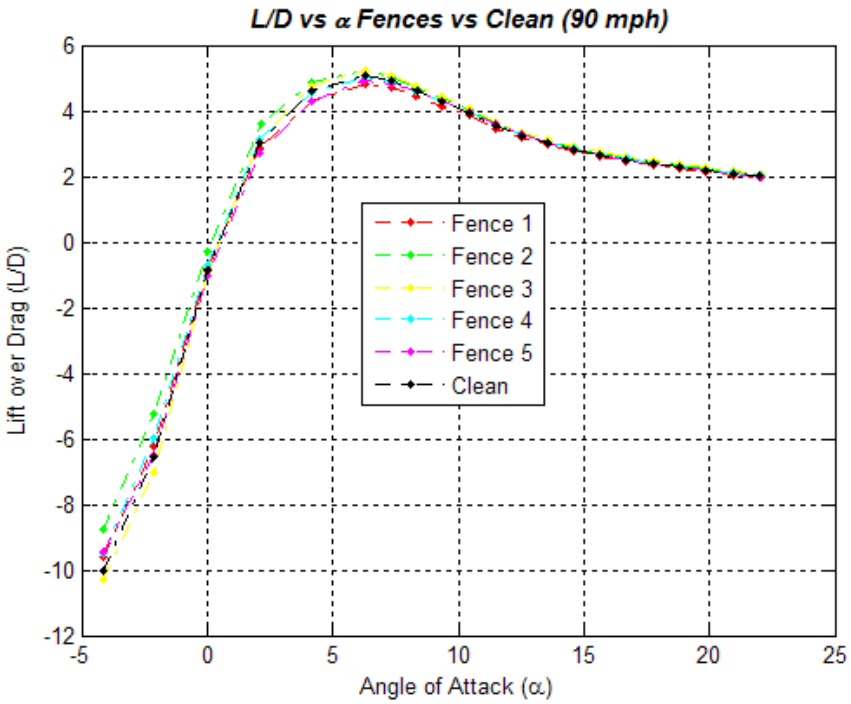

Figure 153. Lift-to-Drag – Fence Comparisons (90 mph)

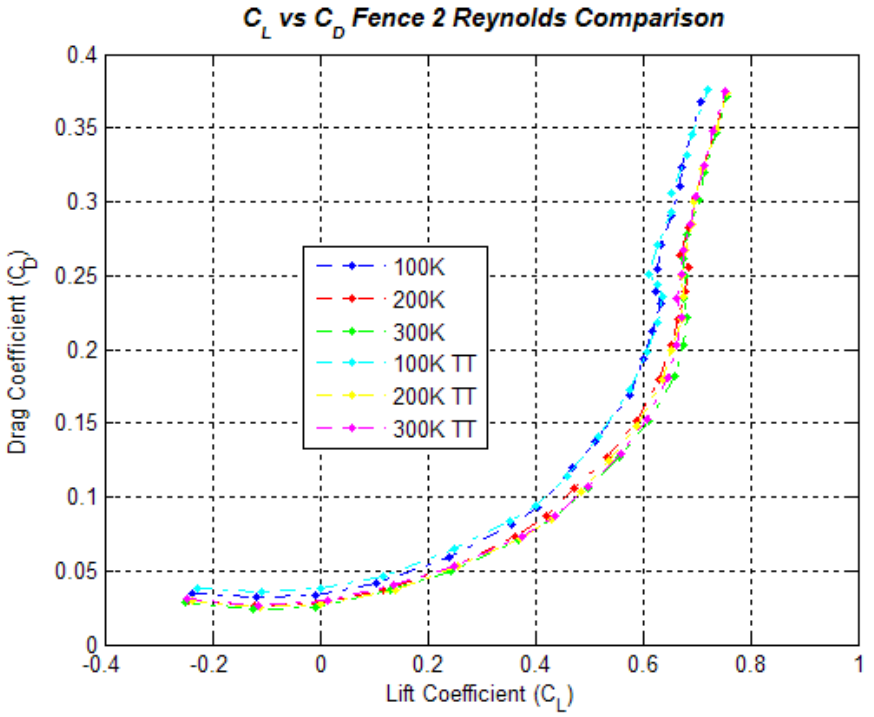

Figure 154. Fence 2 Drag Polar – Reynolds and Trip Tape Comparisons

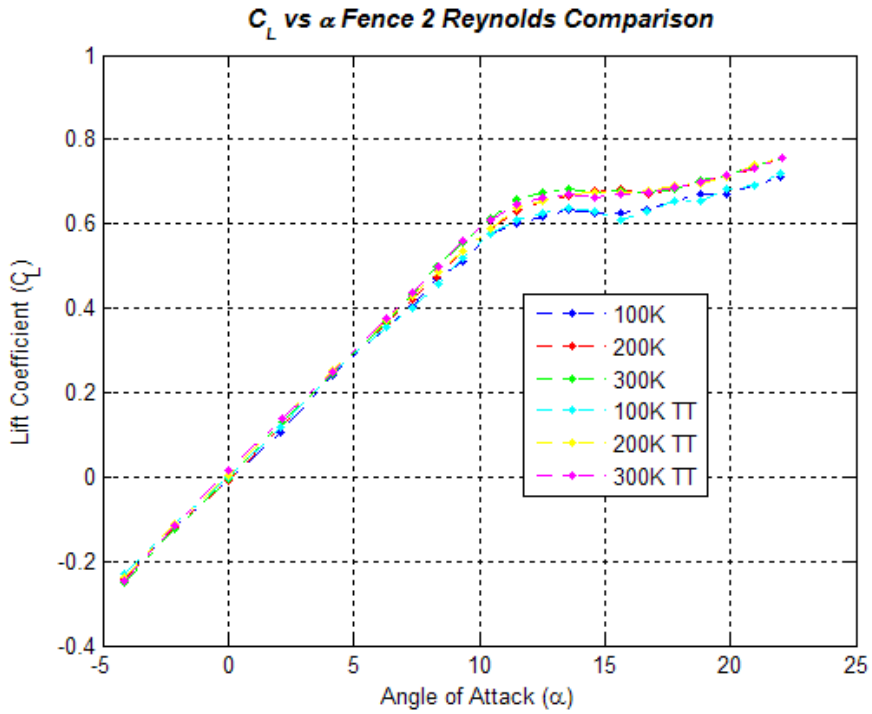

Figure 155. Fence 2 Lift Curve – Reynolds and Trip Tape Comparisons

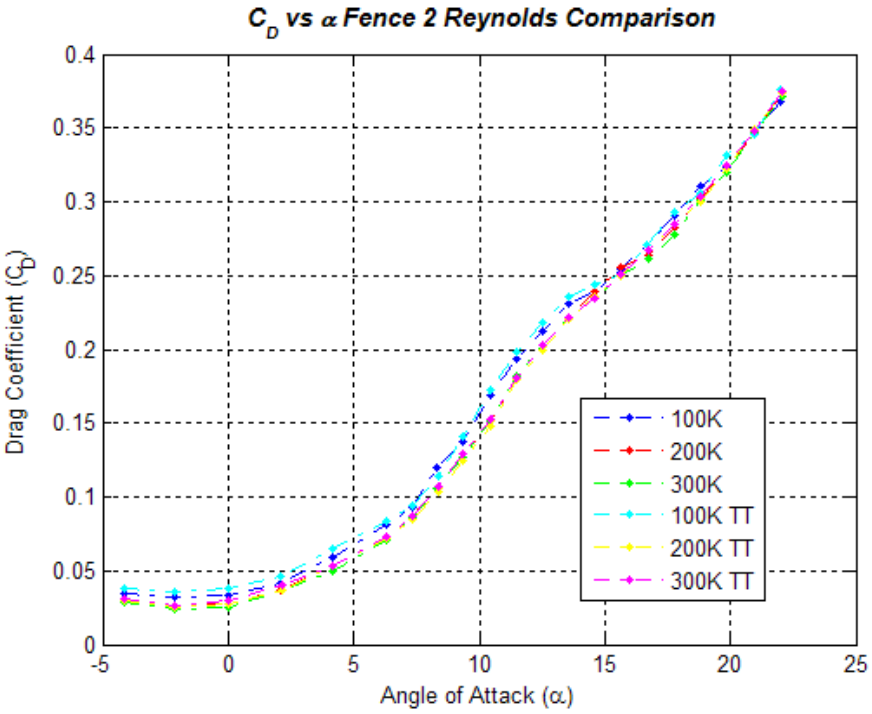

Figure 156. Fence 2 Drag – Reynolds and Trip Tape Comparisons

Appendix D: Wind Tunnel Run Tracker

Table 14. Wind Tunnel Run Tracker

Test Runs Tracker

Configurations	0	Clean Wing	Baseline	TT = Trip Tape					
	1	Fence 1	Wrap / 100% c	.013" thick at 10% chord					
	2	Fence 2	Wrap / 84.6% c matches Dan's						
	3	Fence 3	Wrap / 50% c						
	4	Fence 4	Wrap / 50% c / taper						
	5	Fence 5	Simple / 84.7% c					adj_output for axially adjusted files	
	6	Fuselage Only							

Configuration	Date / Time	Temperature	Pressure	Velocity	AOA range	Tare Filename	Data Filename	Output Filename
1	25-Sep-07	73.2	14.23	30	-4:16.5	Williams_T38_tare_AOAmin5to20_fence1	Williams_T38_30MPH_AOAmin4to15_fence1	output_Williams_T38_30MPH_AOAmin4to15_fence1
1	25-Sep-07	73.2	14.23	60	-4:13.4	Williams_T38_tare_AOAmin5to20_fence1	Williams_T38_60MPH_AOAmin4to15_fence1	output_Williams_T38_60MPH_AOAmin4to15_fence1
1	25-Sep-07	73.2	14.23	90	-4:15.5	Williams_T38_tare_AOAmin5to20_fence1	Williams_T38_90MPH_AOAmin4to15_fence1	output_Williams_T38_90MPH_AOAmin4to15_fence1
1	25-Sep-07	75.6	14.23	30	0	Williams_T38_tare_AOAmin5to20_fence1	Williams_T38 30MPH AOA=none fence1	N/A
1	25-Sep-07	75.6	14.23	60	0	Williams_T38_tare_AOAmin5to20_fence1	Williams_T38 60MPH AOA=none fence1	N/A
1	25-Sep-07	75.6	14.23	90	0	Williams_T38_tare_AOAmin5to20_fence1	Williams_T38 90MPH AOA=none fence1	N/A
0	26-Sep-07	73.7	29.0119	30	-4:22	Williams_T38_tare_AOAmin5to22_clean	Williams_T38_30MPH_AOAmin4to22_clean	output_Williams_T38_30MPH_AOAmin4to22_clean
0	26-Sep-07	73.7	29.0119	60	-4:22	Williams_T38_tare_AOAmin5to22_clean	Williams_T38_60MPH_AOAmin4to22_clean	output_Williams_T38_60MPH_AOAmin4to22_clean
0	26-Sep-07	73.7	29.0119	90	-4:22	Williams_T38_tare_AOAmin5to22_clean	Williams_T38_90MPH_AOAmin4to22_clean	output_Williams_T38_90MPH_AOAmin4to22_clean
2	26-Sep-07	74.2	29.0176	30	-4:22	Williams_T38_tare_AOAmin5to22_fence2	Williams_T38_30MPH_AOAmin4to22_fence2	output_Williams_T38_30MPH_AOAmin4to22_fence2
2	26-Sep-07	74.2	29.0176	60	-4:22	Williams_T38_tare_AOAmin5to22_fence2	Williams_T38_60MPH_AOAmin4to22_fence2	output_Williams_T38_60MPH_AOAmin4to22_fence2
2	26-Sep-07	75.8	29.0254	90	-4:22	Williams_T38_tare_AOAmin5to22_fence2	Williams_T38_90MPH_AOAmin4to22_fence2	output_Williams_T38_90MPH_AOAmin4to22_fence2
1	26-Sep-07	74.8	29.0231	30	-4:22	Williams_T38_tare_AOAmin5to22_fence1B	Williams_T38_30MPH_AOAmin4to22_fence1B	output_Williams_T38_30MPH_AOAmin4to22_fence1B
1	26-Sep-07	74.8	29.0231	60	-4:22	Williams_T38_tare_AOAmin5to22_fence1B	Williams_T38_60MPH_AOAmin4to22_fence1B	output_Williams_T38_60MPH_AOAmin4to22_fence1B
1	26-Sep-07	76.4	29.0257	90	-4:22	Williams_T38_tare_AOAmin5to22_fence1B	Williams_T38_90MPH_AOAmin4to22_fence1B	output_Williams_T38_90MPH_AOAmin4to22_fence1B
4	26-Sep-07	75.4	29.0234	30	-4:22	Williams_T38_tare_AOAmin5to22_fence4	Williams_T38_30MPH_AOAmin4to22_fence4	output_Williams_T38_30MPH_AOAmin4to22_fence4
4	26-Sep-07	75.4	29.0234	60	-4:22	Williams_T38_tare_AOAmin5to22_fence4	Williams_T38_60MPH_AOAmin4to22_fence4	output_Williams_T38_60MPH_AOAmin4to22_fence4
4	26-Sep-07	76.1	29.022	90	-4:22	Williams_T38_tare_AOAmin5to22_fence4	Williams_T38_90MPH_AOAmin4to22_fence4	output_Williams_T38_90MPH_AOAmin4to22_fence4
0	26-Sep-07	73.5	28.9897	30	-4:22	Williams_T38_tare_AOAmin5to22_cleanB	Williams_T38_30MPH_AOAmin4to22_cleanB	output_Williams_T38_30MPH_AOAmin4to22_cleanB
0	26-Sep-07	73.5	28.9897	60	-4:22	Williams_T38_tare_AOAmin5to22_cleanB	Williams_T38_60MPH_AOAmin4to22_cleanB	output_Williams_T38_60MPH_AOAmin4to22_cleanB
0	26-Sep-07	75.1	28.9838	90	-4:22	Williams_T38_tare_AOAmin5to22_cleanB	Williams_T38_90MPH_AOAmin4to22_cleanB	output_Williams_T38_90MPH_AOAmin4to22_cleanB
0	27-Sep-07	74.5	28.9241	30	-4:22	Williams_T38_tare_AOAmin4to22_cleanC	Williams_T38_30MPH_AOAmin4to22_cleanC	output_Williams_T38_30MPH_AOAmin4to22_cleanC
0	27-Sep-07	74.6	28.9214	60	-4:22	Williams_T38_tare_AOAmin4to22_cleanC	Williams_T38_60MPH_AOAmin4to22_cleanC	output_Williams_T38_60MPH_AOAmin4to22_cleanC
0	27-Sep-07	75.1	29.9193	90	-4:22	Williams_T38_tare_AOAmin4to22_cleanC	Williams_T38_90MPH_AOAmin4to22_cleanC	output_Williams_T38_90MPH_AOAmin4to22_cleanC
5	27-Sep-07	73.7	28.9229	30	-4:22	Williams_T38_tare_AOAmin4to22_fence5	Williams_T38_30MPH_AOAmin4to22_fence5	output_Williams_T38_30MPH_AOAmin4to22_fence5
5	27-Sep-07	74.7	28.9194	60	-4:22	Williams_T38_tare_AOAmin4to22_fence5	Williams_T38_60MPH_AOAmin4to22_fence5	output_Williams_T38_60MPH_AOAmin4to22_fence5
5	27-Sep-07	74.5	28.9148	90	-4:22	Williams_T38_tare_AOAmin4to22_fence5	Williams_T38_90MPH_AOAmin4to22_fence5	output_Williams_T38_90MPH_AOAmin4to22_fence5
3	28-Sep-07	74.9	29.1113	30	-4:22	Williams_T38_tare_AOAmin4to22_fence3	Williams_T38_30MPH_AOAmin4to22_fence3	output_Williams_T38_30MPH_AOAmin4to22_fence3
3	28-Sep-07	74.9	29.1193	60	-4:22	Williams_T38_tare_AOAmin4to22_fence3	Williams_T38_60MPH_AOAmin4to22_fence3	output_Williams_T38_60MPH_AOAmin4to22_fence3
3	28-Sep-07	76.4	29.1198	90	-4:22	Williams_T38_tare_AOAmin4to22_fence3	Williams_T38_90MPH_AOAmin4to22_fence3	output_Williams_T38_90MPH_AOAmin4to22_fence3
6	2-Oct-07	74.9	29.03	30	-4:22	Williams_T38_tare_AOAmin4to22_fuselage	Williams_T38_30MPH_AOAmin4to22_fuselage	output_Williams_T38_30MPH_AOAmin4to22_fuselage
6	2-Oct-07	75	29.028	60	-4:22	Williams_T38_tare_AOAmin4to22_fuselage	Williams_T38_60MPH_AOAmin4to22_fuselage	output_Williams_T38_60MPH_AOAmin4to22_fuselage
6	2-Oct-07	76.2	29.0222	90	-4:22	Williams_T38_tare_AOAmin4to22_fuselage	Williams_T38_90MPH_AOAmin4to22_fuselage	output_Williams_T38_90MPH_AOAmin4to22_fuselage
0TT	2-Oct-07	74.8	29.0155	30	-4:22	Williams_T38_tare_AOAmin4to22_cleantriptape	Williams_T38_30MPH_AOAmin4to22_cleantriptape	output_Williams_T38_30MPH_AOAmin4to22_cleantriptape
0 TT	2-Oct-07	74.8	29.013	60	-4:22	Williams_T38_tare_AOAmin4to22_cleantriptape	Williams_T38_60MPH_AOAmin4to22_cleantriptape	output_Williams_T38_60MPH_AOAmin4to22_cleantriptape
0 TT	2-Oct-07	75.3	29.0098	90	-4:22	Williams_T38_tare_AOAmin4to22_cleantriptape	Williams_T38_90MPH_AOAmin4to22_cleantriptape	output_Williams_T38_90MPH_AOAmin4to22_cleantriptape
2 TT	2-Oct-07	74.9	29.006	30	-4:22	Williams_T38_tare_AOAmin4to22_fence2_triptape	Williams_T38_30MPH_AOAmin4to22_fence2_triptape	output_Williams_T38_30MPH_AOAmin4to22_fence2_triptape
2 TT	2-Oct-07	75.1	29.0024	60	-4:22	Williams_T38_tare_AOAmin4to22_fence2_triptape	Williams_T38_60MPH_AOAmin4to22_fence2_triptape	output_Williams_T38_60MPH_AOAmin4to22_fence2_triptape
2 TT	2-Oct-07	75.9	29.0019	90	-4:22	Williams_T38_tare_AOAmin4to22_fence2_triptape	Williams_T38_90MPH_AOAmin4to22_fence2_triptape	output_Williams_T38_90MPH_AOAmin4to22_fence2_triptape

Appendix E: T-38 Aircraft and Wind Tunnel Model Dimensions

Table 15. T-38 Aircraft and Model Dimensions

T-38 Characteristics	Aircraft				CAD Model				Scaled	1:21		
Wing Span	303	inches	25.25	feet	303	inches	25.25	feet	14.43	inches	1.2024	feet
Length	556.4	inches	46.37	feet	463	inches	38.58	feet	22.05	inches	1.84	feet
Height	154.6	inches	12.88	feet	62.202	inches	5.1835	feet	2.96	inches	0.25	feet
NACA Airfoil	65A004.8-64	w/ 1% chord contrast leading edge droop										
		mod with .65 (50) camber										
Wing Area (Total)	170	sq ft					170	sq ft	55.48	in^2	0.3853	sq ft
MAC	92.76	inches	7.73	feet	92.76	inches	7.73	feet	4.42	inches	0.3681	feet
Span / Thickness	51.1											
Overall Thickness Ratio	4.80	%										
Wing Sweep Leading Edge	32	deg										
Wing Sweep c/4	24	deg										
Taper Ratio	0.2											
AR	3.75											
Dihedral	0	deg										
Incidence	0	deg										
Wing Tip Seam (dist from tip)	26.5	inches	82.51	% span					1.2619	inches		
Seam "Jink" Angle @ L.E.	10.31	deg										
Max Thickness at Seam	2.180	inches	assumes symmetry about Zw plane						0.104	inches		
Chord length at seam based on equation	45.42	inches							2.16	inches		
Root chord length	134.65	inches							6.412	inches		
Tip chord length	26.93	inches							1.28	inches		
Tip Max Thickness	1.293	inches	assumes symmetry about Zw plane						0.062	inches		
Flap Area (Total)	18.88	sq ft										
Flap Span (Total)	7.53	feet										
Flaps (60%)	20 deg											
Flaps (100%)	45 deg											
Aileron Area (aft of hinge)	9.18	sq ft										
Aileron Span (Total)	5.31	feet										
Aileron Deflection Limits	35	deg up										
Aileron Deflection Limits	25	deg down										
Assorted Data												
Model Volume (Magics)	75	in^3	0.0434	ft^3								
Model Surface Area (Magics)	308	in^2	2.1389	ft^2								
Fuselage Volume (Magics)	66	in^3	0.0382	ft^3								
Fuselage Surface Area (Magics)	252	in^2	1.7500	ft^2								
Wing Volume (Magics)	9	in^3	0.0052	ft^3								
Wing Surface Area (Magics)	107	in^2	0.7431	ft^2								
Fuselage Dimensions (l,w,h) inches	22.05	3.5	2.96	for separate pieces								
Wing Dimensions (l,w,h) inches	5.3	14.43	0.78	for separate pieces								
Gridgen Nose (x,y,z) inches	0	2.5	-0.395	This checks with T-38 Reference Datum								
Northrop Data **Global** Origin Loc (x,y,z) inches	0	52.5	6	in front of nose (y) and above rear cockpit floor (z)								
Northrop Data Wing Data Ref Location (x,y,z)	0	14.02381	0	centerline (x), wing L.E. and centerline intersection (y), and fuselage reference line (z)								
Balance Moment Center Gridgen (x,y,z) inches	0	15.08109	0.5664	scale/global coordinates								
Dist btwn balance mom ctr and wing data Ref loc	0	1.0573	0.5664									
Dist btwn balance mom ctr and Ref CG Loc	0	1.5339	-0.5664	note: in code y & x swapped								
Reference Loc - CG at Landing (19.1% MAC)	0	16.615	0	Assuming z component on Z=0								
Model CG (x,y,z) Polyworks	0	14.6313	0.1871	Assumes constant density								
Model Weights	kg	lb	oz									
Fuselage	1.3	2.9	46									
Wing w/ full fence	0.2	0.4	8									
Total	1.5	3.3	54									

Appendix F: Wind Tunnel Velocity Matrix

Table 16. Tunnel Velocities - Based on Model, Balance, and Tunnel Limitations

Finding velocities the tunnel can be run at with certain parameters.

Model Scaling 1:21
Based on Standard Atmosphere @ Sea Level

rho	0.002377	slug/ft^3
S	0.3853	ft^2
MAC	0.3681	ft
mu	0.000000384	lbf s/ft^2
a	1116.44	ft/s

AOA	CL
5	0.35
10	0.7
15	0.8
20	0.85
25	0.9

For Real Aircraft

	Vel (kts)
NF Touchdown Speed	145
NF Approach Speed	170
NF Final Turn Speed	190

NF = No Flap

Model Weights

Fuselage	2.9 lb
Wings	.4 lb
Total	3.3 lb

Lift Force = lb

MAC	7.73	ft
	Vel (ft/s)	Re#
	244.73245	1.1710E+07
	286.9277	1.3729E+07
	320.6839	1.5345E+07

Velocity (mph)	Velocity (ft/s)	RE#	Mach Number	Lift (5 deg AOA)	Lift (10 deg AOA)	Lift (15 deg AOA)	Lift (20 deg AOA)	Lift (25 deg AOA)
10	14.67	3.3419E+04	0.013	0.03	0.07	0.08	0.08	0.09
15	22.00	5.0129E+04	0.020	0.08	0.16	0.18	0.19	0.20
20	29.33	6.6838E+04	0.026	0.14	0.28	0.32	0.33	0.35
25	36.67	8.3548E+04	0.033	0.22	0.43	0.49	0.52	0.55
30	44.00	1.0026E+05	0.039	0.31	0.62	0.71	0.75	0.80
35	51.33	1.1697E+05	0.046	0.42	0.84	0.97	1.03	1.09
40	58.67	1.3368E+05	0.053	0.55	1.10	1.26	1.34	1.42
45	66.00	1.5039E+05	0.059	0.70	1.40	1.60	1.70	1.80
50	73.33	1.6710E+05	0.066	0.86	1.72	1.97	2.09	2.22
55	80.67	1.8381E+05	0.072	1.04	2.09	2.38	2.53	2.68
60	88.00	2.0051E+05	0.079	1.24	2.48	2.84	3.01	3.19
65	95.33	2.1722E+05	0.085	1.46	2.91	3.33	3.54	3.75
70	102.67	2.3393E+05	0.092	1.69	3.38	3.86	4.10	4.34
75	110.00	2.5064E+05	0.099	1.94	3.88	4.43	4.71	4.99
80	117.33	2.6735E+05	0.105	2.21	4.41	5.04	5.36	5.67
85	124.67	2.8406E+05	0.112	2.49	4.98	5.69	6.05	6.41
90	132.00	3.0077E+05	0.118	2.79	5.59	6.38	6.78	7.18
95	139.33	3.1748E+05	0.125	3.11	6.22	7.11	7.56	8.00
100	146.67	3.3419E+05	0.131	3.45	6.90	7.88	8.37	8.87
105	154.00	3.5090E+05	0.138	3.80	7.60	8.69	9.23	9.77
110	161.33	3.6761E+05	0.145	4.17	8.34	9.54	10.13	10.73
115	168.67	3.8432E+05	0.151	4.56	9.12	10.42	11.07	11.72
120	176.00	4.0103E+05	0.158	4.96	9.93	11.35	12.06	12.77
125	183.33	4.1774E+05	0.164	5.39	10.77	12.31	13.08	13.85
130	190.67	4.3445E+05	0.171	5.83	11.65	13.32	14.15	14.98
135	198.00	4.5116E+05	0.177	6.28	12.57	14.36	15.26	16.16
140	205.33	4.6787E+05	0.184	6.76	13.51	15.45	16.41	17.38
145	212.67	4.8458E+05	0.190	7.25	14.50	16.57	17.60	18.64

Appendix G: Flight Test Accelerometer Corrections for Center of Gravity

x-accelerometer z-accelerometer

$l_{xx}=x_{cg} - p_{xx}$ $l_{xz}=x_{cg} - p_{xz}$

x-distance from center of gravity to accelerometer, positive foward

$l_{zx}=z_{cg} - p_{zx}$ $l_{zz}=z_{cg} - p_{zz}$

x-distance from center of gravity to accelerometer, positive down

Each of the variables on the right hand side of the equations above were distances from the (0,0,0) reference point for the x and z center of gravity locations in the equations:

$$N_{xcg} = N_{xaccel} + \frac{l_{xx}}{g} \cdot (q^2 + r^2) + \frac{l_{yx}}{g} \cdot (\dot{r} - p \cdot q) - \frac{l_{zx}}{g} \cdot (\dot{q} - p \cdot r)$$

$$N_{zcg} = N_{zaccel} - \frac{l_{zz}}{g} \cdot (q^2 + r^2) - \frac{l_{xz}}{g} \cdot (\dot{q} - r \cdot p) + \frac{l_{yz}}{g} \cdot (\dot{p} + q \cdot r)$$

where g = *gravity* and N_{xaccel} and N_{zaccel} were equations:

N_{xaccel} = longitudinal load factor at the x-accelerometer = $\frac{X}{g}$

N_{zaccel} = normal load factor at the z-accelerometer = $-\frac{Z}{g}$

Where X, Z = measured accelerations from the x- and z-accelerometers

N_{xcg}, N_{zcg} = longitudinal and normal load factors corrected to the center of gravity

Assuming that yaw and roll rates were zero, the above equations simplify to:

$$N_{xcg} = N_{xaccel} + \frac{l_{xx}}{g} \cdot (q^2) + \frac{l_{zx}}{g} \cdot (\dot{q})$$

$$N_{zcg} = N_{zaccel} - \frac{l_{zz}}{g} \cdot (q^2) - \frac{l_{xz}}{g} \cdot (\dot{q})$$

Appendix H: Flight Test Engine Trim Cards

J85-5 ENGINE TRIM SHEET ENG S/N 130817 DATE 20080320 CELL # 3
REASON FOR TEST AB mp 2.1c INCOMING TAG TEMP 665°C 1229°F
STATIC THRUST -12 LBS

PARAMETER	UNIT	IDLE	MIL	MAX
RPM	%RPM	49.3	99.8	99.8
EGT	F	878	1229	1229
OIL PRESS	PSID	10.7	32.1	32.5
A/C OIL PRESS	PSID	9.1	31.0	31.3
OIL TEMP	F	251	257.9	251
OIL TANK PRESS	PSIG	4.6	5.4	5.3
MAIN SUMP PRESS	PSIG	.2	12.9	12.8
A/C FUEL FLOW	PPH	552	2404	
TARGET FUEL FLOW	PPH		2450	
CELL FUEL FLOW	PPH	447	2387	7921
NOZZLE POSITION	0-100	81.3	6.1	69.0
CDP	PSIG	6.7	69.7	69.8
CIT	F	69	66	66
CELL BAROMETER	IN/HGA	27.6	27.6	27.6
THRUST	LBS	48	2475	3544
FUEL INLET PRESS	PSIG		31.1	29.7
VIB 1	MILS	.8	1.0	1.1
VIB 2	MILS	.2	.4	.5
VIB 3	MILS	.4	.7	.7

VIB 1 S/N ~~20055~~ 20168 2 20114 3 20109
VIB SENS ~~115.164~~ 103.155 2 101.418 3 103.337

(WET) MOTOR CHECK AT 12% RPM
FUEL FLOW 284 PPH

START CHECK AT 12-14% RPM
BREAKOUT FUEL FLOW 342 PPH
LIGHT OFF TIME 3 SECONDS
START TIME 10 SECONDS

OSG CHECK
STABILIZED CUT IN SPEED 96.5 %RPM

ANTI-ICE CHECK
EGT RISE 19 F CDP DROP 3.1 PSIG
VIB 1 1.2 2 .4 3 .6

BLEED VALVE SCHEDULE CHECK
START TO CLOSE 80.9 %RPM CIT 68 F
START TO OPEN 95.1 %RPM CIT 66 F
AIR LEAK CK 18" AWAY AT MIL 01981

NOZZLE SCHEDULE CHECK
CRUISE FLAT NOZZLE AT 60 PLA 25.6
NOZZLE BREAK POINT 76.0 PLA

VEN AIR LEAK CHECK
IDLE ____ MIL ____ MAX ____

MIN A/B CHECK CDP 69.9 PSIG
PILOT MANIF PRESS 3.4 PSIG

AFTERBURNER CHECKS
A/B IN 97.5 PLA A/B OUT 93.6 PLA
MAX MINUS MIL W/F 5534 PPH

ACCEL CHECKS IDLE TO MIL NOZZLE HESITATES AT 42
THEN CLOSES TO A MIN OF .6 BEFORE OPENING ON T5
IDLE - MIL 5 SEC PEAK EGT 1244F
MIL - MAX 3 SEC PEAK EGT 1359 F ROLLBK TO 98.9 %RPM
88.5 - MAX 6 SEC PEAK EGT 1345 F ROLLBK TO 98.9 %RPM

OIL CONSUMPTION CK 0 OZ/HOUR
OVERBOARD LEAK CHECK 01981
HOT SPOT INSP 00800

PERFORMANCE CHECK MIN REQ'D MIL THRUST ____ LBS MIN REQ'D MAX THRUST ____ LBS
EGT THERMOCOUPLE CHECK EGT MINUS T-5 AMP EGT AT MIL 5 F (LIMIT +-25)

	1	2	3	4	5	6	7	8
STOP	0835	1140	1305	1335				
START	0800	1130	1230	1325				
TOTAL	35	20	35	10				
EGT	1186	1236	1208	1217				
COASTDOWN	46	45	40	40				

CREW CHIEF Cutler OPERATOR Seifert MECHANIC Cabrido
MAIN LOOP RIG CHECK 00860 TAG TEMP OUT 665°C -5R NOZZLE CLOSED N/A
ENGINE ACCEPTED 12 Cutler 0860 ENGINE REJECTED

412 CMS/MXMP J85 RUN CHECKSHEET NOV 2007

Figure 157. Engine #1 Test Cell Trim Sheet – Mar 2008

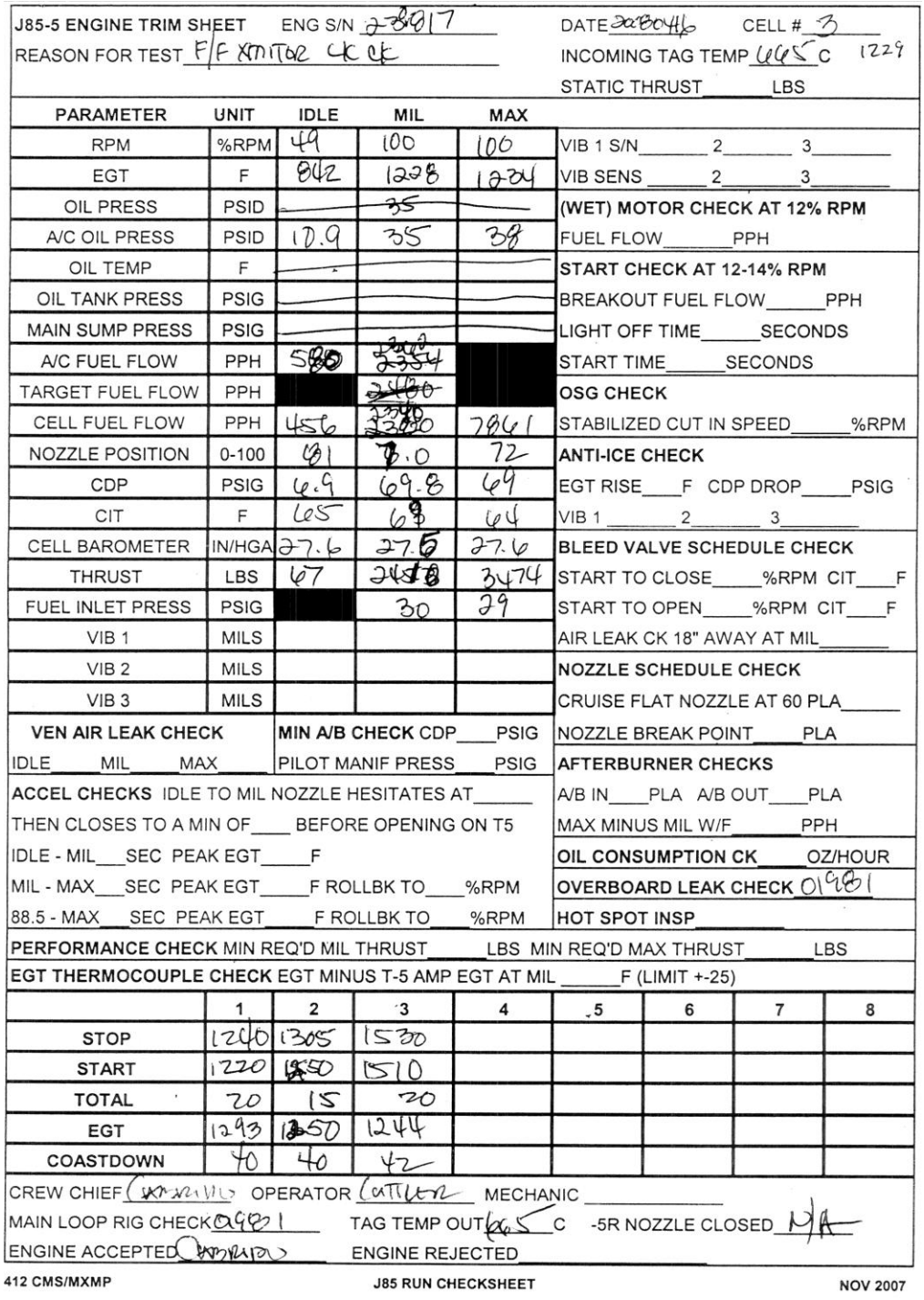

J85-5 ENGINE TRIM SHEET ENG S/N 23817 DATE 20 APR 08 CELL # 3
REASON FOR TEST F/F XMITTER CK CK INCOMING TAG TEMP 65 C 1229
STATIC THRUST _____ LBS

PARAMETER	UNIT	IDLE	MIL	MAX
RPM	%RPM	49	100	100
EGT	F	842	1228	1234
OIL PRESS	PSID		35	
A/C OIL PRESS	PSID	17.9	35	38
OIL TEMP	F			
OIL TANK PRESS	PSIG			
MAIN SUMP PRESS	PSIG			
A/C FUEL FLOW	PPH	580	2354	
TARGET FUEL FLOW	PPH		2340	
CELL FUEL FLOW	PPH	456	2340	7861
NOZZLE POSITION	0-100	81	70	72
CDP	PSIG	6.9	69.8	69
CIT	F	65	69	64
CELL BAROMETER	IN/HGA	27.6	27.6	27.6
THRUST	LBS	67	2418	3474
FUEL INLET PRESS	PSIG		30	29
VIB 1	MILS			
VIB 2	MILS			
VIB 3	MILS			

VIB 1 S/N _____ 2 _____ 3 _____
VIB SENS _____ 2 _____ 3 _____
(WET) MOTOR CHECK AT 12% RPM
FUEL FLOW _____ PPH
START CHECK AT 12-14% RPM
BREAKOUT FUEL FLOW _____ PPH
LIGHT OFF TIME _____ SECONDS
START TIME _____ SECONDS
OSG CHECK
STABILIZED CUT IN SPEED _____ %RPM
ANTI-ICE CHECK
EGT RISE ____ F CDP DROP _____ PSIG
VIB 1 _____ 2 _____ 3 _____
BLEED VALVE SCHEDULE CHECK
START TO CLOSE _____ %RPM CIT ____ F
START TO OPEN _____ %RPM CIT ____ F
AIR LEAK CK 18" AWAY AT MIL _____
NOZZLE SCHEDULE CHECK
CRUISE FLAT NOZZLE AT 60 PLA _____
NOZZLE BREAK POINT _____ PLA
AFTERBURNER CHECKS
A/B IN ____ PLA A/B OUT ____ PLA
MAX MINUS MIL W/F _____ PPH
OIL CONSUMPTION CK _____ OZ/HOUR
OVERBOARD LEAK CHECK 01981
HOT SPOT INSP _____

VEN AIR LEAK CHECK
IDLE _____ MIL _____ MAX _____

MIN A/B CHECK CDP ____ PSIG
PILOT MANIF PRESS ____ PSIG

ACCEL CHECKS IDLE TO MIL NOZZLE HESITATES AT _____
THEN CLOSES TO A MIN OF ____ BEFORE OPENING ON T5
IDLE - MIL ___ SEC PEAK EGT _____ F
MIL - MAX ___ SEC PEAK EGT _____ F ROLLBK TO ____ %RPM
88.5 - MAX ___ SEC PEAK EGT _____ F ROLLBK TO ____ %RPM

PERFORMANCE CHECK MIN REQ'D MIL THRUST _____ LBS MIN REQ'D MAX THRUST _____ LBS

EGT THERMOCOUPLE CHECK EGT MINUS T-5 AMP EGT AT MIL _____ F (LIMIT +-25)

	1	2	3	4	5	6	7	8
STOP	1240	1305	1530					
START	1220	1250	1510					
TOTAL	20	15	20					
EGT	1293	1250	1244					
COASTDOWN	40	40	42					

CREW CHIEF [illegible] OPERATOR CUTLER MECHANIC _____
MAIN LOOP RIG CHECK 01981 TAG TEMP OUT 65 C -5R NOZZLE CLOSED N/A
ENGINE ACCEPTED [illegible] ENGINE REJECTED _____

412 CMS/MXMP J85 RUN CHECKSHEET NOV 2007

Figure 158. Engine #1 Test Cell Trim Sheet – Apr 2008

J85-5 ENGINE TRIM SHEET ENG S/N 232732 DATE 9/24/08 CELL # 3

REASON FOR TEST AB, no Lite INCOMING TAG TEMP 666 C 123/A

STATIC THRUST -9 LBS

PARAMETER	UNIT	IDLE	MIL	MAX
RPM	%RPM	~~49.3~~	100.1	100.2
EGT	F	965	1231	1233
OIL PRESS	PSID	9.7	27	27
A/C OIL PRESS	PSID	18.7	29	26
OIL TEMP	F	271	270	283
OIL TANK PRESS	PSIG	3.8	4.1	4.1
MAIN SUMP PRESS	PSIG	0.2	11.0	11.1
A/C FUEL FLOW	PPH	535	2250	
TARGET FUEL FLOW	PPH		2290	
CELL FUEL FLOW	PPH	4155	2260	7905
NOZZLE POSITION	0-100	86	11.1	74.5
CDP	PSIG	10.3	66	65
CIT	F	92	91	92
CELL BAROMETER	IN/HGA	27.3	27.3	27.3
THRUST	LBS	45	2292	3255
FUEL INLET PRESS	PSIG		40	40
VIB 1	MILS	.4	.5	.5
VIB 2	MILS	.2	.3	.4
VIB 3	MILS	.4	.4	.6

VIB 1 S/N 22009 2 22005 3 22035

VIB SENS 103.1 2 111.1 3 115.6

(WET) MOTOR CHECK AT 12% RPM

FUEL FLOW 260 PPH

START CHECK AT 12-14% RPM

BREAKOUT FUEL FLOW 301 PPH

LIGHT OFF TIME 9 SECONDS

START TIME 8 SECONDS

OSG CHECK

STABILIZED CUT IN SPEED 96.8 %RPM

ANTI-ICE CHECK

EGT RISE 20 F CDP DROP 3 PSIG

VIB 1 .3 2 .3 3 1.0

BLEED VALVE SCHEDULE CHECK 92

START TO CLOSE 83.7 %RPM CIT ~~95~~ F

START TO OPEN 97.5 %RPM CIT 92 F

AIR LEAK CK 18" AWAY AT MIL @1367

NOZZLE SCHEDULE CHECK

CRUISE FLAT NOZZLE AT 60 PLA 25.5

NOZZLE BREAK POINT 75.5 PLA

VEN AIR LEAK CHECK

IDLE ____ MIL ____ MAX ____

MIN A/B CHECK CDP 69 PSIG

PILOT MANIF PRESS 315 PSIG

AFTERBURNER CHECKS

A/B IN 97.7 PLA A/B OUT 73.7 PLA

MAX MINUS MIL W/F ~~514~~ PPH

ACCEL CHECKS IDLE TO MIL NOZZLE HESITATES AT 49.1

THEN CLOSES TO A MIN OF 2.6 BEFORE OPENING ON T5

IDLE - MIL 5 SEC PEAK EGT 1295 F

MIL - MAX 3.5 SEC PEAK EGT 1349 F ROLLBK TO 97.9 %RPM

88.5 - MAX 4 SEC PEAK EGT 1352 F ROLLBK TO 93.3 %RPM

OIL CONSUMPTION CK 0 OZ/HOUR

OVERBOARD LEAK CHECK @1367

HOT SPOT INSP @1367

PERFORMANCE CHECK MIN REQ'D MIL THRUST 2234 LBS MIN REQ'D MAX THRUST 3174 LBS

EGT THERMOCOUPLE CHECK EGT MINUS T-5 AMP EGT AT MIL 8 F (LIMIT +-25)

	1	2	3	4	5	6	7	8
STOP	1015	1125	1225	1300	1600	1650		
START	0935	1010	~~1245~~	1245	1530	1630		
TOTAL	45	~~120~~	10	15	30	20		
EGT	1208	1490	975	1155	1330	1252		
COASTDOWN	46	50	48	50	45	45		

CREW CHIEF Hoskins OPERATOR 01743 MECHANIC 00387

MAIN LOOP RIG CHECK @1367 TAG TEMP OUT 666 C -5R NOZZLE CLOSED N/A

ENGINE ACCEPTED Hoskins ENGINE REJECTED ____

412 CMS/MXMP J85 RUN CHECKSHEET NOV 2007

Figure 159. Engine #2 Test Cell Trim Sheet – Sept 2008

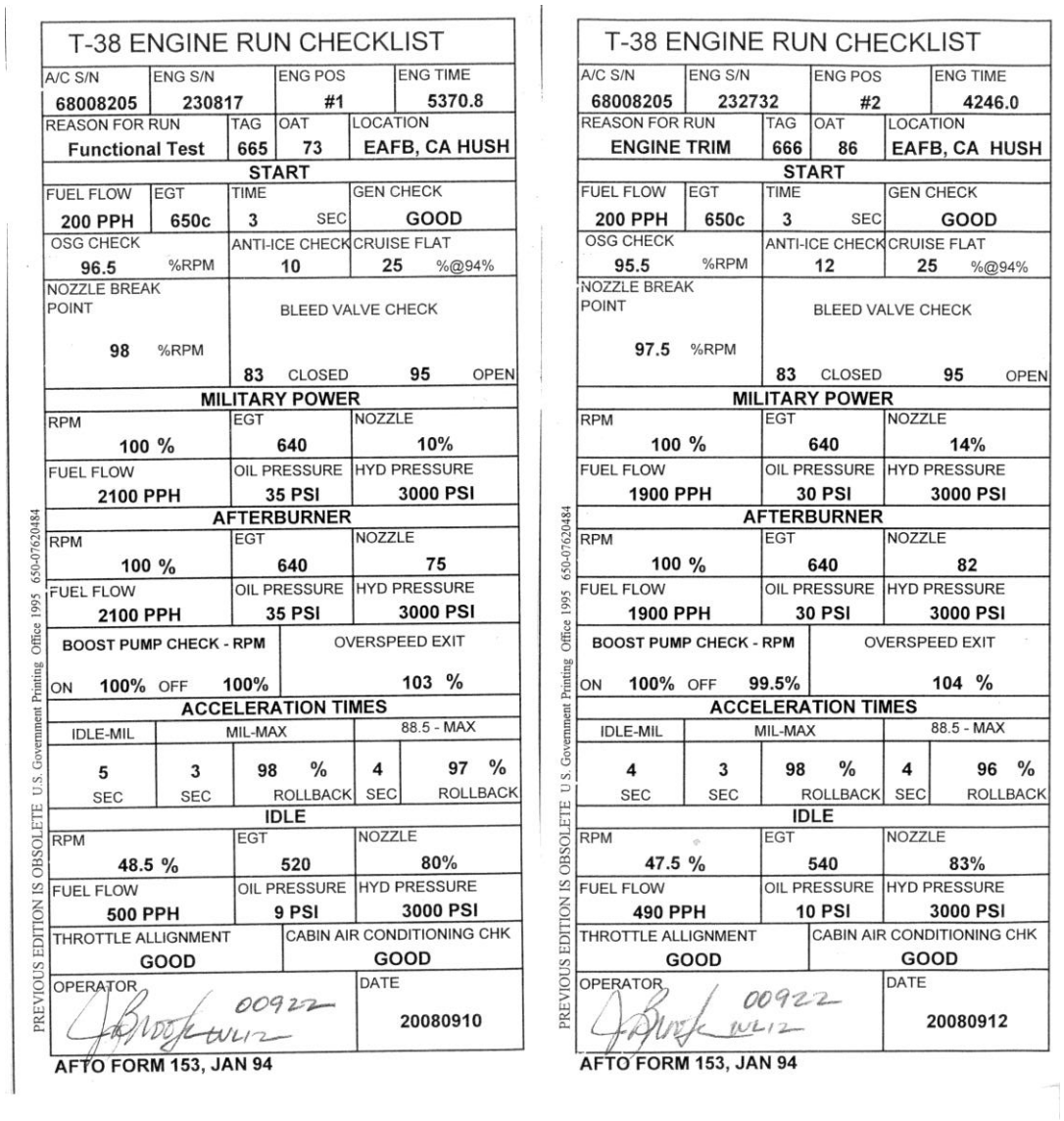

T-38 ENGINE RUN CHECKLIST

A/C S/N	ENG S/N	ENG POS	ENG TIME
68008205	230817	#1	5370.8

REASON FOR RUN	TAG	OAT	LOCATION
Functional Test	665	73	EAFB, CA HUSH

START

FUEL FLOW	EGT	TIME	GEN CHECK
200 PPH	650c	3 SEC	GOOD

OSG CHECK	ANTI-ICE CHECK	CRUISE FLAT
96.5 %RPM	10	25 %@94%

NOZZLE BREAK POINT	BLEED VALVE CHECK
98 %RPM	83 CLOSED 95 OPEN

MILITARY POWER

RPM	EGT	NOZZLE
100 %	640	10%

FUEL FLOW	OIL PRESSURE	HYD PRESSURE
2100 PPH	35 PSI	3000 PSI

AFTERBURNER

RPM	EGT	NOZZLE
100 %	640	75

FUEL FLOW	OIL PRESSURE	HYD PRESSURE
2100 PPH	35 PSI	3000 PSI

BOOST PUMP CHECK - RPM	OVERSPEED EXIT
ON 100% OFF 100%	103 %

ACCELERATION TIMES

IDLE-MIL	MIL-MAX		88.5 - MAX	
5 SEC	3 SEC	98 % ROLLBACK	4 SEC	97 % ROLLBACK

IDLE

RPM	EGT	NOZZLE
48.5 %	520	80%

FUEL FLOW	OIL PRESSURE	HYD PRESSURE
500 PPH	9 PSI	3000 PSI

THROTTLE ALLIGNMENT	CABIN AIR CONDITIONING CHK
GOOD	GOOD

OPERATOR	DATE
00922 WLI2	20080910

AFTO FORM 153, JAN 94

PREVIOUS EDITION IS OBSOLETE U.S. Government Printing Office 1995 650-07620484

T-38 ENGINE RUN CHECKLIST

A/C S/N	ENG S/N	ENG POS	ENG TIME
68008205	232732	#2	4246.0

REASON FOR RUN	TAG	OAT	LOCATION
ENGINE TRIM	666	86	EAFB, CA HUSH

START

FUEL FLOW	EGT	TIME	GEN CHECK
200 PPH	650c	3 SEC	GOOD

OSG CHECK	ANTI-ICE CHECK	CRUISE FLAT
95.5 %RPM	12	25 %@94%

NOZZLE BREAK POINT	BLEED VALVE CHECK
97.5 %RPM	83 CLOSED 95 OPEN

MILITARY POWER

RPM	EGT	NOZZLE
100 %	640	14%

FUEL FLOW	OIL PRESSURE	HYD PRESSURE
1900 PPH	30 PSI	3000 PSI

AFTERBURNER

RPM	EGT	NOZZLE
100 %	640	82

FUEL FLOW	OIL PRESSURE	HYD PRESSURE
1900 PPH	30 PSI	3000 PSI

BOOST PUMP CHECK - RPM	OVERSPEED EXIT
ON 100% OFF 99.5%	104 %

ACCELERATION TIMES

IDLE-MIL	MIL-MAX		88.5 - MAX	
4 SEC	3 SEC	98 % ROLLBACK	4 SEC	96 % ROLLBACK

IDLE

RPM	EGT	NOZZLE
47.5 %	540	83%

FUEL FLOW	OIL PRESSURE	HYD PRESSURE
490 PPH	10 PSI	3000 PSI

THROTTLE ALLIGNMENT	CABIN AIR CONDITIONING CHK
GOOD	GOOD

OPERATOR	DATE
00922 WLI2	20080912

AFTO FORM 153, JAN 94

PREVIOUS EDITION IS OBSOLETE U.S. Government Printing Office 1995 650-07620484

Figure 160. Line Maintenance Engine Trim Sheets for Installed Engines – Sept 2008

Appendix I: Flight Test Upwash Correction

An attempt was made to correct for upwash on the angle of attack (AOA) vane on the noseboom of the test aircraft. Tower fly-bys were used to determine the upwash on the AOA vane of the noseboom. Ideally, the aircraft's vertical velocity when crossing the tower fly-by line should be zero. At this level flight condition, the pitch angle of the aircraft should be equal to the AOA of the aircraft. By comparing the indicated AOA to the pitch angle, the upwash angle may be calculated. It was expected that the measured AOA would be greater than the pitch angle since the presence of upwash will increase the indicated AOA. Additionally, the magnitude of the upwash should increase with increasing AOA. Based on previous flight tests using nosebooms, the upwash should have been approximately 10 percent of the indicated AOA. Flight test data did not follow the expected pattern. The indicated pitch angle was actually greater than the indicated AOA. The calculated upwash angle was 2.6 to 3.5 degrees with the wrong sign and was almost independent of the indicated AOA. On average, there was a 2.98 degree difference between the pitch angle and measured AOA. Table 17 presents the data from the tower fly-bys. Figure 161 below presents the calculated upwash as a function of measured AOA.

Table 17. Tower Flyby Data

AIRSPEED	AOA*	PITCH	DIFFERENCE
185	6.75	9.79	-3.04
202	5.12	8.03	-2.91
213	4.28	7.27	-2.99
220	3.61	6.64	-3.03
220	4.28	7.15	-2.87
245	3.27	6.02	-2.76
253	2.57	5.39	-2.82
259	2.75	5.36	-2.61
275	2.23	5.55	-3.33
300	1.70	4.46	-2.76
300	0.98	4.48	-3.50

*Note: Without 1.8 degree AOA correction that was applied to lift curve and drag polar calculations.

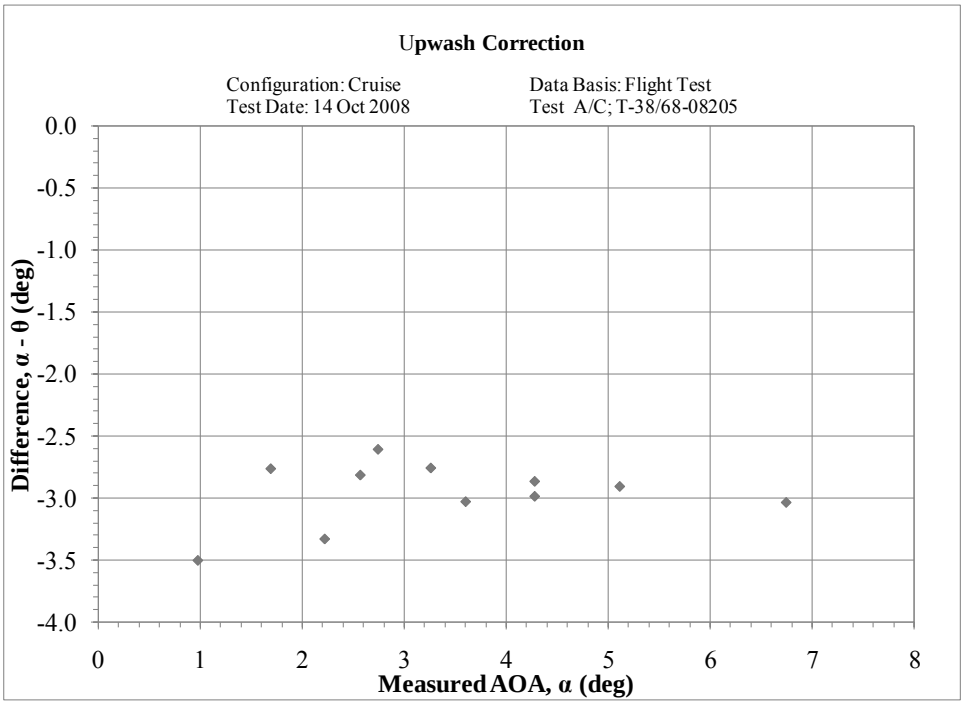

Figure 161. Upwash Correction as a Function of Measured Angle of Attack

*Note: Without 1.8 degree AOA correction that was applied to lift curve and drag polar calculations.

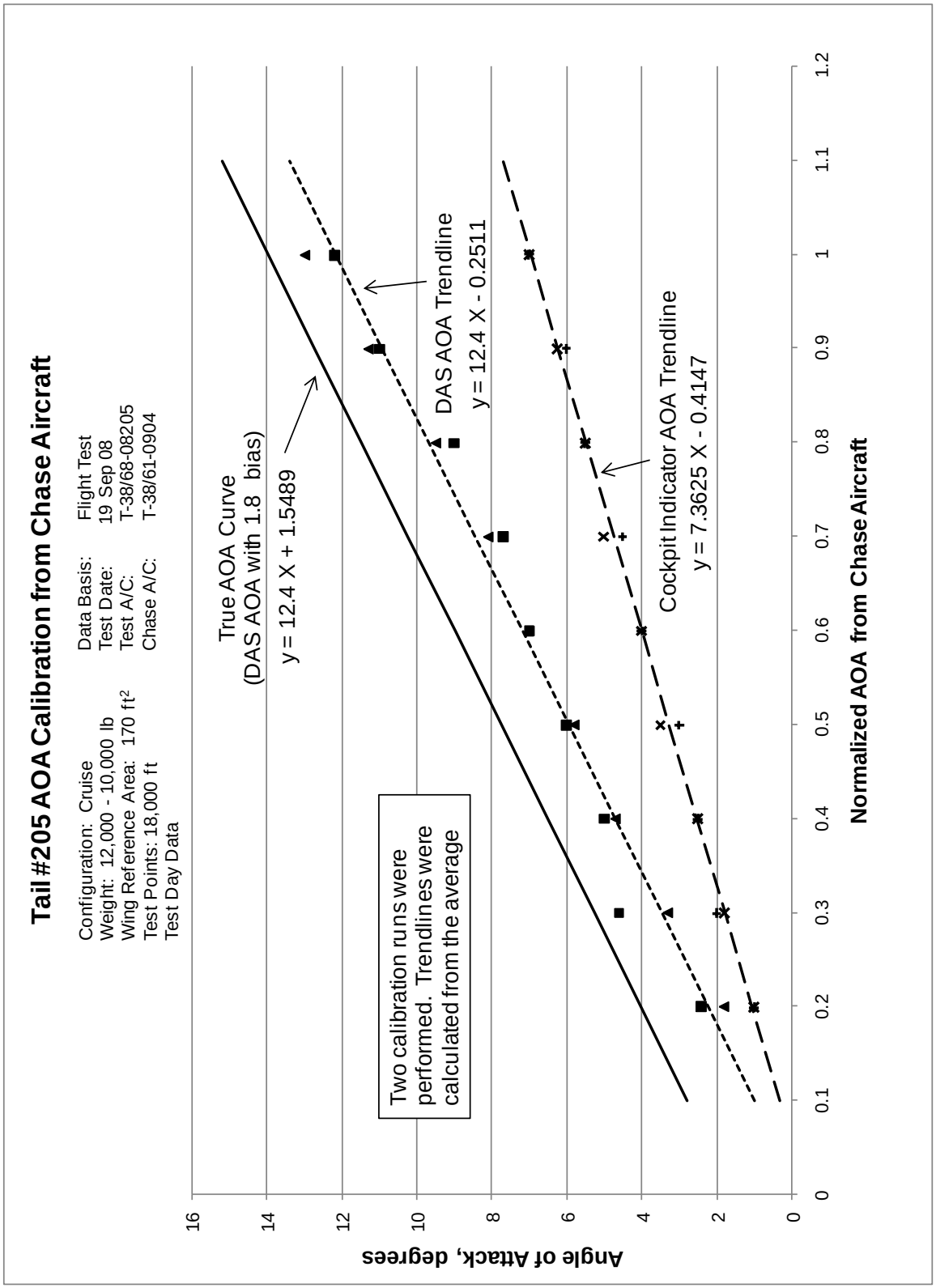

Figure 162. Angle of Attack Calibration Curves – Normalized to Cockpit and DAS

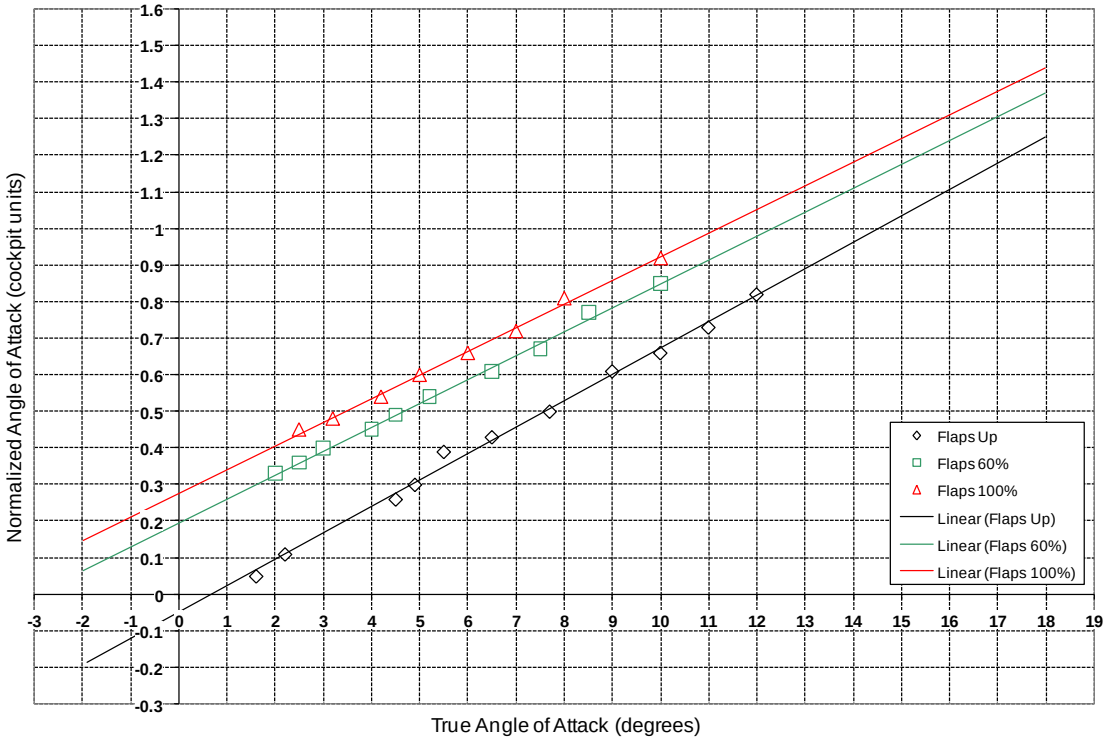

Figure 163. Approximate T-38 Normalized vs. True AOA (courtesy of USAF TPS)

Appendix K: Flight Test Data Parameter List

Table 18. Flight Test Data Parameter Summary 1

PARAMETER NAME	*DATA SOURCE*	*DATA RANGE*	*RESOLUTION*	*APPROXIMATE MEASUREMENT UNCERTAINTY*	*SAMPLES PER SEC*	*REQUIRED* [1]
RIGHT ENGINE						
Right Engine Fuel Flow	Transducer	0.5 to 10 GPM	0.05 GPM	0.05 GPM	54.25	Obj 1
Right Afterburner Fuel Flow	Transducer	15 to 25 GPM	0.05 GPM	0.05 GPM	54.25	
Right Fuel Used	Transducer -20 Bit	0 to 2000 gal	0.01 gal	0.1 GPM *	54.25	Obj 1
Right Engine RPM	Transducer	25 to 102 %RPM	0.15%	0.75%	108.5	Obj 1
Right Engine Fuel Temp	Transducer	-50° to 150° C	0.3° C	1.5° C	108.5	
LEFT ENGINE						
Left Engine Fuel Flow	Transducer	0.5 to 10 GPM	0.05 GPM	0.05 GPM	54.25	Obj 1
Left Afterburner Fuel Flow	Transducer	15 to 25 GPM	0.05 GPM	0.05 GPM	54.25	
Left Fuel Used	Transducer- 20 Bit	0 to 2000 gal	0.01 gal	0.1 GPM *	54.25	Obj 1
Left Engine RPM	Transducer	25 to 102 %RPM	0.15%	0.75%	108.5	Obj 1
Left Engine Fuel Temp	Transducer	-50° to 150° C	0.3° C	1.5° C	108.5	
MISC						
Event Counter	Transducer	0 to 99 Count	Discrete	N/A	108.5	
Event Marker	Transducer	0 or 1	Discrete	N/A	108.5	
IRIG Time					217.01	Obj 1
Voice					2604.2	
STICK AND RUDDER PEDAL POSITIONS AND FORCES						
Left Rudder Pedal Force	Transducer	0 to -150 lbs	0.15 lbs	0.75 lbs	108.5	

Table 19. Flight Test Data Parameter Summary 2

PARAMETER NAME	*DATA SOURCE*	*DATA RANGE*	*RESOLUTION*	*APPROXIMATE MEASUREMENT UNCERTAINTY*	*SAMPLES PER SEC*	*REQUIRED*[1]
Right Rudder Pedal Force	Transducer	0 to 150 lbs	0.15 lbs	0.75 lbs	108.5	
Longitudinal Stick Position	Transducer	-4 to 7 in	0.02 in	0.1 in	108.5	Obj 2
Lateral Stick Position	Transducer	±8 in	0.02 in	0.1 in	108.5	Obj 2
Rudder Pedal Position	Transducer	±3 in	0.01 in	0.05 in	108.5	
BODY AXIS PARAMETERS						
Theta - Pitch Angle	Transducer	±70°	0.06°	0.3°	108.5	Obj 2
Phi - Roll Angle	Transducer	±175°	0.35°	1.75°	108.5	Obj 2
p - Roll Rate	Transducer	±360°/sec	0.7°/sec	3.5°/sec	108.5	
q - Pitch Rate	Transducer	±20°/sec	0.05°/sec	0.25°/sec	108.5	Obj 1
r - Yaw Rate	Transducer	±20°/sec	0.05°/sec	0.25°/sec	108.5	
Normal Acceleration	Transducer	-3 to 6 G	0.01 G	0.05 G	108.5	Obj 1
Lateral Acceleration	Transducer	±1 G	0.002 G	0.01 G	108.5	
Longitudinal Acceleration	Transducer	±1 G	0.002 G	0.01 G	108.5	Obj 1
AIR DATA						
Total Pressure	Transducer	0.4 to 38 PSIA	0.0002 PSIA	0.0038 PSIA	54.25	Obj 1
Static Pressure	Transducer	0.4 to 38 PSIA	0.0002 PSIA	0.0038 PSIA	54.25	Obj 1
Alpha - Angle of Attack	Transducer	-10 to 30°	0.04°	0.2°	108.5	Obj 1, Obj 2
Beta - Angle of Sideslip	Transducer	±20°	0.04°	0.2°	108.5	
Total Air Temperature	Transducer	-55° to 85° C	0.11° C	0.5° C	108.5	Obj 1
SURFACE POSITIONS						
Stabilator Position	Transducer	-6° to 16°	0.03°	0.15°	108.5	
Right Aileron Position	Transducer	-25° to 35°	0.08°	0.4°	108.5	
Left Aileron Position	Transducer	-35° to 25°	0.08°	0.4°	108.5	
Rudder Position	Transducer	±30°	0.07°	0.35°	108.5	

[1]REQUIRED refers to whether that parameter was required (for data reduction) and for which objective it was required.

Appendix L: Flight Test Limitations

The following limitations and resulting impacts were noted during testing:

- A fuel quantity calibration / longitudinal center of gravity accelerometer misalignment check was not performed in the weight and balance hanger as a result of schedule and availability limitations. This could have minimized and/or corrected two issues:
    - Served as a truth source for fuel quantity indicators and weight calculations
    - Estimated the accelerometer errors / misalignments
- Pre- and post-flight weighing was not performed for each flight to "calibrate" the fuel flow sensors as a result of schedule and availability limitations. These would have provided a "truth source" for the fuel flow sensors and would have reduced the uncertainty in the aircraft gross weight. Additionally, fuel flow data were inaccurate and could not have been used to calculate gross weight.
- The outputs of the longitudinal and normal accelerometers, the AOA vane, and the pitch angle from the pitch gyro all had significant errors.
    - The weight and balance hanger was not available during the testing period to perform a ground test to better quantify the accelerometer errors. The team added 6 percent to N_{Zbody}, about 60 milli-gs. The team added 0.040 g to N_{Xbody}, about 40 milli-gs.
    - The test team assumed that AOA was equal to the measured AOA plus 1.8 degrees based on engineering judgment.
    - The team did not use the pitch gyro computed pitch angle except in the failed attempt to determine an upwash correction (either the AOA or the

pitch angle or both had errors equivalent to about 4 degrees). The team assumed that upwash was zero.

- A misalignment between the body axis and the noseboom was not determined. It was buried in the AOA calibration. Angle of attack was critical in the team's effort to convert body-axis accelerations into flight path axis accelerations.

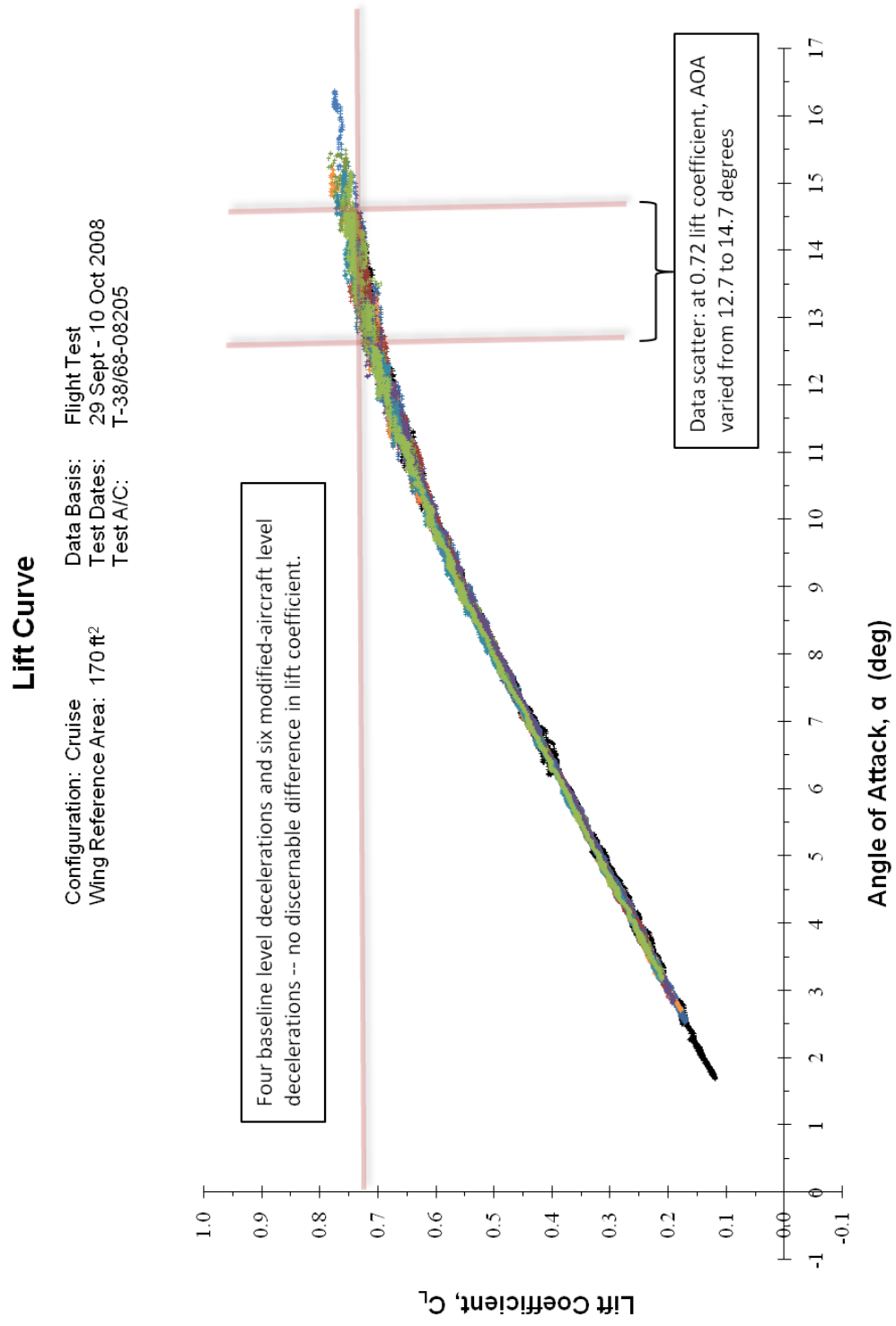

Figure 164. Lift Curve for Modified and Baseline Aircraft

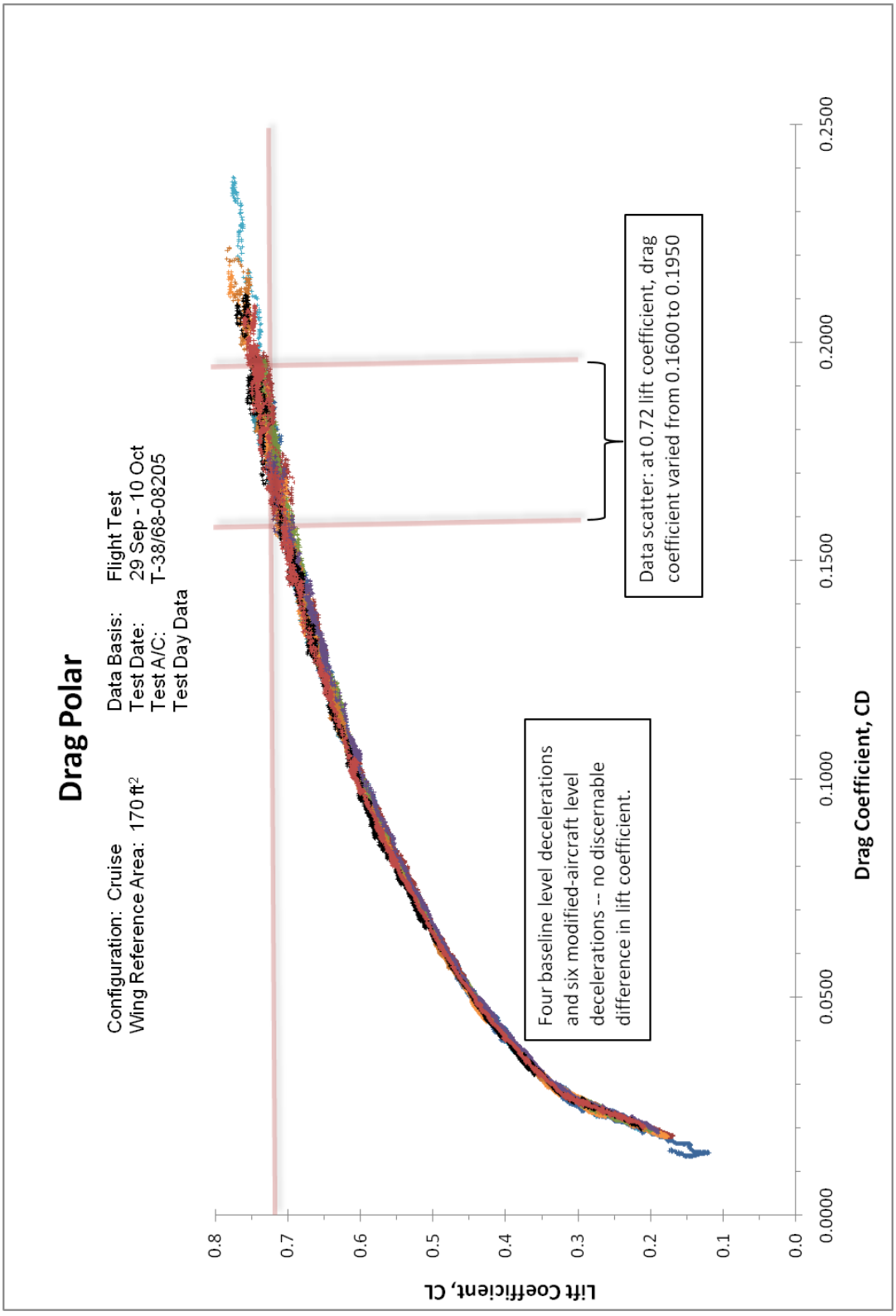

Figure 165. Drag Polar for Modified and Baseline Aircraft

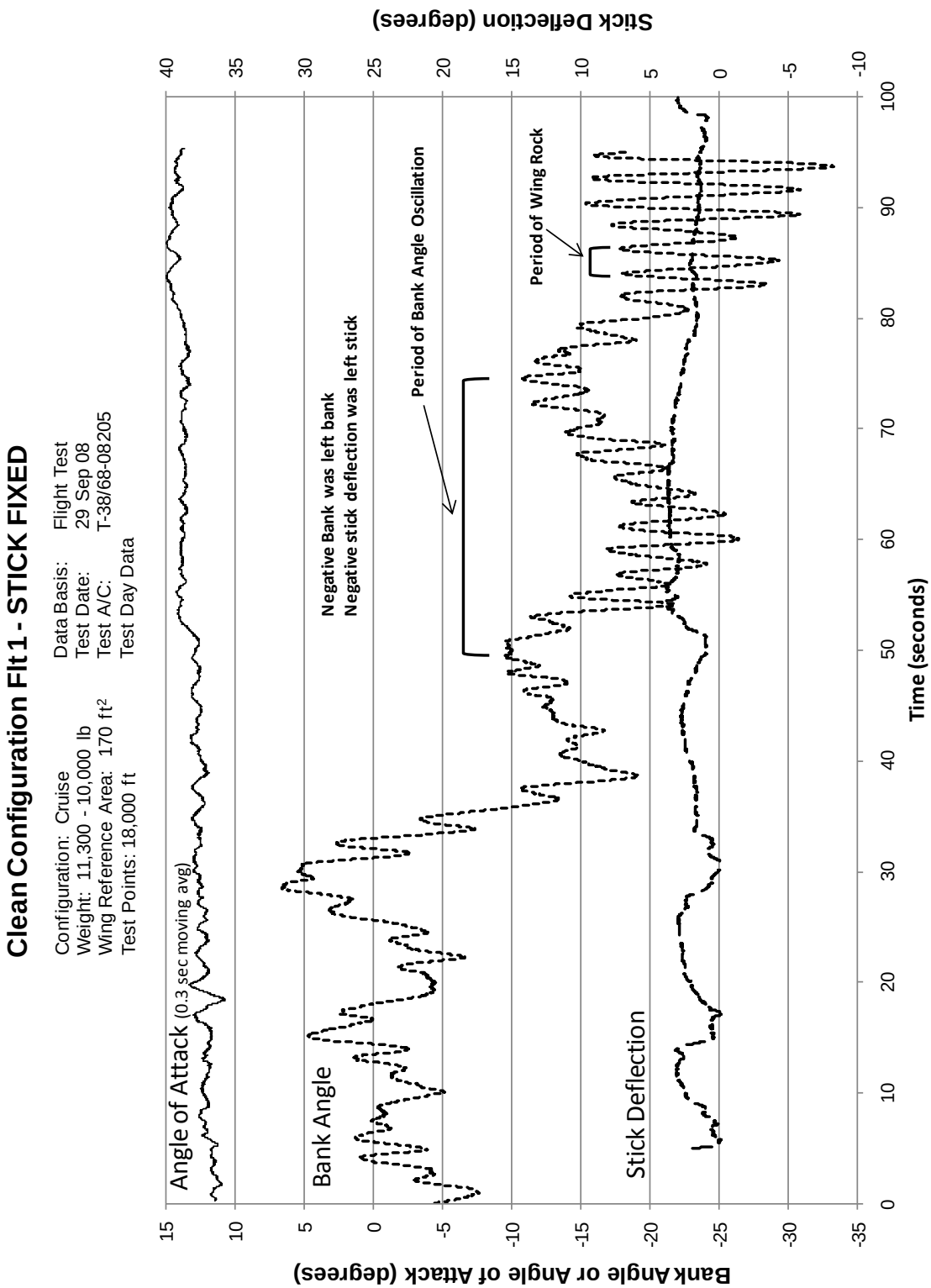

Figure 166. Baseline Stick-Fixed Approach to Stall, Flight 1

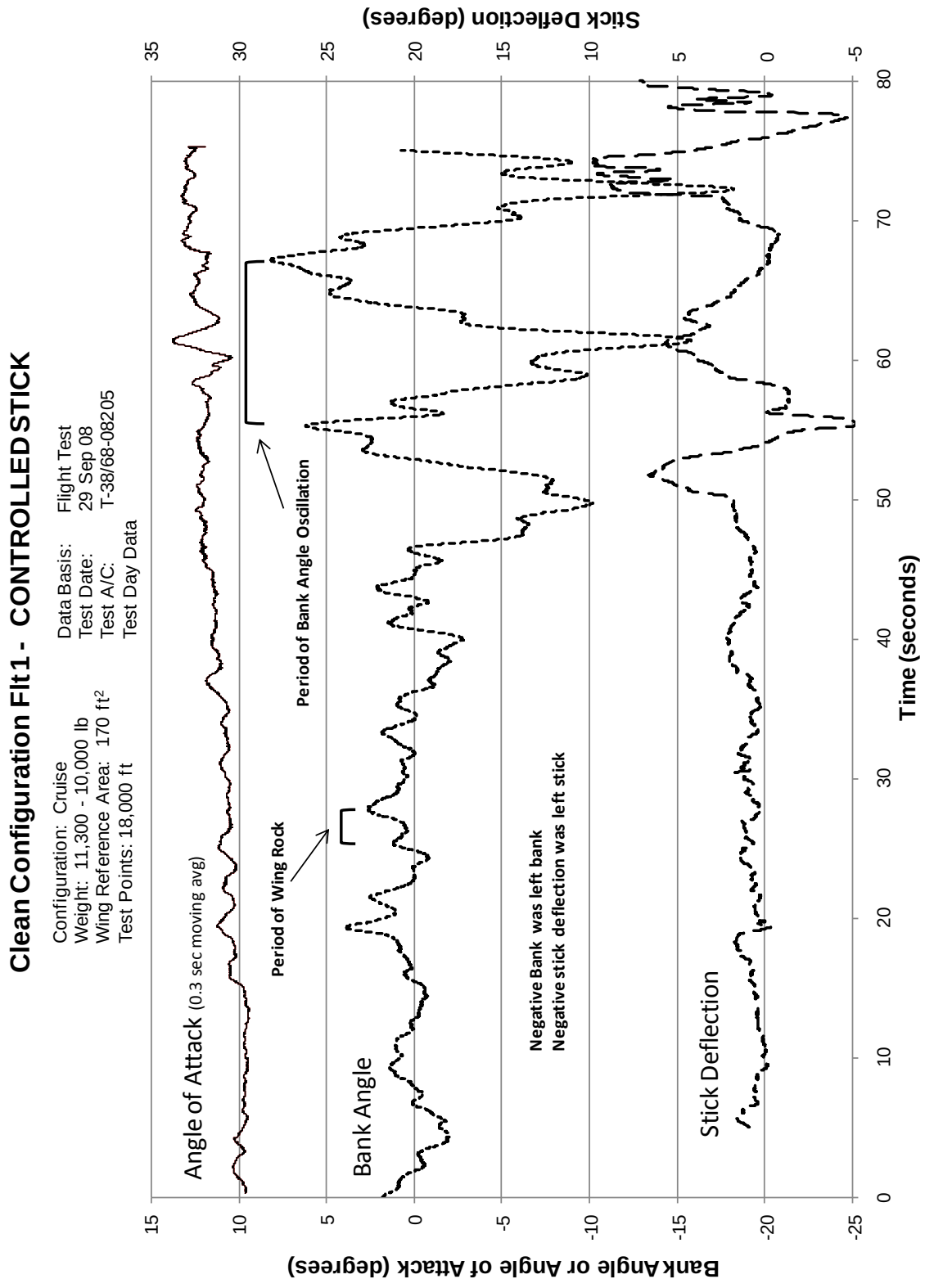

Figure 167. Baseline Stick-Controlled Approach to Stall, Flight 1

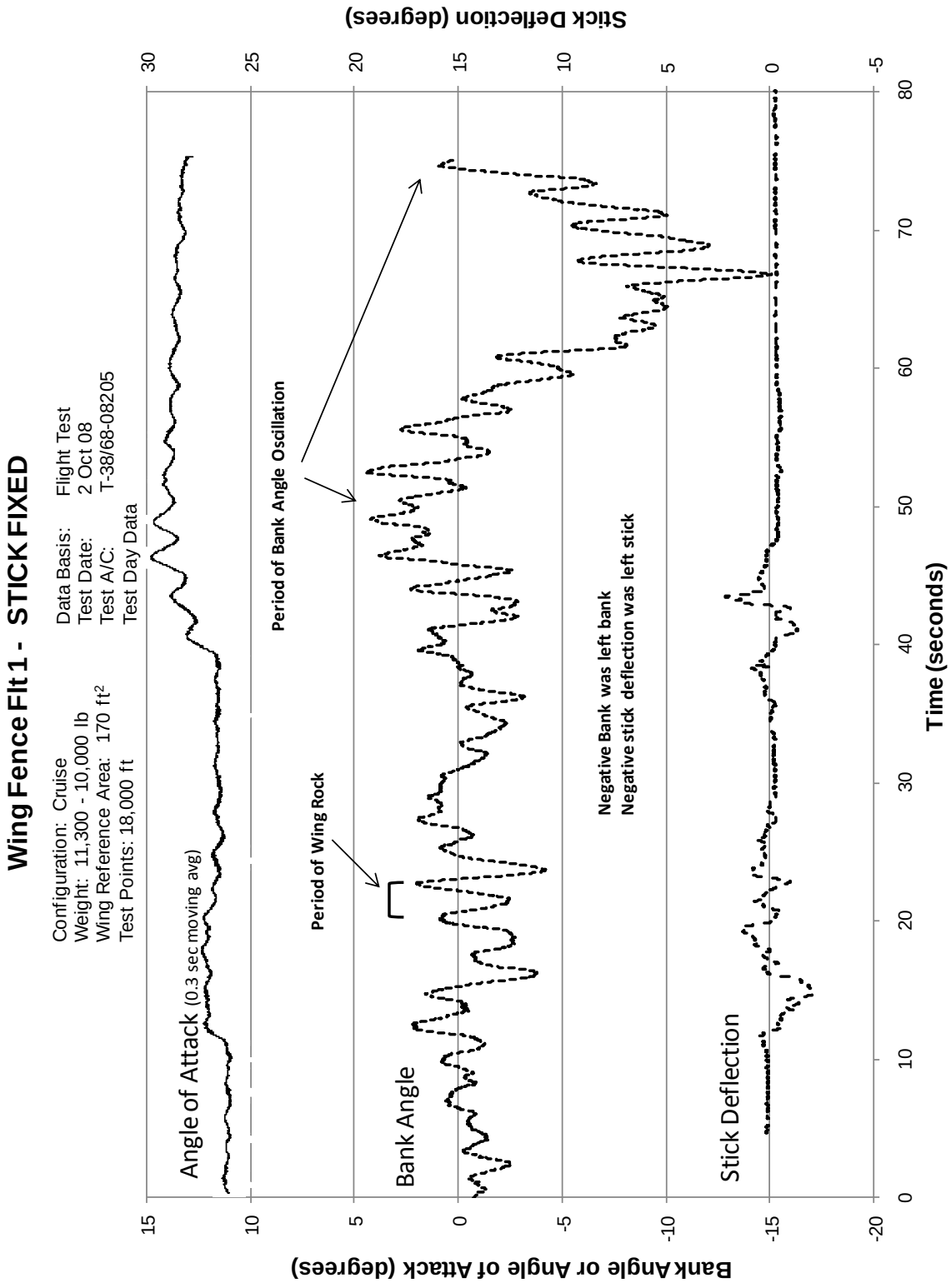

Figure 168. Wing Fence Stick-Fixed Approach to Stall, Flight 1

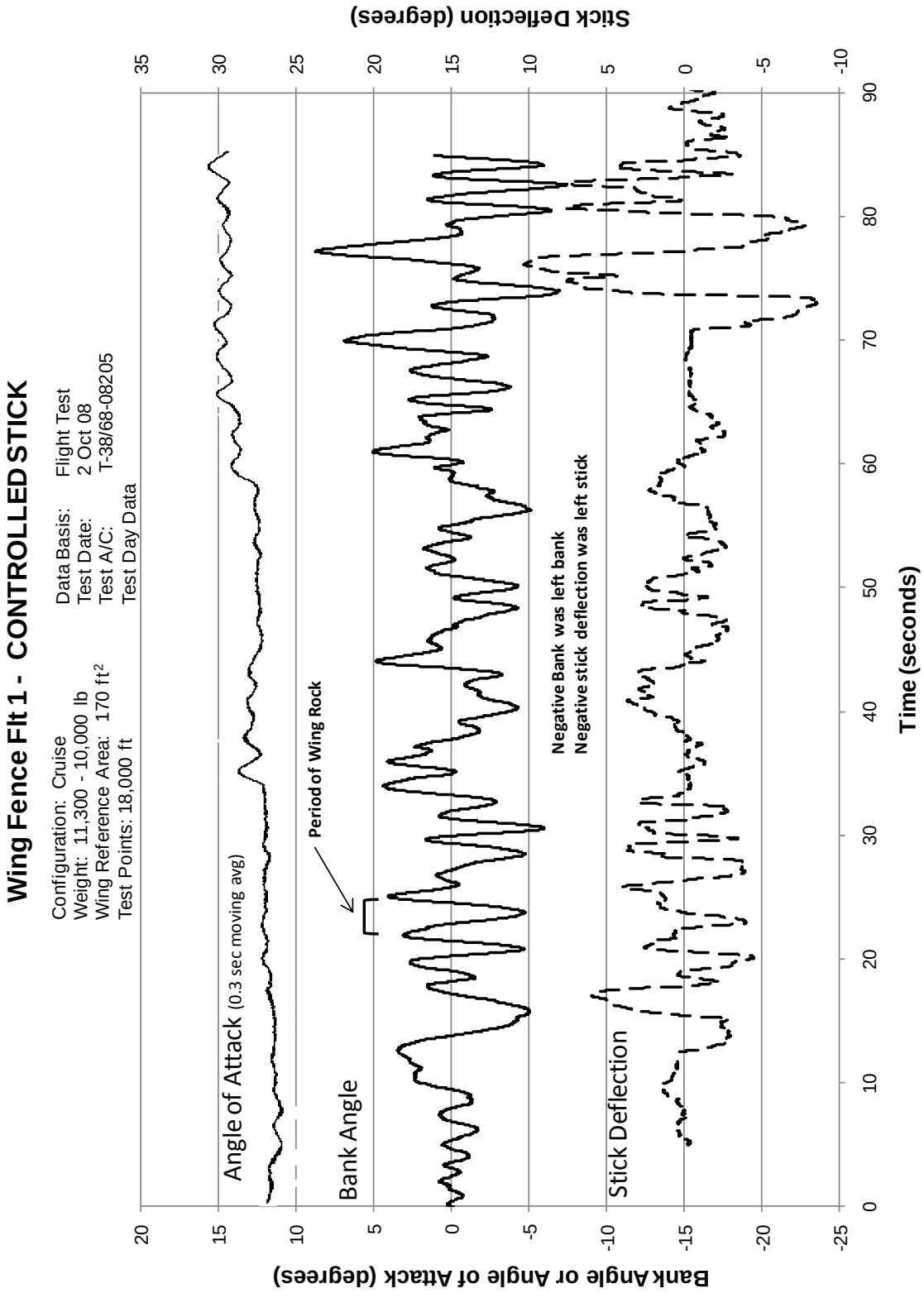

Figure 169. Wing Fence Stick-Controlled Approach to Stall, Flight 1

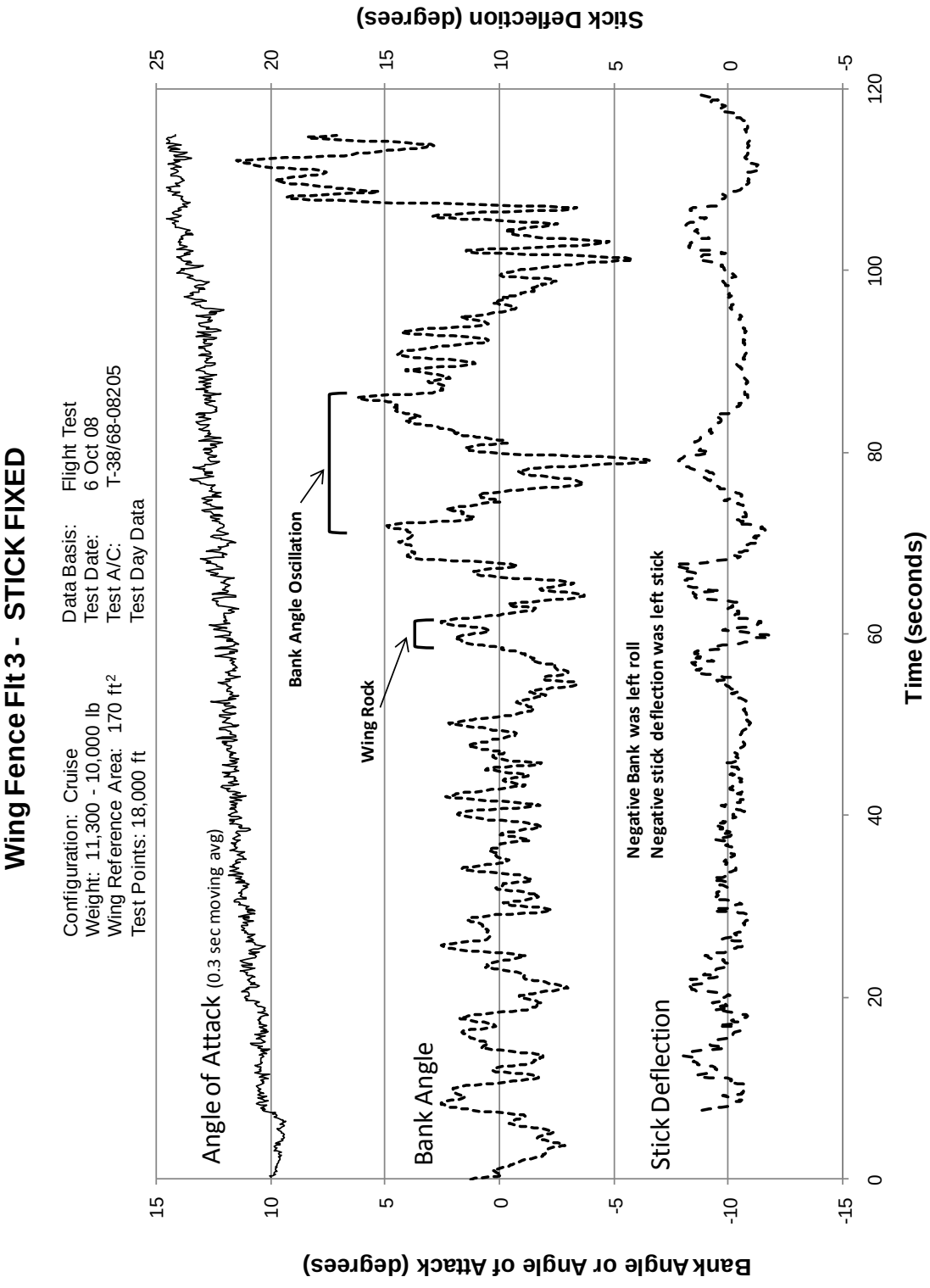

Figure 170. Wing Fence Stick-Fixed Approach to Stall, Flight 3

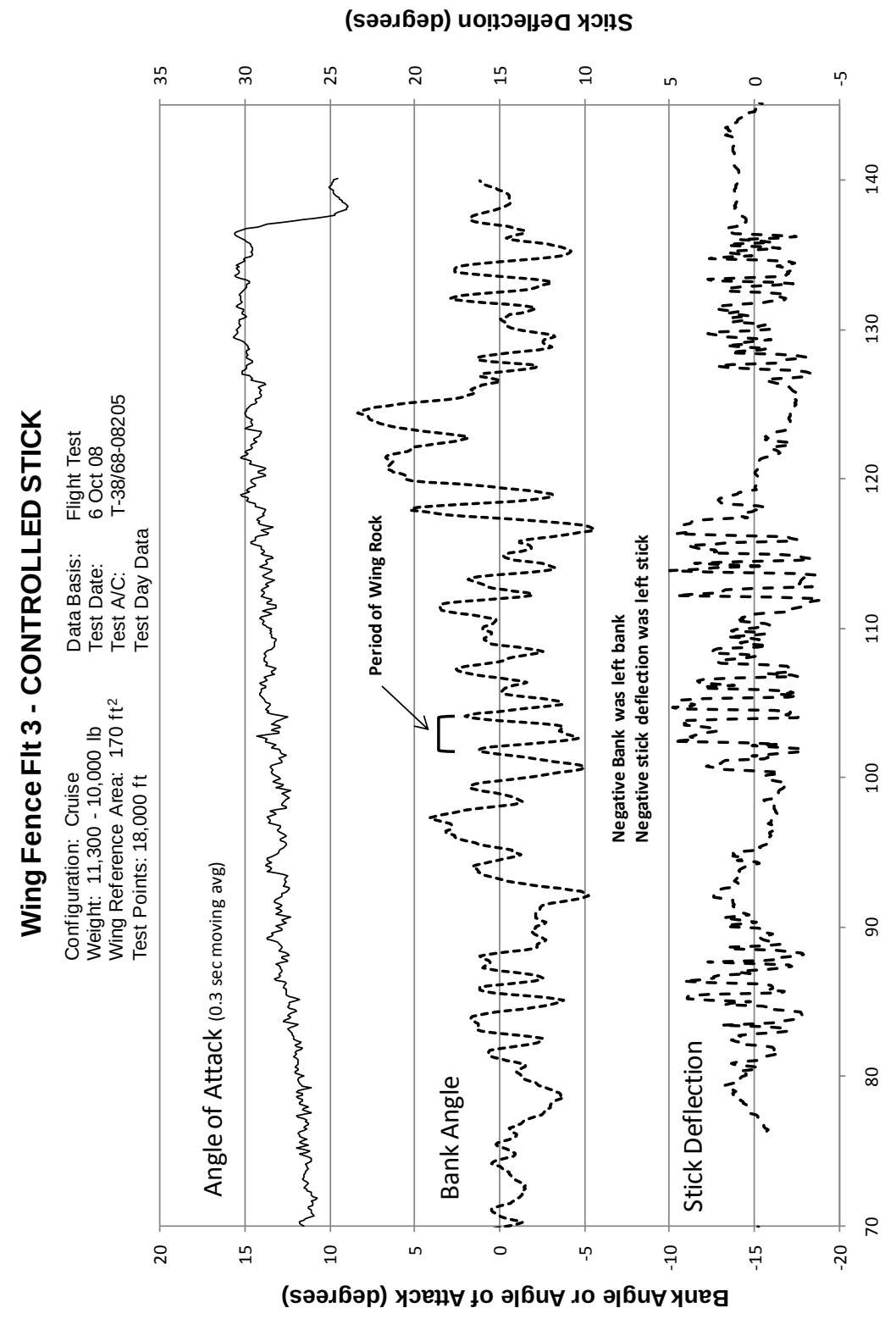

Figure 171. Wing Fence Stick-Controlled Approach to Stall, Flight 3

Appendix N: Flight Test - Tufted Flow Visualization

The following photographs are the complete compilation of the stable angles of attack from 8.1 to 14.9 degrees (°) (0.53 – 1.0 normalized) and Reynolds numbers, based on mean aerodynamic chord, of 7.61×10^6 to 9.98×10^6.

Figure 172. Fence Tufted Wing at 8.1° AOA (0.53 normalized) and 195 KCAS

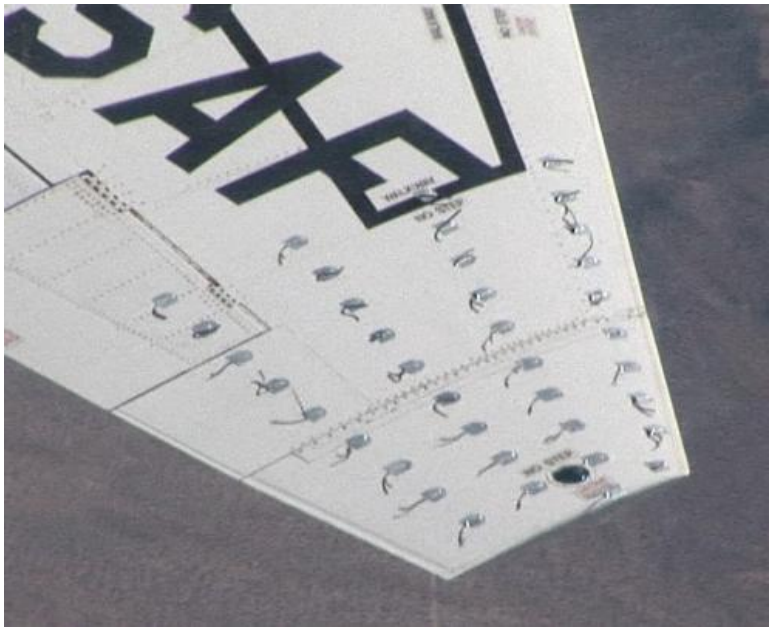

Figure 173. Clean Tufted Wing at 8.1° AOA (0.53 normalized) and 192 KCAS

Figure 174. Fence Tufted Wing at 8.4° AOA (0.56 normalized) and 185 KCAS

Figure 175. Clean Tufted Wing at 8.4° AOA (0.56 normalized) and 188 KCAS

Figure 176. Fence Tufted Wing at 8.6° AOA (0.58 normalized) and 179 KCAS

Figure 177. Clean Tufted Wing at 8.6° AOA (0.58 normalized) and 183 KCAS

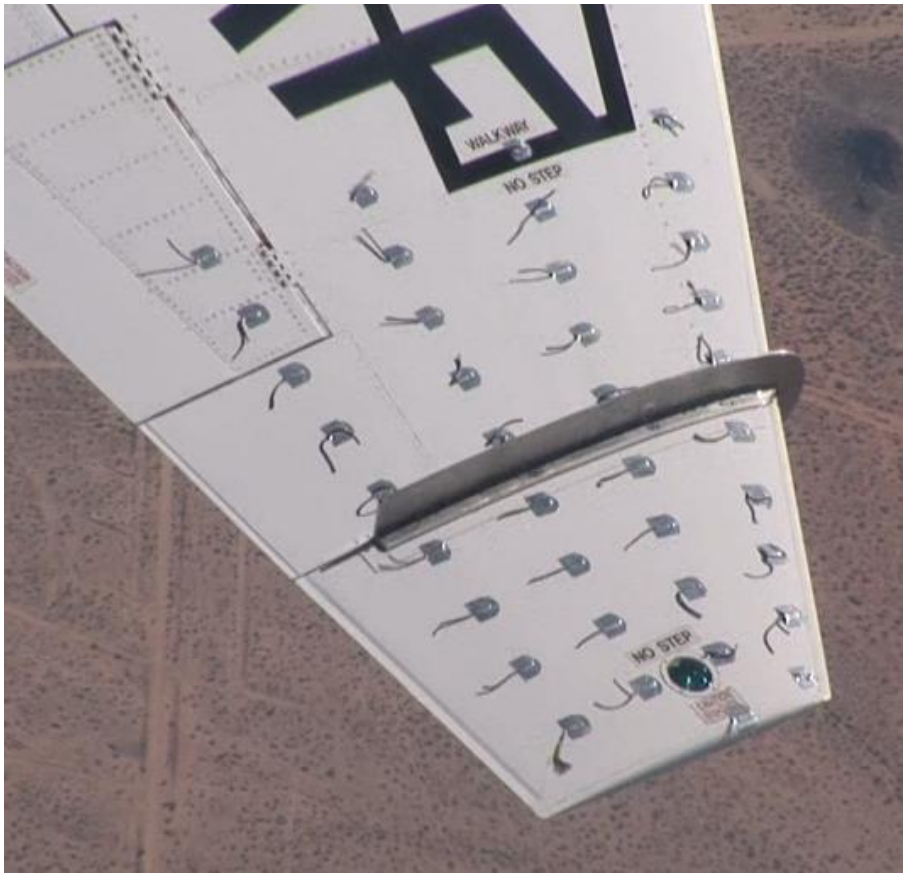

Figure 178. Fence Tufted Wing at 9.3° AOA (0.63 normalized) and 168 KCAS

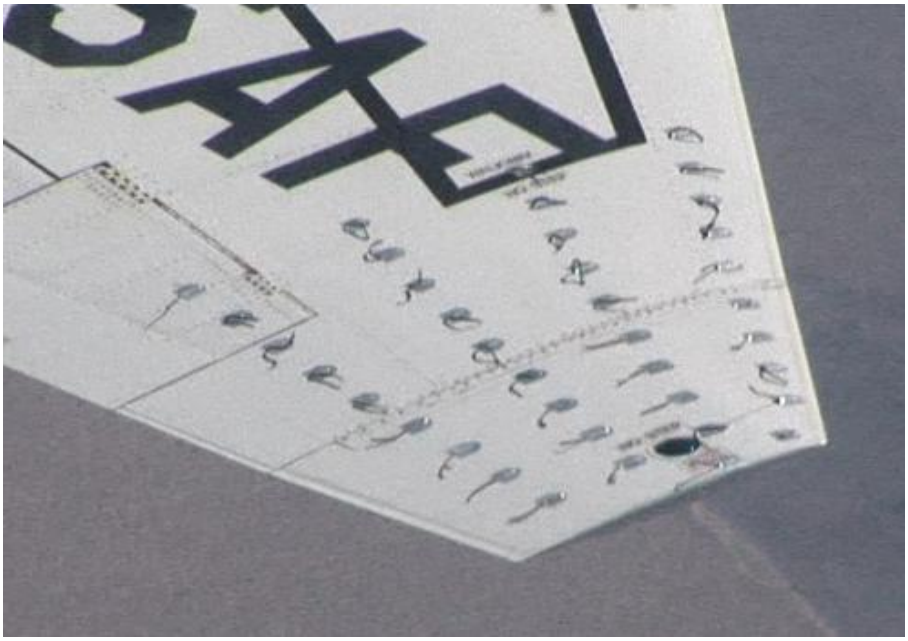

Figure 179. Clean Tufted Wing at 9.3° AOA (0.63 normalized) and 185 KCAS

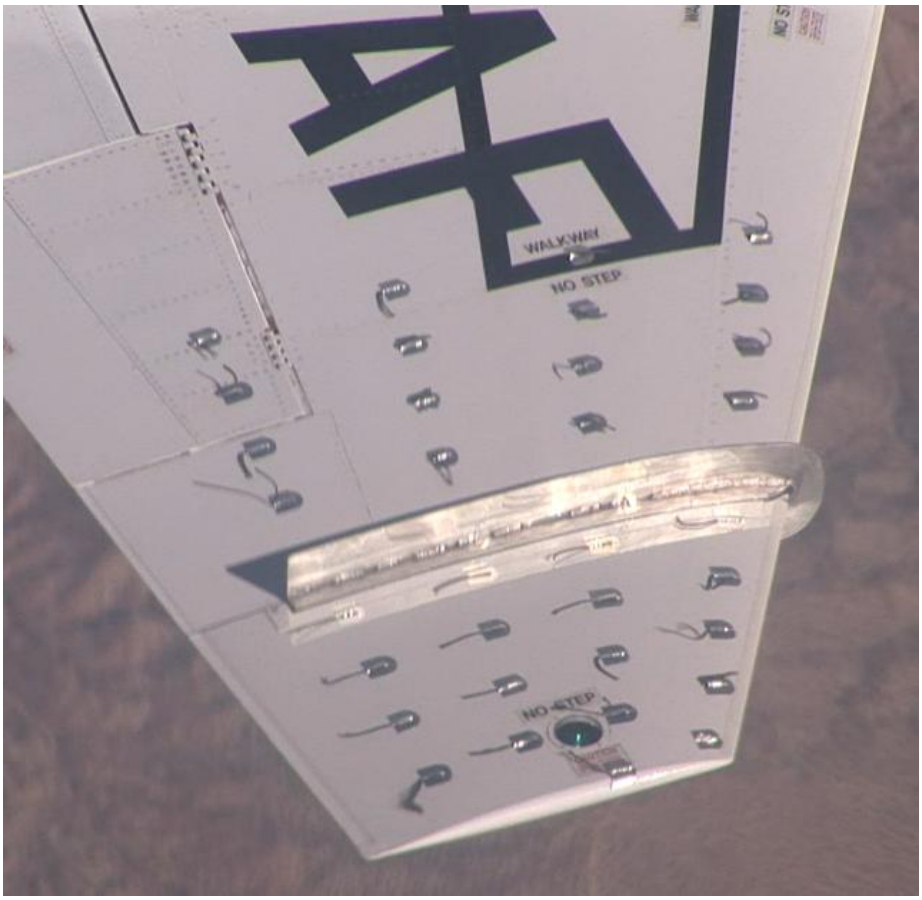

Figure 180. Fence Tufted Wing at 9.5° AOA (0.64 normalized) and 179 KCAS

Figure 181. Clean Tufted Wing at 9.5° AOA (0.64 normalized) and 179 KCAS

Figure 182. Fence Tufted Wing at 9.6° AOA (0.65 normalized) and 174 KIAS

Figure 183. Clean Tufted Wing at 9.6° AOA (0.65 normalized) and 175 KCAS

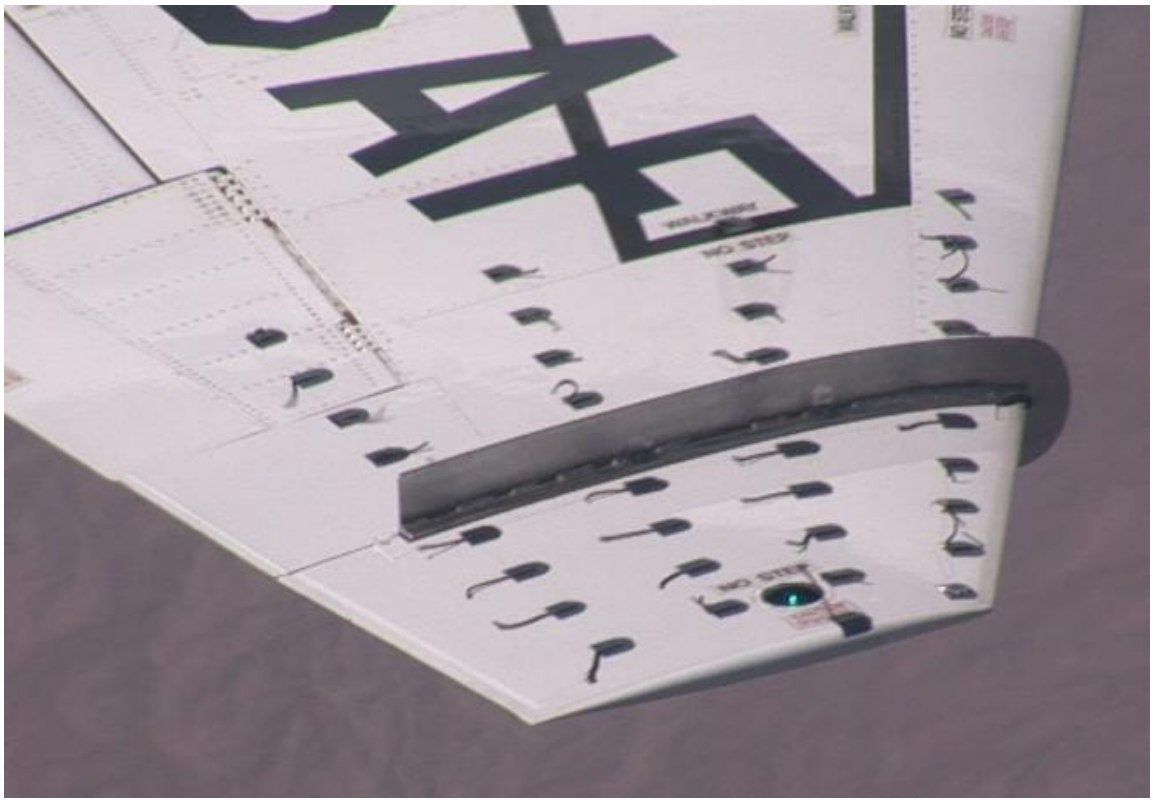

Figure 184. Fence Tufted Wing at 10.3° AOA (0.69 normalized) and 169 KCAS

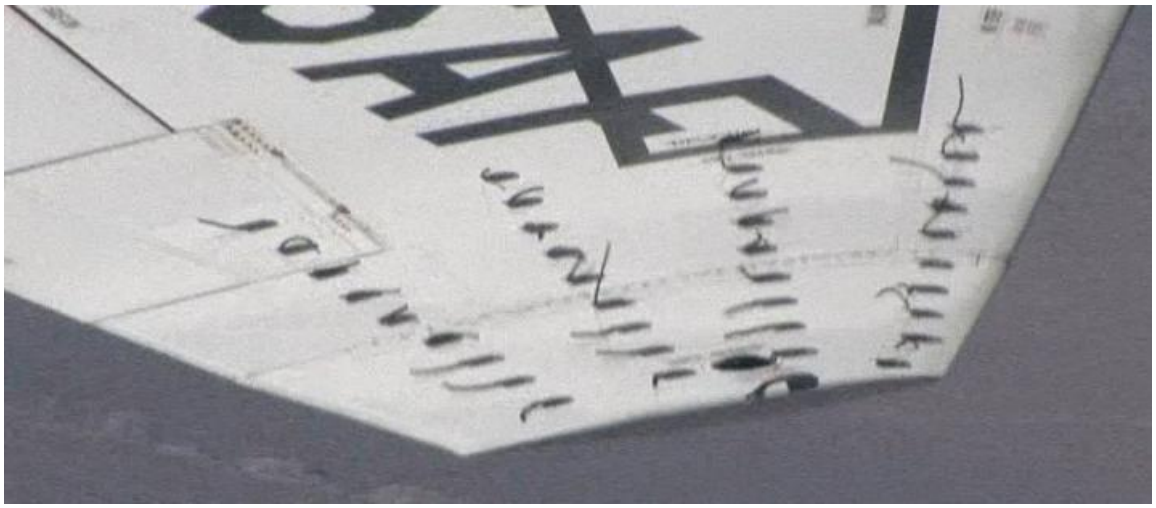

Figure 185. Clean Tufted Wing at 10.3° AOA (0.69 normalized) and 170 KCAS

Figure 186. Fence Tufted Wing at 10.7° AOA (0.72 normalized) and 169 KCAS

Figure 187. Clean Tufted Wing at 10.7° AOA (0.72 normalized) and 169 KCAS

Figure 188. Fence Tufted Wings at 10.7° AOA (0.72 normalized) and 164 KCAS

Figure 189. Clean Tufted Wing at 10.7° AOA (0.72 normalized) and 165 KCAS

Figure 190. Fence Tufted Wing at 11.4° AOA (0.77 normalized) and 159 KCAS

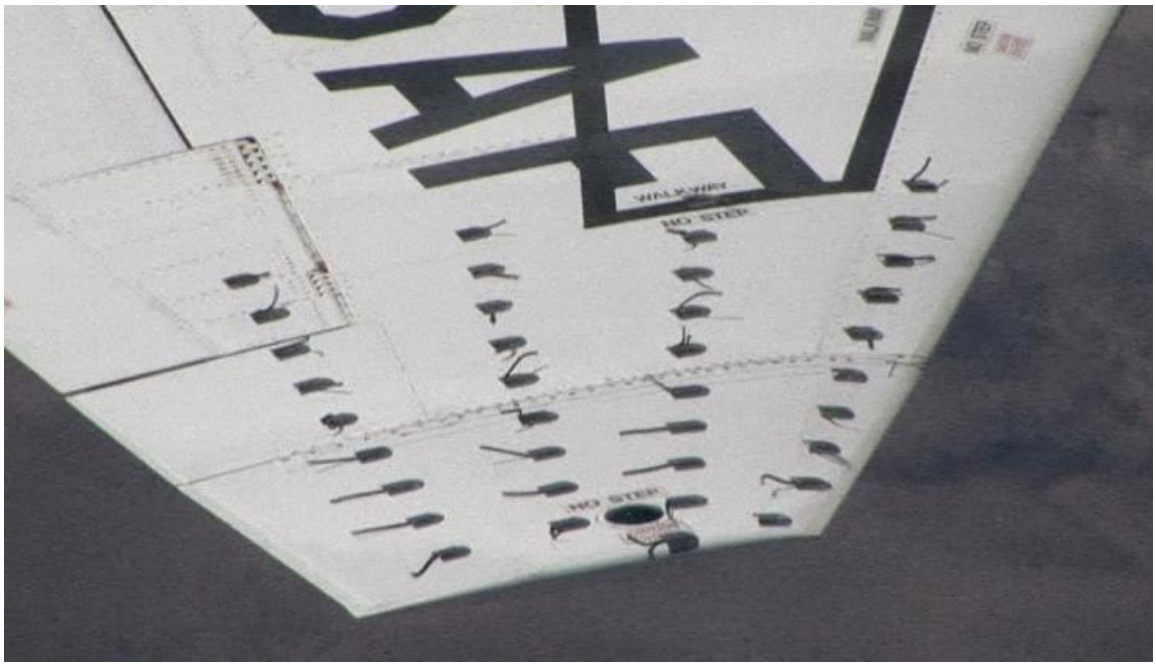

Figure 191. Clean Tufted Wings at 11.4° AOA (0.77 normalized) and 161 KCAS

Figure 192. Fence Tufted Wings at 11.9° AOA (0.80 normalized) and 151 KCAS

Figure 193. Clean Tufted Wing at 11.9° AOA (0.80 normalized) and 164 KIAS

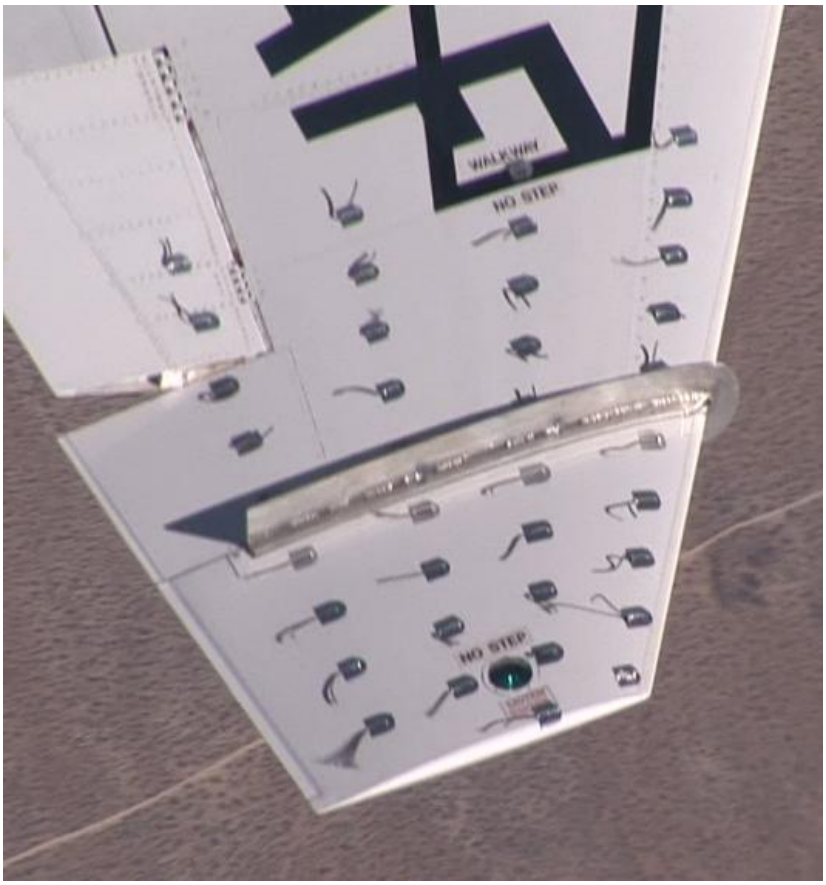

Figure 194. Fence Tufted Wings at 12.4° AOA (0.83 normalized) and 159 KCAS

Figure 195. Clean Tufted Wing at 12.4° AOA (0.83 normalized) and 159 KCAS

Figure 196. Fence Tufted Wings at 12.4° AOA (0.83 normalized) and 154 KCAS

Figure 197. Clean Tufted Wing at 12.4° AOA (0.83 normalized) and 156 KCAS

Figure 198. Fence Tufted Wings at 13.4° AOA (0.90 normalized) and 154 KCAS

Figure 199. Clean Tufted Wing at 13.4° AOA (0.90 normalized) and 153 KCAS

Figure 200. Fence Tufted Wings at 13.9° AOA (0.92 normalized) and 149 KIAS

Figure 201. Clean Tufted Wing at 13.9° AOA (0.92 normalized) and 153 KCAS

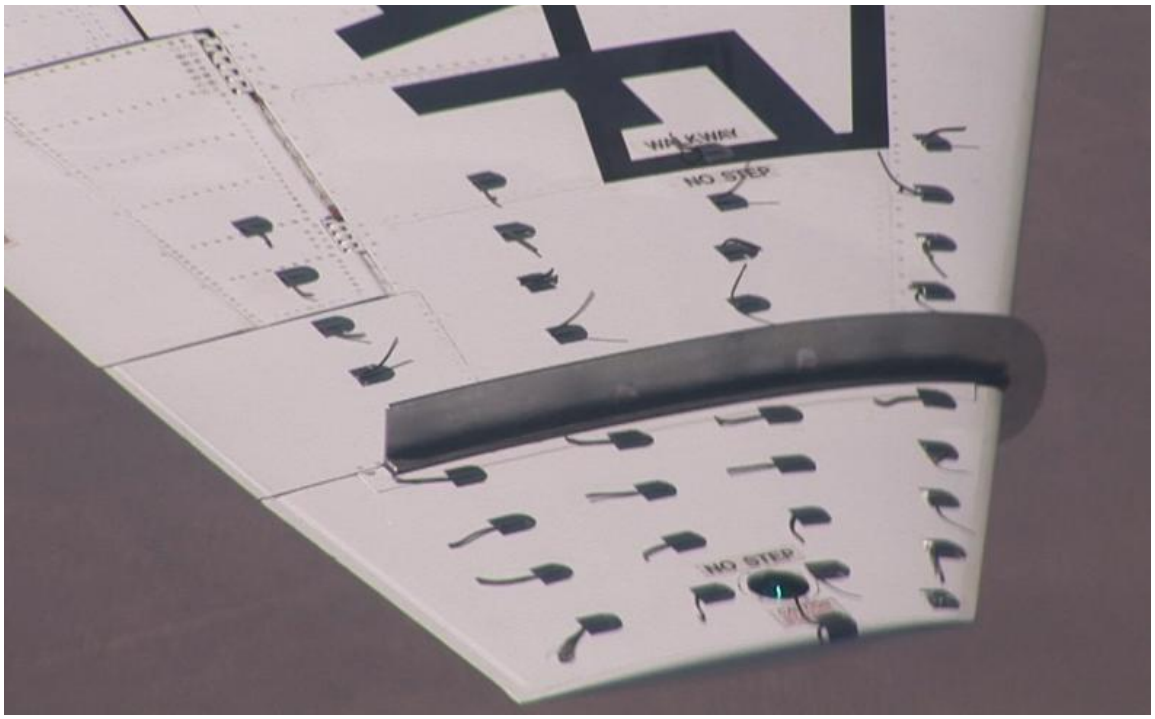

Figure 202. Fence Tufted Wing at 14.2° AOA (0.94 normalized) and 146 KCAS

Figure 203. Clean Tufted Wing at 14.2° AOA (0.94 normalized) and 152 KCAS

Figure 204. Fence Tufted Wings at 14.9° (1.0 normalized) AOA and 153 KCAS

Figure 205. Clean Tufted Wing at 14.9° (1.0 normalized) AOA and 152 KCAS

Appendix O: Wind Tunnel Fuselage-Only Plots

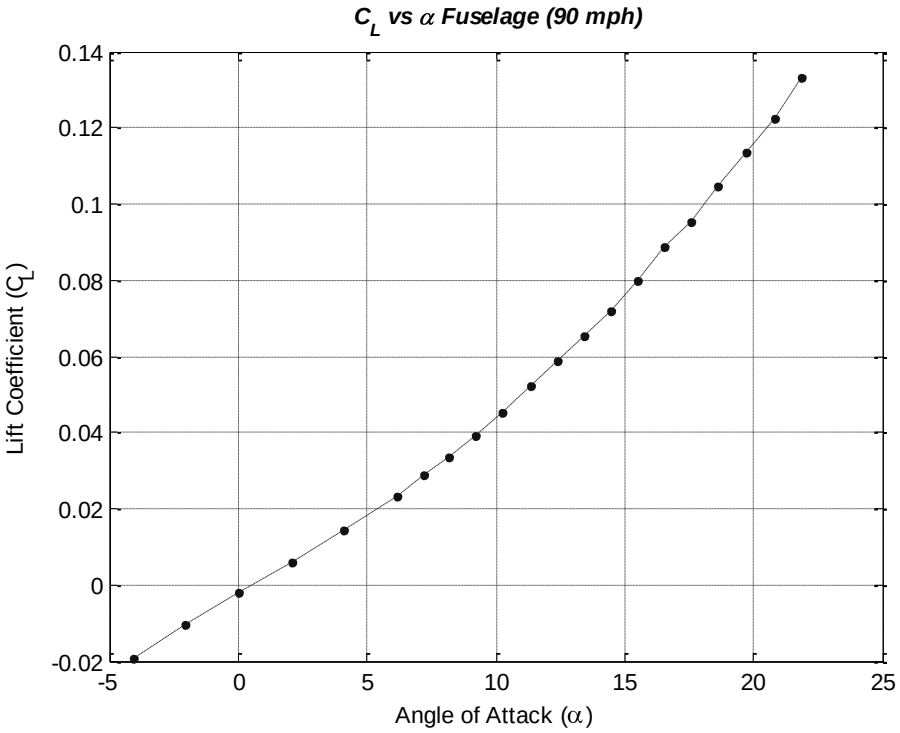

Figure 206. Fuselage-Only Contribution to Lift Coefficient.

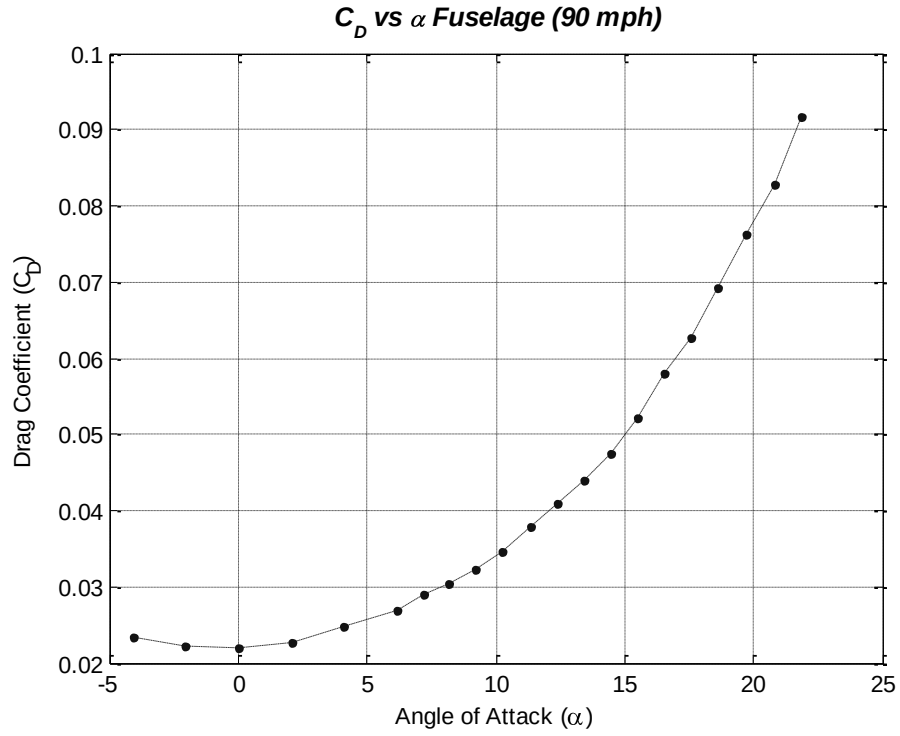

Figure 207. Fuselage-Only Contribution to Drag Coefficient.

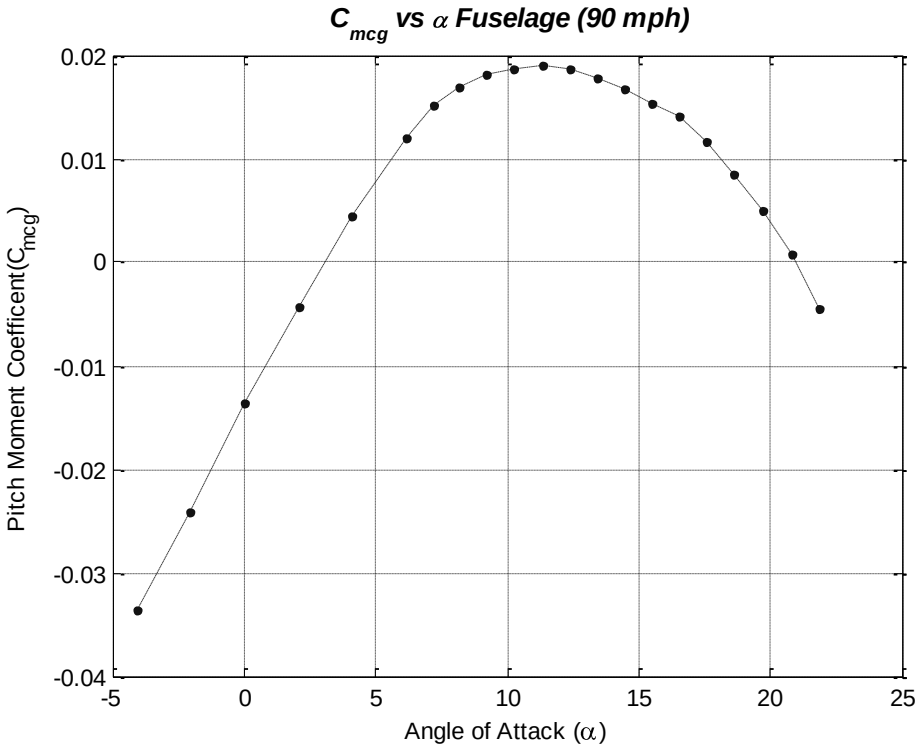

Figure 208. Fuselage-Only Contribution to Pitching Moment Coefficient.

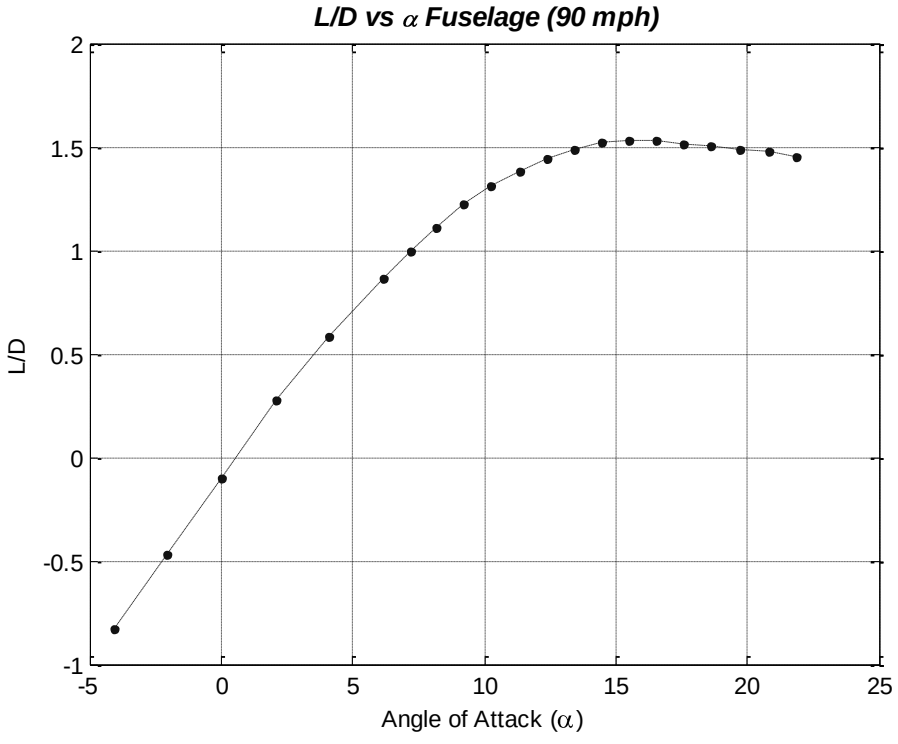

Figure 209. Fuselage Only Contribution to Lift-to-Drag Ratio.

Bibliography

1. AFFTC Modification Package. "T-38 Wing Fence." *M08A205A*. 2008.

2. Anderson, John D. *Introduction to Flight*. McGraw-Hill Higher Education, Madison WI, fourth edition, 2000.

3. Barlow, J. B., W.H. Rae, and A. Pope. *Low-Speed Wind Tunnel Testing.* New York: John Wiley & Sons, 1999.

4. Barrett, Ron and Saeed Faokhi. "On the Aerodynamics and Performance of Active Vortex Generators". *AIAA-93-23447-CP*, 1993.

5. Boltz and Shibata. "Pressure Distribution at Mach Numbers Up to 0.90 on a Cambered and Twisted Wing Having 40º of Sweepback and an Aspect Ratio of 10, Including the Effects of Fences." *RM A52K20.* NACA, 1953.

6. Federation of American Scientists, www.fas.org. *Photo of C-17, AV-8B, and Gulfstream V with vortex generators,* 2007.

7. Foster and Fitzpatrick. "Longitudinal-Stability Investigation of High-Lift and Stall-Control Devices on a 52º Sweptback Wing With and Without Fuselage and Horizontal Tail at a Reynolds Number of 6.8 x 10^6." *RM No. L8I08.* NACA, 1948.

8. Global Security. "XF-92A Dart", *www.globalsecurity.org/military/systems/aircraft/f-92.htm*, 2007

9. Guy, L.D. "Some Effects of Chordwise Fences on the Aerodynamic Characteristics of Four Moderately Sweptback Wings in the Low-Lift Range at Transonic Mach Numbers and at Mach Number 1.9." *RM L50E16.* NACA, 1950.

10. Jaquet, B.M. "Effects of Chord Discontinuities and Chordwise Fences on Low-Speed Static Longitudinal Stability of an Airplane Model Having a 35º Sweptback Wing." *RM L52C25.* NACA, 1952.

11. Johnsen, Frederick A., *Northrop F-5/F-20/T-38.* Warbird Tech Series, vol. 44. Minnesota: Specialty Press Publishers and Wholesalers, 2006.

12. Ken's Aviation, www.shanaberger.com. *Photo of MiG with Wing Fence.* 2007.

13. Killian, D. N. *The Aerodynamic Performance of the Houck Configuration Flow Guides*. Thesis, Air Force Institute of Technology, WPAFB OH, June 2007.

14. Macmillan Science Library: Space Sciences©. "T-38 Trainers", http://www.bookrags.com/T-38_Talon, 2006.

15. Modern Machine & Tool Co., Inc. *Balance Schematic.* Newport News VA, 2004.

16. NASA Technology Facts. "Winglets." *TF-2004-15 DFRC.* 2004.

17. Nichols, Robert H. “Turbulence Models and Their Application to Complex Flows". *Mississipi State University*, 2001.

18. Nickel, Karl and Micahel Wohlfahrt. *Tailless Aircraft.* American Institute of Aeronautics and Astronautics, Inc., New York NY, first edition, 1994.

19. Northrop Aircraft, Inc. “T-38 Basic Dimensions.” *Report No. 57-84.* 1957.

20. Northrop Corporation. *NAI-58-578 and NOR-65-212*, 1958 and 1965.

21. Queijo, M.J., Byron Jaquet, and Walter Wolhart. “Wind Tunnel Investigation at Low Speed of the Effects of Chordwise Wing Fences and Horizontal Tail Position on the Static Longitudinal Stability Characteristics of an Airplane Model with a 35º Sweptback Wing.” *Report 1203.* NACA, 1954.

22. Skow, A. “Strakes for Landing Speed Reduction.” *United States Patent.* Patent Number 5,249,762, October 1993.

23. Solfelt, Daniel A. *CFD Analysis of a T-38 Wing Fence*. Thesis, Air Force Institute of Technology, WPAFB OH, June 2007.

24. Solfelt, Daniel A. and Raymond C. Maple. “CFD Analysis of a T-38 Wing Fence,” *46th AIAA Aerospace Sciences Meeting and Exhibit.* AIAA 2008-331. January 2008.

25. Stuart, William G., *Northrop F-5 Case Study in Aircraft Design.* American Institute of Aeronautics and Astronautics, 1978.

26. Tennison, James G., James H. Manly, and Robert W. Parker. “Innovative Vortex Lift Enhancement concepts to Delay Buffet Onset and Reduce the Landing Approach Speed of the T-38.” *TR 92-001.* 1992.

27. United States Air Force Test Pilot School. *Flying Qualities Textbook: Volume II Part 2.* 1986.

28. United States Air Force. “Figure 2-2.” *T.O. 1T-38A-5.*

29. United States Air Force. *Modification Flight Manual, USAF Series Aircraft T-38A/B*, Edwards AFB CA.

30. United States Air Force. *T-38A Flight Manual,* August 2005.

31. United States Air Force. “Fact Sheet: T-38 Talon”, www.af.mil/factsheets/factsheet.asp?fsID=126, 2006.

32. Urban, Daniel A., and Roger J. Tanner. “T-38A Aircraft SETOS Performance Spot Check.” *AFFTC-TR-05-57*, Edwards AFB CA, June 2006.

33. White, F.M. *Viscous Fluid Flow.* New York: McGraw-Hill, third edition, 2006.

34. Williams, Michael, Jonathan Dietrich, Gian Luca Greco, Joshua Schneider, and Matthew Wroten. “Limited Evaluation of T-38 Wing Fence,” *Test Plan*, Edwards AFB CA, September 2008.

35. Williams, Michael, Jonathan Dietrich, Gian Luca Greco, Joshua Schneider, and Matthew Wroten. “Limited Evaluation of T-38 Wing Fence,” *Safety Plan*, Edwards AFB CA, September 2008.

36. Williams, Michael, Jonathan Dietrich, Gian Luca Greco, Joshua Schneider, and Matthew Wroten. “Limited Evaluation of T-38 Wing Fence.” *AFFTC-TIM-08-08*. Edwards AFB CA, September 2008.

37. Woolf, Reagan K. and Benjamin J. Reid. “T-38C Aircraft Performance Evaluation.” *AFFTC-TR-03-18*, Edwards AFB CA, September 2004.

38. Yechout, T. R. and S.L. Morris. *Introduction to Aircraft Flight Mechanics: Performance, Static Stability, Dynamic Stability, and Classical Feedback Control*. Reston, VA: American Institute of Aeronautics and Astronautics, 2003.

39. Zhidkosti, Mekhanika. “Flow on a Swept Wing in the Region of a Fence.” *Journal of Fluid Dynamics Vol. 3 No.6,* 84-86. July 1968.

Vita.

Michael Williams was born in Bartlesville, OK. He graduated from Bartlesville High School, in Bartlesville, OK in 1993. He went on to earn a Bachelors degree in Aeronautical Engineering from the United States Air Force Academy in Colorado Springs, CO from 1993 to 1997. Following graduation, he was commissioned as an Officer in the United States Air Force. In the fall of 2006 he began attending the Air Force Institute of Technology at Wright Patterson Air Force Base, Ohio for completion of his Masters Degree in Aeronautical Engineering. After graduation in March 2009, he will be stationed in Edwards AFB, CA in the 419 FLTS.

REPORT DOCUMENTATION PAGE

Form Approved
OMB No. 074-0188

1. REPORT DATE *(DD-MM-YYYY)*	2. REPORT TYPE	3. DATES COVERED *(From – To)*
26-03-2009	Master's Thesis	October 2006 – March 2009

4. TITLE AND SUBTITLE

Wind Tunnel Analysis And Flight Test of A Wing Fence On A T-38

5a. CONTRACT NUMBER

5b. GRANT NUMBER

5c. PROGRAM ELEMENT NUMBER

6. AUTHOR(S)

Williams, Michael D., Maj, USAF

5d. PROJECT NUMBER

5e. TASK NUMBER

5f. WORK UNIT NUMBER

7. PERFORMING ORGANIZATION NAMES(S) AND ADDRESS(S)
Air Force Institute of Technology
Graduate School of Engineering and Management (AFIT/ENY)
2950 Hobson Way, Building 640
WPAFB OH 45433-7765

8. PERFORMING ORGANIZATION REPORT NUMBER

AFIT/GAE/ENY/09-M20

9. SPONSORING/MONITORING AGENCY NAME(S) AND ADDRESS(ES)
United States Air Force Test Pilot School
Mr. Gary Aldrich
220 South Wolfe Avenue
Edwards AFB, CA 93524
661-277-8881

10. SPONSOR/MONITOR'S ACRONYM(S)

11. SPONSOR/MONITOR'S REPORT NUMBER(S)

12. DISTRIBUTION/AVAILABILITY STATEMENT

APPROVED FOR PUBLIC RELEASE; DISTRIBUTION UNLIMITED.

13. SUPPLEMENTARY NOTES

14. ABSTRACT

A low-speed wind tunnel study and flight tests were performed to examine the effects of a wing fence on the T-38A. Wind tunnel results were based upon force and moment data collected with a six-component balance and flow visualization at Reynolds numbers up to 0.3 x 10^6, based on mean aerodynamic chord. The model did not include the last 7.79 feet of the aircraft, and the engine and exhaust were modeled as through-holes. Five fence geometries, placed at wing station 125 (±0.825 semispan), were compared. The best performer of these designs, based on drag polar, was the fence that wrapped the leading edge and extended 84.6 percent of the local chord length along the wing's upper surface. Wind tunnel data showed that this fence increased the lift coefficient by up to 6.3 ± 0.6 percent and reduced spanwise and separated flow outboard the fence. The flight-tested fence was based on the best performing fence design from the wind tunnel study. The results were based on aircraft instrumentation and flow visualization at Reynolds numbers up to 9.98 x 10^6. It was inconclusive whether the fence caused an increase in lift coefficient. The fence reduced the roll-off tendency and wing rock during approaches to stall. Tuft visualization on the aircraft wing suggested that the fence reduced spanwise and separated flow outboard the fence, which agreed with the wind tunnel results.

15. SUBJECT TERMS

T-38 Aircraft, T-38A Aircraft, Stall, Wing Fence, Buffet, Tuft, Vortex Flow, Flow Visualization, T-38 Lift Curve, T-38 Drag Polar, Unsteady Flow, Air Photography, Flight Test, Vortices

16. SECURITY CLASSIFICATION OF:			17. LIMITATION OF ABSTRACT	18. NUMBER OF PAGES	19a. NAME OF RESPONSIBLE PERSON
a. REPORT	b. ABSTRACT	c. THIS PAGE			Dr. Mark Reeder
U	U	U	UU	267	19b. TELEPHONE NUMBER *(Include area code)* (937) 255-6565, ext 4530 (mark.reeder@afit.edu)